Fluid Dynamics of Hot Gas Ingress

Wang, Kevin

Award date:
2016

Awarding institution:
University of Bath

Fluid dynamics of hot gas ingress

Xiaohan Wang

A thesis submitted for the degree of Doctor of Philosophy

University of Bath

Department of Mechanical Engineering

June 2016

Abstract

The gas turbine engine, as an adaptable source of power, has been used extensively for electric power generation, mechanical drive and jet propulsion. Driven by competition within the industry, gas turbine engine manufactures strive to produce ever more efficient products that also comply with emission regulations. The overall efficiency, as a crucial parameter governing engine performance and life cycle operating costs, depends on a high turbine inlet temperature, as well as an appropriately high pressure ratio across the compressor. The turbine components operating at elevated temperatures could experience serious problems, such as unwanted creep, oxidation or thermal fatigue, which compromise the integrity and reduce lifespan. In modern gas turbine engines, cooling air bled from the compressor is used to prevent overheating of the turbine, through the secondary air system. As much as 25% of the compressor air bypasses combustion to be used for cooling and sealing purposes.

Hot gas ingress is one of the most important and intricate problems of the secondary air system faced by engine designers. Ingress occurs when the hot gas from the mainstream is ingested into the wheel-space, formed by the turbine disc and its adjacent casing. A rim seal is fitted at the periphery of the wheel-space, and a sealing flow of coolant is used to purge the cavity reducing or preventing ingress. Sufficient sealing flow is required, but an excessive use of coolant decreases overall engine efficiency. Therefore, from engine designers' perspective the use of sealing air must be minimised. Optimisation of the rim-seal design is a crucial approach to fulfil the purpose.

The double-clearance rim seal is widely employed in gas turbines, which consists of an outer-seal at the periphery of the wheel-space and an inner-seal located radially inboard. The annular cavity formed between the double-seal arrangement is known to predominantly confine the ingested hot gases, thus significantly reducing ingestion inboard of the inner seal. In order to study how double-clearance seals operate in depth, this thesis describes a new single stage turbine research facility, designed for conducting extensive and comprehensive experimental studies on ingress for different rim-seal configurations. Experimental study conducted with the new facility is reported for a variety of generic but engine-representative double-clearance seal configurations, to gain insights into the sealing effectiveness and fluid dynamics associated with different rim-seal design features.

Besides being adaptable for various rim-seal configurations, the research facility was also designed to be highly versatile in respect of wheel-space geometries and gas path blading, in order to investigate the impact on ingress from the aerodynamics both inboard and outboard of the rim seal. Extensive instrumentation was incorporated into the turbine stage for the measurements of pressure, swirl velocities, gas concentration and temperature. Additionally, the facility is capable of modelling

leakage flow paths found in actual gas turbines to explore novel techniques that could reduce ingress by utilising the leakage air.

A parametric study is presented for a range of double-clearance rim seal configurations, characterised by various design features both on the stator side and rotor side of the turbine disc system. Gas concentration measurements were made for each configuration to assess the relative sealing performance. The sealing effectiveness was determined both in the outer wheel-space between the double clearances, and in the inner wheel-space radially inboard of the inner-seal. These measurements constitute a research database that will support the design approach at Siemens, in conjunction with the theoretical model previously developed at Bath, which treats the seal clearance as an orifice ring and uses adapted Bernoulli's equation to correlate sealing flow rate and pressure difference across the seal. The sealing effectiveness is correlated with pressure and swirl ratio in the wheel-space to study the fluid dynamics associated with different rim-seal features, in support of rim-seal design and optimisations for secondary air systems.

Acknowledgements

First and foremost I would like to thank my supervisors Dr Carl Sangan and Professor Gary Lock for giving me the opportunity to join the gas turbine research group, work on the research project and complete my PhD. They have been truly supportive during my PhD study, providing valuable advice for my research and sharing their research experience, which helped me overcome difficulties during the design and commissioning of the test facility. Carl has offered constructive comments and suggestions on my PhD thesis during the final stage of my study.

I also would like to thank Professor Mike Owen for all the expertise on the ingress research that he has shared. His passionate elaborations of research topics provides valuable insights into the subject.

Dr Mike Wilson is also thanked for sharing his knowledge and understanding of the topic from the theoretical and computational aspects of the project.

Technical acknowledgement is given to Steve Thomas and Vijay Rajput for the their dedication in the construction and commissioning of the test rig, and the sharing of experience in solving problems throughout the research project.

Finally a special thank you is given to my colleagues in the aero-thermo postgraduate office, particularly GeonHwan Cho, James Scobie, Izzi Mear-Stone, Yogi Lalwani, Mario Patinios and Hui Tang from the gas turbine research group, Chen Chen and Jason Zhang from the aerospace group for the support they offered and also for making the office such a pleasant place to work.

Table of contents

Table of figures

Nomenclature

Symbols

A	area
b	outer radius of wheel-space; radius of simple disc
c	concentration
$C_{d,i}$, $C_{d,e}$	discharge coefficients for ingress, egress
C_F	flow coefficient [$= W/\Omega b$]
C_p	pressure coefficient in the annulus [$= (p_2 - \bar{p}_2)/(1/2)\,\rho\Omega^2 b^2$]
$C_{p,w}$	pressure coefficient in the wheel-space [$= (p_1 - p_{1,ref})/(1/2)\,\rho\Omega^2 b^2$]
C_w	non-dimensional flow rate [$= \dot{m}/\mu b$]
$C_{w,i}$, $C_{w,e}$	non-dimensional flow rates for ingress, egress
$C_{w,0}$	non-dimensional sealing flow rate
$C_{w,min}$	minimum value of $C_{w,0}$ to prevent ingress
C_{β_1}	modified internal swirl ratio [$= {\beta_1}^2(1 - {r_1}^2/{r_2}^2)$]
C_{β_2}	modified external swirl ratio [$= {\beta_2}^2({r_2}^2/{r_1}^2 - 1)$]
d	diameter
f	frequency
g	normalised pressure difference across seal clearance [$= (p_1 - p_{2,min})/\Delta p$]
G	gap ratio [$= S/b$]
G_c	seal clearance ratio [$= s_c/b$]
h_{out}	radial height of the outer wheel-space for double-clearance seals
K	empirical constant
K_t	stress concentration factor
$\dot{m}$	mass flow rate
$\dot{m}_i$, $\dot{m}_e$	mass flow rate for ingress, egress
N	safety factor
p	static pressure
q	heat
r	radius
R	correlation coefficient for linear fitting
Re_w	axial Reynolds number in the annulus [$= \rho W b/\mu$]
${Re_w}^*$	alternative definition of axial Reynolds number in annulus [$= \rho W c_x/\mu$]
Re_ϕ	rotational Reynolds number [$= \rho\Omega b^2/\mu$]
s	entropy

s_c	seal clearance
s_{ol}	axial overlap of radial clearance seal
S	axial clearance between stator and rotor
t_c	rotor-blade tip clearance
T	temperature; torque
U	bulk-mean velocity through rim-seal clearance [$= \dot{m}/2\pi\rho b s_c$]
v	volume
V_r	radial component of velocity
V_z	axial component of velocity
V_ϕ	tangential component of velocity
W	axial velocity in annulus
x	non-dimensional radius [$= r/b$]
z	axial distance
β	swirl ratio in wheel-space [$= V_\phi/\Omega r$]
Γ_c	ratio of discharge coefficients [$= C_{d,i}/C_{d,e}$]
Γ_p	pressure parameter [$= C_p/C_{\beta_1}$]
Γ_β	swirl parameter [$= C_{\beta_1}/C_{\beta_2}$]
ΔC_p	non-dimensional pressure difference [$= \Delta p/(1/2)\,\rho\Omega^2 b^2$]
Δp	external pressure difference [$= p_{2,max} - p_{2,min}$]
Δp_{in}	pressure drop across the inner seal [$= p_{out} - p_{in}$]
δ	radial deformation
ε	sealing effectiveness [$= C_{w,o}/C_{w,e} = \Phi_0/\Phi_e$]
ε_c	concentration effectiveness [$= (c_s - c_a)/(c_o - c_a)$]
ε_p	pressure effectiveness [$= 1 - \Gamma_c\{(1-g)/g\}^{3/2}$]
τ	shear stress
Φ	non-dimensional sealing parameter [$= C_w/2\pi G_c Re_\phi$]
Φ_i, Φ_e	value of Φ when $C_w = C_{w,i}$, $C_w = C_{w,e}$
Φ_{min}	value of Φ when $C_w = C_{w,min}$
Φ_0	value of Φ when $C_w = C_{w,0}$
θ	non-dimensional vane pitch
λ_T	turbulent flow parameter [$= C_{w,0}/({Re_\phi}^{0.8})$]
μ	dynamic viscosity
ρ	density
σ	stress; standard deviation

σ_{tys}	tensile yield strength of material
$\hat{\sigma}$	maximum stress
Ω	angular velocity of rotating disc

Subscripts

a	annulus
c	concentration
e	egress
EI	externally-induced ingress
hoop	hoop stress
i	ingress
in	inner wheel-space
max	maximum
min	minimum
out	outer wheel-space
rad	radial (stress)
ref	reference
RI	rotationally-induced ingress
r	radial coordinate; rotor
rev	revolution of rotor
s	stator
sf	safety factor
shear	shear stress
tys	tensile yield strength
ust	unsteady
z	axial coordinate
0	sealing flow
1,2	location in the wheel-space, annulus
ϕ	angular coordinate

Superscripts

$\bar{}$	averaged value
$\hat{}$	maximum value; outermost position

Abbreviations

SR	single-clearance radial seal configuration
DS	double-clearance seal configuration
FS	finned-seal configuration

Chapter 1 Introduction

1.1 History and development of industrial gas turbines

The first patent for a gas turbine concept was granted to John Barber in England in the year 1791, when reciprocating steam engines were still predominantly used for power generation. The conceptual drawing of the gas turbine arrangement is shown in Figure 1.1. In the following century, however, the focus of scientific and engineering workers was on the improvement of steam engines, rather than gas turbines.

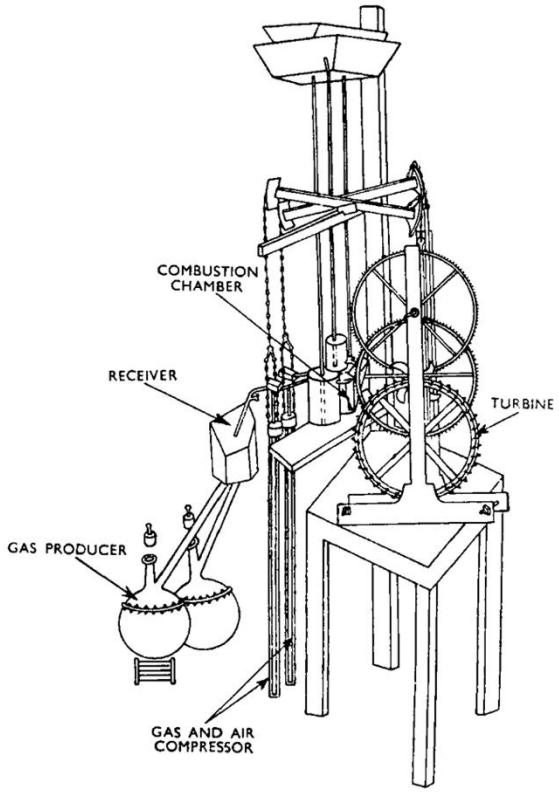

Figure 1.1 Drawing of a gas turbine concept – John Barber's patent (1791)

In the late 19th century, the first gas turbine was developed and built by Stolze. It comprised a multistage reaction gas turbine and a multistage axial compressor, which was highly novel at that time. Test runs, conducted between 1900 and 1904, were without success because massive amounts of compressed air were required for mixing with hot gases in order to reduce the thermal stress of turbine blades. The compressor struggled to meet the requirement, leading to the net output being negligible.

In 1905, Holzwarth developed an explosion turbine, also known as the constant-volume turbine. A mixture of fuel and compressed air exploded in the closed combustion chamber, causing a steep rise

in pressure. The compressor was no longer required to operate with a high efficiency, which was almost impossible to achieve at the time. Additionally, only a small excess of air was necessary for combustion, due to the use of water for cooling purposes. Brown Boveri built and tested a Holzwarth gas turbine between 1909 and 1913, which produced a net output of only 200 hp. In 1928, Brown Boveri manufactured an upgraded Holzwarth turbine. In 1933, it was installed in a German steel plant and operated with blast furnace gas. A photographic image of this turbine on site is shown in Figure 1.2.

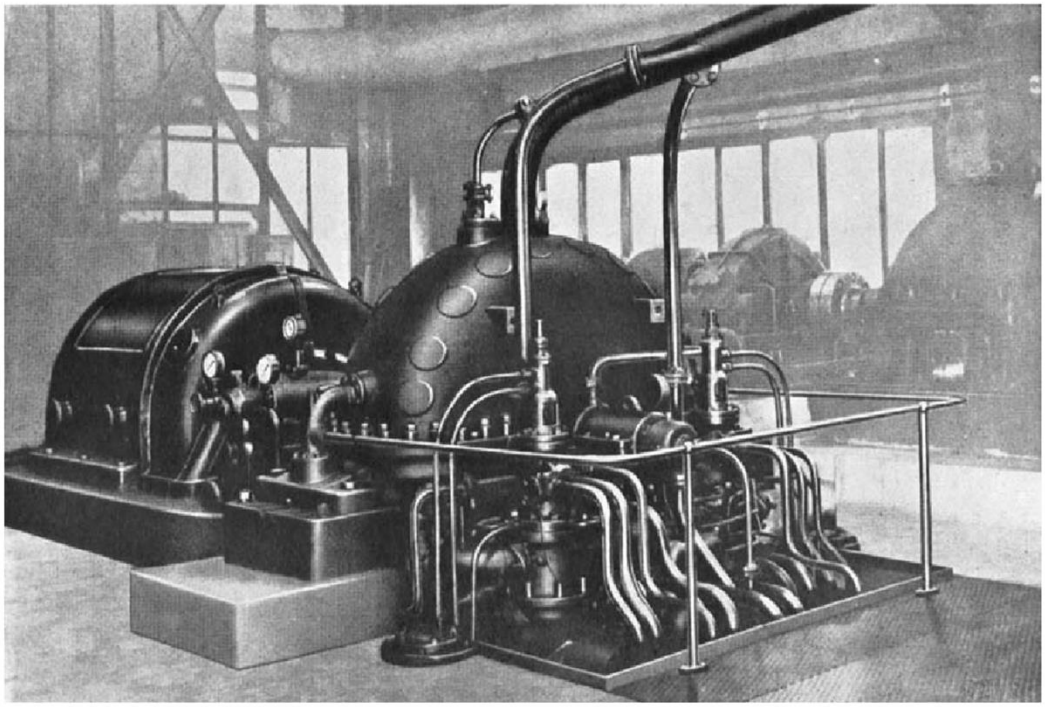

Figure 1.2 Holzwarth gas turbine on site – Meyer (1939)

The work done by Brown Boveri and Holzwarth boosted the development of the Velox boilers, which also led to the development of gas turbines, resulting in the 10 to 12 stage compressors and 4 to 5 stage reaction turbines. The cycle efficiency of gas turbine engines increases with turbine inlet temperature, which will be discussed in detail in section 1.2. At the time, a temperature of 810 K was considered safe for heat resisting steel turbine blades without cooling techniques; an output of 2000~8000 KW was achievable with compressor and turbine efficiencies of 73~75%, and an overall cycle efficiency of 17~18% (Meyer (1939)).

The economic use of a gas turbine engine for the generation of electricity was realised in 1939. A gas turbine set was ordered from Brown, Boveri & Cie (BBC), a Swiss turbine company, by the Municipal power station in Neuchatel, Switzerland. This turbine unit, known as the Neuchatel gas turbine, was the first successful electric power generation machine. It went into commercial operation as a standby unit, with a power output of 4 MW and an efficiency of 17.4%. The turbine operated at

3000 rpm with an inlet temperature of 823 K (ASME landmark award (2007)). The schematics diagram of the Neuchatel gas turbine power plant is illustrated in Figure 1.3.

In the same year, Adolf Meyer as the former director of BBC presented a paper entitled "The Combustion Gas Turbine: Its History, Development and Prospects" to the Institution of Mechanical Engineers. The author suggested future prospects of gas turbines based on the upcoming increase in the turbine inlet temperature from 810 K to 922 K (for the Neuchatel turbine), which corresponded to an increase in cycle efficiency from 18% to 23%.

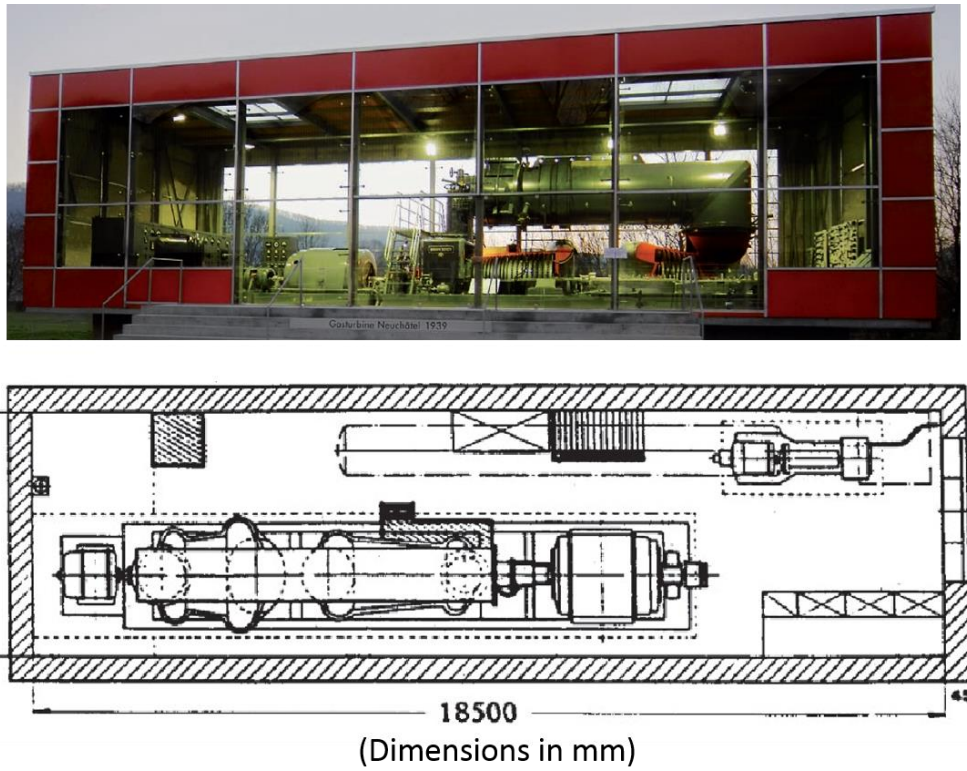

Figure 1.3 Neuchatel gas turbine power plant – ASME landmark award (2007)

Since then, tremendous effort was made to achieve higher cycle efficiencies by increasing the turbine inlet temperature. A combination of materials, thermal barrier coatings and cooling technologies was required to enable higher turbine inlet temperatures and boost the performance of gas turbines. The increase in performance predicted by Meyer in 1939 was later realised by Siemens on its VM 3 gas turbine, which had an output of 2.8 MW and an efficiency of 26% at a firing temperature of 922 K using uncooled vanes and blades. Meanwhile, a larger scale turbine was also under development. This was the VM 5 featuring an output of 5.6 MW and an efficiency of 29% with a turbine inlet temperature of 973 K.

The development of industrial gas turbines from 1940s to 2010s was characterised by the steady advancement achieved by Westinghouse, General Electric and Siemens, three major manufacturers

of industrial gas turbines during this period. Figure 1.4 shows the increase in the power output and cycle efficiency of gas turbine engines over the period from 1940s until present. Figure 1.5 illustrates the rising trend of the turbine inlet temperature and the overall pressure ratio in the same period. It can be seen the engines produced by different manufactures follow a similar path of improvement. The data used to produce the figures was extracted from Diakunchak *et al*. (2008) and Hunt (2011).

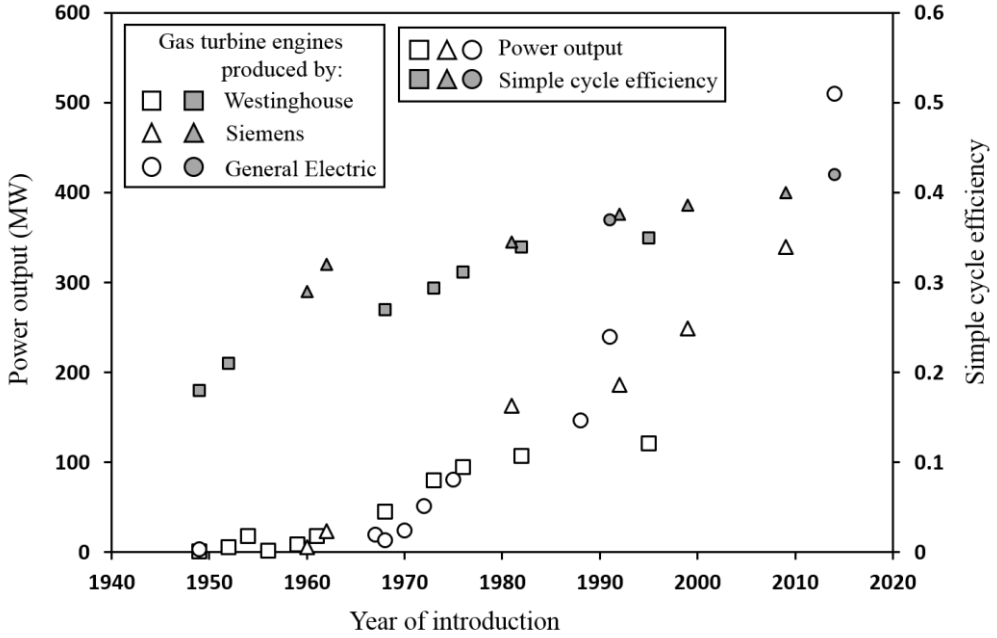

Figure 1.4 Trend of power output and efficiency for gas turbine engines

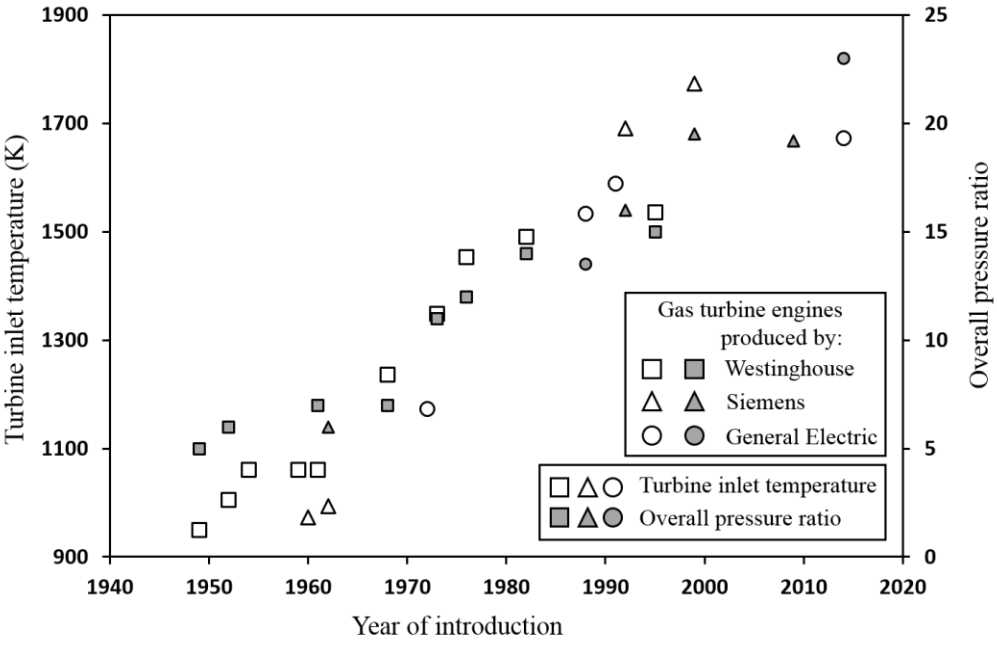

Figure 1.5 Trend of turbine inlet temperature and pressure ratio for gas turbine engines

1.1.1 Development at Westinghouse

In early 1960s, Westinghouse developed the W191 model, which was the most successful of the Westinghouse gas turbines at the time, with over 182 being sold. It was designed based on the W81, the first successful commercial unit made by the company. The W191 had a 18 MW output with a turbine inlet temperature of 1061 K. The unit was still being manufactured into the 1980s.

The power output was significantly increased on the next model W501 (1968), which featured a power generation of 45 MW, and a turbine inlet temperature of 1236 K. The engine series was continuously developed over the next 30 years, which comprised models from W501A to W501G. By the late 1990s, the power output of W501 series engines had increased from 45 MW to a level of 250 MW. The turbine inlet temperature was increased by more than 500 K, to about 1773 K found in the W501G; this was made possible by the advance in cooling and material technologies. The pressure ratio was enhanced from 7:1 to 20:1. The cycle efficiency was improved from 27% to 39%.

Gas turbine engines can be used for power generation in a simple-cycle power plant, or can be employed in a combined-cycle power plant using both gas and steam turbines together to produce more power from the same fuel than a traditional simple-cycle plant. In a combined cycle, the waste heat from the gas turbine engine is routed to the nearby steam turbine, which generates extra power.

It should be noted that the W501F model (shown in Figure 1.6, now designated as SGT6-5000F) was designed for both simple and combined cycle applications. The engine could operate in a combined cycle at 57% efficiency, compared with the 38% efficiency in a simple cycle application. The engine was also designed to be, to some extent, environment-friendly. Significant advances were made in its combustion system for reducing the NOx emission to the environment.

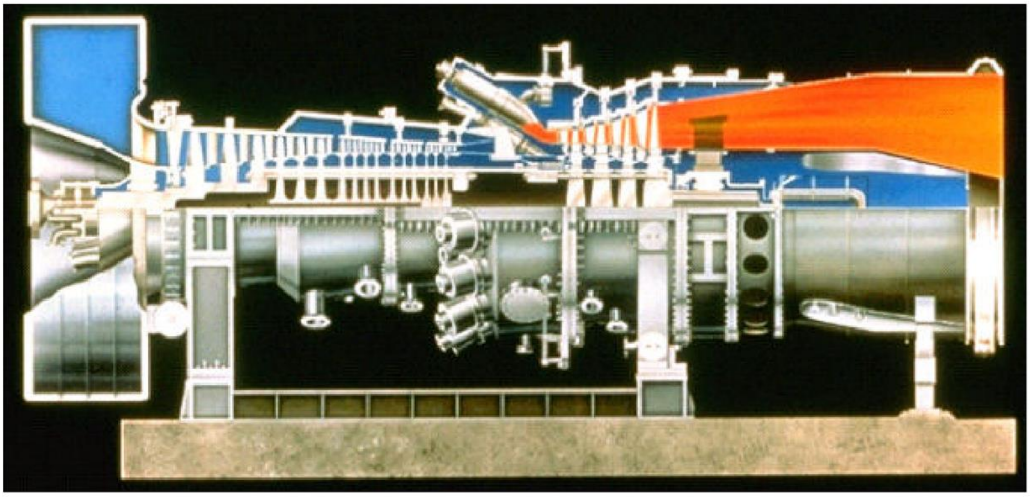

Figure 1.6 Westinghouse W501F (SGT6-5000F) gas turbine engine – Diakunchak *et al*. (2008)

The final model in the W501 series was the W501G. In 1992, Westinghouse entered a technology transfer agreement with Rolls Royce, which allowed the Rolls Royce aero engine design tools and codes to be employed in the design of W501G. Evolved from the previous W501F model, this engine incorporated further advancement in materials, cooling technology and aerodynamic design. When the W501G was introduced in 1997, it could operate with a combined-cycle efficiency of nearly 59%. The development of the W501G model was closely followed by the acquisition of Westinghouse by Siemens in 1998. Today it is referred to as the SGT6-6000G gas turbine.

1.1.2 Development at General Electric

General Electric (GE) heavy duty gas turbine delivered a 3.5 MW engine to the Belle Isle plant of Oklahoma Gas and Electric Company in 1949. This unit became the first gas turbine used for electric power generation in the United States. In the 1960s, GE introduced gas turbine models with an output level of 20MW, which were matched by those manufactured by Westinghouse and Siemens at the time. The advancement of GE gas turbines in the 1970s was characterised by the F series engines. The output had increased from 24 MW, generated by the F5 model, to about 80 MW featured by the F9 model. During 1960s and 1970s, aero-derivative engines were also developed in GE, namely the LM series. These engines were widely used in power generation, mechanical drive and marine applications. The power rating ranged from 4.5MW for the LM500 model to 100MW for the LMS100 model. Although aero-derivative engines proved to be equally powerful, there were discussions about overall economics and maintenance aspects relative to heavy duty industrial gas turbines.

From 1980 onwards, the E model engine was developed with unit rating increased above 100 MW. The E model continued to evolve during the 1990s, but with a modest turbine inlet temperature around 1393 K. A further step was taken in 1991 to introduce the FA series; the turbine inlet temperature was increased to above 1573 K and the output was enhanced to 240 MW. More recently, GE introduced its 9HA series gas turbine which could generate a simple cycle output of 510 MW with a turbine inlet temperature above 1673 K.

1.1.3 Development at Siemens

In order to consolidate its position in the gas turbine market, Siemens decided to build large scale engines in the 1960s. VM 80 was designed with a mass flow of 184 kg/s, a pressure ratio of 6:1, an output of 23.4 MW with an efficiency of 32% and a turbine inlet temperature of 993 K. The engine, shown in Figure 1.7, went into operation in 1962. A transition was made in the rotor design at the time. A ‘spool’ configuration was employed which is commonly seen in modern-day Siemens gas turbines. The new arrangement, referred to as the single case design, featured a common rotor shared by the compressor and the turbine, supported by two bearings. The drive to the generator was at the

compressor end allowing a straight through exhaust system. This design was applied to a different model VM 51, also shown in Figure 1.7.

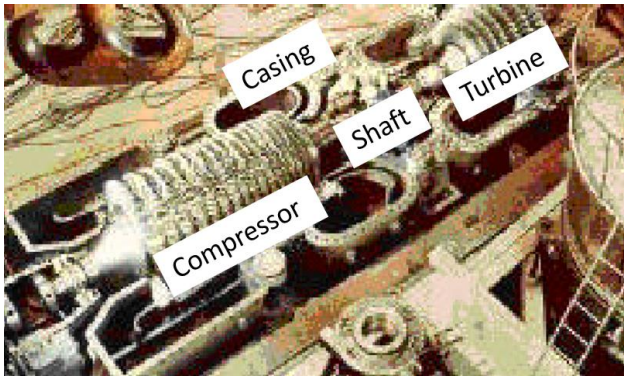

(a) Image of Siemens VM 80 gas turbine engine

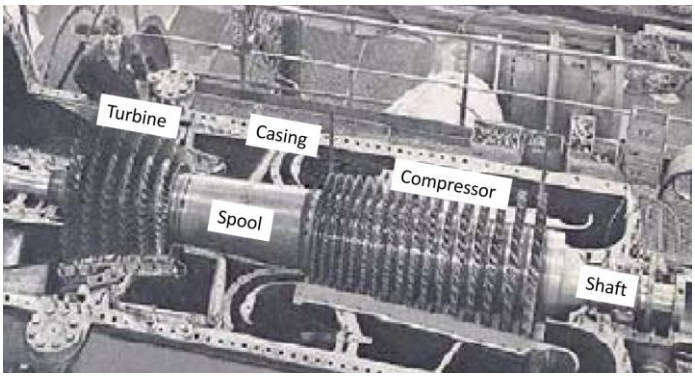

(b) Image of Siemens VM 51 gas turbine engine

Figure 1.7 Siemens VM series gas turbine engines – Diakunchak *et al.* (2008)

In the 1970s, Siemens developed the V94.2 model (for 50 Hz application) to meet the demand for heavy duty gas turbines (The equivalent 60 Hz version was designated as V84.2). The design was a success, as more than 240 units were deployed. The output, after extensive design improvements, was 163 MW with a simple cycle efficiency of 34.5%. Like the Westinghouse turbines during the same period, the V94.2 model could be used for both simple and combined cycle power plants, and met the target for emission reduction at the time. This model was more powerful than its rival of similar scale at Westinghouse.

The V-series engines were further developed by Siemens. The design of the Vx4.3A series was based on the proven technologies from Pratt and Whitney aero engines, as well as tested Siemens mechanical-design concepts. The Vx4.3A series were launched with the prototype V84.3A model, which was tested up to full load in Siemens' Berlin test bed in 1994. It achieved a new simple cycle efficiency record of 38% at the time. Since their introduction, the Vx4.3A series underwent enhancements in the compressor and turbine aerodynamic performance, and increases in mass flow and turbine inlet temperature.

Following the acquisition of Westinghouse Power Generation by Siemens in 1998, the decision was made to develop a new gas turbine that would utilise the experience and technology from both manufacturers. This is the SGT5-8000H model (Figure 1.8) featuring an output of 340 MW. It could also generate 530 MW with an efficiency above 60% in a combined cycle. Key features of the Vx4.3A series were kept and developed on this new model, such as the blade tip-clearance optimisation system.

New features were added, including an advanced sealing system for low cooling air demand and advanced materials for a higher turbine inlet temperature. The first operation of the engine was in Irsching power plant in 2007 (Figure 1.9). The SGT5-8000H was designed to operate with a high efficiency and meet low-emission targets, to maximise the profits of power plants while minimising environmental impacts in the future.

Compared with GE, Siemens is currently following a similar path in producing reliable, highly efficient and high power-density gas turbine engines to help operators meet increasingly dynamic power demands and low-emission targets.

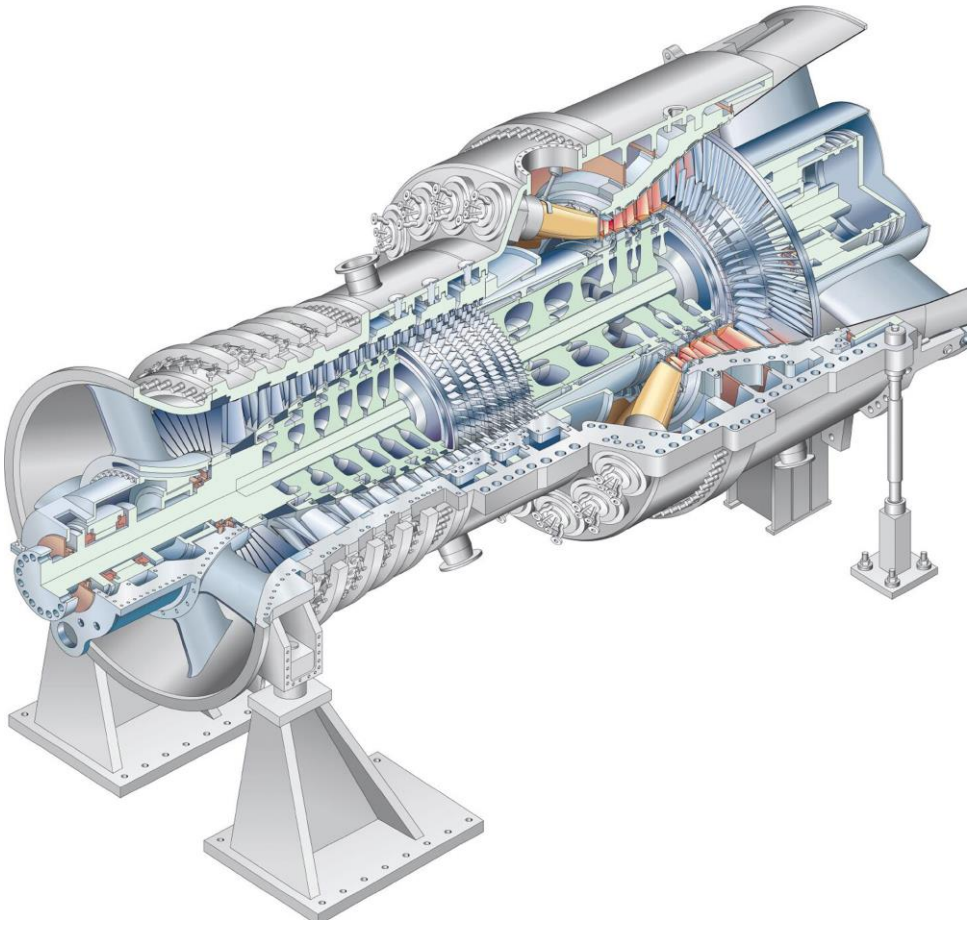

Figure 1.8 Siemens SGT5-8000H gas turbine engine

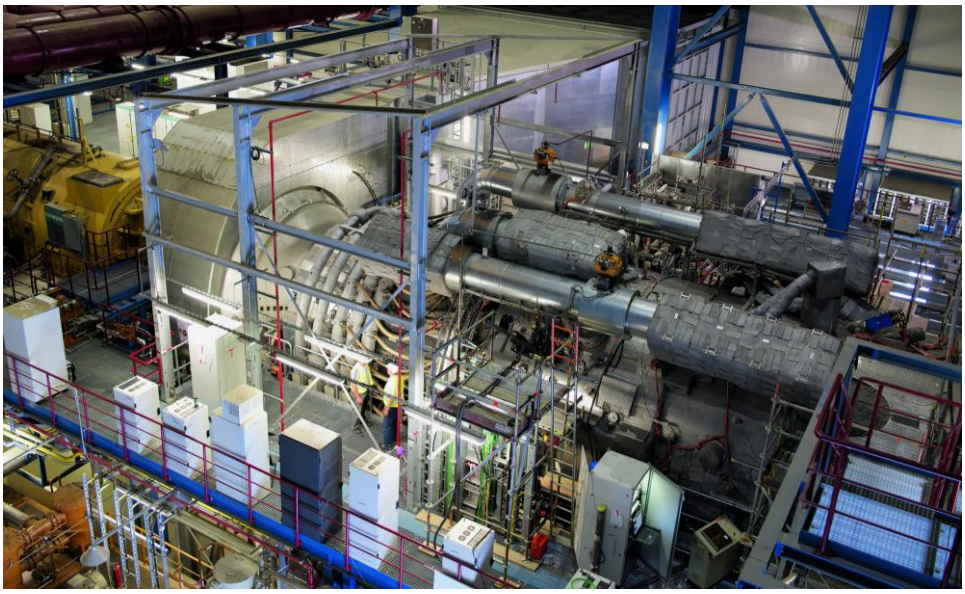

Figure 1.9 Photographic image of SGT5-8000H on site

The research into hot gas ingress documented in this thesis is closely related to the advancement of modern-day Siemens gas turbines. The work conducted by the author is aimed to support engine designers for the secondary air system, which provides the cooling and sealing of turbine components and cavities. With a highly efficient rim seal to reduce ingestion, the cooling flow of sealant bled from the compressor, which exerts penalty on engine efficiency, can be decreased. The turbine inlet temperature can be increased without causing overheating of turbine components, thus enhancing the engine efficiency and reducing the specific fuel consumption. The design of the research facility documented in this thesis is based on a Siemens industrial gas turbine; generic but engine-representative rim-seal configurations are studied to provide insights into ingestion problem.

1.2 Theoretical basis of gas turbine engines

This section introduces the theoretical basis of a simple gas turbine engine. The thermodynamic processes are described for an ideal Brayton cycle and the actual cycle considering irreversibility, followed by the effect of turbine inlet temperature and compressor pressure ratio on the overall cycle efficiency.

A simple gas turbine engine usually consists of a compressor unit, a combustion chamber unit and a turbine unit. The schematic diagram of a simple gas turbine engine is illustrated in Figure 1.10. Ambient air, as the working fluid, is drawn into the compressor. Work is done to the fluid by the compressor, increasing the air pressure and temperature. This air then enters the combustion chamber, which is located downstream of the final compressor stage. Fuel is injected and burnt in the combustion chamber resulting in high-temperature gases. These gases, with a high level of internal

energy, expand in the turbine stages while producing power by driving the turbine blades. The turbine drives the compressor, enabling a continuous operation of the engine.

When a gas turbine engine is used for aircraft propulsion, such as the turbojet, the turbine produces enough power to drive the compressor and the high-velocity exhaust gases produce the forward thrust for the aircraft. For an industrial gas turbine engine, the turbine produces more power than that required for driving the compressor. Therefore the turbine could also drive an electric power generator as in a power plant, or a propeller as for the naval application.

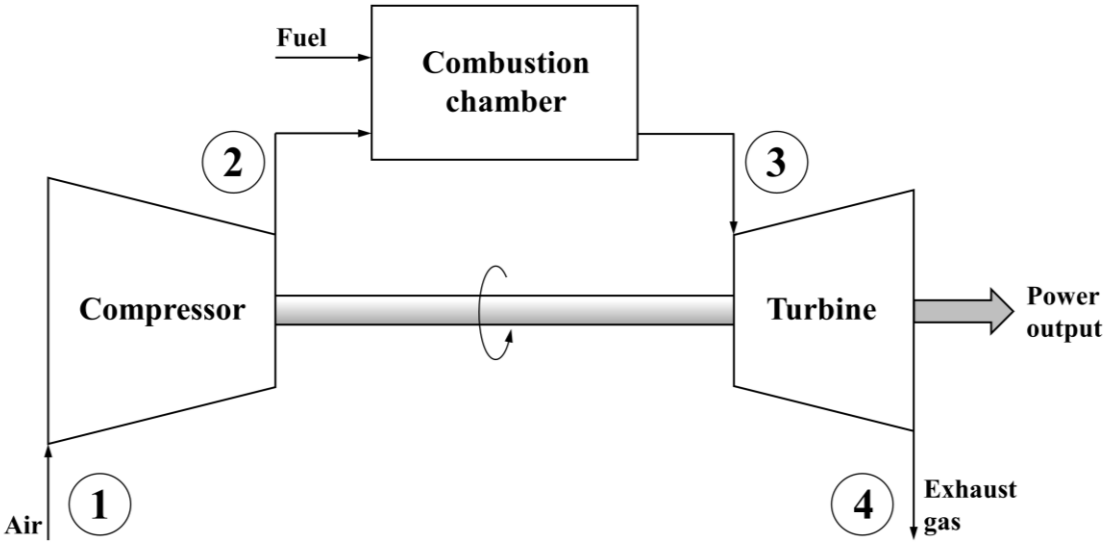

Figure 1.10 Schematic diagram of a simplified gas turbine engine

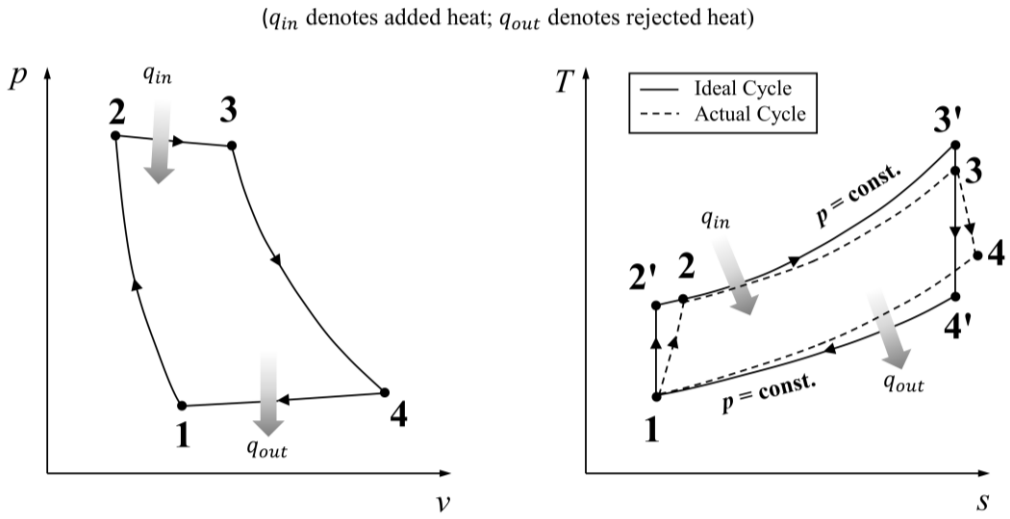

(a) *p-v* diagram (b) *T-s* diagram

Figure 1.11 Ideal and actual thermodynamic cycles for gas turbine engines

The ideal and actual thermodynamic cycles of gas turbine engines are shown in Figure 1.11. It should be noted that the state points in the *T-s* diagram and the *p-v* diagram correspond to those labelled in Figure 1.10. For an ideal cycle, the working fluid undergoes isentropic compression and isentropic expansion in the compressor and turbine respectively. In the combustion chamber, constant-pressure heat addition process takes place. However, for the actual gas turbine cycles, pressure drop in the combustion process is inevitable, and entropy increases in the compression and expansion processes due to irreversibility such as friction. The actual work input to the compressor is more and actual work output from the turbine is less because of the non-isentropic processes. The difference between ideal and actual cycles is highlighted on the *T-s* diagram shown in Figure 1.11 (b).

It can be seen from the thermodynamic cycle that the highest temperature occurs at state 3 at the end of the combustion process, namely the turbine inlet temperature. The cycle efficiency and work output of the engine depend on the turbine inlet temperature and the compressor pressure ratio. For a given pressure ratio, the cycle efficiency and work output increase with the turbine inlet temperature. However, this temperature is always limited by the maximum temperature that turbine components can withstand. For a fixed turbine inlet temperature, both efficiency and work output increase with pressure ratio before reaching a maximum, and reduce as the pressure ratio is further increased. Engine designers often choose an appropriately high pressure ratio which provides the levels of efficiency and work output that meet design targets.

1.3 Secondary air system of gas turbine engines

In order to achieve high cycle efficiencies and power outputs, the turbine inlet temperature has been steadily increased from about 800 K in the 1940s to over 1700 K today. Development of new materials and coating technologies has always been crucial for the turbine components to withstand such high temperatures. In spite of the significant advancement in metallurgy, components such as turbine blades, made of even the most heat-resistant alloy available today, would melt in a modern day gas turbine if no cooling is applied.

Figure 1.12 illustrates the development of material temperature limits and turbine inlet temperature in the 20th century. In the 1940s, the increase in material temperature limit was almost the same as the increase in the turbine inlet temperature. The turbine could operate normally with virtually no cooling air supplied. However, since the 1950s the gap gradually became larger between the temperature experienced by turbines and that allowed by metallurgy. In late 1990s, the gap had reached about 500 K and overheating of the turbine components could lead to catastrophic consequences. Therefore the cooling of turbine components is highly crucial to ensure the normal operation and functioning of the engine.

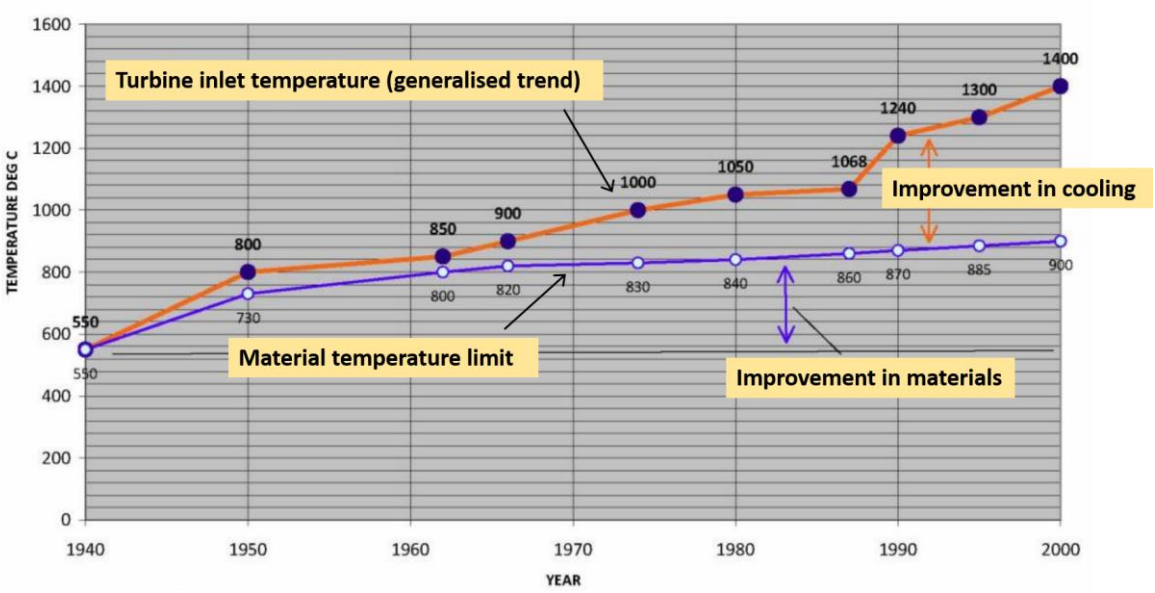

Figure 1.12 Development of turbine inlet temperature and material limits – Hunt (2011)

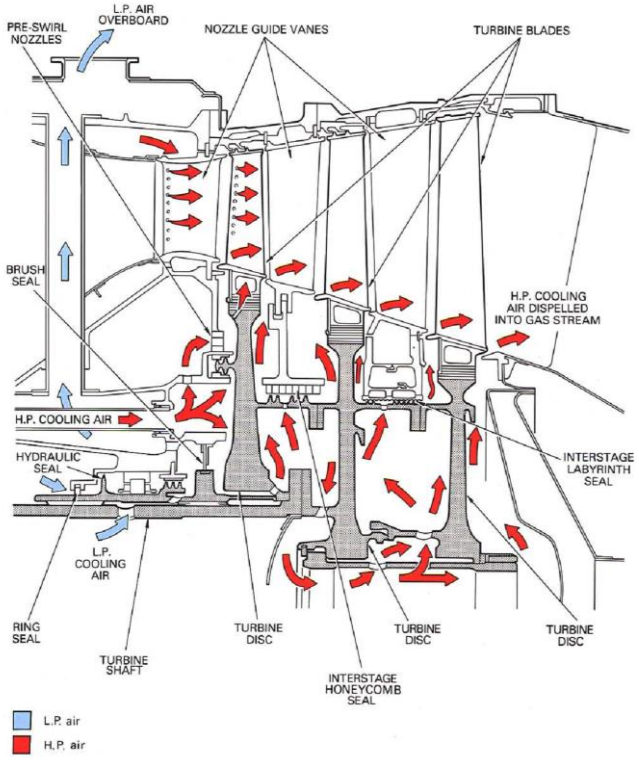

Figure 1.13 Cooling and sealing flows in a typical secondary air system – Rolls Royce (1996)

Cooling air, usually bled from the main flow path of the compressor, has been used to cool the turbine components. This air is distributed by the secondary air system, where the airflows do not directly contribute to engine thrust or power generation. The system performs important functions, including the cooling of turbine components (vanes, blades, discs, etc.), and the sealing of disc cavities and

bearing chambers. The demonstration of a typical secondary air system is shown in Figure 1.13. It should be noted that the compressed air used for cooling and sealing purposes comes at the expense of engine efficiency and work output. Up to 25% of the working fluid in the compressor mainstream may be directed to the secondary air system. It has been one of the most important tasks for designers to maintain the component integrity for an acceptable lifetime, while minimising the amount of secondary air required for this purpose.

1.4 Hot gas ingestion

Hot gas ingestion has been one of the most important and difficult problems facing engine designers. The hot gases in the mainstream annulus can be ingested into the wheel-space formed between the rotating disc and its adjacent stationary casing. The heat transfer between the ingested gases (ingress) and the turbine discs affects metal temperature gradients. The thermal stresses in the rotating disc can be raised significantly, reducing the component's cycle life. Overheating of the turbine disc can lead to structural failure and compromise the component integrity, causing catastrophic damages to the engine.

Hot gas ingress can be caused by the non-axisymmetric pressure variation (pressure asymmetries) in the annulus as the flow passes over the gas path blading (vanes and blades). Ingress and egress (fluid discharged from the wheel-space to the annulus) occur where the pressure in the mainstream is higher and lower respectively relative to the wheel-space. This type of ingress is referred to as the externally-induced (EI) ingress, as illustrated in Figure 1.14.

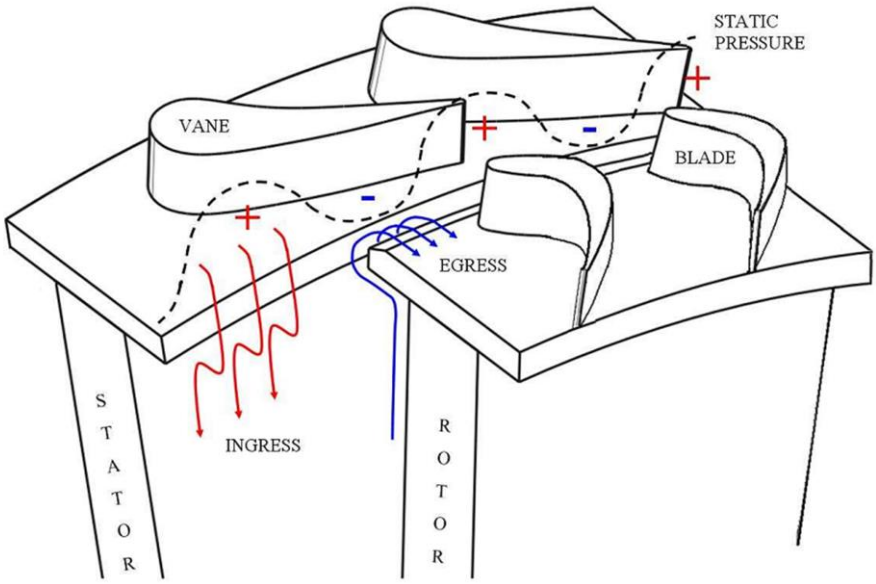

Figure 1.14 Externally-induced ingress and egress – Sangan *et al.* (2013a)

Ingestion can still occur when the external flow is axisymmetric. The fluid near the rotating disc is accelerated by friction, causing it to be pumped radially outwards. This leads to a reduction in pressure inside the wheel-space and can cause a pressure drop from the annulus to the wheel-space. A radially inward flow is driven by the pressure difference, causing the ingress into the wheel-space. This type of ingress is referred to as the rotationally-induced (RI) ingress. When the effects of EI and RI ingress are both significant, the term combined ingress (CI) is used.

In order to reduce or prevent hot gas ingress, a rim-seal arrangement is usually fitted at the periphery of turbine discs; a cooling flow of sealant, bled from the mainstream of compressor, is introduced into the wheel-space through the secondary air system. Figure 1.15 demonstrates the rim seal found in a typical high-pressure turbine stage. The sealing air pressurises the wheel-space and reduces hot gas ingestion. If too much working fluid in the compressor is used as the sealing air, the decrease in engine efficiency leads to an increase in specific fuel consumption. However, if the sealing flow is insufficient, the turbine components can be overheated causing serious damages. Therefore the engine designers want to minimise the amount of sealing flow required to ensure the turbine discs operating at acceptable thermal conditions. Experimental research plays a vital role in providing valuable insights into the complex flows and supporting the validation of 3D unsteady CFD codes as well as numerical design tools employed by engine designers.

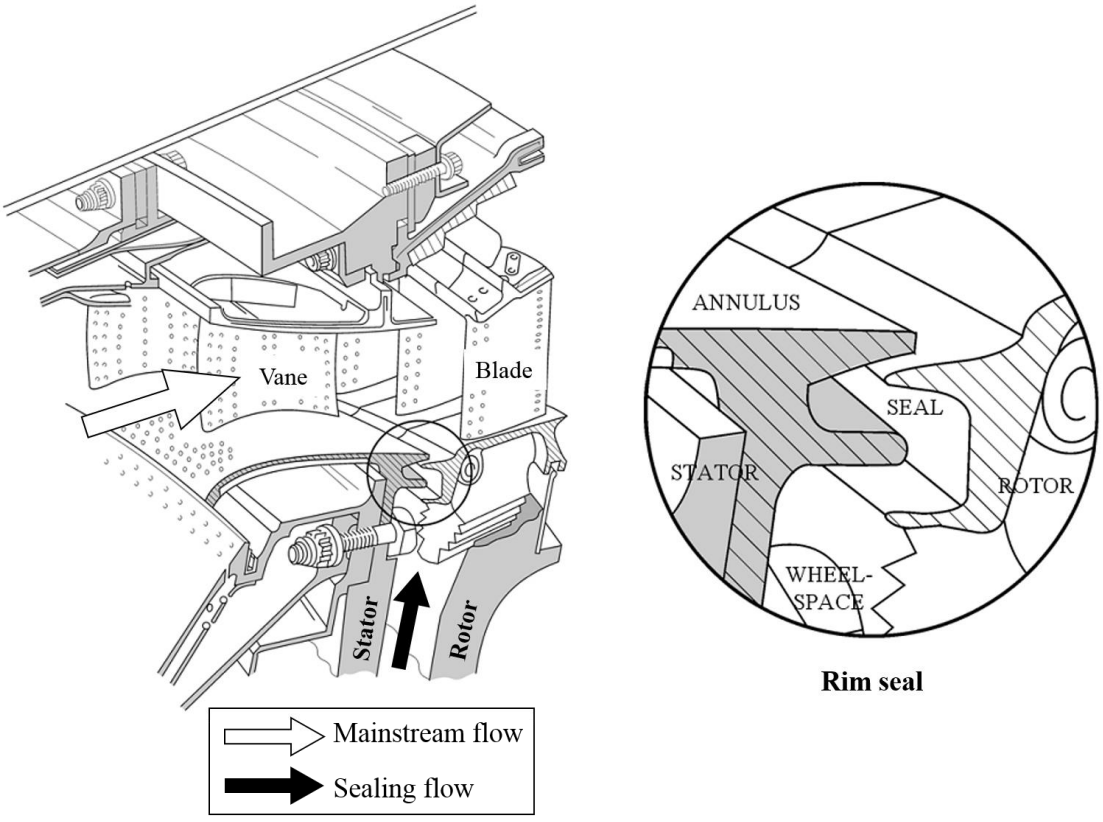

Figure 1.15 A typical high-pressure turbine stage with a rim-seal configuration

1.5 Thesis aims

Hot gas ingress, as a crucial cooling-air problem faced by engine designers, occurs when the hot gas from the mainstream is ingested into the turbine wheel-space through the rim seal. An efficient rim seal is required to minimise the sealing flow of coolant used to reduce ingress, thus bringing benefit to the engine's overall efficiency. The double-clearance rim seal with a higher sealing effectiveness, compared with the single-clearance seal, is widely employed in gas turbines. The double-clearance arrangement significantly reduces ingress by confining the ingested hot gas in the space between the outer-seal at the periphery of turbine discs and the inner-seal located radially inboard. This thesis aims at deepening the understanding of how generic but engine-representative double seals operate, and gaining insights into the fluid dynamics associated with the design features for both rim seals and wheel-space. The study shall be undertaken on a new research facility, designed not only to investigate rim-seal performance, but also for extending research into the ingress problem.

A new single-stage gas turbine experimental facility will be designed, constructed and commissioned. The turbine stage of the facility shall be specifically designed for conducting extensive and comprehensive experimental studies on ingress for different rim-seal configurations, including the double-clearance seals widely used in engines. Extensive instrumentation will be incorporated into the turbine stage for detailed measurements both in the wheel-space and the mainstream. Modular design approach will be applied to achieve high versatility for the wheel-space system: variable wheel-space geometries and gas path blading which alter the aerodynamics both inboard and outboard of the rim seal, allowing the impact on ingress to be studied. Moreover, the modelling of leakage flow paths existing in actual gas turbines shall be included in the design; novel techniques that exploit the leakage flow to reduce ingestion can be explored on the facility.

Following the commissioning of the facility, an experimental study will be undertaken for generic, but engine-representative double-clearance rim seal configurations with different design features. Measurements of gas concentration, pressure and swirl velocities will be used to assess the relative performance of each rim-seal configuration. Correlation of pressure and swirl ratio with sealing effectiveness determined from concentration measurements will lead to an improved understanding of wheel-space flow in relation to each specific seal configuration. This will support engine designers respecting rim-seal optimisation. Successful completion of this research will create an extensive database that can be rapidly exploited for the design methodology at Siemens.

1.6 Thesis outline

Chapter 1 introduces the history and development of industrial gas turbines. The theoretical basis for a gas turbine engine is briefly explained. The internal cooling and sealing air delivered through the secondary air system is described, followed by an introduction to the hot gas ingestion through rim seals. Finally the thesis aims are outlined.

Chapter 2 reviews the open literature respecting the research on hot gas ingestion. The fundamental flow physics of a simple disc and a rotor-stator system are described. This is followed by an extensive literature review of existing experimental, computational and theoretical research into hot gas ingress. The review also includes a summary of turbine test facilities at various research centres worldwide.

Chapter 3 details the design of the new single-stage gas turbine experimental facility. The structural design and instrumentation arrangements are described. The versatility of the modular facility is discussed, along with the capability enabling future research work.

Chapter 4 describes the baseline testing of the facility and experimental measurements for a generic single-clearance rim seal. The baseline testing studies the rotor dynamics of the turbine disc and determines the flow conditions in the annulus. The single-clearance seal performance is assessed based on the concentration measurements; the pressure and swirl velocities in the wheel-space are studied.

Chapter 5 presents a parametric study of generic, but engine-representative double-clearance rim seals with different stator-side features. The sealing effectiveness and fluid dynamics for each seal are evaluated and compared. Ranking of the seal performance is given.

Chapter 6 describes a study of double-clearance rim seals with different rotor-side features. The sealing effectiveness and fluid dynamics for each seal are evaluated and compared, followed by a ranking of seal performance.

Chapter 7 reports a comprehensive analysis for the studies documented in Chapter 5 and 6. Correlation of sealing effectiveness with pressure and swirl ratio is shown, to provide an improved understanding of the fluid dynamics for double-clearance seal.

Chapter 8 concludes the thesis and suggests future research possibilities.

1.7 Publication

Wang, X., Lock, G. D., Sangan, C. M., 2016. "An improved understanding of the performance and fluid dynamics for double-clearance rim seals". To be submitted to IMechE Journal: part C.

Chapter 2 Literature review

This chapter presents a review of literature respecting the research into hot gas ingress. The review begins with an introduction to the flow physics found in rotor-stator disc systems, to form a basic understanding of the fluid dynamics in turbine disc cavities and the secondary air systems. An extensive review on the ingress research is then presented, including the early-stage research work on the rotationally-induced ingress and the following studies on the externally-induced ingress. The literature is grouped by different research centres worldwide, and their respective contributions to this research field are detailed. This chapter ends with a brief review on some operating gas turbine research facilities that enlighten the rig design documented in this thesis.

2.1 Flow physics of rotor-stator disc systems

In order to study the flow physics in turbine-stage disc systems, a free disc rotating in a quiescent atmosphere is examined first. This scenario forms the basis for understanding the rotating flow in a rotor-stator disc system, formed by a rotating disc (known as rotor) and an adjacent stationary disc (known as stator). It is followed by a stationary disc surrounded by rotating fluid, which accounts for the stator-side flow characteristics in the system. These models are developed further to consider the complete rotor-stator disc system, representative of the turbine wheel-space formed by the turbine rotor disc and its adjacent stationary casing.

2.1.1 Free disc rotating in a quiescent atmosphere

The case of a rotating simple disc in an initially stationary air is traditionally known as the 'free disc'. A radius of b, and an angular velocity of Ω about the z-axis, are assumed for the free disc shown in Figure 2.1. The surrounding fluid is accelerated by friction from zero velocity in the free stream, to the disc speed, $V_\phi = \Omega r$, at the disc surface. The shear motion of fluid leads to a boundary layer developing on the disc surface. Inside the boundary layer, there is a radially outward flow resulting from the centrifugal force. To satisfy the conservation of mass, fluid is entrained axially into the boundary layer providing this radial outflow. The rotor acts as a 'pump' to continuously drive the fluid from the free stream to the periphery of the disc, usually known as the 'free disc pumping effect'.

Boundary layers develop on both sides of the free disc; only one side of the disc is considered in the figure due to symmetric flow physics. The flow regime in the boundary layer is governed by the local rotational Reynolds number defined as follows:

$$Re_{\phi,local} = \frac{\rho \Omega r^2}{\mu} \tag{2.1}$$

where r is the local radius on the disc surface.

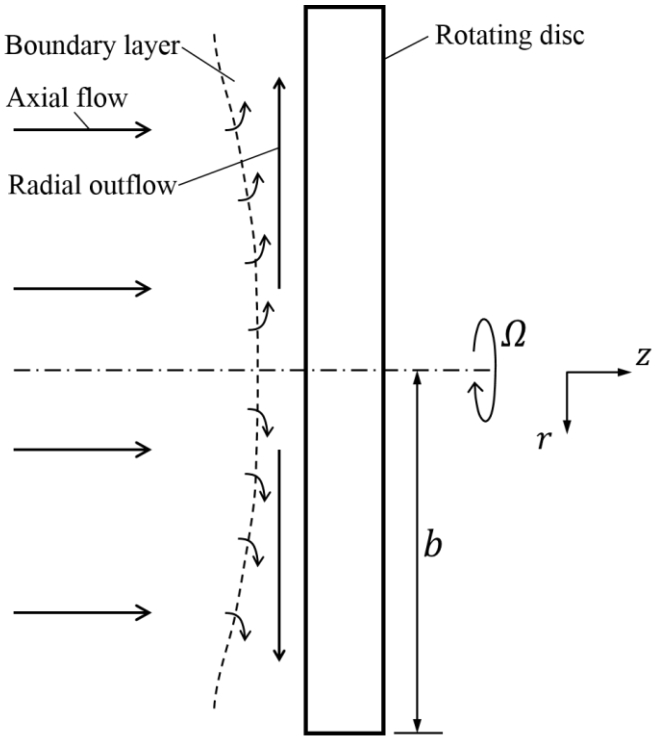

Figure 2.1 Free disc rotating in a quiescent atmosphere

Childs (2011) suggested the breakdown of laminar flow and the onset of transitional flow could begin at a local rotational Reynolds number of $Re_{\phi,local} \approx 2 \times 10^5$; the actual value may depend on the specific local flow condition and the disc-surface smoothness. The flow is usually laminar near the disc centre with all values of Ω; at a higher radius the flow may become turbulent for large values of Ω, with transitional flow between the two regions.

Daily and Nece (1960) experimentally investigated the flow regimes in a rotor-stator system; four regimes, as shown in Figure 2.2, were categorized as a function of the rotational Reynolds number Re_ϕ and the gap ratio G. The Re_ϕ was defined as

$$Re_\phi = \frac{\rho \Omega b^2}{\mu} \tag{2.2}$$

where the disc radius b was used for the characteristic dimension.

The gap ratio G was defined as

$$G = \frac{s}{b} \tag{2.3}$$

where s was the axial gap between the stator and rotor.

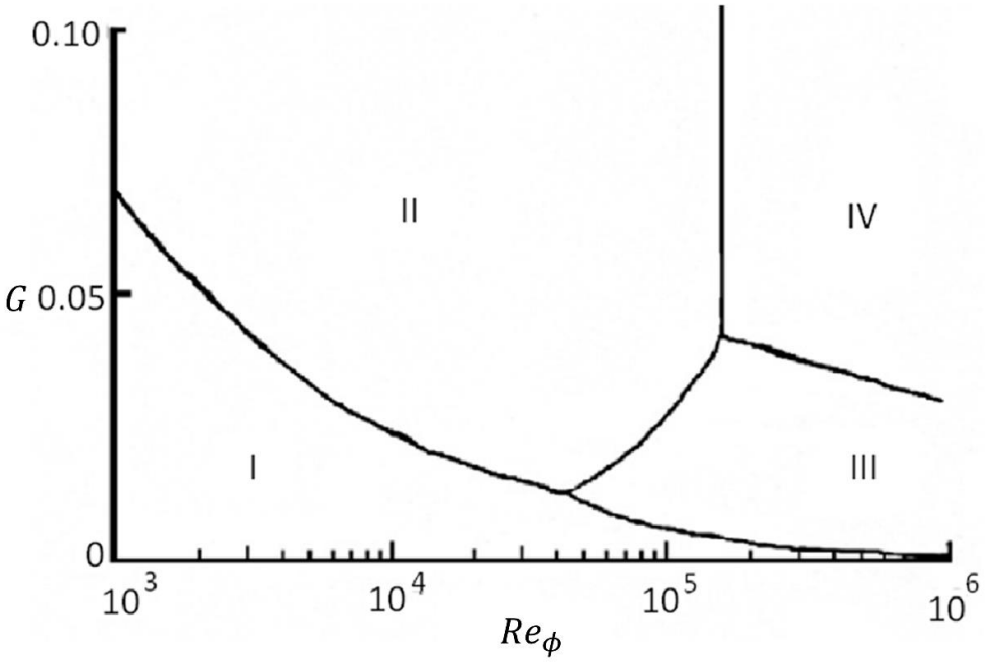

Flow regime	Characteristics
I	Laminar flow and low values of G, with merged boundary layers
II	Laminar flow and high values of G, with separate boundary layers and a rotating core
III	Turbulent flow and low values of G, with merged boundary layers
IV	Turbulent flow and high values of G, with separate boundary layers and a rotating core

Figure 2.2 Flow regimes in a rotor-stator system – Daily and Nece (1960)

2.1.2 Stationary disc in a rotating fluid

This section discusses a stationary simple disc surrounded by a rotating flow of air with an angular velocity of Ω about the z-axis, as shown in Figure 2.3. For the rotating flow to remain at a steady state, there must be a radial pressure gradient to balance the centrifugal force.

For the rotating flow near the stationary disc, the rotational velocity is decreased from Ωr in the free stream to zero on the disc surface. A boundary layer develops on the disc surface; inside the boundary layer is a radial inflow of air driven by the pressure gradient. An axial flow away from the disc is formed by the fluid leaving the boundary layer. The air in the free stream is entrained into the boundary layer from the periphery of the disc to satisfy the conservation of mass. The flow physics discussed above is expected to be found near the stator of a rotor-stator disc system.

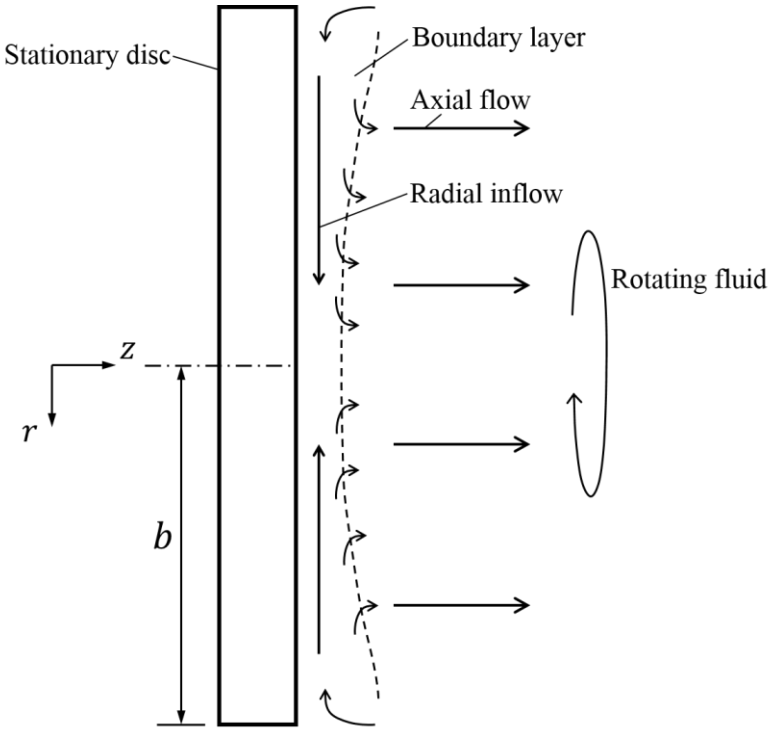

Figure 2.3 Stationary disc in a rotating fluid

2.1.3 Flow physics in a rotor-stator system

Rotor-stator systems are commonly found in gas turbine stages. A generic rotor-stator disc system is shown schematically in Figure 2.4. A cavity is formed between the rotor and stator, traditionally known as the wheel-space. Prior to the advent of numerous experimental measurements and numerical analysis, theories were developed for the flow structure in the wheel-space.

Batchelor (1951) proposed that there was a rotating core of fluid between the rotor and stator and the core rotated at an angular velocity that was a fraction of the rotational velocity for the rotor. It was implied that boundary layers developed on both the rotor and stator disc surfaces, separated by the central core. The fluid in the core would be entrained into the rotor-side boundary layer and pumped radially outwards. On the stator side, fluid would enter the boundary layer at the periphery of the stator, and flow radially inwards providing for an efflux from the stator to the rotating core, in line with the pattern discussed in the previous section.

This type of flow structure, traditionally referred to as the Batchelor flow model, was later supported by Mellor *et al*.(1968) and Chew and Vaughan (1988). A simplified diagram for the Batchelor flow model is shown in Figure 2.5.

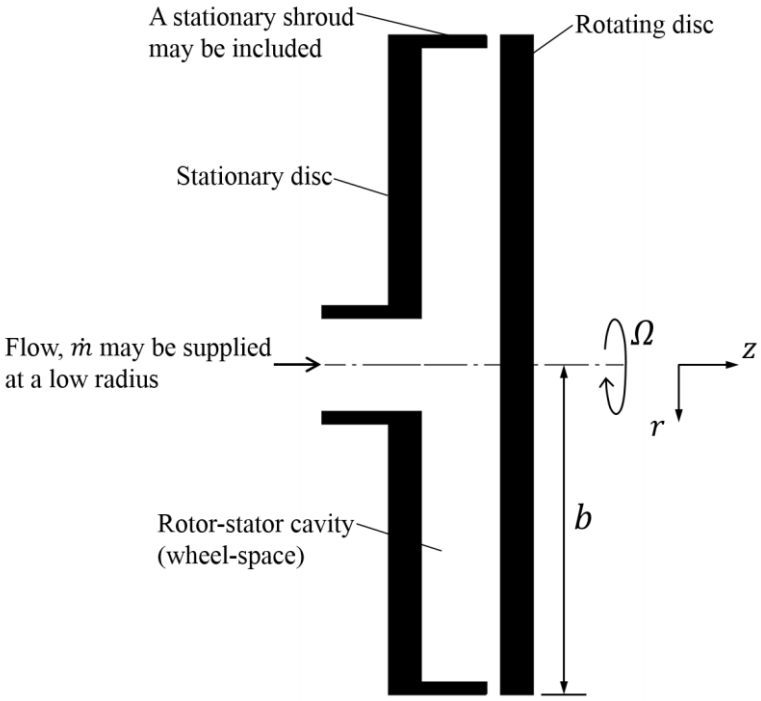

Figure 2.4 A generic rotor-stator disc system

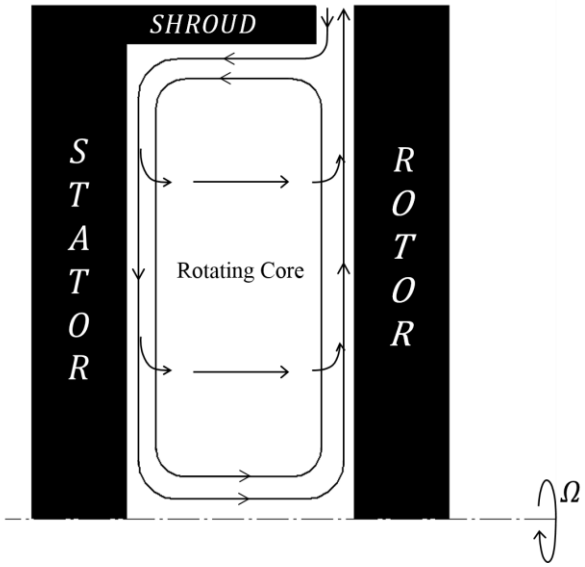

Figure 2.5 Diagram for the Batchelor flow model in a rotor-stator disc system

Also in the 1950s, Stewartson (1953) suggested a different flow model with no rotating core existing in the wheel-space. According to the Stewartson flow model, the flow structure was similar to the free disc case, where the tangential velocity in the rotor-side boundary layer would decrease from the disc speed to zero away from the boundary layer.

Childs (2011) summarised the characteristic velocity profiles in a rotor-stator system for both flow models, as shown in Figure 2.6. For the Batchelor flow model, there is a rapid change of tangential velocity inside each boundary layer. The radial velocity profile shows the radial outflow and inflow on the rotor and stator surface respectively. In the rotating core, the tangential and axial velocity components are virtually invariant with the axial distance from the disc surface; the radial velocity component is close to zero. For the Stewartson flow model, the tangential velocity component decreases continuously from the disc speed on the rotor to zero on the stator; the radial velocity profile shows the radial outflow in the entire wheel-space, with the radial velocity component decreasing gradually from rotor to stator.

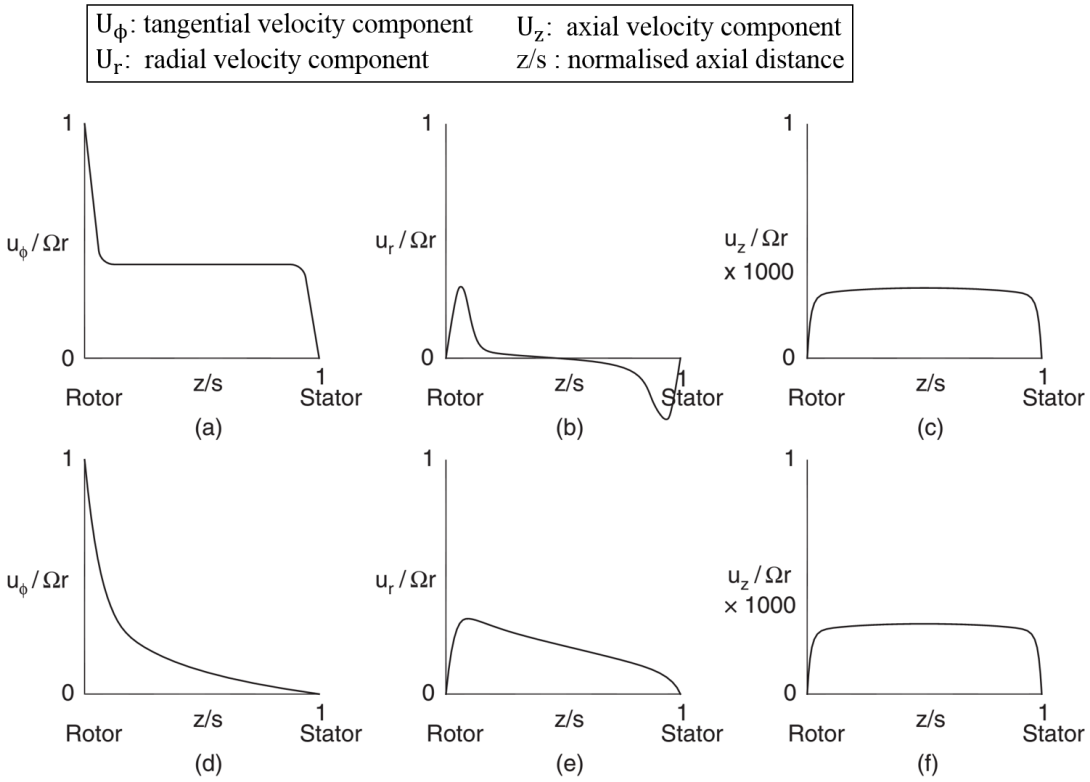

Figure 2.6 Characteristics velocity profiles in a rotor-stator system – Childs (2011)
((a), (b) and (c) for the Batchelor flow model; (e), (d) and (f) for the Stewartson flow model)

For a rotor-stator system with shrouds fitted at the periphery of the discs, Picha and Eckert (1958) showed that the core rotation did exist. In general, the core rotation decreases with an increase in the flow rate for a superposed flow entering the system from a low radius (Poncet *et al*. (2005)). Once a critical level of sealing flow rate (free-disc entrainment rate) is surpassed, the core rotation will reduce to zero and the Batchelor flow may transform to the Stewartson flow. Calculation by Owen and Rogers (1989) showed this critical flow rate for turbulent flow over a free disc to occur when $\lambda_T = 0.22$, where λ_T is the turbulent flow parameter defined as follows:

$$\lambda_T = C_{w,o} Re_\phi^{-0.8} \tag{2.4}$$

where $C_{w,o}$ is the non-dimensional sealing flow rate.

For the rotor-stator system studied in this thesis, the rotor and stator are both shrouded discs. The level of sealing flow rate introduced into the system is much smaller than the critical value. Therefore the Batchelor flow is expected to be found in the wheel-space of the turbine stage investigated in this thesis, based on the wheel-space configuration and the flow conditions employed in the experimental research.

2.2 Research into hot gas ingress

Based on the introduction in the flow physics of rotor-stator systems, this section reviews the research into hot gas ingress, including the early-stage research work focused on the rotationally-induced ingress and the more recent studies on the externally-induced ingress. Contributions made by various research groups are detailed, followed by a brief review on some operating gas turbine research facilities that enlighten the rig design documented in this thesis.

2.2.1 Rotationally-induced ingress

Early-stage research into the hot gas ingress was performed at University of Sussex, supported by Rolls-Royce Ltd. Experimental measurements were conducted using a rotor-stator disc system that modelled a single turbine stage.

Bayley and Owen (1970) experimentally studied an air-cooled turbine disc using a rotor-stator disc configuration which resembled the disc system shown in Figure 2.4. The wheel-space was superposed with a cooling flow which entered the cavity from the stator centre. Due to the pressure gradient created by the rotating fluid in the system, the pressure in the wheel-space was sub-atmospheric and external fluid was drawn into the wheel-space, thus allowing the rotationally-induced (RI) ingress to occur. Increasing the superposed flow rate gradually increased the pressure in the wheel-space and consequently reduced the amount of ingress. With sufficiently high flow rates, the ingress was prevented completely, and the system was 'sealed'. Correlation was conducted, which showed $C_{w,min}$, the minimum sealing flow rate to seal the system, was proportional to the seal clearance ratio G_c ($G_c = s_c/b$), and the rotational Reynolds number, Re_ϕ. An empirical criterion was proposed as follows:

$$C_{w,min} = 0.61 G_c Re_\phi \tag{2.5}$$

where $Re_\phi \leq 4 \times 10^6$ and $G_c \ll G$ (gap ratio, $G = s/b$).

The research into RI ingress was expanded by Phadke and Owen (1983). Pressure measurements were used to assess ingress through radial-clearance rim seals fitted at the periphery of the wheel-space. Experiments were conducted with a gap ratio of $G = 0.1$ and $Re_\phi \leq 4 \times 10^6$. For the radial seals where the stationary shroud overlapped the rotor, pressure in the wheel-space was found to increase, rather than decrease, with increasing rotational speed. This phenomenon was referred to as the 'pressure-inversion effect' by the authors. This effect was found to be beneficial for the reduction of $C_{w,min}$ and was shown to be stronger with a larger shroud overlap. It was suggested that the free disc pumping effect was not the cause, and a definitive explanation needed further research. Seal configurations with different clearances and overlaps were tested. Results showed the configuration with the largest overlap had the best seal performance among all the evaluated seals.

Phadke and Owen (1988a) expanded on their research into RI ingress with seven different rim-seal geometries. Measurements of pressure, gas concentration and flow visualisation were performed. Nitrous oxide was injected into the sealing flow and the concentration was sampled in the wheel-space. It was shown that there was little axial variation of gas concentration in the rotating core of fluid. The schematic diagrams for the flow structures were presented by the authors, as shown in Figure 2.7.

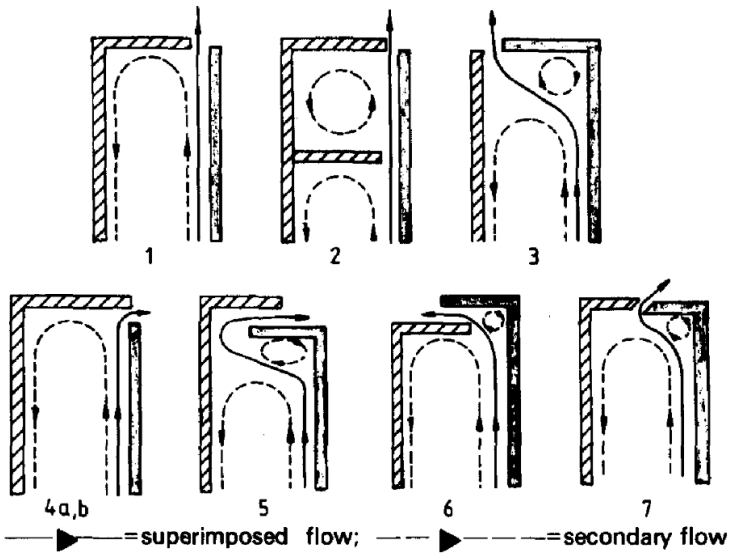

Figure 2.7 Diagrams of flow structures for different seal geometries – Phadke and Owen (1988a)

The aforementioned pressure-inversion effect was seen again for seal configuration 4 and 5. Flow visualisations revealed the radial outflow impinged on the stator for these two seal configurations. The authors suggested that a fluid curtain was probably created at the periphery of the wheel-space which helped reduce the flow through the seal clearance, thus allowing the internal pressure to increase with rotational speed.

Phadke and Owen (1988b) developed their research by adding external flow to the rotor-stator system. There was no stationary nozzle guide vane or rotor blade included and the mainstream gas path was set for an axisymmetric flow condition. Three previously studied seal configurations were re-examined with flow visualisation, pressure and gas concentration measurements. Both rotational Reynolds number (Re_ϕ) and external-flow Reynolds number (Re_w) were varied to generate different levels of flow coefficient ($C_F = Re_w/Re_\phi$). The results were qualitatively similar irrespective of measurement techniques.

Two regimes were found depending on the flow coefficient C_F. With low values of C_F, the rotor-stator system was shown to be in a rotation-dominated regime; with high values of C_F, the

system was governed by an external-flow dominated regime. For every tested configuration, both regimes were visible as demonstrated in Figure 2.8. With low levels of C_F, the $C_{w,min}$ was shown to increase with Re_ϕ in line with the correlation reported by Bayley and Owen (1970). With high levels of C_F, the $C_{w,min}$ was shown to increase with Re_w, but the effect of Re_ϕ was relatively insignificant.

It was suggested by the authors that low-magnitude pressure asymmetries were created in the mainstream flow because of the annulus configuration, although the annulus was set for an axisymmetric flow condition. With an increasing level of Re_w, it was shown that there was a greater impact on ingress from the increasing external pressure asymmetries; ingress was probably no longer dominated by the disc rotation as shown in earlier studies of the RI ingress.

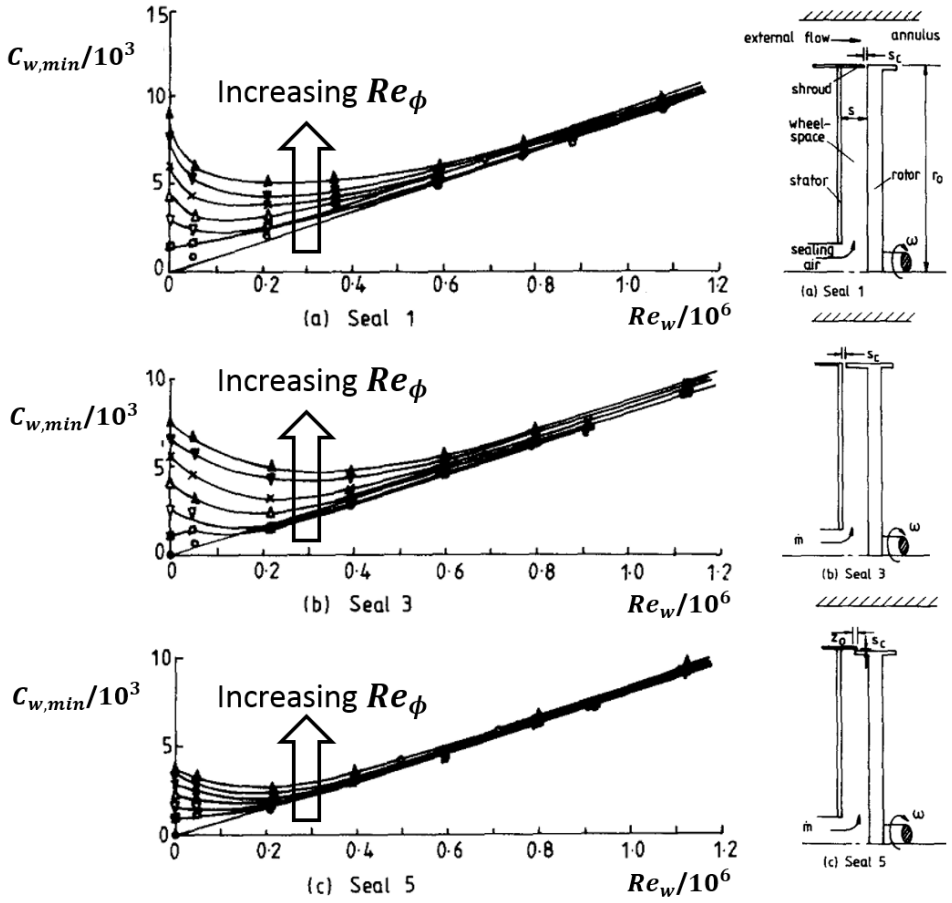

Figure 2.8 Variation of minimum purge flow rate with flow coefficient – adapted from Phadke and Owen (1988b)

Following the experimental studies reviewed above, theoretical modelling became another important approach adopted by the Sussex group in the 1990s. Chew (1991) proposed a mathematical model based on momentum integral methods to predict the minimum sealing flow rate. It was shown that

there was a good agreement between the theoretical prediction and the measurements made by Graber *et al*. (1987), as demonstrated in Figure 2.9.

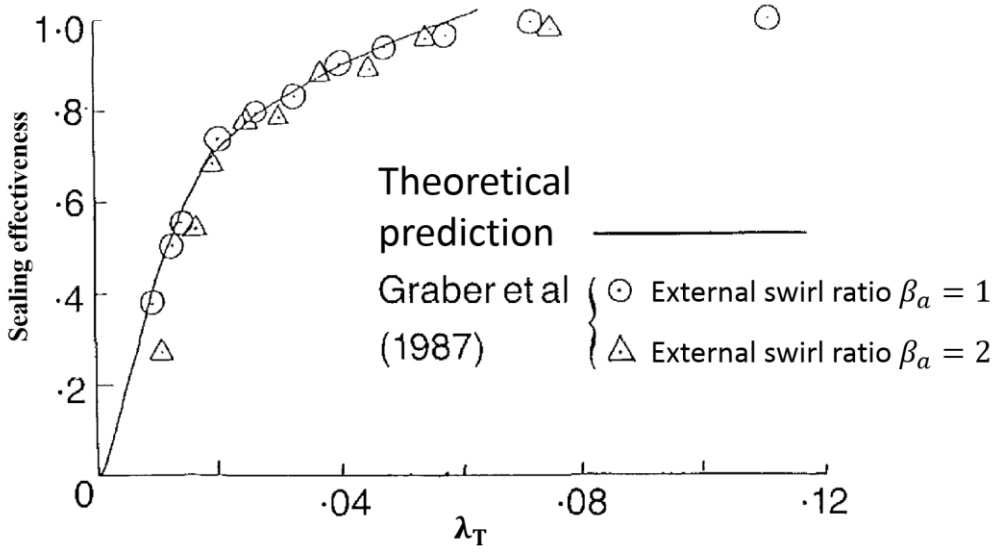

Figure 2.9 Comparison between theoretical prediction and measurements – adapted from Chew (1991)

In conjunction with the theoretical model reviewed above, Dadkhah *et al*. (1992) experimentally studied two different radial-clearance seal configurations with axisymmetric external flow in a 1.5 stage turbine. These two seals were installed in the upstream and the downstream wheel-space respectively. Pressure and concentration measurements were made to assess the performance of each seal. The swirl ratio determined in the wheel-space was shown to be in fair agreement with the theoretical prediction for low sealing flow rates. The experimental measurements and theoretical modelling were conducted in support of each other for the research into RI ingress. Chew *et al*. (1992) re-evaluated their theory with the research data from Dadkhah *et al*. (1992).

Hot gas ingress was also studied in the UTRC (United Technologies Research Center) at East Hartford, supported by Pratt & Whitney Ltd. Graber *et al*. (1987) and Daniels *et al*. (1992) reported experimental studies on the RI ingress with an internal air systems facility for different rim-seal configurations. The rim seals were formed with modular attachments fitted to the turbine rotor disc. The diameter of the stator disc was modified to achieve different radial-clearance seal configurations. The stator could also be moved along the axial direction allowing the variations of wheel-space gap and the seal overlap.

An axisymmetric flow of air was introduced in the annulus to form the main gas path, and a sealing flow of coolant was directed into the system at a low radius from the stator side. Measurements of

gas concentration were made to determine the sealing effectiveness ε_c. A non-dimensional coolant flow rate, η_t, was defined as follows:

$$\eta_t = \left(\frac{\dot{m}_o}{4\pi\mu b}\right) / Re_\phi{}^{0.8} = \frac{\lambda_T}{4\pi} \tag{2.6}$$

where $\dot{m}_o$ was the coolant mass flow rate and b was the radius of rim seal.

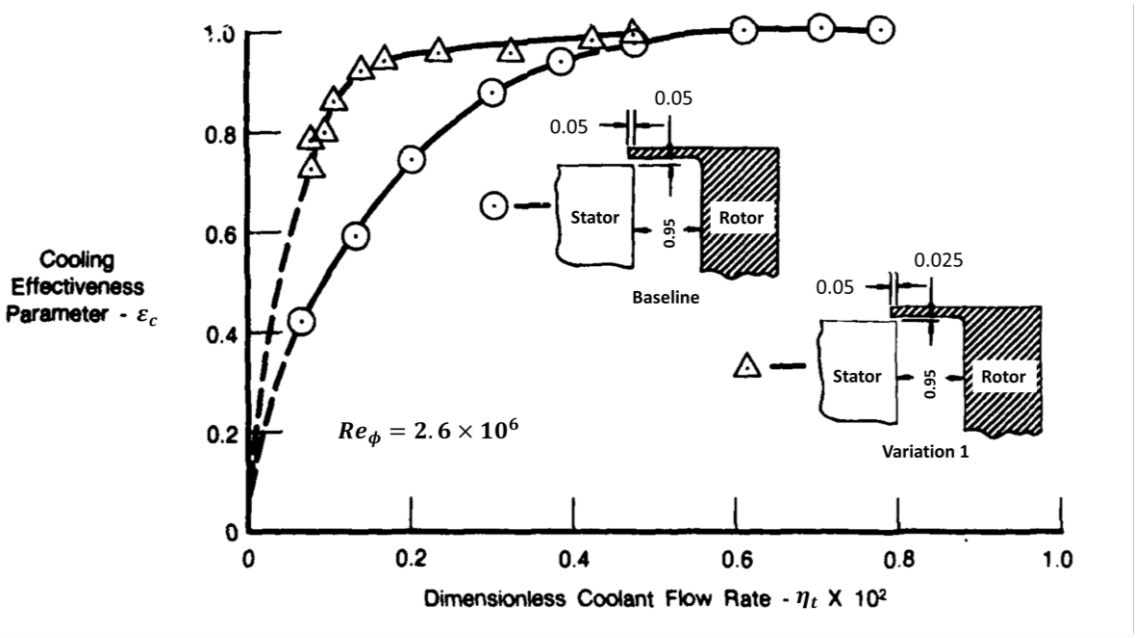

(a) Variation in the radial seal clearance (dimensions in inches)

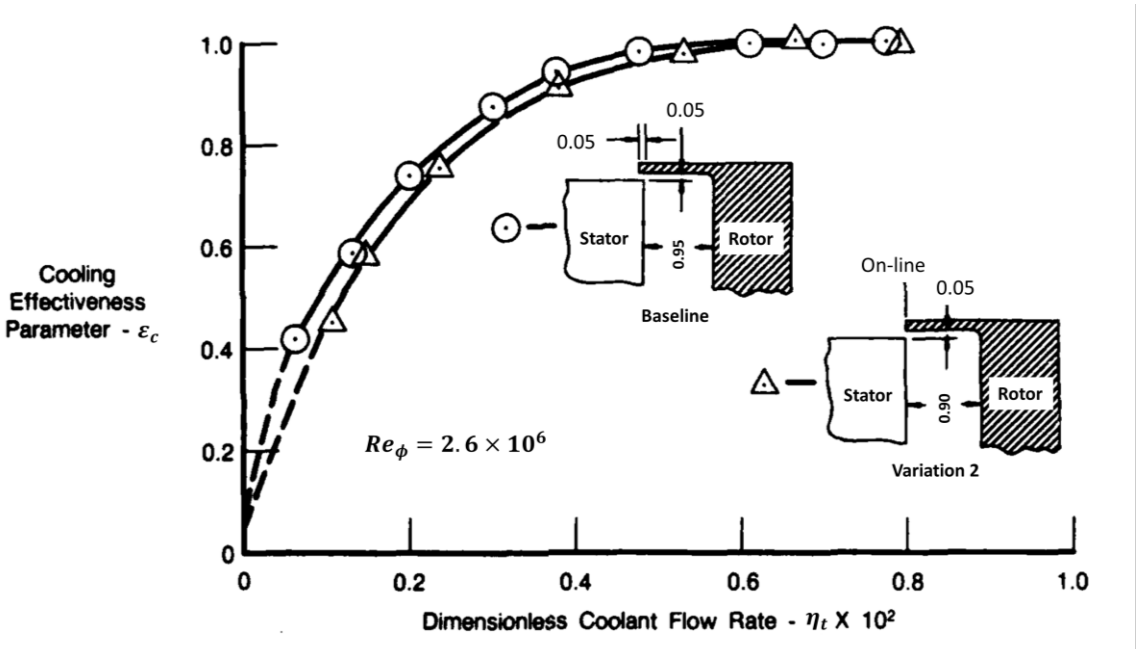

(b) Variation in the axial overlap (dimensions in inches)

Figure 2.10 Variation of sealing effectiveness with coolant flow rate – adapated from Graber *et al*. (1987)

The variation of ε_c with η_t was evaluated by Graber *et al*. (1987) for different seal configurations, as shown in Figure 2.10. With the same level of η_t, the sealing effectiveness was shown to increase significantly as the radial clearance was narrowed; the increase in the axial overlap was found to increase the sealing effectiveness only marginally.

The early-stage research work on hot gas ingress was often conducted with a rotor-stator system without external flow or with axisymmetric external flow. It was initially believed that hot gas ingress was predominately governed by the disc pumping flow resulting from the disc rotation. However, most of the research work reviewed in this section all indicated the need to account for the effect of non-axisymmetric external flow in the annulus. The investigators therefore continued to develop their research to study the externally-induced (EI) ingress, which will be reviewed in the next section.

2.2.2 Externally-induced ingress

Abe *et al*. (1979) were among the first to study the externally-induced (EI) ingress driven by external pressure asymmetries in the mainstream gas path. The research was conducted with a gas turbine rig that included stationary nozzle guide vanes positioned upstream of the rim-seal arrangement. The external flow supplied to the annulus was turned by approximately $50°$ across the row of stator vanes. Pressure asymmetries were created downstream in the vane wakes, above the seal clearance. Measurements of pressure, flow velocities and gas concentration were made to assess the relative performance of several rim-seal configurations. The ingress was found to be affected by the flow rate ratio of sealant to mainstream flow, together with the seal geometry and clearance. In contrast to the aforementioned correlation described by Bayley and Owen (1970) for RI ingress, the impact of rotational speed was shown to be negligible. It was also suggested that the ingress could be dominated by external pressure asymmetries. The experiments for the RI ingress conducted in the absence of external pressure asymmetries may under-predict the level of hot gas ingress found in actual engines.

The research work at University of Sussex was developed further to investigate the EI ingress. The research facility employed for the RI ingress was modified to create unique pressure asymmetries in the annulus. Phadke and Owen (1988c) experimentally determined the variation of $C_{w,min}$ with Re_w for six different levels of pressure symmetries created in the mainstream flow. The $C_{w,min}$ was shown to increase linearly with Re_w and also increase monotonically with the magnitude of pressure asymmetries, as demonstrated in Figure 2.11.

With constant values of Re_ϕ, the $C_{w,min}$ was correlated with the maximum pressure difference in the annulus using

$$C_{w,min} = 2\pi K G_c {P_{max}}^{1/2} \tag{2.7}$$

where K was an empirical constant and P_{max} was the non-dimensional maximum pressure difference.

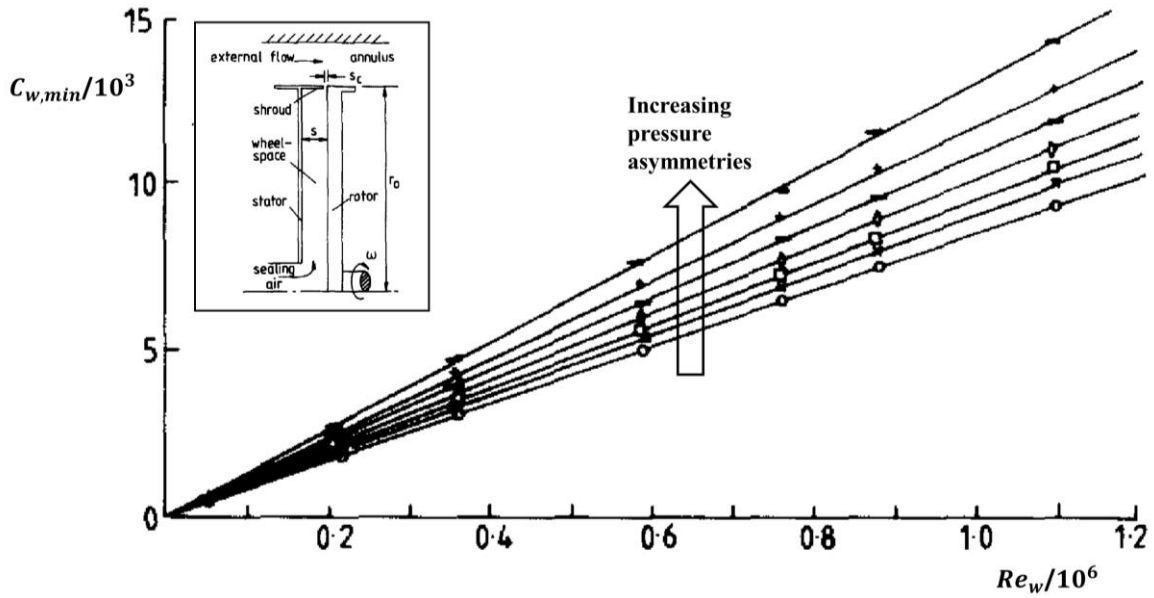

Figure 2.11 Variation of minimum sealing flow rate with external flow Reynolds number for different levels of pressure asymmetries – adapted from Phadke and Owen (1988c)

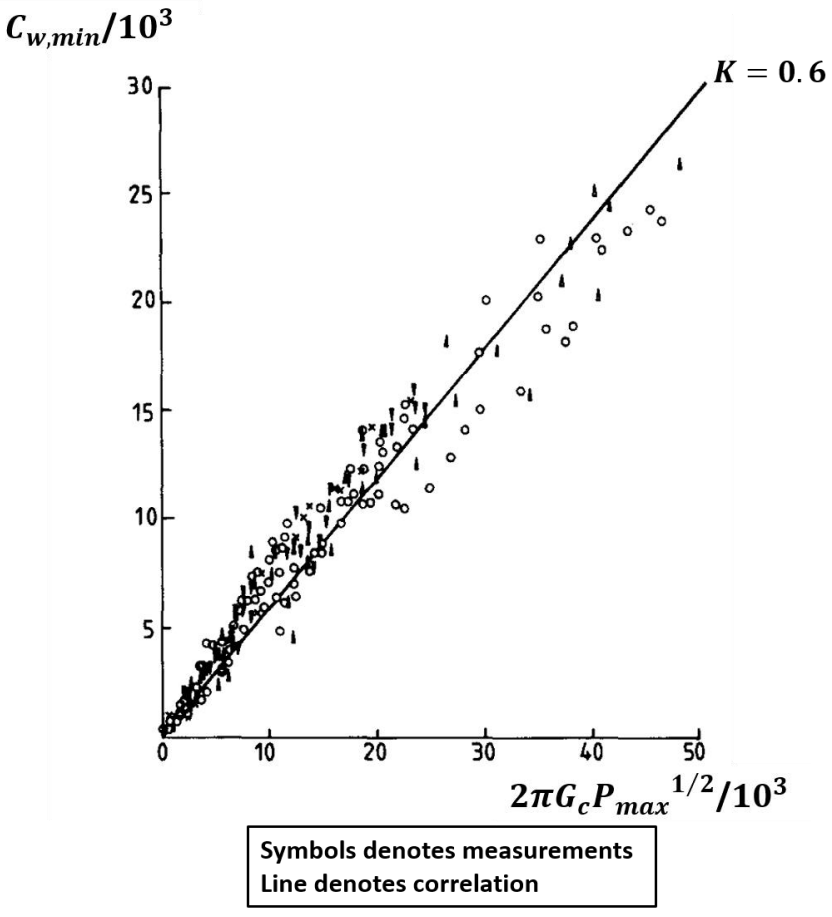

Figure 2.12 Correlation of minimal sealing flow rate with the maximum pressure difference in the mainstream annulus – Phadke and Owen (1988c)

Figure 2.12 shows the experimental measurements were correlated reasonably well using a value of $K = 0.6$ in Eq. (2.7). The variation of P_{max} was obtained by changing the level of pressure asymmetries, together with the level of Re_w. It was suggested that the $C_{w,min}$ could be estimated using the maximum pressure difference P_{max}, irrespective of the spatial distribution of external pressure asymmetries. The authors were able to separate the effects of pressure asymmetries and the mainstream flow rate in the annulus in determining the minimum sealing flow rate required to prevent hot gas ingress. The significance of future experiments with vanes and blades included in the gas path was highlighted by the authors.

Chew *et al*. (1994) developed a theoretical model for the EI ingress in conjunction with experimental measurements, following the earlier modelling work for the RI ingress. The ingestion was shown to be dominated by pressure asymmetries in the annulus for most of the experimental range covered. The theoretical prediction showed some trends in agreement with the measurements, but overestimated the degree of ingestion. It was suggested that a better agreement could be reached if the swirl velocity component and inertial effects were to be considered in the model. Computational fluid dynamics (CFD) investigations were conducted based on the experimental conditions, and some encouraging agreement with the measurements was found. However, further CFD developments were needed due to the limitation of computing resource.

More advanced CFD work was conducted at University of Sussex by Hills *et al*. (2002). An unsteady three-dimensional CFD was performed, which provided strong support for the prediction that unsteadiness due to the rotor blades usually lead to an increase in hot gas ingress. The theoretical model reported by Chew *et al*. (1994) was developed further to consider the effect of swirl velocities in the wheel-space and the annulus.

Green and Turner (1994) conducted an experimental study with both stationary vanes and rotor blades included in the mainstream gas path. A generic axial-clearance seal was employed and measurements of pressure and gas concentration were made. The sealing effectiveness was evaluated for different annulus flow conditions. The least ingestion was found for the condition of zero annulus flow (for RI ingress to occur). With mainstream flow supplied in the annulus, the rotating blades were shown to surprisingly reduce the ingress. It was suggested that the pressure symmetries may be attenuated by the blades, rather than enhanced by the vane-blade interaction as expected. Though not conclusive, this study was expected to inspire future research into the blade effect on ingestion. Different vane-blade configurations and rim-seal arrangements could be investigated in future tests.

Gentilhomme *et al*. (2003) conducted experimental research and CFD for a single stage turbine. Measurements of pressure and gas concentration were performed. It was found that the swirl velocity in the wheel-space was increased by the highly swirling ingress from the mainstream for low levels

of sealing flow rate. Steady and unsteady 3D CFD studies provided the pressure asymmetry decay in the annulus, as shown in Figure 2.13. The pressure asymmetries at the rim-seal dominated by the vanes were only slightly affected by the rotor blades. However, the pressure asymmetries created by the blades were significantly modified by the flow field in the wakes of stator vanes. This assessment of external pressure was used to test the model described by Hills *et al*. (2002). It was suggested that a recalibration of the model could result in a reasonable agreement between the measurements and the theoretical prediction.

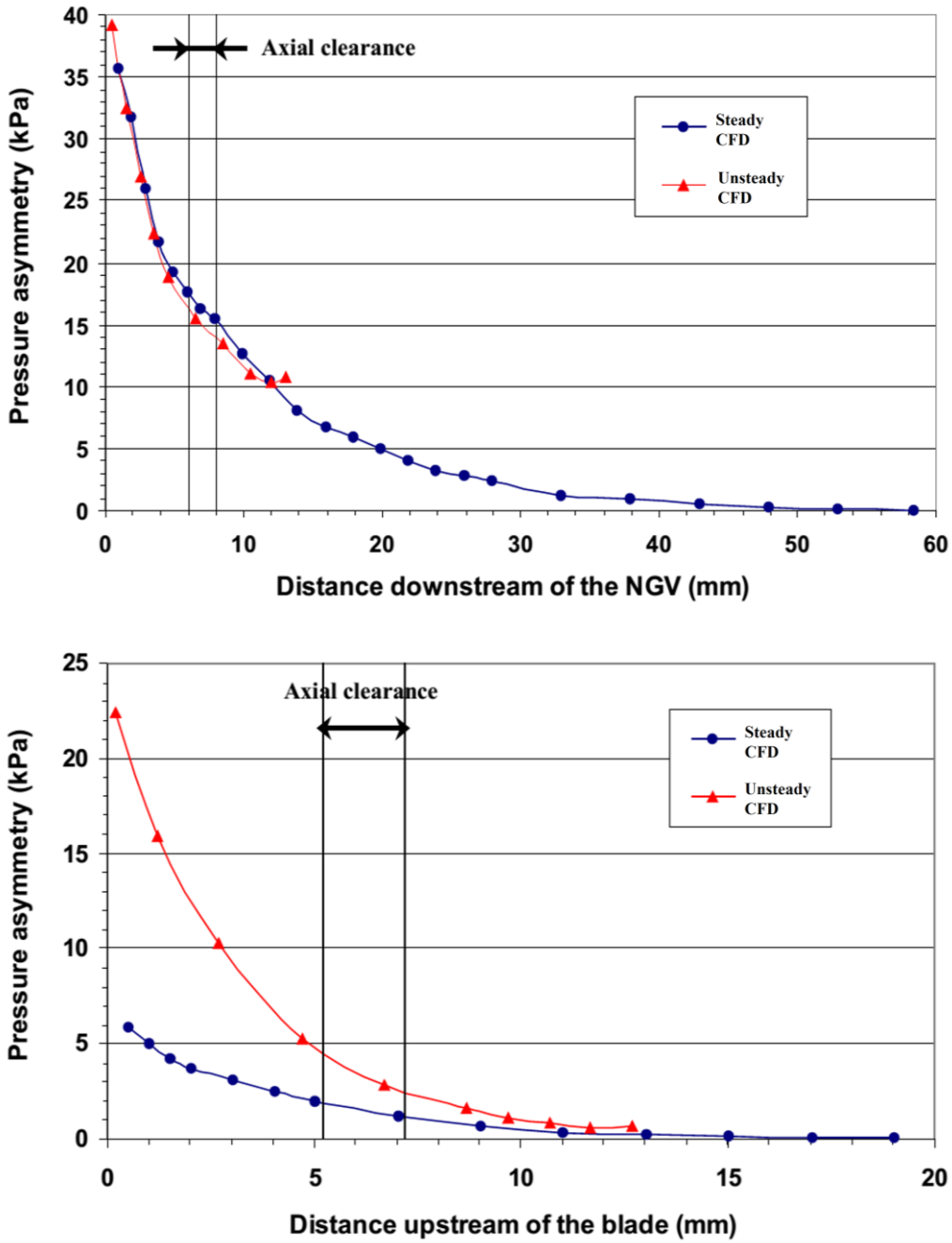

Figure 2.13 Axial decay of pressure asymmetries downstream of the stator vanes and upstream of the rotor blades – Gentilhomme *et al*. (2003)

In the 1990s, investigators at Aachen University began their research into the EI ingress. The research facility employed in the studies, as described by Bohn *et al*. (1995), featured a circumferentially traversable stator with nozzle guide vanes. No blade was included in the gas path. Measurements of pressure and gas concentration were made; the velocity distribution in the wheel-space was assessed with 2-D LDV measurements. It was shown that ingress could occur on the rotor side, as well as the stator side. A 2D CFD was conducted based on the turbine stage configuration, and the numerical data corresponded qualitatively well with the measurements.

Bohn *et al*. (1999) expanded on their research with the turbine rig significantly upgraded. A complete axial turbine stage with stator vanes and rotor blades was designed and constructed. The radial variation of sealing effectiveness was evaluated with gas concentration measurements, as shown in Figure 2.14 for a radial-clearance seal. The effectiveness was virtually invariant with radius, indicating a nearly complete mixing occurred between the sealing flow and the ingress in close proximity to the seal clearance. The sealing effectiveness increased with sealing flow rate and decreased with increasing rotation Reynolds number in line with expectation.

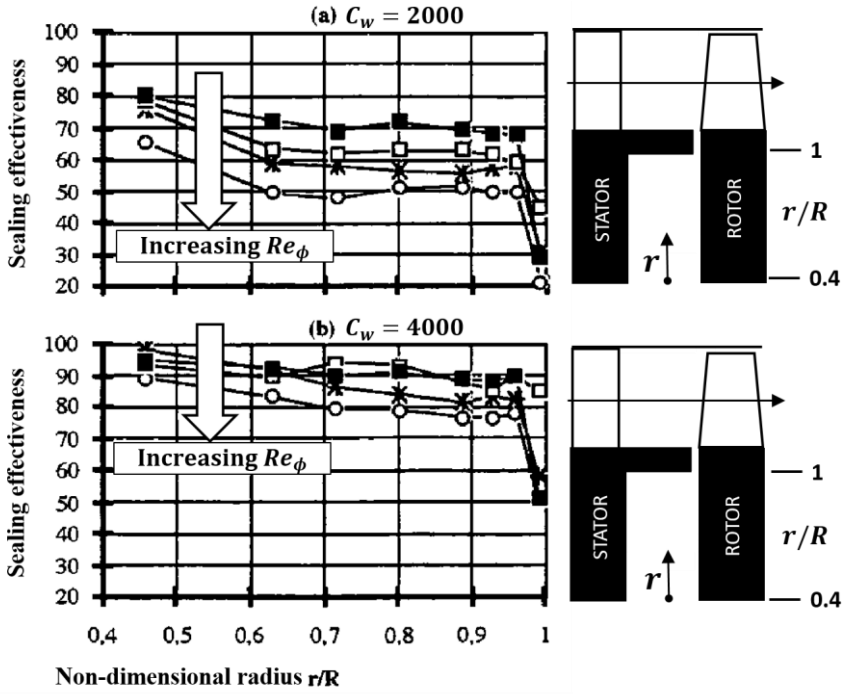

Figure 2.14 Radial variation of sealing effectiveness in the wheel-space – adapted from Bohn *et al*. (1999)

Bohn and Wolff (2003) investigated four different rim-seal configurations, including a configuration where the wheel-space was virtually open to the mainstream. The $C_{w,min}$ determined for each tested seal was correlated with the external flow Reynolds number, external pressure asymmetries and the

seal clearance ratio. The result was compared with that presented by Phadke and Owen (1988c), as shown in Figure 2.15.

The result shown by Phadke and Owen (1988c) was independent of seal configurations, and an empirical constant of $K = 0.6$ provided the best fitting of data. However, the four seal configurations investigated in this study were characterised by different values of K. Except for the configuration featuring an open wheel-space, it was shown that the prediction of $C_{w,min}$ by Phadke and Owen was conservative. An approximation for the measurements with a polynomial equation was proposed to evaluate the seal performance.

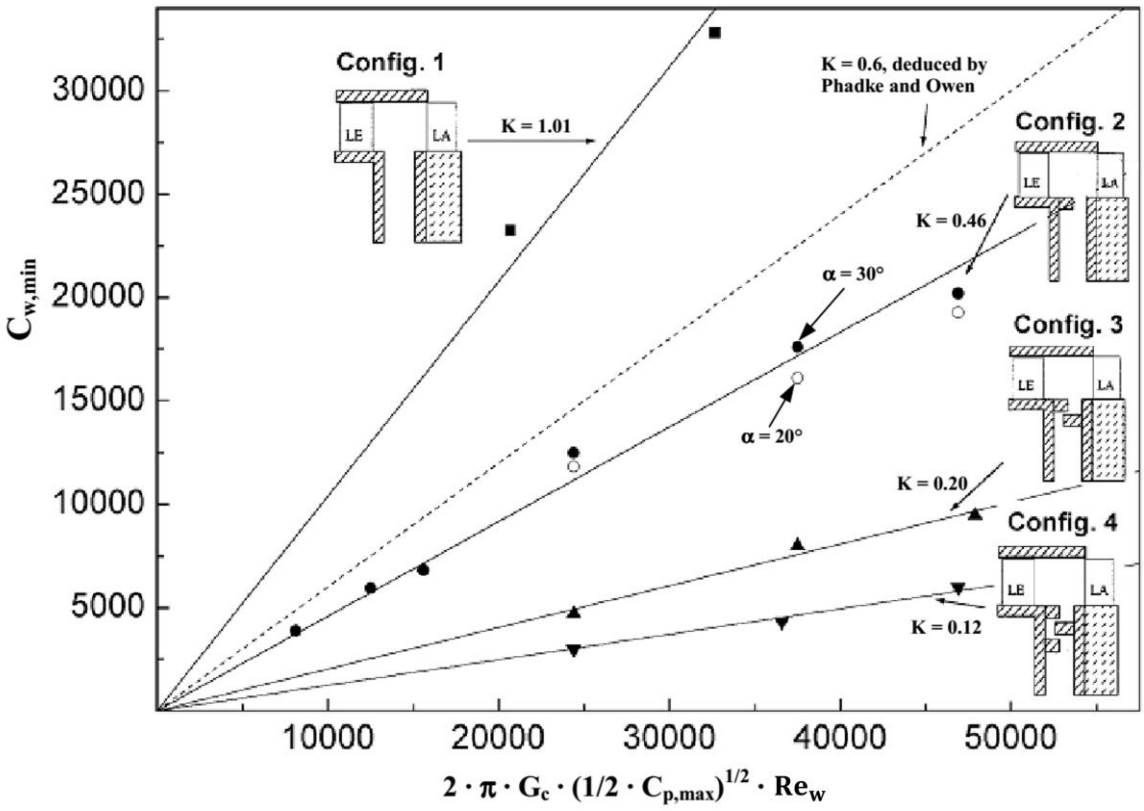

Figure 2.15 Correlation of experimental measurements – Bohn and Wolff (2003)

Bohn *et al*. (2003) conducted extensive flow velocity measurements for the rim seal of a 1.5 stage turbine, to determine the time-dependent velocity distribution for ingress and egress. The flow velocity measurements indicated a strong effect of the vane-blade interaction on hot gas ingress. Ingress intensified when the rotor blades passed by the vane wakes, compared with other relative positions between the vanes and blades. The effect of gas path blading interaction reduced with a decrease in radius inside the wheel-space.

With the same research facility, Bohn *et al*. (2006) evaluated the interaction of sealing flow with the mainstream. A 'spoiling effect' was seen as the increase in sealing flow rate gradually reduced the level of pressure asymmetries in the annulus. Gas concentration measurements showed a superior performance of a radial-clearance seal relative to an axial-clearance seal, in line with expectation.

Arizona State University joined the research into hot gas ingress in collaboration with Pratt & Whitney at East Hartford, USA. Roy *et al*. (2005) studied the effect of vane-blade configuration on the EI ingress in a single stage turbine. Two configurations featuring different vane turning angles were tested for a range of flow coefficient. The instantaneous pressure field governing the EI ingress was revealed by unsteady pressure measurements. Frequency spectrum analysis showed a strong peak at the blade-passing frequency, and a weaker peak at lower frequencies probably due to some unsteady flow patterns in the rim-seal region as suggested by the authors. The three-dimensional and unsteady flow field in the rim-seal region was influenced by the mainstream and sealing flow rates, the rotor speed as well as the stage configuration. Concentration measurements showed that the EI ingress was significantly affected by the flow coefficient, which determined the velocity triangle in the gas path.

Roy *et al*. (2007) expanded on their research to study the EI ingress with PIV velocity measurements and CFD. The calculation broadly agreed with the measurements. Figure 2.16 shows the contours provided by the CFD for the radial and tangential (swirl) velocity components in the rim-seal region. Recirculation cells were spotted and there was an increase in the tangential velocity and a decrease in the radial velocity in close proximity to the seal clearance.

It was suggested that the high-swirl and low-swirl fluid corresponded to the ingress and egress respectively. The combined experimental and computational study provided insights into the flow physics at the rim seal and helped deepen the understanding of local ingress-egress interaction.

Zhou *et al*. (2011) studied the EI ingress for three different rim-seal configurations, including a baseline single radial-clearance seal and two variants of a double-clearance seal configuration. PIV velocity measurements provided the radial velocity distribution in the wheel-space as shown in Figure 2.17. The regions for ingress and egress were identified at different circumferential positions, and the general trend of radial velocity was shown to be irrespective of the seal geometries.

An unsteady 3D CFD was conducted with a sector model, and the simulation under-predicted the level of ingestion compared with the measurements. It was suggested that there may be rotating low-pressure zones in the outer wheel-space, formed between the outer and inner seal for the double-clearance seal configurations. These flow zones could not be captured using the sector model. A full 360-degree CFD may be necessary to understand the complex flow structure.

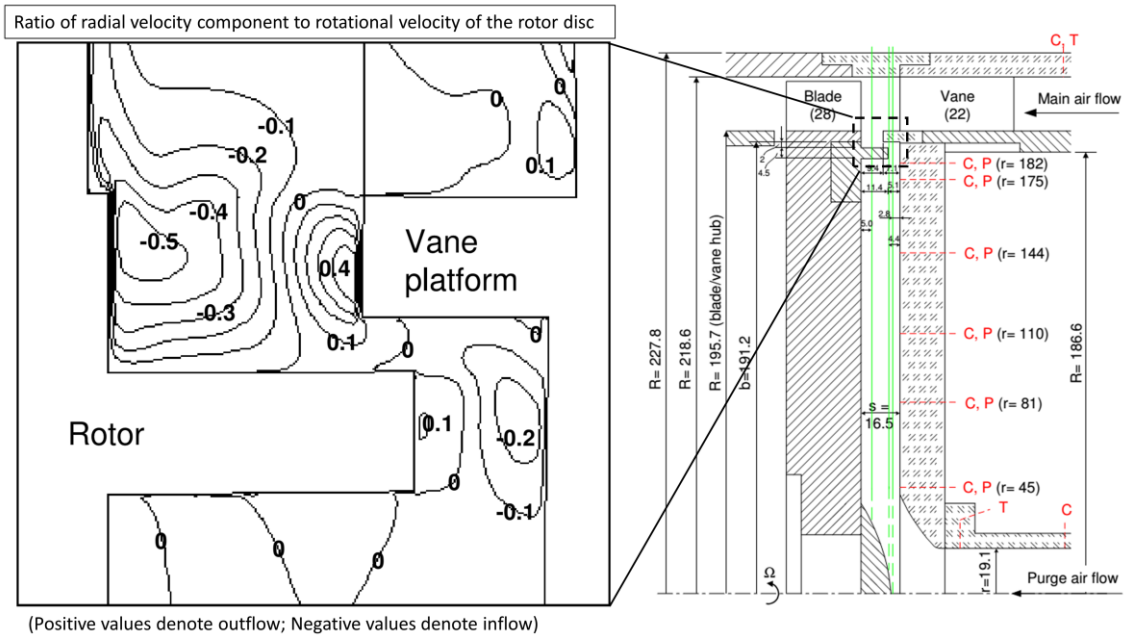

(a) Contour for the radial velocity component

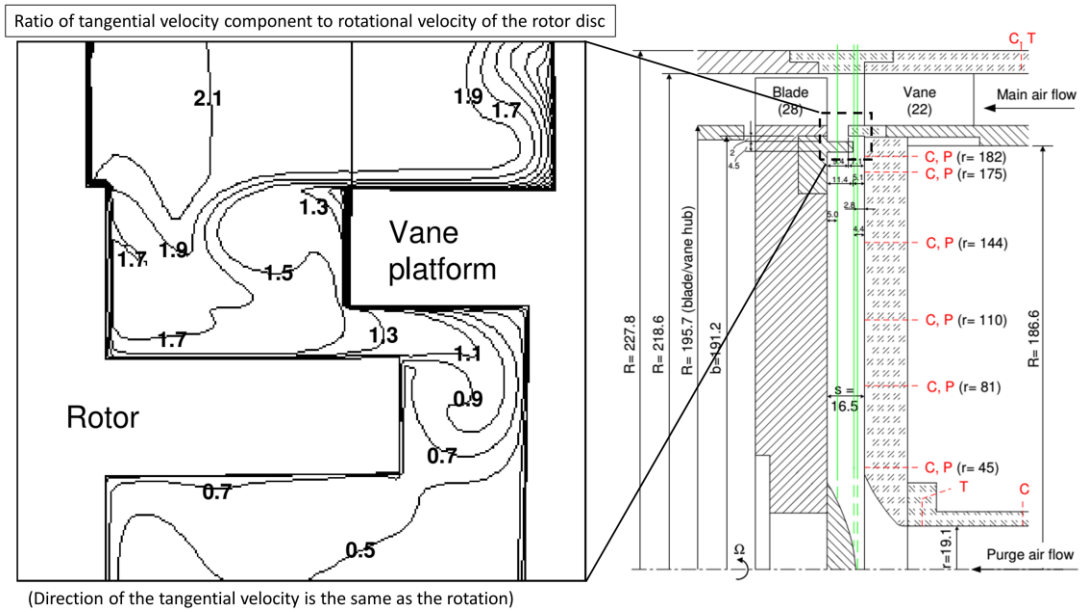

(b) Contour for the tangential velocity component

Figure 2.16 CFD velocity contours in the rim-seal region – adapted from Roy *et al*. (2007)

Following the study reviewed above, Wang *et al*. (2013) performed a full 360-degree unsteady CFD based on a double-clearance seal configuration previously tested by Zhou *et al*. (2011). Complex pressure patterns in the outer wheel-space were captured, demonstrating the advantage of using 360-degree models relative to sectors. Twelve large-scale flow structures in the outer wheel-space were seen to rotate at a lower velocity than the rotor disc. The ingress and egress periodicity

corresponding to the blade passing frequency was observed with high sealing flow rates. For the sealing effectiveness, the CFD results were in a general agreement with experimental measurements.

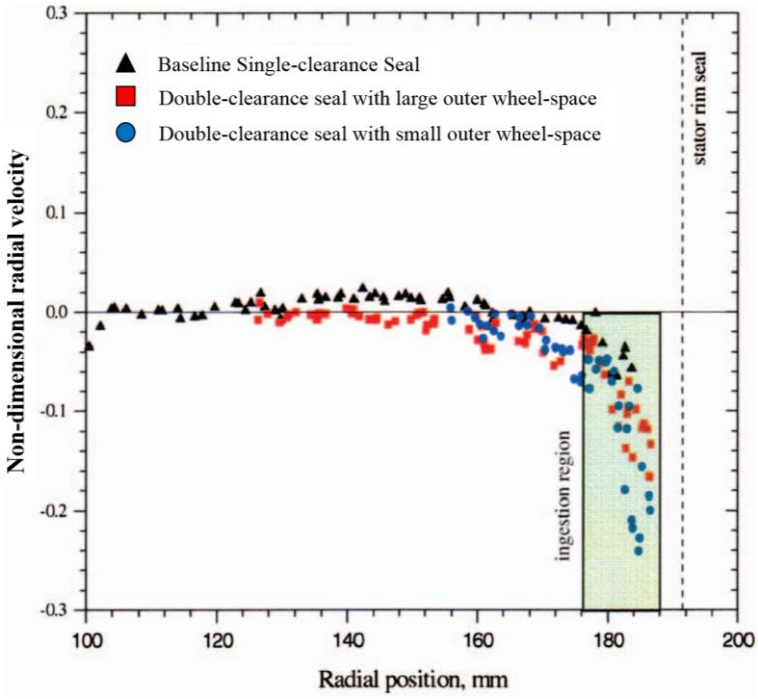

(a) Distribution of radial velocity showing the region of ingress

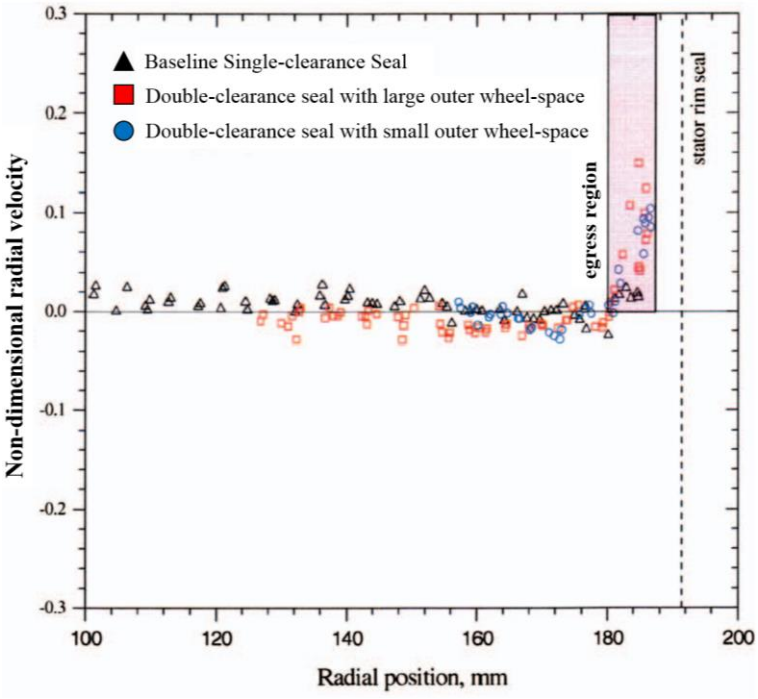

(b) Region of egress

Figure 2.17 Radial velocity distribution in the region of ingress and egress – Zhou *et al*. (2011)

Similar large-scale flow structures were seen in an earlier study at University of Surrey. Cao *et al*. (2003) conducted a combined experimental and CFD research into the interaction of annulus flow and the egress from the wheel-space. Both the measurements and the numerical simulation revealed large-scale flow structures in the wheel-space. These flow patterns featuring time-dependent pressure variations, were shown to rotate at a slightly lower velocity than that of the rotor disc. The unsteadiness was weakened as ingestion was suppressed by reducing the seal clearance or increasing the sealing flow rate. The simulation with two different CFD models was compared with experimental measurements. The full 360-degree model showed the best agreement demonstrating the advantage over sector models. This was supported by Wang *et al*. (2013) in a completely different study.

Balasubramanian *et al*. (2015) reported the experimental measurements in a single stage turbine and a simple theoretical model of an axially-overlapping radial-clearance seal. Discharge coefficients for ingress and egress, as empirical parameters, were determined with pressure and gas concentration measurements in the wheel-space and gas path. The theoretical model together with the discharge coefficients could be used in the design of rim seals and internal air systems.

The external pressure was taken adjacent to the seal edge and the internal pressure was taken in the outer wheel-space for the calculation of discharge coefficients. It was suggested that the seal region was more appropriate to define the internal pressure. The ingress discharge coefficient was shown to decrease as the sealing flow rate increased, but the opposite trend applied to the egress. The authors suggested that a comprehensive database of discharge coefficients would be needed in future for various wheel-space configurations.

The theoretical modelling was performed by investigators not only at Arizona State University. In collaboration with Aachen University and supported by Alstom Power, Johnson *et al*. (2006) developed a simple-orifice theoretical model to estimate the ingestion using calculated time-dependent pressure distribution in the annulus. Compared with previous modelling work, this method incorporated the influence of the vane-blade interaction.

The theoretical prediction of sealing effectiveness was compared with experimental data to determine the value of a discharge coefficient (C_d) included in the model. Two vane-blade configurations with different spacing were tested. A good agreement was seen for a discharge coefficient of $C_d = 0.4$, irrespective of vane-blade spacing in the gas path. It was suggested that the orifice model, in conjunction with CFD, could be used to estimate the sealant flow rate required to obtain a specific sealing effectiveness.

Johnson *et al*. (2008) expanded on their previous modelling by including two discharge coefficients ($C_{d,i}$ and $C_{d,e}$) for ingress and egress respectively. It was shown that the dual-coefficient model could

characterise the effect of swirl velocities by adjusting values of the two empirical coefficients, without the need of more swirl-related parameters. The theory was compared with experimental measurements for a radial-clearance seal configuration, and the values of discharge coefficients were determined for a good agreement to be reached. It was suggested that this model could improve the flexibility for the ingestion prediction, although more data was needed for further validation.

University of Bath joined the research into hot gas ingress in collaboration with Siemens Fossil Power Generation. Owen (2011a) developed an orifice model and derived the orifice equations for the prediction of sealing effectiveness. The model was based on an imaginary 'orifice ring' as shown in Figure 2.18. The ingress and egress were assumed to cross the ring through respective flow areas. The sum of these two areas equalled to the area of the seal clearance. The model used variations of Bernoulli's equation, including the swirl terms, to correlate the sealing flow rate and the pressure difference across the rim seal. Discharge coefficients ($C_{d,i}$ and $C_{d,e}$) were used to account for viscous losses; $C_{d,i}$ for ingress and $C_{d,e}$ for egress could be determined empirically. Although compressible flow was found in the annulus of an actual turbine, the author suggested that incompressible orifice equations were acceptably accurate for the modelling.

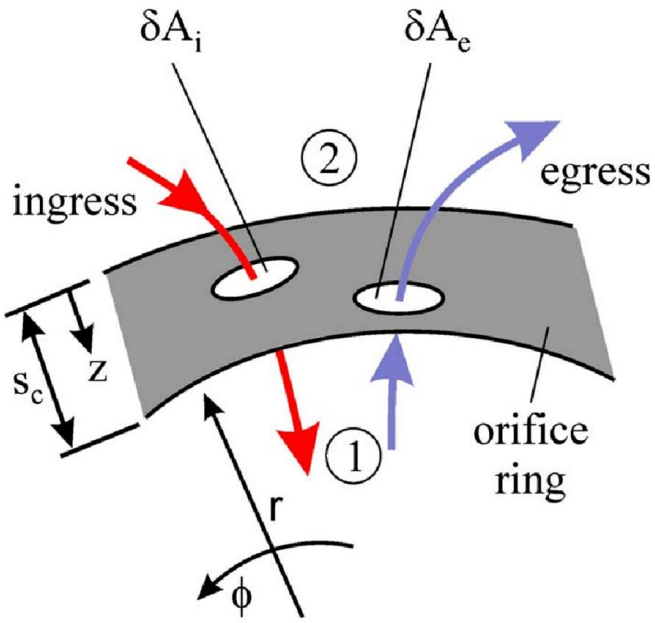

Figure 2.18 The orifice ring of the theoretical model – Owen (2011a)

The definitions of some important parameters employed in the modelling are given as follows:

The non-dimensional sealing flow parameter, Φ_0, was defined to combine the effects of $C_{w,o}$, G_c and Re_ϕ as follows:

$$\Phi_0 = \frac{C_{w,o}}{2\pi G_c Re_\phi} \tag{2.8}$$

This parameter is also used in the experimental measurements documented in this thesis. It is an inviscid parameter due to the cancellation of viscous terms included in both $C_{w,o}$ and Re_ϕ. An alternative definition may be more appropriate as suggested by the author:

$$\Phi_0 = \frac{U}{\Omega b} \tag{2.9}$$

where U denoted the bulk mean radial velocity of sealing flow through the rim-seal clearance. Φ_{min} was the value of Φ_0 when the wheel-space was sealed completely.

The sealing effectiveness ε was defined as

$$\varepsilon = 1 - \frac{\Phi_i}{\Phi_e} = \frac{\Phi_0}{\Phi_\mathrm{e}} = \frac{\Phi_0}{\Phi_0 + \Phi_i} \tag{2.10}$$

where Φ_i and Φ_e were the flow parameters for ingress and egress respectively. It is worth mentioning that Φ_i is positive when there is ingress and Φ_e is positive when there is egress. It followed that $\Phi_0 = \Phi_e - \Phi_i$.

For the RI ingress, a basic theory was proposed where $C_{d,i} = C_{d,e}$ and the external swirl was negligible. It followed that

$$\Phi_{min,RI} = C_{d,e} {C_{\beta_1}}^{1/2} \tag{2.11}$$

where C_{β_1} is the modified internal swirl ratio defined as:

$$C_{\beta_1} = {\beta_1}^2 \left(1 - \frac{{r_1}^2}{{r_2}^2}\right) \tag{2.12}$$

The correlation from Bayley and Owen (1970) was used and the ε was expressed in terms of $C_{w,o}$ theoretically. The prediction of ε was in good agreement with measurements made by Graber *et al*. (1987).

Owen (2011b) expanded on the theoretical modelling to consider the EI ingress. In order to evaluate the external pressure asymmetries driving the EI ingress, a 'saw-tooth' model, similar to that described by Hamabe and Ishida (1992), was used to approximate the circumferential pressure distribution in the annulus. This saw-tooth model was shown to perform very well by Owen *et al*. (2012). The orifice equations were solved analytically for EI ingress, so that

$$\Phi_{min,EI} = \frac{2}{3} C_{d,e} \Delta {C_p}^{1/2} \tag{2.13}$$

where ΔC_p is the non-dimensional peak-to-trough pressure difference in the annulus. As the driving potential for EI ingress (Owen *et al*. (2012)), this parameter is also used for studies documented in this thesis.

For conditions when neither RI nor EI ingress dominate, the combined ingress (CI) regime was reached. The model provided a relation in terms of Φ_{min} for the CI ingress and the RI ingress as follows:

$$\frac{\Phi_{min,CI}}{\Phi_{min,RI}} = \frac{2}{3}\frac{C_{d,e,CI}}{C_{d,e,RI}}\frac{\left(1+\Gamma_{\Delta p}\right)^{3/2}-1}{\Gamma_{\Delta p}} \tag{2.14}$$

where $\Gamma_{\Delta p} = \Delta C_p / C_{\beta_1}$.

Figure 2.19 shows the RI and EI ingress regimes with the CI regime featuring the transition between the two. As $\Gamma_{\Delta p}$ increases the external pressure asymmetries begin to dominate the ingress; with the reduction in $\Gamma_{\Delta p}$, the ingress is eventually governed by the pumping flow resulting from the disc rotation.

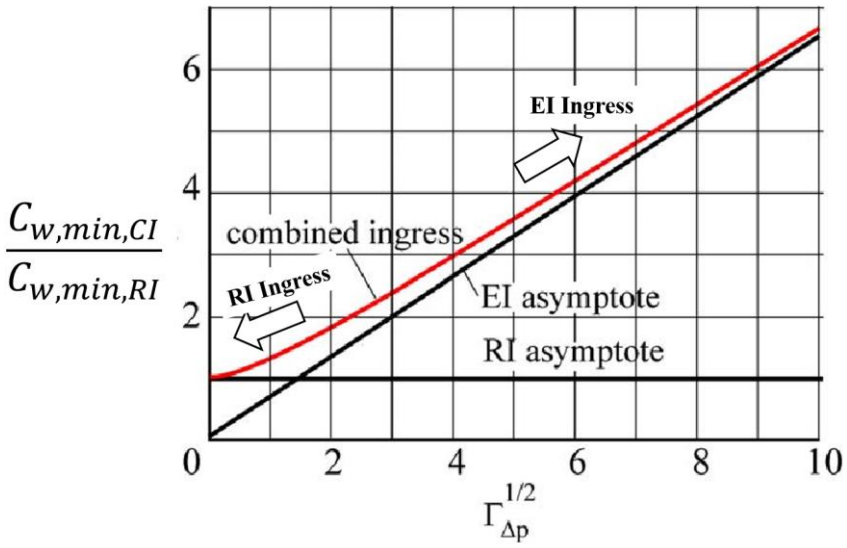

Figure 2.19 Theoretical transition from RI to EI ingress regime – adapted from Owen (2011b)

Sangan *et al*. (2013a,b) experimentally investigated two single-clearance seal configurations for EI and RI ingress. The variation of sealing effectiveness (ε) with the non-dimensional sealing flow parameter (Φ_0) was obtained. A statistical fitting technique based on the maximum likelihood estimation method was developed by Zhou *et al*. (2013). The orifice model was applied in conjunction with the statistical fitting method to predict Φ_{min} and the ratio of discharge coefficients for both seal configurations. The theoretical curves were in excellent agreement with experimental

data, as shown in Figure 2.20. The orifice model could be used to extrapolate the discharge coefficients determined from rig testing to engine conditions for similar seal geometries, making it a powerful tool for turbine rim-seal design.

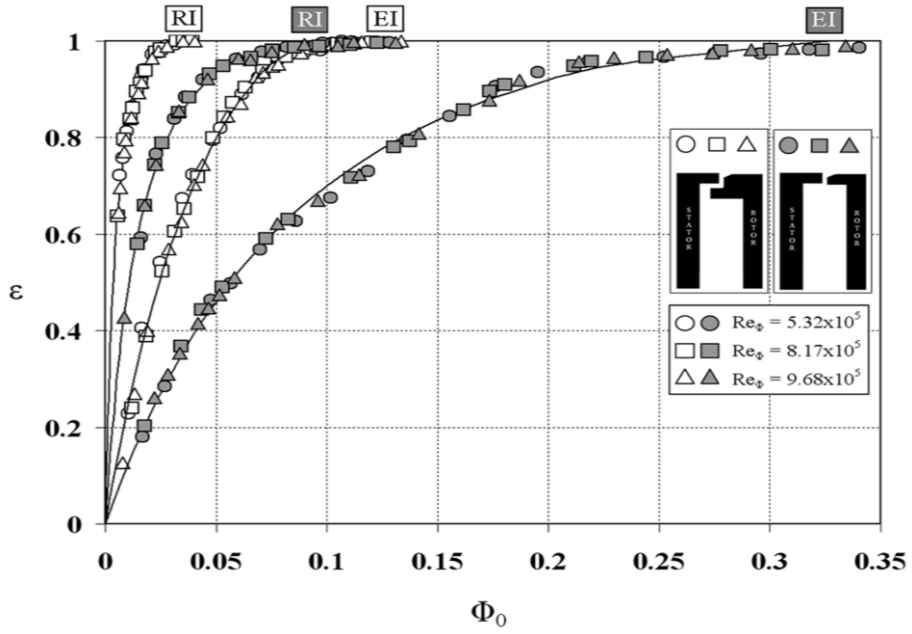

Figure 2.20 Variation of sealing effectiveness with sealing flow rate – Sangan *et al*. (2013b)

Scobie *et al*. (2014) investigated the effect of flow coefficient on the annulus pressure asymmetries and the EI ingress through rim seals. The $\Delta {C_p}^{1/2}$ determined with time-averaged pressure measurements was shown to increase proportionally with flow coefficient. Compared with CFD, the measurements showed lower magnitudes of pressure asymmetries for low levels of flow coefficient, probably because the blade unsteady effect was not captured by the time-averaged measurements. The prediction by the orifice model was shown to agree well with the experimental data for a complete range of flow coefficient.

Owen *et al*. (2015) extended the previously published EI orifice model to determine the sealing effectiveness from pressure measurements in an engine, ε_p, using effectiveness acquired by concentration measurements, ε_c. The ε_p equalled to ε_c at a hypothetical "sweet spot" on the stator vane platform. For a radial-clearance seal, it was shown that the hypothetical pressure difference at the sweet spot was linearly related to the pressure difference measured at a pre-defined location (where the pressure could be conveniently measured). There was a good agreement between values of ε_p calculated using the theoretical model and values of ε_c from concentration measurements, as shown in Figure 2.21.

A 3D steady CFD was conducted to reveal the axial location of the sweet spot, which was shown to be very close to the upstream edge of the seal clearance. The significance of this research is that it

demonstrates how experimental measurements in a turbine rig could be used, in principle, to calculate the sealing effectiveness in a turbine engine.

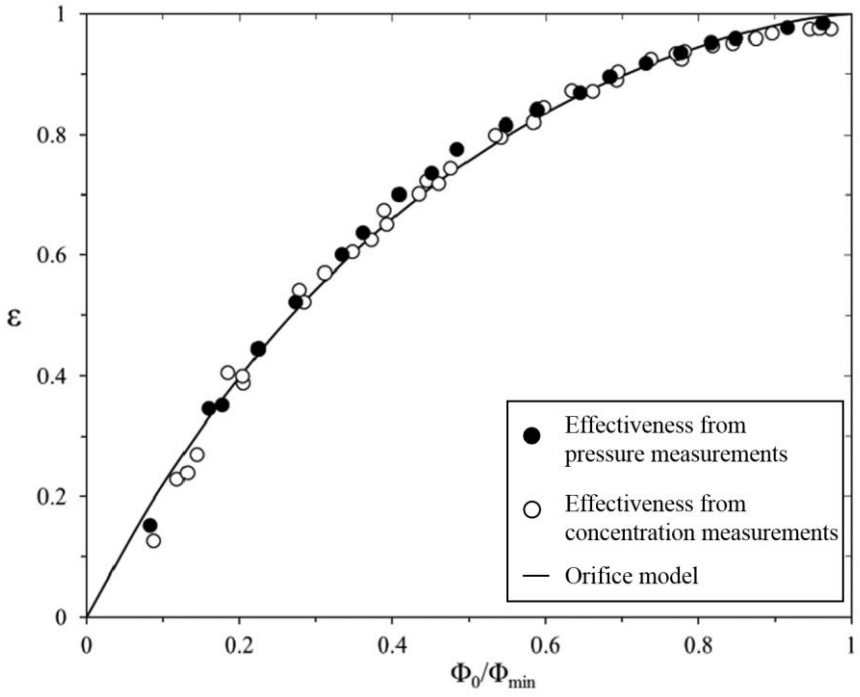

Figure 2.21 Comparison of sealing effectiveness determined from pressure and gas concentration measurements – adapted from Owen *et al*. (2015)

2.2.3 Review of gas turbine research facilities

The design and construction of gas turbine research facility are crucial for the research into hot gas ingress. A well-designed, fully functioning turbine rig can produce useful research data that validates numerical simulation codes and evaluates theoretical models, thus providing insights into the ingestion problem. The literature review reported in previous sections focuses on the experimental results or analysis based on the measurements. This section, however, moves on to review briefly some of the turbine rigs that were recently designed, built and employed by different research groups. Typical operating points for these facilities are summarised in the section.

The research facility at Aachen University was documented by Bohn *et al*. (2003). It was referred to as the Aachen rig featuring a 1.5 stage turbine modified from a previous rig described by Bohn *et al*. (1999). Independent sealing flow paths were designed for both upstream and downstream wheel-spaces. The widths of the wheel-spaces could be varied by adding or removing spacers. Interchangeable stator discs and rotor inserts allowed different cavity and rim-seal configurations to be tested. The test section for the Aachen rig is shown in Figure 2.22.

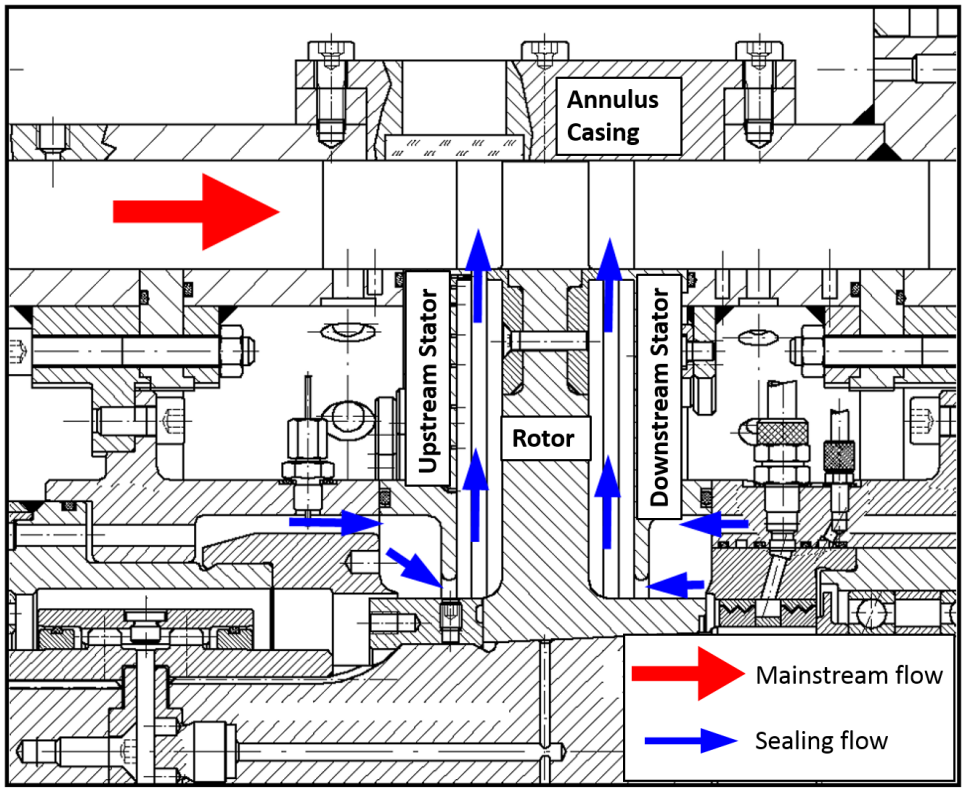

Figure 2.22 Test section of the Aachen rig – adapted from Bohn *et al*. (2003)

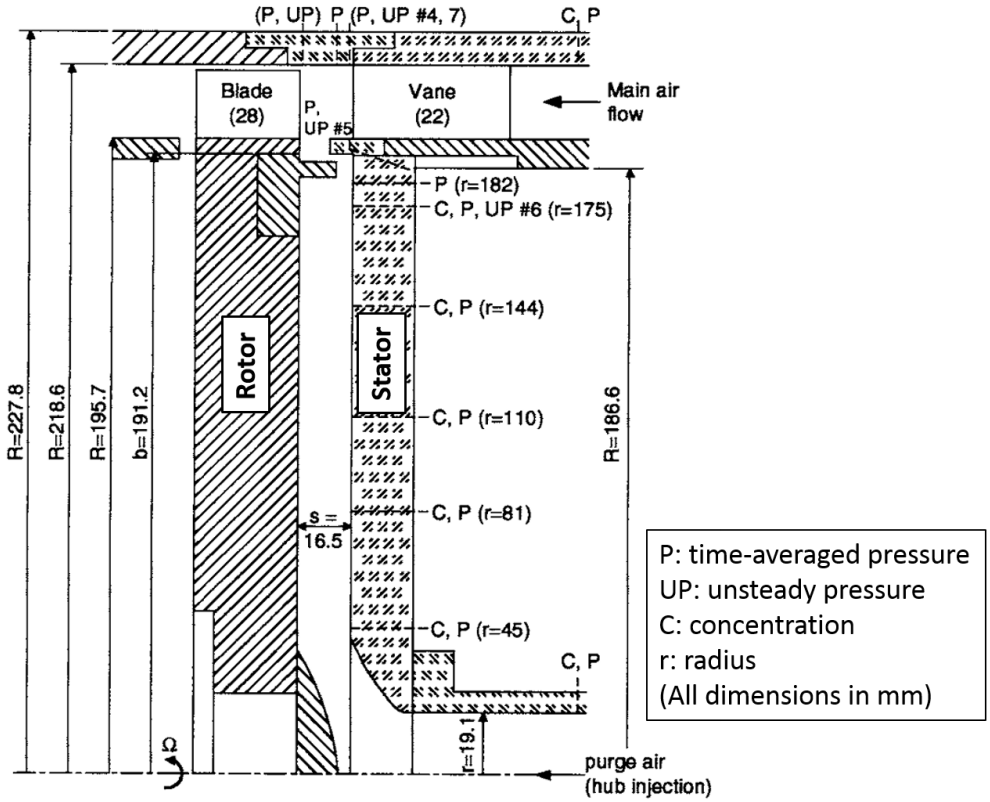

Figure 2.23 Test section of the ASU rig (PW) – adapted from Roy *et al*. (2005)

The gas turbine rig at Arizona State University, which was designed based on a Pratt & Whitney engine, was described by Roy *et al*. (2005) and is referred to as the ASU rig (PW). It was evolved from a previous rig designed based on a Honeywell engine, as documented by Roy *et al*. (1999), which is referred to as the ASU rig (H). The turbine stage for the ASU rig (PW) is shown in Figure 2.23. The tapping locations for the measurements of pressure and concentration are shown; the locations for unsteady pressure measurements are seen in the gas path and in the region close to the rim-seal clearance. Modular attachments are shown to be installed on the turbine discs and annulus casing to enhance the versatility of the rig.

The test facility at University of Sussex was described by Gentilhomme *et al*. (2003). The Sussex rig consists of a complete axial turbine stage, which is based on a modified Gnome helicopter engine enclosed in an annular channel as shown in Figure 2.24. The mainstream flow and the sealing air are provided by separate compressors, and several levels of temperature difference and density ratio can be achieved for different operating points as demonstrated by the authors. Extensive measurements of pressure and gas concentration can be performed in the annulus and the wheel-space to evaluated ingestion. A new two stage gas turbine rig at University of Sussex was introduced by Eastwood *et al*. (2012), and the rim-seal exchange and re-ingestion flows are studied with the facility.

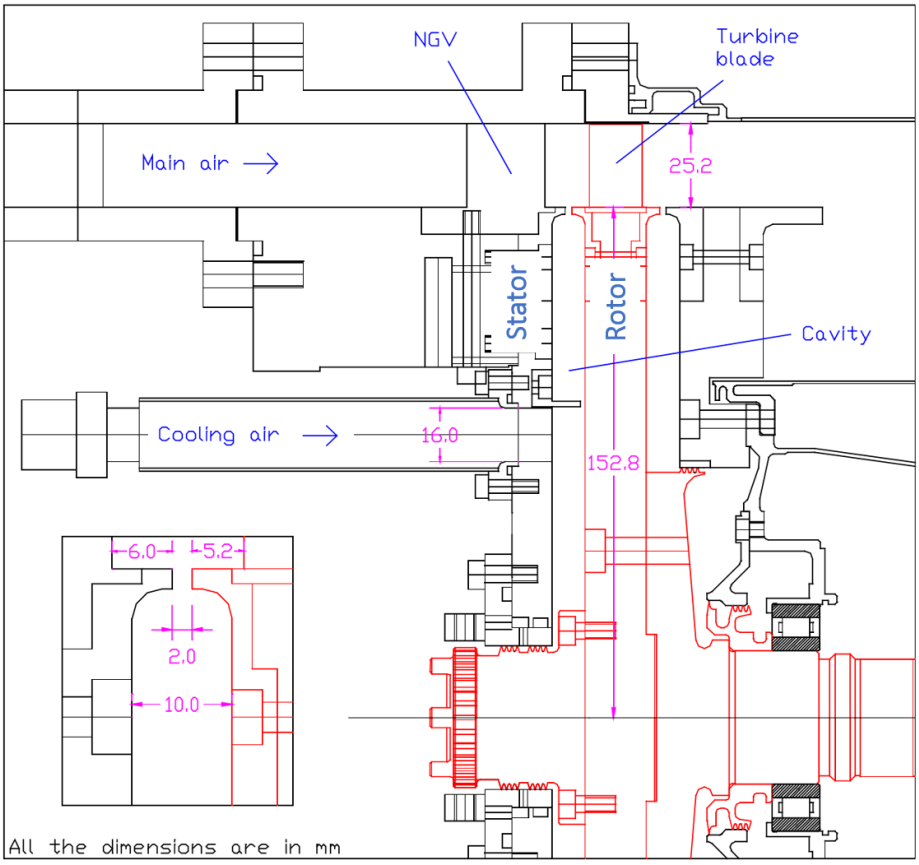

Figure 2.24 Test section of the Sussex rig – adapted from Gentilhomme *et al*. (2003)

A General Electric hot gas ingestion rig based on a current generation heavy-duty gas turbine was introduced by Palafox *et al*. (2013). The GE rig, shown in Figure 2.25, features a 1.5 stage axial gas turbine designed to operate at engine-matched conditions. The flow physics of relevant rim seal geometries can be reproduced while maintaining critical Mach and Reynolds numbers. Multiple purge and leakage flow paths were created and can be independently controlled to model the fluid dynamics found in secondary air systems. The test data produced by the facility will be used to validate reduced order models, including unsteady CFD models, to support the design and optimisation of gas turbine engines.

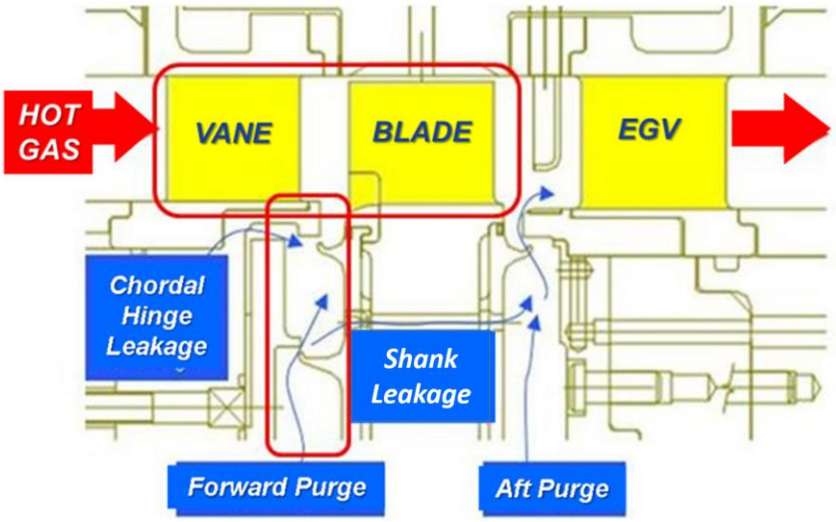

Figure 2.25 Test section of the GE rig – adapted from Palafox *et al*. (2013)

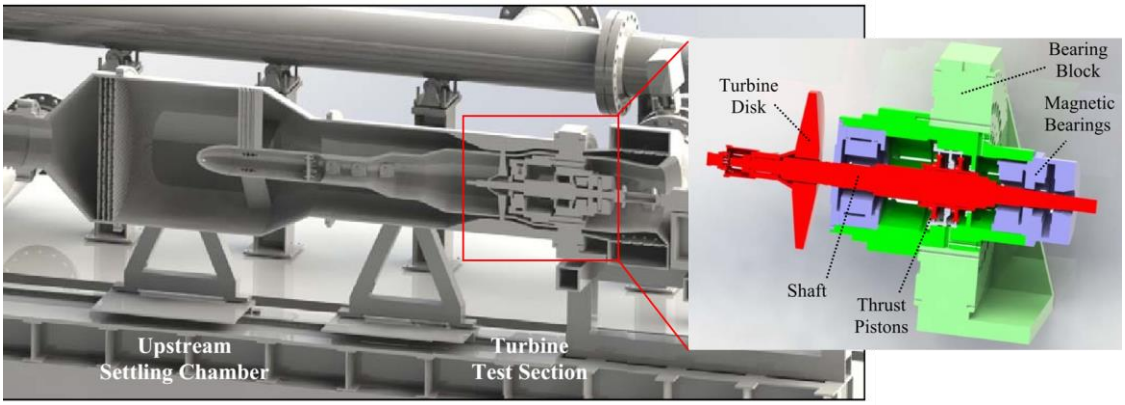

Figure 2.26 General assembly of the PSU rig – adapted from Barringer *et al*. (2014)

A high-speed gas turbine rig at Pennsylvania State University was described by Barringer *et al*. (2014), referred to as the PSU rig. It consists of a 1.5-stage turbine designed to study the fundamental flow effects of rotation on secondary air systems and the aero-thermal cooling in gas turbine engines. The uniqueness of this rig includes a continuous-duration operation with engine-relevant Reynolds

numbers and Mach numbers at the blade inlet. A magnetic bearing system was employed for accurate, continuous rotor placement and feedback during high-speed rotation. Two phases of experimental research are planned targeting the behaviour of inner-stage leakage flow and the novel cooling methods for turbine components respectively. The general assembly of the facility is shown in Figure 2.26, with the rotor and bearing assembly highlighted. Other research facilities were designed and built at different research centres to study various aspects of fluid dynamics and heat transfer characteristics found in secondary air systems, such as the two-stage, low-speed rig at Purdue University (Gallier *et al*. (2000)) and the 1.5 stage turbine at University of Notre Dame (Schmitz (2010)).

Figure 2.27 shows the operating conditions for some of the gas turbine research facilities reviewed in the section. The figure was created based on typical operating points found in open literature and no limitation is specified for each facility. The operating points are expressed in terms of $Re_w{}^*$and Re_ϕ, where $Re_w{}^*$ is the external flow Reynolds number based on the axial chord length of the stator vane.

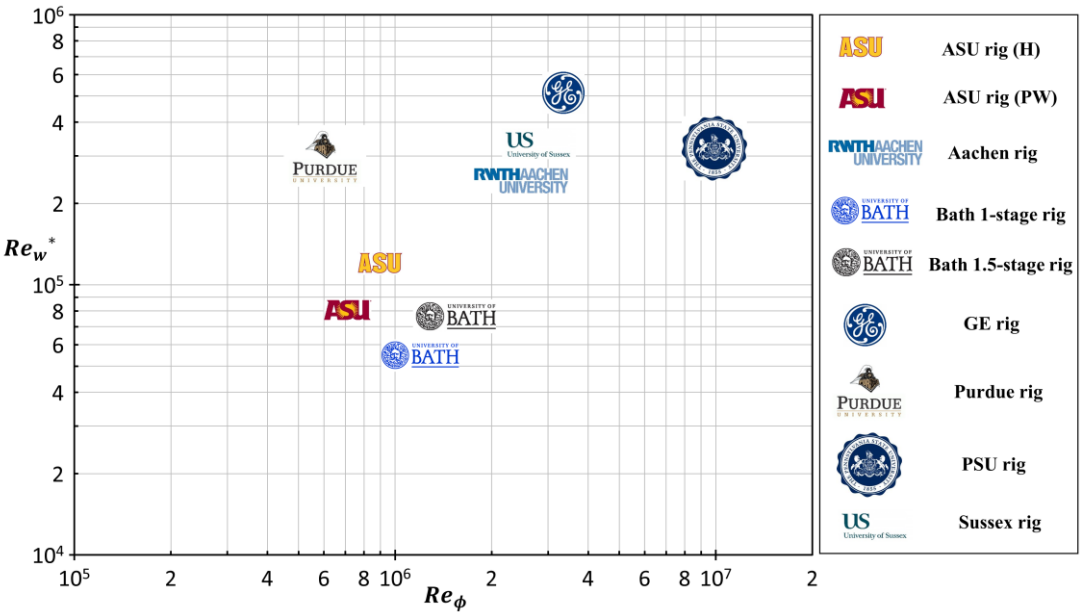

Figure 2.27 Typical operating points of gas turbine research facilities

Typical Reynolds numbers found in real engines are usually above 1.0×10^7. All the current research facilities are shown to operate at scaled conditions. One practical reason is that it is usually more cost effective and often efficient to operate at more benign conditions due to less implications from high speed and high flow rates. In spite of the difference between the rigs and engines, the fluid dynamics and heat transfer behaviours are successfully modelled, with experimental data extrapolated to engine conditions through the use of theoretical models and CFD codes.

Chapter 3 Design of a single-stage gas turbine test facility

This chapter describes the design of a single-stage gas turbine experimental facility. The aim was to establish a highly versatile experimental facility with unique capabilities. The turbine stage of the facility was specifically designed for conducting extensive and comprehensive experimental studies on ingress for different rim-seal configurations, including the double-clearance seals widely used in engines. Extensive instrumentation was incorporated in the mainstream and wheel-space for detailed measurements of pressure, swirl velocities, gas concentration and temperature. Modular design approach was applied to achieve variable wheel-space geometries and gas path blading, which alter the aerodynamics both inboard and outboard of the rim seal, allowing their impacts on ingress to be studied. The modelling of leakage flow paths found in gas turbine engines was also incorporated in the design to explore a novel technique that exploits leakage flow to reduce hot gas ingress. With all the unique features, this new research facility will offer capability in new areas of ingress research that provides valuable insights for engine designers. The entire design and all the drawings shown in this chapter were completely accomplished by the author of this thesis.

3.1 Overview

Figure 3.1 shows the turbine stage of the research facility, where the components are colour-coded in an open-section view. It comprises a rotating disc referred to as the rotor, adjacent to a coaxial stationary disc referred to as the stator. A rotor-stator cavity is formed, traditionally known as the wheel-space. An annulus casing surrounds the rotor-stator system to form the mainstream flow path. Cover-plates were designed for the stator and rotor with details to be discussed in later sections. Upstream of the rotor-stator system, the mainstream air is guided through a transition unit, where the flow from discrete pipes mixes and accelerates towards a continuous annular area. The sealing air is introduced into the system through the central area of the stator (not shown in the figure). Detailed flow paths will be shown in the following sections.

The design of the stator and rotor discs, along with the respective cover-plates, was aimed at objectives as follows:

(I) To enable extensive rim-seal configurations to be installed and tested by employing modular seal attachments onto the turbine discs and cover-plates.

(II) To achieve the variation of wheel-space geometries, irrespective of rim-seal arrangements, through the use of interchangeable cover-plates and attachments.

(III) To achieve the variation of gas path blading including stator vanes and rotor blades, irrespective of the wheel-space and rim-seal configurations, by means of modular stator and rotor discs with different blading features.

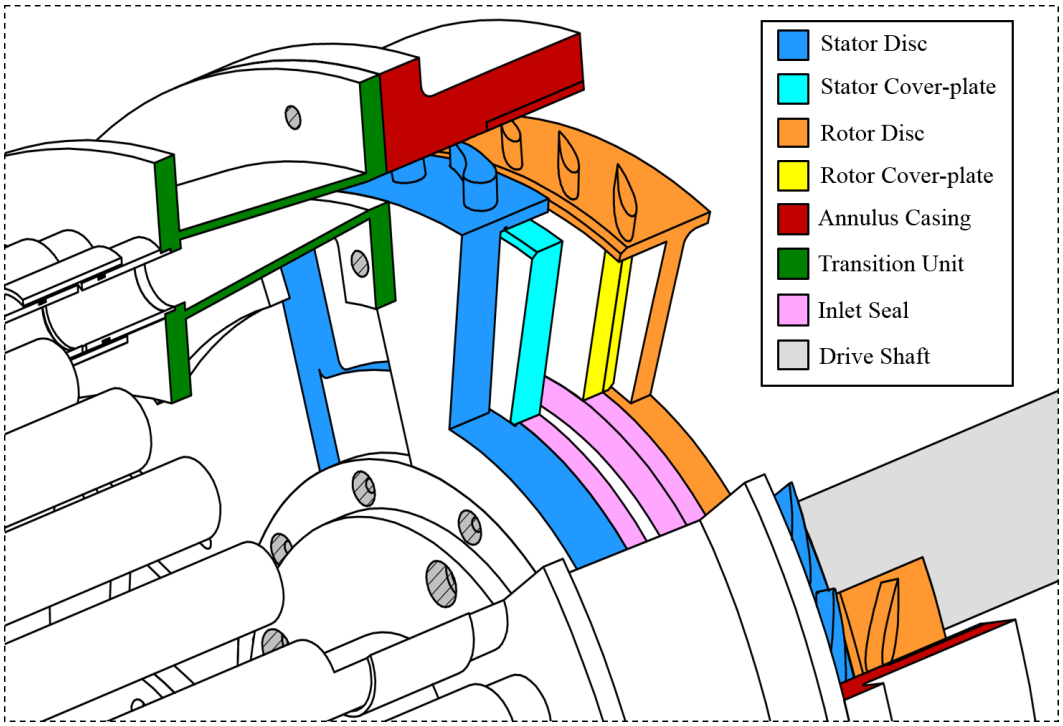

Figure 3.1 Section view of the turbine stage of the facility

(IV) To enable a complete insulation on metal surfaces of the wheel-space, with a foam material of low thermal conductivity, for heat transfer experiments using heated sealing flow.

(V) To promote the capability and versatility of instrumentation, e.g. a cover-plate equipped with instrumentation for the measurements of pressure and gas concentration can be rapidly changed to a second one specifically designed and constructed for heat transfer measurements, with consistent wheel-space and rim-seal arrangements.

(VI) To enable the modelling of stator-side leakage flow paths in close proximity to the rim seal, for utilising the leakage air to reduce ingestion.

A mainstream annulus was formed by the outer casing and gas path blading, together with stator and rotor shrouds. The blade tip clearance, which is the clearance between the casing and the tips of rotor blades, was designed to be 5% of the blade span. Instrumentation was placed in the annulus casing for detailed pressure measurements in the mainstream, including time-averaged measurements with pressure taps and time-dependent measurements with unsteady transducers installed at specifically designed positions. These assessments of pressure characteristics provide insights into the driving potential for externally-induced ingress into the wheel-space through rim seals.

The powertrain for driving the turbine rotor consists of an electric motor, a shaft driven by the motor via a flat belt transmission and a bearing unit supporting the shaft. A new carriage system was

designed which the complete powertrain was mounted upon. The aim of this carriage system is to achieve precision alignment of turbine discs for testing engine-representative rim seals, and to enable quick access to the wheel-space instrumentation, while ensuring alignment repeatability once the system is re-assembled. The carriage system comprises a carriage-plate assembly that can slide along linear guide rails, and an end-stop system designed to accurately control the clearance between the stator and rotor discs. The detailed description of the carriage system shall be given in the next section. The overview of the research facility is shown in Figure 3.2, and the general assembly is shown in Figure 3.3.

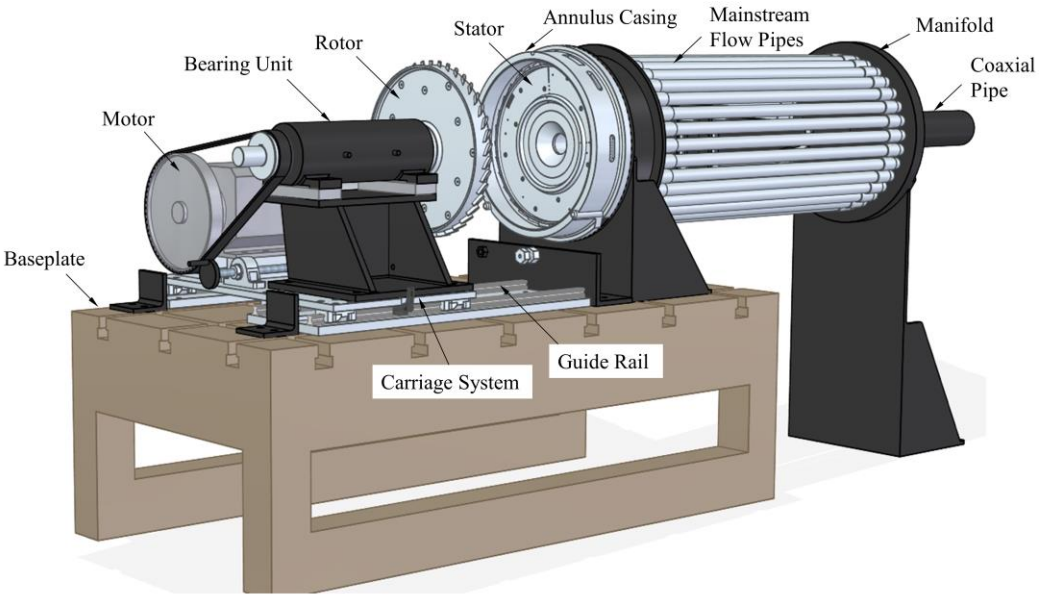

(a) 3D CAD model of the turbine rig with wheel-space in open state

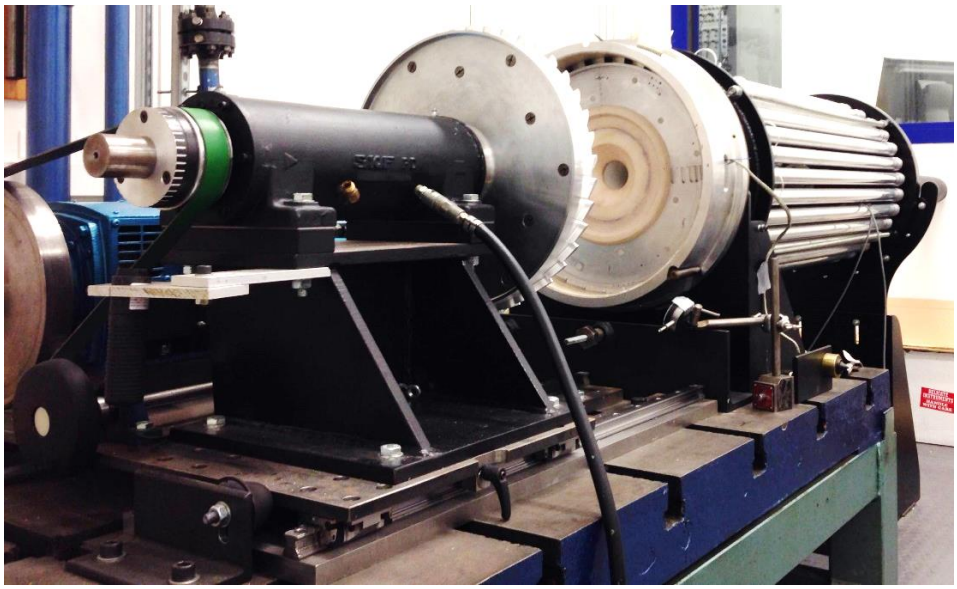

(b) Photographic image of the turbine rig with wheel-space in open state

Figure 3.2 Overview of the turbine research facility

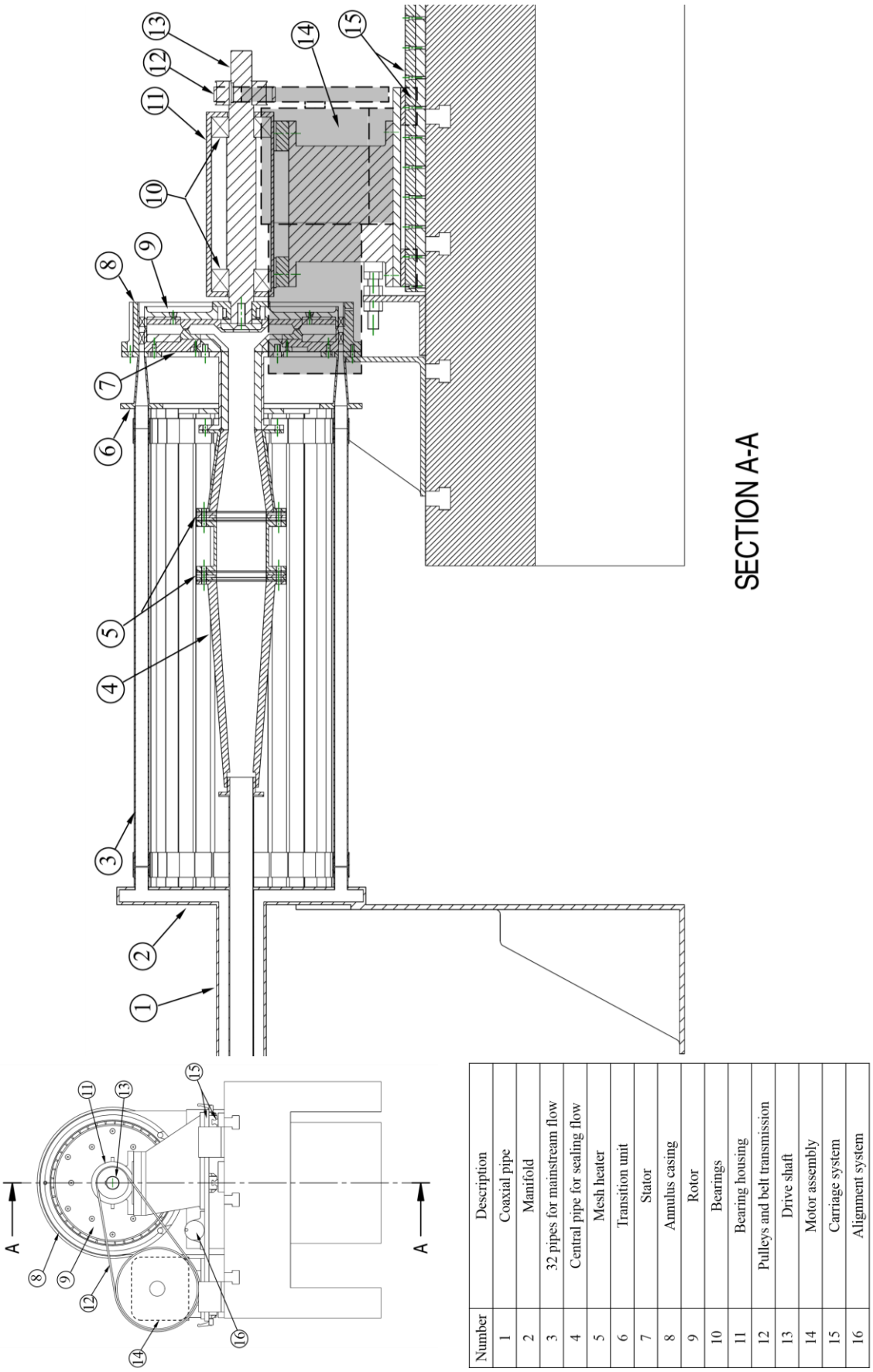

Number	Description
1	Coaxial pipe
2	Manifold
3	32 pipes for mainstream flow
4	Central pipe for sealing flow
5	Mesh heater
6	Transition unit
7	Stator
8	Annulus casing
9	Rotor
10	Bearings
11	Bearing housing
12	Pulleys and belt transmission
13	Drive shaft
14	Motor assembly
15	Carriage system
16	Alignment system

Figure 3.3 General assembly of the turbine research facility

3.2 Inlet configuration and the drive system

Figure 3.4 shows the inlet configuration for mainstream and sealing flows. Compressed air is supplied through a coaxial pipe that consists of a two-inch pipe for sealing flow and a four-inch external pipe feeding the mainstream flow. The coaxial pipe is connected to a manifold, in which the mainstream flow expands radially outwards and moves into 32 identical stub pipes evenly distributed circumferentially. These stub pipes are adjoined by one-metre long straight pipes which are connected to another sets of stub pipes located on an annulus transition unit. O-ring and sleeves were employed in combination to seal the joints at both ends of the annulus flow pipes. The sleeves can slide off thus allowing the long pipes to be detached. This enables access to the back of the stator where instrumentation arrangements can be adjusted. The mainstream flow from discrete pipes mixes and accelerates towards a continuous annular area in the transition, which is contracted to form a 10 mm annulus height equal to that of the turbine stage.

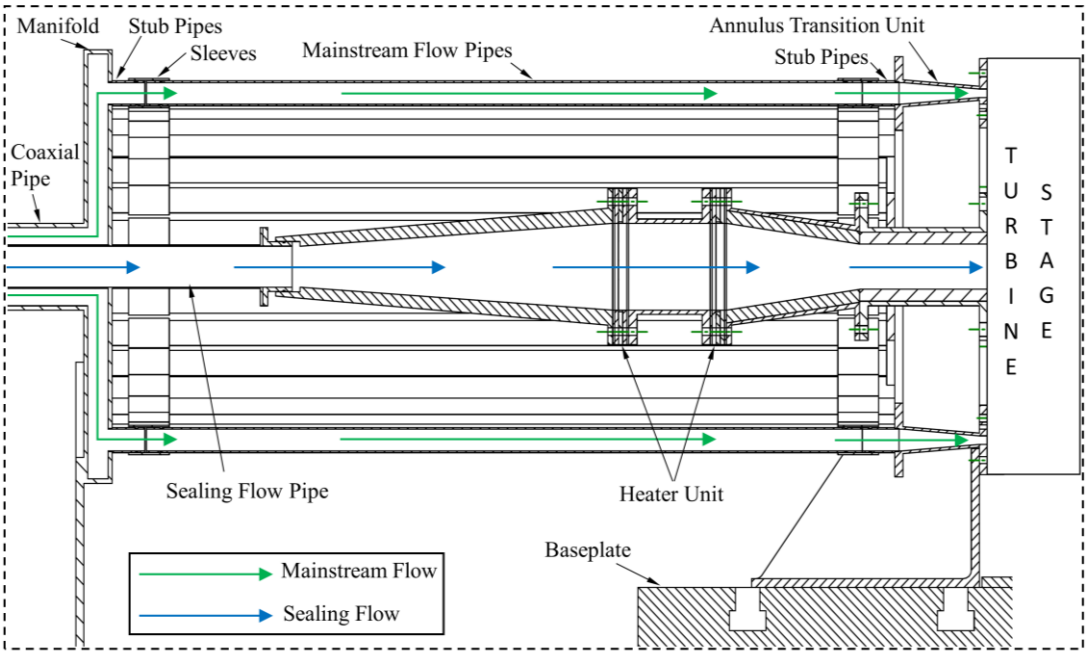

Figure 3.4 Inlet configuration for mainstream and sealing flows

The two-inch sealant line from the coaxial pipe supplies a middle section which contains two stages of mesh heater units required to raise the sealant temperature for reverse heater transfer experiments (beyond the scope of this thesis). Two transition sections are connected to the heater units from upstream and downstream sides respectively, to enable the change of cross-section. The pipes downstream of the heater units are internally insulated to prevent unwanted heat transfer through the walls. The sealing air can be seeded with approximately 1% CO_2 (injection point not shown in the

figure) as a tracer gas to determine the degree of ingestion. The CO_2 gas concentration can be measured at the inlet to the system and inside the wheel-space to assess a dilution in concentration in order to determine the sealing effectiveness.

The axis-symmetry of pressure upstream of the vanes was evaluated in the feed system for the mainstream flow. Static pressure measurements were made on each of the 32 stub pipes connected to the annulus transition. As shown in Figure 3.5, the circumferential distribution of pressure is plotted versus angular position, and the difference in pressure is shown to be within ± 1.5% (± 0.4 mbar) of the average value.

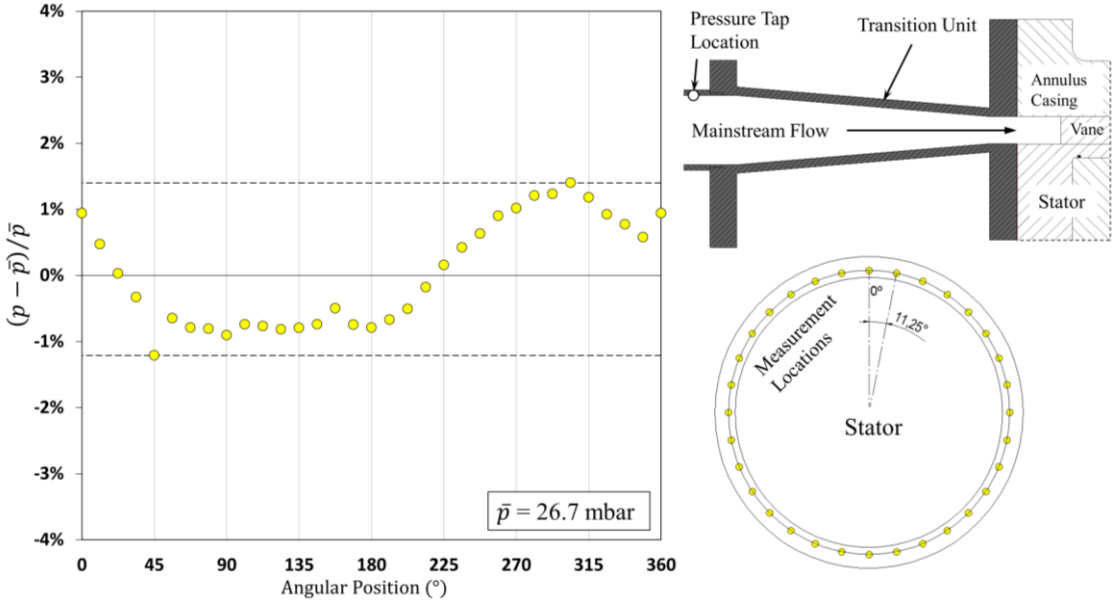

Figure 3.5 Circumferential distribution of pressure in the feed system for mainstream

The drive system for the turbine rotor consists of the powertrain and a carriage system as shown in Figure 3.6. The powertrain comprises an electric motor, a shaft driven by the motor via a flat belt transmission and a bearing unit supporting the shaft. A new carriage system was designed to carry the complete powertrain. The design of this carriage system is aimed to achieve precision alignment of turbine discs in support of testing engine-representative rim seals, and to enable quick access to the wheel-space instrumentation, and to ensure repeatability in seal clearances after a re-alignment is performed.

The carriage system comprises a carriage-plate assembly (Figure 3.6 (a)), and a precision end-stop mechanism (Figure 3.6 (b)) designed for the accurate control of positioning, enabling the seal clearances between the stator and rotor to be set with an accuracy of 0.05 mm. Ball-bearing runner blocks were installed to the carriage-plate to enable sliding motions; two clamping units were fixed on the plate to lock the system during operation of the rig. The Bosch Rexroth® guide rails provide

an accuracy of 10 μm in positioning. The end-stop mechanism includes a lead-screw assembly for motion controls and a pair of adjustable end-stop units fixed on the baseplate and on the drive system respectively.

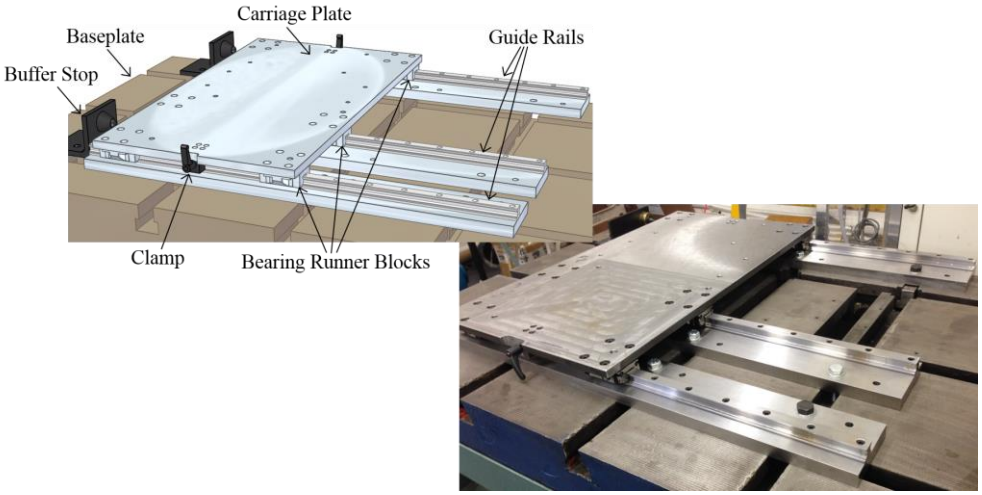

(a) CAD model and photographic image of the carriage-plate assembly on guide rails

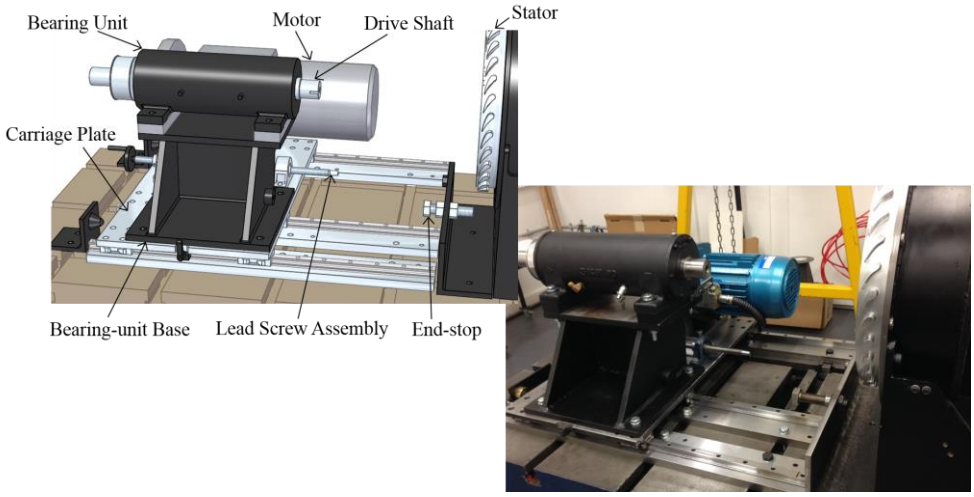

(b) CAD model and photographic image of the drive system

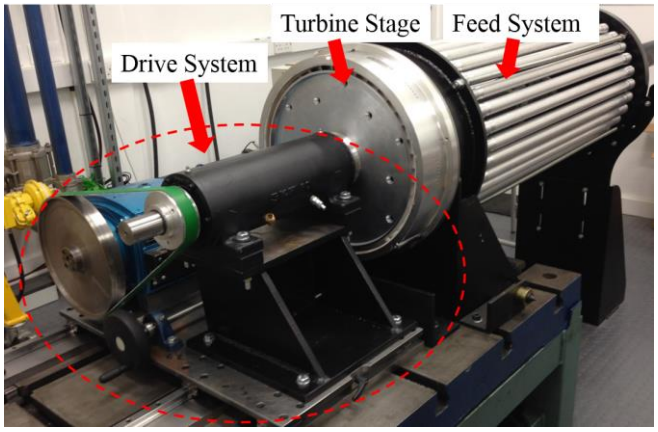

(c) Photographic image of the drive system with the rig fully assembled

Figure 3.6 Images of the drive system for turbine rotor

3.3 Design of the rotor-stator system

The cross-section of the rotor-stator system is shown diagrammatically in Figure 3.7, where the mainstream and sealing flows are indicated by $\dot{m}_a$ and $\dot{m}_0$ respectively. The components are colour-coded, consistent with those shown in Figure 3.1. A rim seal is located at the periphery of the wheel-space, which is formed between the stator and rotor. The sealing flow enters the system at the central bore of the stator and moves radially outwards. It flows through the inlet seal to enter the wheel-space. The mainstream flow passes the vanes and blades in the annulus path, creating pressure asymmetries that drive ingestion into the wheel-space.

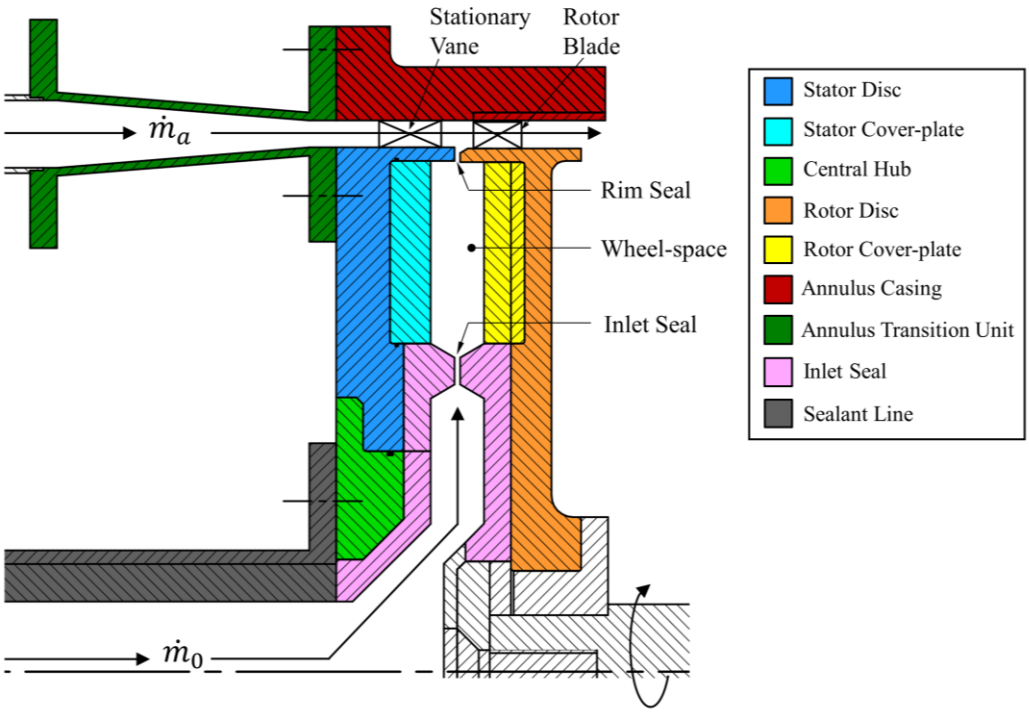

Figure 3.7 Cross-section of the turbine stage

Figure 3.8 details the dimensions for the turbine stage. The aspect ratio of the wheel-space and the seal clearance were determined in order to investigate engine-representative rim seals. The height of the mainstream annulus was set to achieve appropriate flow velocities in the gas path. Dimensions of the stator and rotor discs were designed to enable the variation of wheel-space geometries. Modular rim-seal components can be attached to the turbine discs and cover-plates, where mounting holes were specifically designed. Dimensions of cover-plates attached on the stator and rotor discs can be varied to control the width of the wheel-space; geometric features of the inlet seal can also be modified to control the radial dimension of the wheel-space.

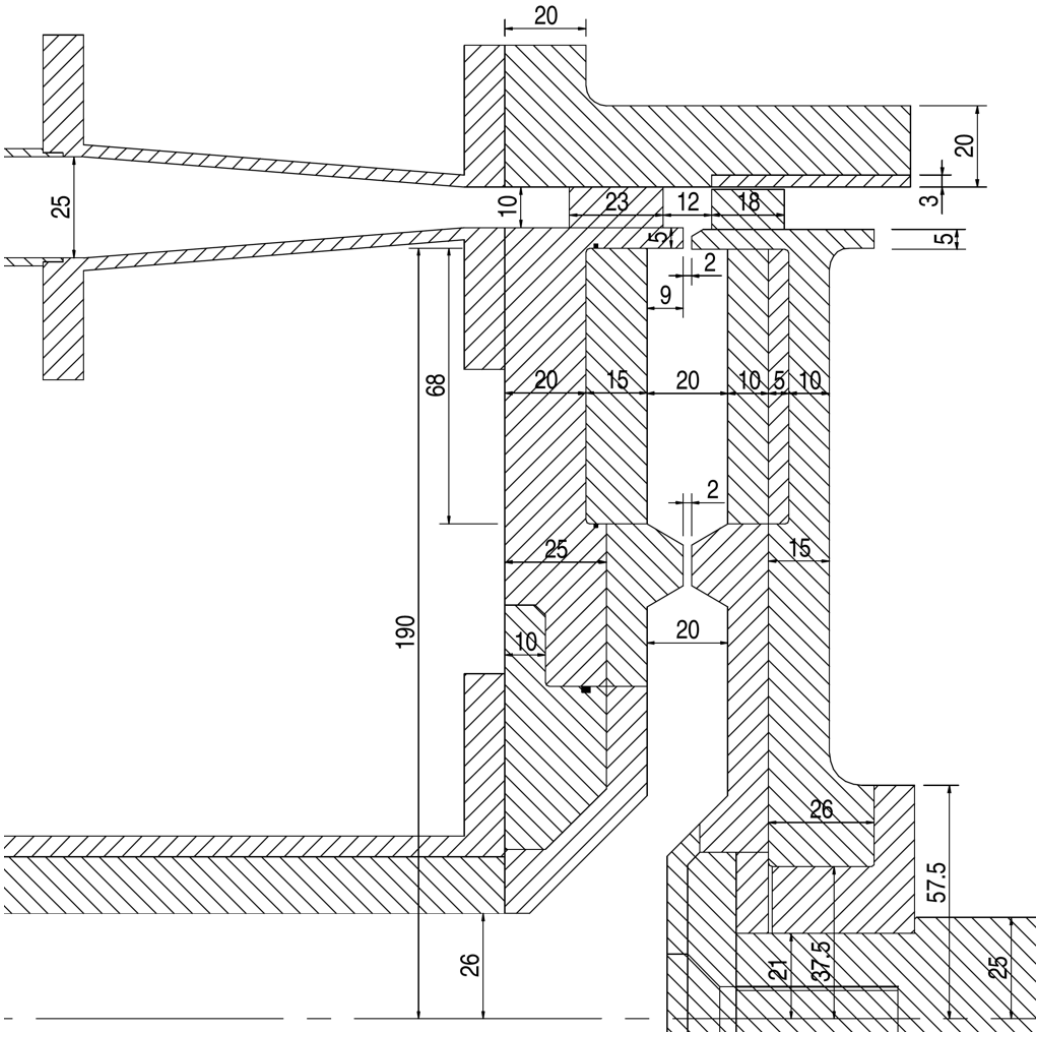

Figure 3.8 Geometric properties of the turbine stage
(dimensions in mm)

3.3.1 Vane and blade configuration

Figure 3.9 shows the vane and blade profiles and the corresponding velocity triangle for the mainstream flow between the vanes and blades. An engine-representative vane profile was modelled in the rig, with a small fillet manufactured at the trailing edge. The stator vane features zero inlet angle, due to the purely axial flow entering the vane row. The vane profile has an exit angle of 76.5° relative to the axial direction. Symmetric aerofoil NACA0018 was employed for the rotor blade profile with an inlet angle of 56.7° relative to the axial direction. Supported by computational work at Siemens, these symmetric blades were able to produce unsteadiness at the rim-seal region, with ingress effects not substantially altered without the inclusion of turned blades. The use of symmetric blades also obviates the need for a dynamometer under on-design operating conditions, which experiments in this thesis are predominantly conducted at. The numbers of vanes and blades are 32

and 41 respectively; these quantities, in conjunction with the blading geometries and vane-blade separation gap, provide a scaled engine-representative pressure field under design conditions.

The nomenclature used in the velocity triangle is defined as follows: the turbine operates with an angular velocity, Ω, for the rotor, and the mean tangential velocity for the rotor blades is assumed to be, Ωb, where b is the mean radius. The mainstream flow enters the vane row with an axial velocity, W, and leaves with a velocity, C_2, in a stationary frame of reference, with an angle of α_2 which equals to the vane exit angle. In a rotational frame of reference with an angular velocity, Ω, the vane exit flow velocity is V_2 with an angle of β_2. When β_2 equals the blade inlet angle, the turbine stage operates at a condition that is referred to as the on-design condition.

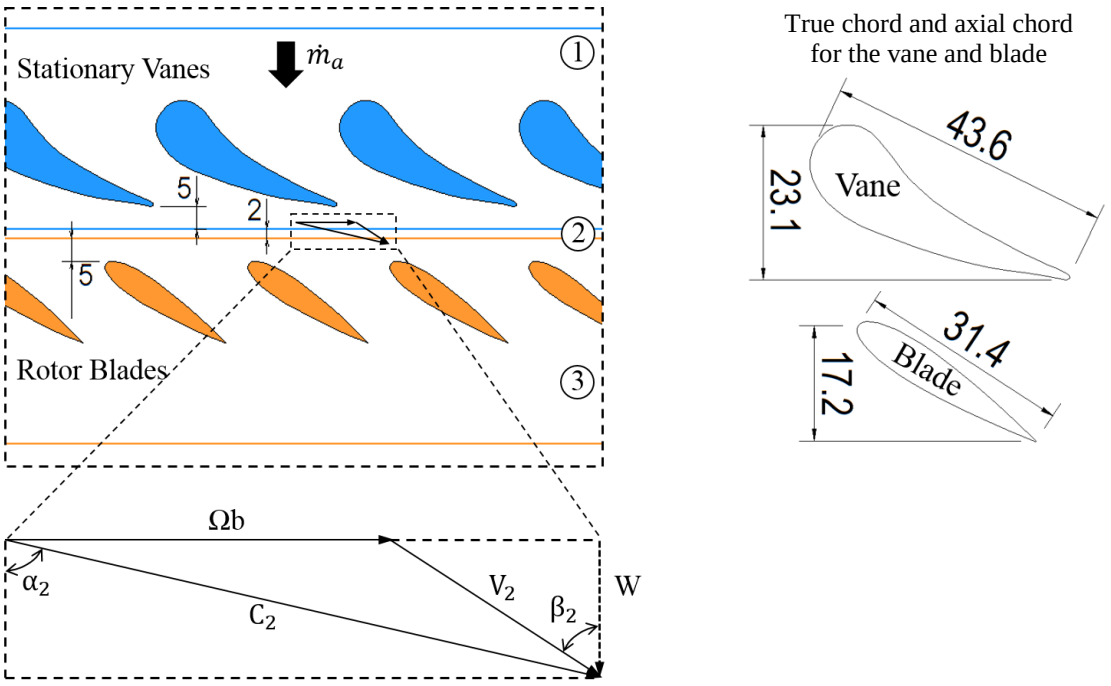

Figure 3.9 Vane and blade configuration and velocity triangle
(dimensions in mm)
(the subscript '2' denotes the space between the vanes and blades)

The on-design operating conditions for two rotor disc speeds are shown in Table 3.1. Based on the velocity triangle, the turbine rig operates with a flow coefficient ($C_F = Re_w/Re_\phi$) of 0.38 as the design point. The flow exiting the vane stage was treated as incompressible due to the relatively low Mach numbers. The density, temperature and viscosity of the air were determined from pressure and temperature measurements in the mainstream annulus. The rotor disc can be rotated up to 4000 rpm, resulting in a maximum rotational Reynolds number of 10^6, which is an order of magnitude less than that found in engines. However, according to Owen and Rogers (1989), the turbulent flow structure in boundary layers only depends weakly on Re_ϕ for rotating flow; it is principally governed by the

turbulent flow parameter, λ_T, which combines the effects of purge flow and rotational speeds. The flow structure in the rotor-stator system is considered to be representative of that found in an actual gas turbine wheel-space. More discussions about the effect of Re_ϕ on ingress will be made in the following chapters in conjunction with experimental measurements.

Table 3.1 On-design operating conditions

Parameter	**On-design operating conditions**	
Rotor Disc Speed (rpm)	2000	3000
Vane Exit Angle (α_2)	76.5°	
Blade Inlet Angle (β_2)	56.7°	
Tangential Velocity of Blades (Ωb)	39.8 m/s	59.7 m/s
Vane Exit Velocity (C_2)	64.4 m/s	96.6 m/s
Blade Inlet Velocity (V_2)	27.3 m/s	41.2 m/s
Axial Velocity Component (W)	15.0 m/s	22.6 m/s
Mainstream Flow Rate ($\dot{m}_a$)	0.24 kg/s	0.36 kg/s
Axial Flow Reynolds Number (Re_w)	2.0×10^5	3.0×10^5
Rotational Reynolds Number (Re_ϕ)	5.3×10^5	7.9×10^5
Vane Exit Mach Number (M)	0.20	0.30
Flow Coefficient (Re_w/Re_ϕ)	0.38	0.38

3.3.2 Material selections

Figure 3.10 shows the material selections for the turbine stage of the research facility. The stator and rotor discs were made of aerospace-grade aluminium alloy (Al 7075-T6). The stator (rotor) disc was designed with the vanes (blades) integrated, to form a bladed disc, traditionally known as blisc. Each blisc was manufactured from a single piece of aluminium alloy, with blading profiles shaped by 5-axis CNC (Computer Numerical Control) machining. The annulus casing was also made of aluminium alloy, with a lining attached on the inner surface in case of abrasion between the blade tips and the casing during assembling processes. The material for the lining is a Rohacell foam, which is a low-density structural foam.

The stator was designed to be located on an aluminium central hub, which was connected to the end section of the sealing flow pipe made of mild steel. Thermal insulation was incorporated in the design for the sealing flow path, including the pipe and the turbine disc surfaces. Rohacell foam was used again as an insulation lining material due to its low thermal conductivity. Surfaces of the linings were meticulously filled to obtain required smoothness. The linings are constantly applied along the path

from the mesh heater in the sealant line, up to the inlet of the wheel-space, irrespective of the sealing flow temperature. For a cold sealing flow, insulation is not needed, thus not applied in the wheel-space.

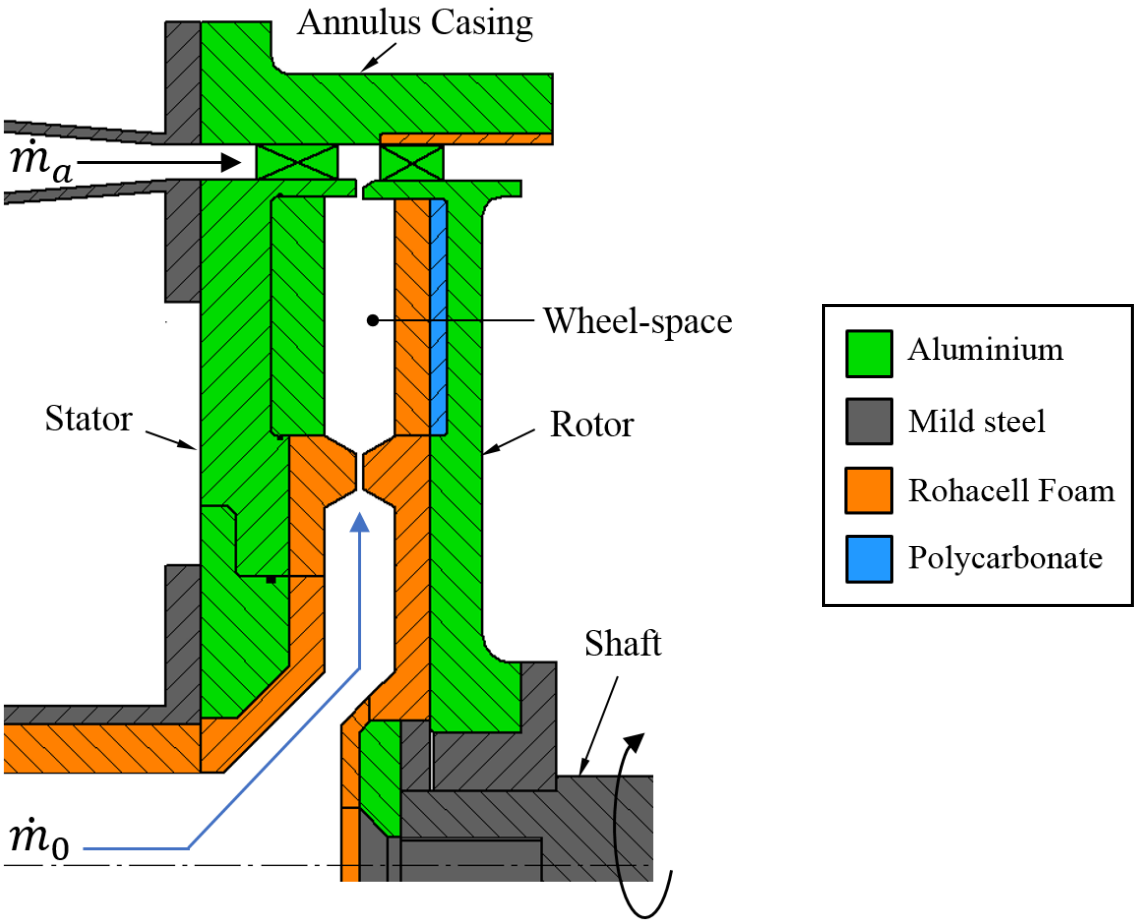

Figure 3.10 Material selections for the turbine stage with a cold sealant air

In the wheel-space, modular cover-plates were designed to be attached on turbine discs. For the stator cover-plate in a cold-sealant test, aluminium was selected to maximise the capability of instrumentation due to manufacturing reasons. The rotor cover-plate features a light-weight dual-layer structure, where the foam was epoxied to a polycarbonate plate, which is then affixed to the rotor disc.

For heat transfer measurements with a hot sealing flow, changes would be made to the cover-plates, as shown in Figure 3.11. An insulation lining was designed for the stator cover-plate. Moreover, inner surfaces of the shrouds were also insulated, though resulting in a slight change of wheel-space configuration. This research facility was designed with capability to perform extensive heat transfer measurements to study thermal effects of hot gas ingress. However, the heat transfer experiments are beyond the scope of this thesis.

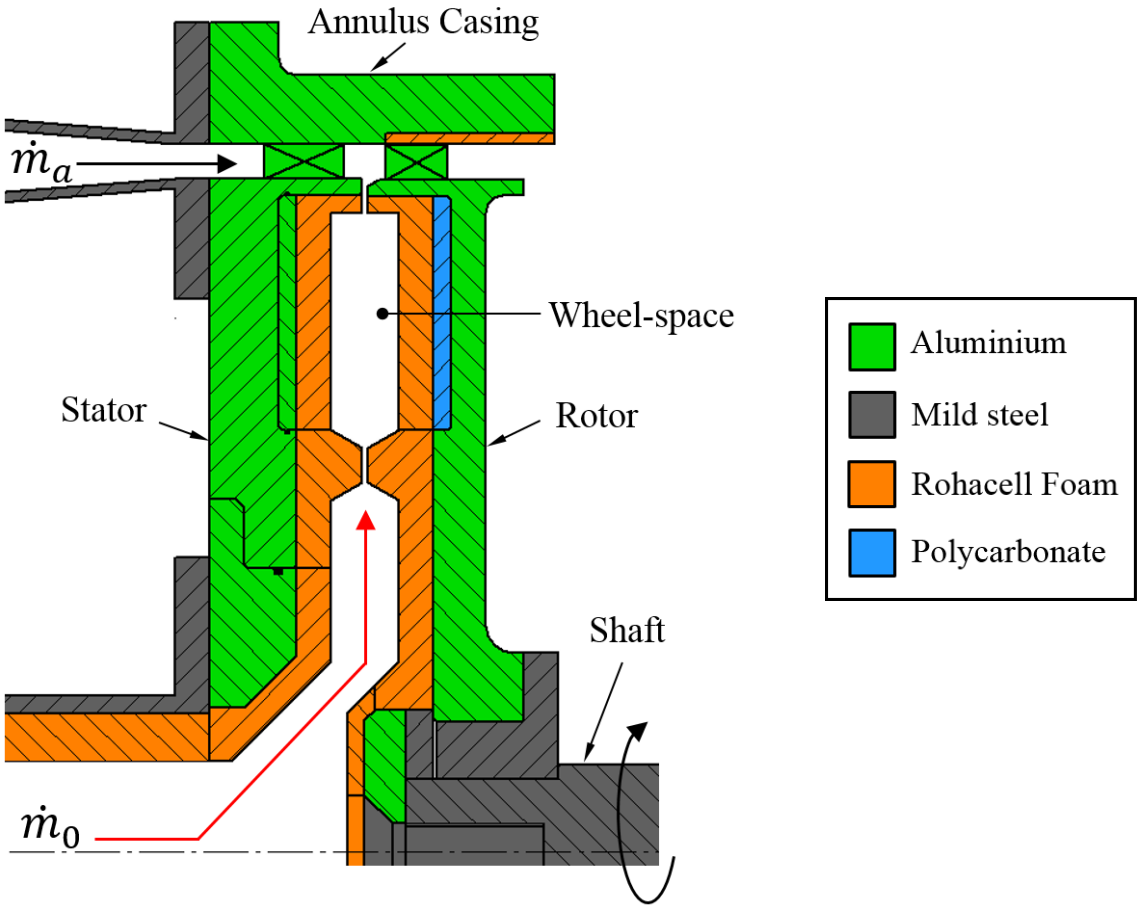

Figure 3.11 Material selections for the turbine stage with a hot sealant air

3.3.3 Stator and rotor assemblies

The rotor-stator system of the facility is formed by a rotor assembly adjacent to a coaxial stator assembly, with the rotor and stator discs as the most essential components. Other parts attached to the discs were designed to play important roles in respect of instrumentation and wheel-space configurations. A principal aim for the design was to build a highly versatile system for undertaking extensive research on hot gas ingress.

The stator and rotor discs were both designed with blading integrated to form bliscs, as shown in Figure 3.12. This design obviates the need for attachment of vanes and blades onto the turbine discs, thus promoting structural simplicity and integrity. A high level of consistency was ensured for the vane and blade passages. Moreover, the geometric tolerances of the bliscs were more effectively controlled in terms of overall diameters, concentricity and roundness; these brought a benefit to the fitting of annulus casing and the stator, and provided an axisymmetric blade tip clearance.

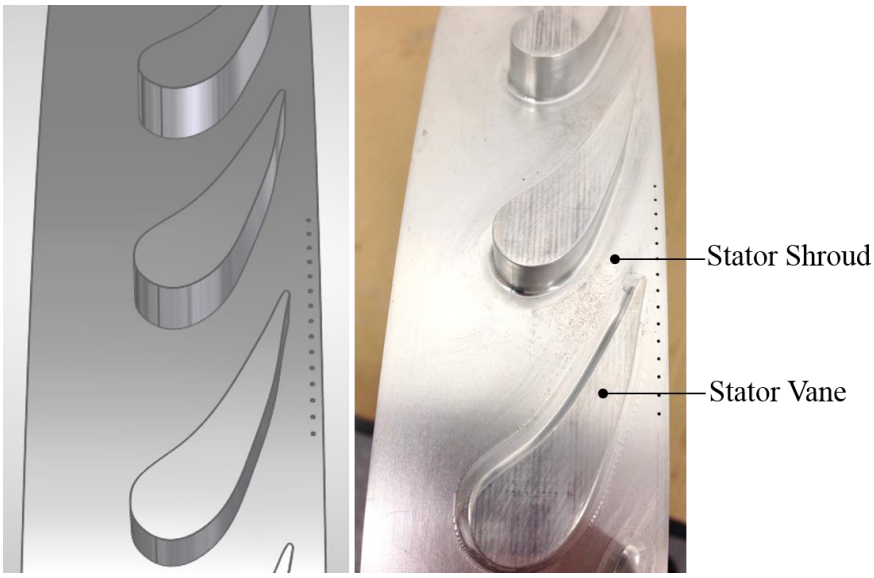

(a) CAD model and photographic image of the stator blisc

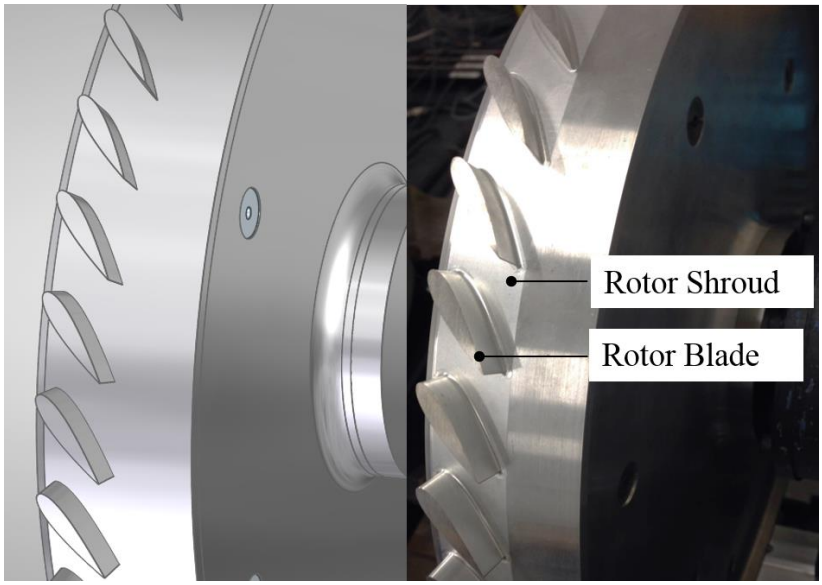

(b) CAD model and photographic image of the rotor blisc

Figure 3.12 Images of the bladed turbine discs

The stator assembly consists of a stator disc, a central hub, a cover-plate and an inlet-seal attachment; an exploded view of the assembly is shown in Figure 3.13. Modular design approach was applied to this assembly, which forms the stationary stage of the rig. The stator disc is located on the annulus transition unit and the central hub, which is connected to the sealant line, as shown in Figure 3.7. A baseline stator disc could be detached and substituted by a different modular stator for a specific testing programme, and this change of stator could be achieved conveniently. The cover-plate was designed to enhance adaptability of the wheel-space and the instrumentation capability; several cover-plates were designed for different research aims, including the fluid dynamics for different

rim-seal configurations and the thermal effects of hot gas ingress. Additionally, the modular cover-plates, together with the inlet-seal attachment, enable the variation of wheel-space geometries, which will be discussed in the next section.

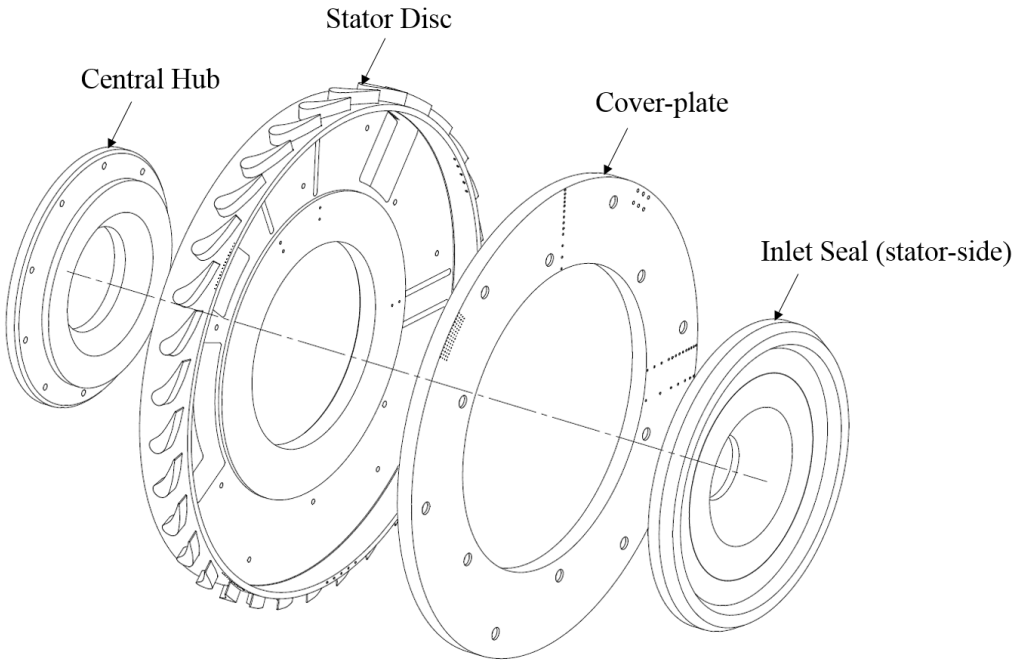

(a) Components of the stator assembly

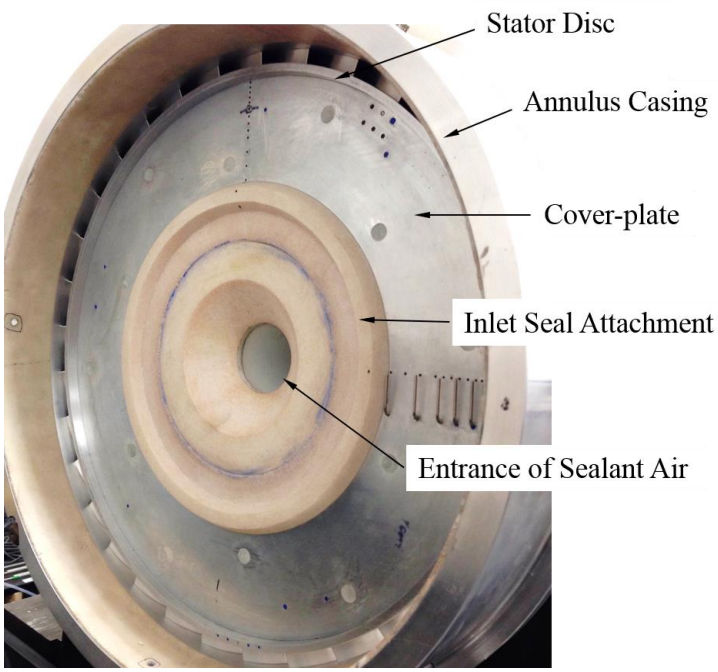

(b) Photographic images of the stator assembly

Figure 3.13 Images of the stator assembly

The rotor assembly comprises a rotor disc, a set of rotor cover-plates, an inlet-seal attachment and a locking device, which connects the rotor to the drive shaft and transmits torque via keys. The rotor assembly is shown in Figure 3.14. The cover-plate features a light-weight dual-layer configuration, with a foam plate epoxied to a polycarbonate plate as indicated in Figure 3.10. This leads to a decrease in the torque required to drive the rotor and in the overall stress level. Fasteners are used to affix the cover-plate to the rotor disc and the clamping force is taken by the polycarbonate plate. Clearance holes were machined on the foam plate that allows fasteners to go through; these holes were filled with removable silicone plugs to enable a smooth rotor surface for testing.

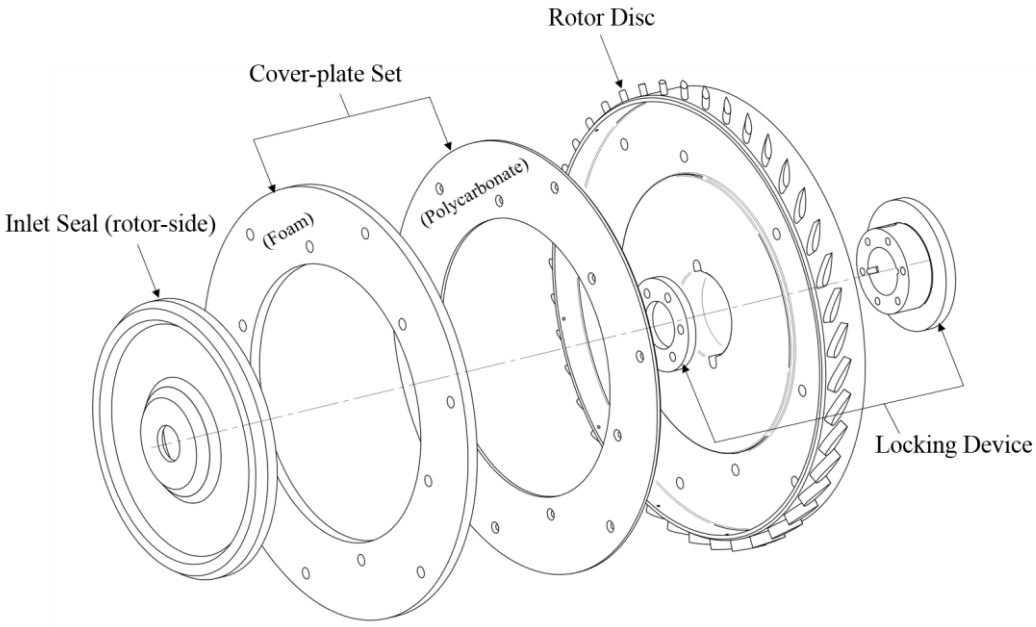

(a) Components of the rotor assembly

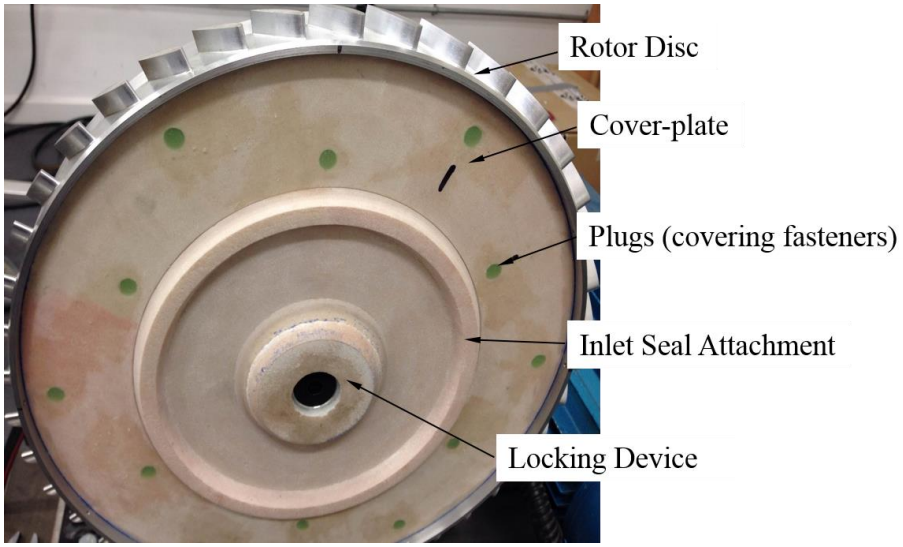

(b) Photographic images of the rotor assembly

Figure 3.14 Images of the rotor assembly

Figure 3.15 details the connection of the rotor disc to the shaft via a locking device, together with keys and keyways. The rotor is clamped by the locking assembly consisting of a flange that was shrunk fit to the shaft end and a cap on the opposite side of the disc. The flange provides accurate positioning for the rotor disc, and the cap fastened to the flange creates the clamping force.

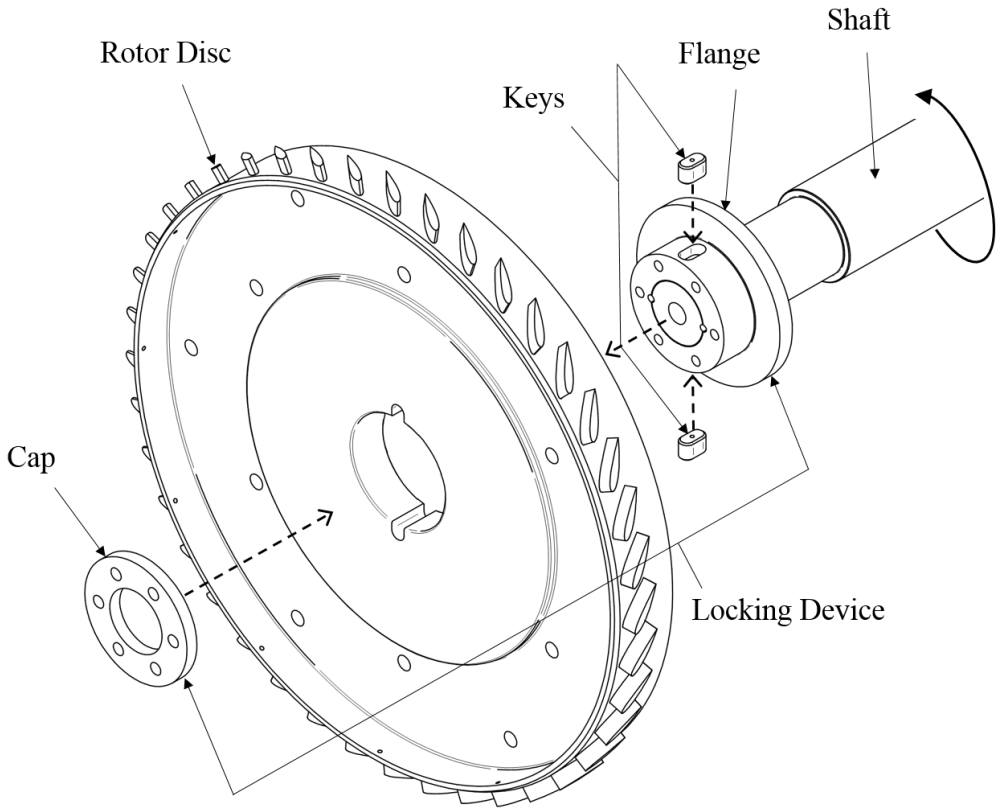

Figure 3.15 Connection of the rotor disc and drive shaft

Two identical keys were designed to transmit the torque from the drive shaft to the rotor. Two key seats, spaced 180 degrees apart, were machined in the flange of the locking device. Corresponding to those in the flange, two keyways were also cut in the rotor bore. Sharp edges were avoided to reduce the stress concentration, but the keyways were still expected to act as stress raisers. Therefore calculations of stresses and safety factors were undertaken; the main results are documented in this section.

Figure 3.16 (a) shows the geometry of the key. Figure 3.16 (b) shows the cross-section of the rotor bore region with the disc mounted onto the shaft. Over the cross-sectional area of A_{shear} as indicated in the figure, the shear stress in each key was calculated using

$$\tau = \frac{T}{d \cdot A_{shear}} \tag{3.1}$$

where T is the torque transmitted by that key; d is the bore diameter, with a value of 75 mm. A_{shear} is the area taking the shear stress with a value of 80 mm^2.

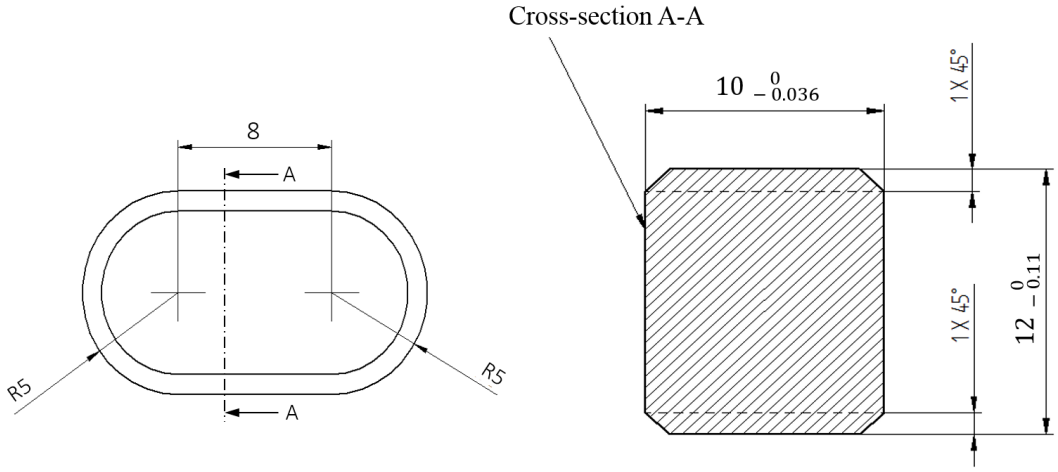

(a) Geometric property of the key

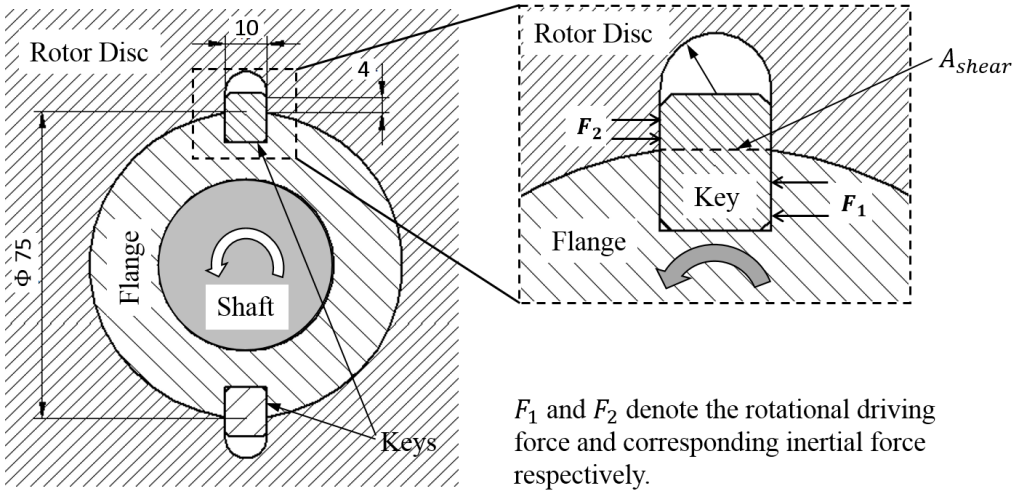

(b) Bore region of the rotor showing the shaft and keys

Figure 3.16 Design of keys and keyways for torque transmission (dimensions in mm)

The torque was estimated to be $T = 6.3$ N · m. This estimation was based on an exaggerated scenario when the rotor was accelerated from 0 to 3000 rpm (or decelerated) in 5 seconds, to simulate a extremely rapid change of rotational speed which is unlikely to take place. Based on the design of keys, the shear stress in each key was calculated to be $\tau = 1.05$ MPa. In conjunction with the shear strength of carbon steel, which the keys were made of, a safety factor was calculated to be $N_{key} > 10$.

For the theoretical calculations of hoop and radial stresses in the rotor disc, a 2D simple disc model was developed based on the rotor geometries. The mass of blades were circumferentially averaged and represented by a ring added to the periphery of the simple disc, as shown in Figure 3.17 (a). The model features an uniform thickness thus providing an averaged prediction relative to the actual disc. A 3D axisymmetric model was also produced more closely related to the rotor configuration as shown in Figure 3.17 (b), in order to perform a structural FEA (finite element analysis).

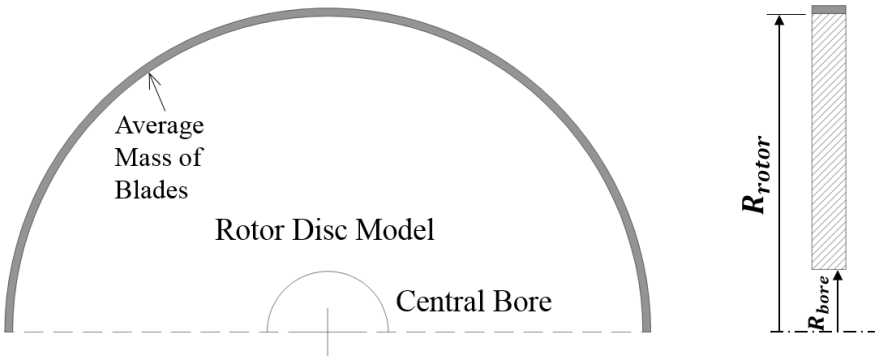

(a) Theoretical model of the rotor disc

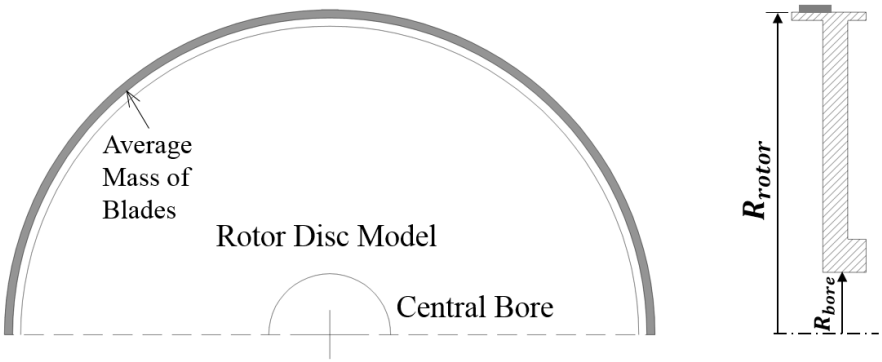

(b) FEA model of the rotor disc

Figure 3.17 Rotor disc models for theoretical and FEA calculations

The hoop and radial stresses of the rotor were calculated theoretically with the simple disc model, using the method described by Morley (1944). A steady-state FEA was conducted with a commercial simulation code (ANSYS Static Structural v15.0). The distributions of stresses were evaluated on the mid-plane of the FEA disc model over a full range of radius. Figure 3.18 and Figure 3.19 show the radial variations of hoop and radial stresses respectively. There is a good agreement for the variation of hoop stress between the FEA and theory. The hoop stress decreases with increasing radius, with a maximum of 9.3 MPa seen at the central bore. The radial stress increases with radius to reach a maximum value, followed by a decrease as radius further increases; this trend is seen for both calculation methods. The maximum value calculated with FEA is 3.5 MPa, approximately 15%

higher relative to the theory. The radial locations for the two peak values are both seen at one quarter of radial distance from the bore to the disc rim. The difference in the radial stress level may be attributed to the different modelling of the rotor shroud and positioning of blades between the two calculation methods.

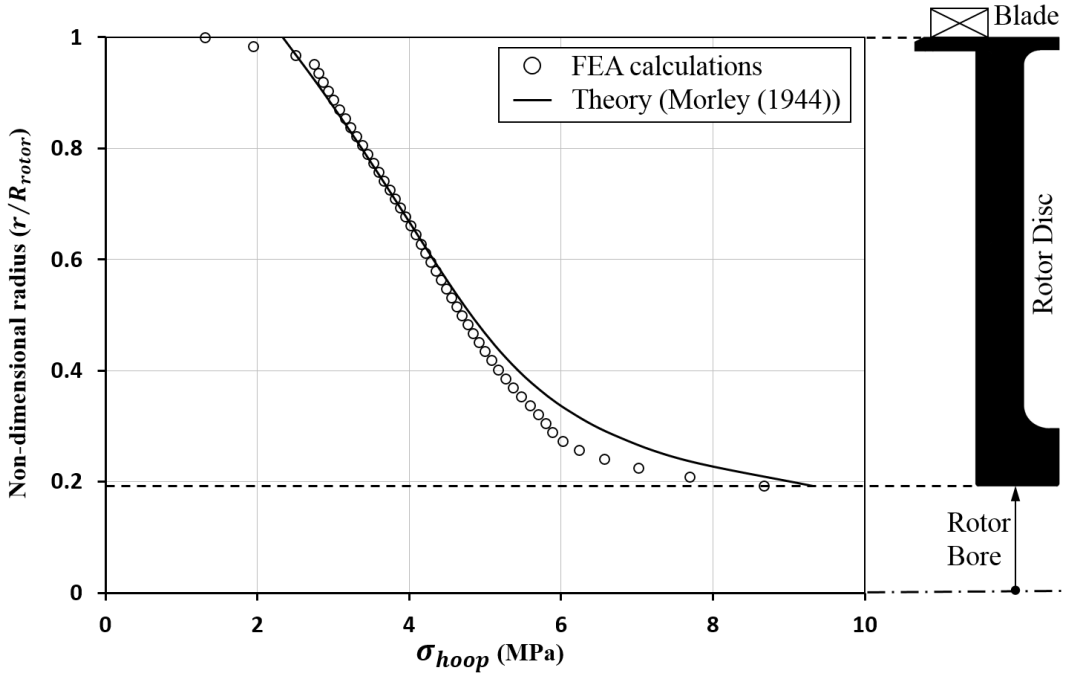

Figure 3.18 Hoop stress of the rotor from theoretical and FEA calculations

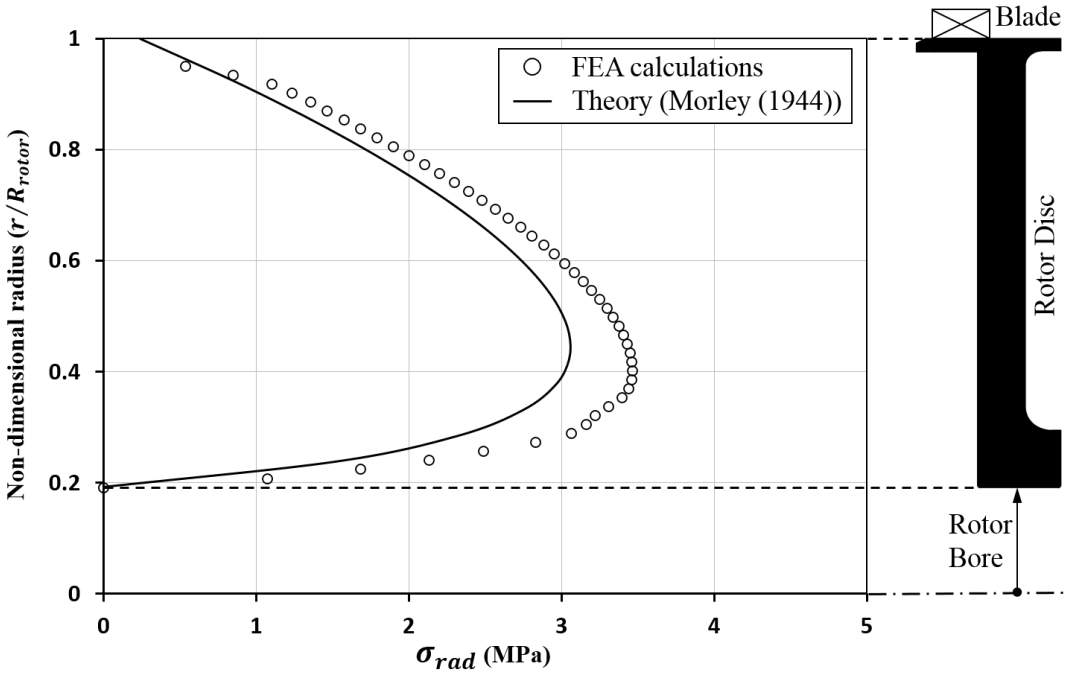

Figure 3.19 Radial stress of the rotor from theoretical and FEA calculations

Recall the rotor design shown in Figure 3.15, two keyways were cut in the rotor disc at the bore, acting as stress raisers. According to behaviours of stress raisers described by Peterson (1974), a stress concentration factor (K_t) with a value of 7 was determined based on the keyway geometries; moreover, a factor of 3 was used for the circular holes located at relatively high radii. The central bore is thus the critical region with the lowest safety factor, according to the radial variations of hoop and radial stresses in conjunction with the effect of keyways. Therefore a safety factor for the rotor disc could be calculated using

$$N_r = \frac{\sigma_{tys}}{K_t \cdot \hat{\sigma}_{hoop}} \tag{3.2}$$

where σ_{tys} denoted the tensile yield strength of the rotor material (Aluminium 7075-T6) with a value of 434 MPa. Only the maximum hoop stress $\hat{\sigma}_{hoop}$ was included in this calculation because it is the dominant stress at the bore region. The safety factor for the rotor, N_r, was calculated to be 6.7.

3.3.4 Variation of the wheel-space geometries

The stator and rotor assemblies were designed with the capability to vary the wheel-space geometries, including the axial width in the system, and the radial height from the inlet to the rim seal. Interchangeable cover-plates with different thicknesses were designed to change the wheel-space width, as illustrated in Figure 3.20.

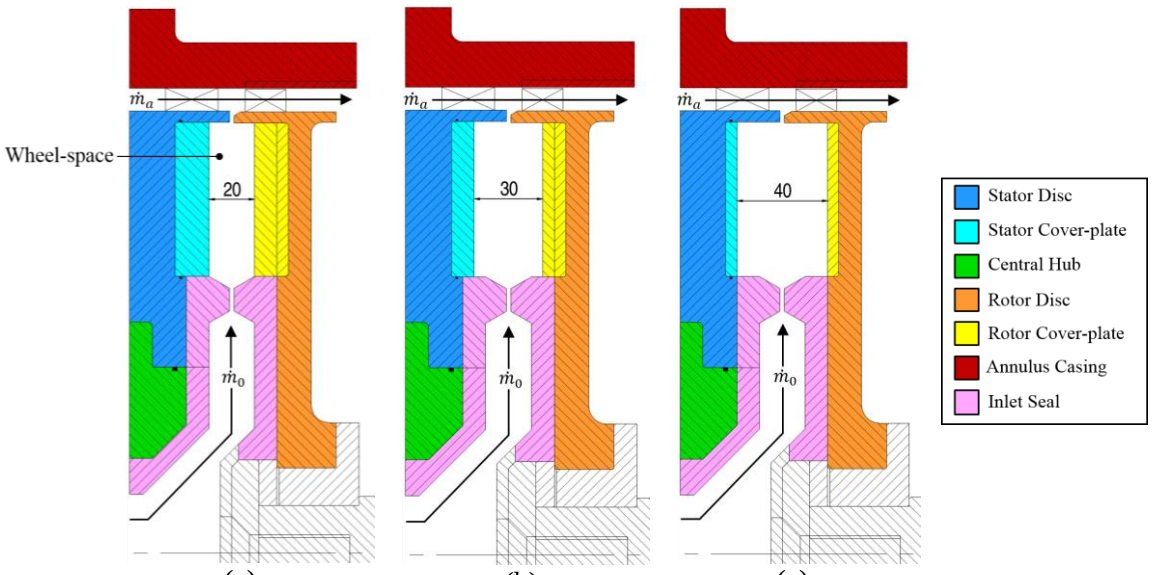

(a) (b) (c)

Geometric properties for wheel-space	Width (S) (mm)	Height (H) (mm)	Stator CP width (mm)	Rotor CP width (mm)	Gap ratio (S/b)	Aspect ratio (S/H)
(a)	20	68	15	15	0.105	0.294
(b)	30	68	10	10	0.158	0.441
(c)	40	68	5	5	0.211	0.588

(CP: cover-plate; b: outer radius of the wheel-space)

Figure 3.20 Variation of wheel-space width

These changes could be made without the need for repositioning the turbine discs, thus ensuring consistency for alignment. Tabulated geometric properties corresponding to each arrangement are provided in the figure. The wheel-space aspect ratio could be varied in the range between approximately 0.3 and 0.6, representative of those found in secondary air systems of gas turbine engines.

The radial height of the wheel-space can be varied by using modular inlet-seal attachments, as shown in Figure 3.21. One set of inlet seal attachments could be conveniently replaced by another set with different geometries, without the necessity of adjustment to the rest of the assemblies. The variation in the wheel-space height is achievable by design with a datum wheel-space width of 20 mm. The wheel-space aspect ratio could be varied in the range between approximately 0.2 and 0.53, as shown by the tabulated geometric features.

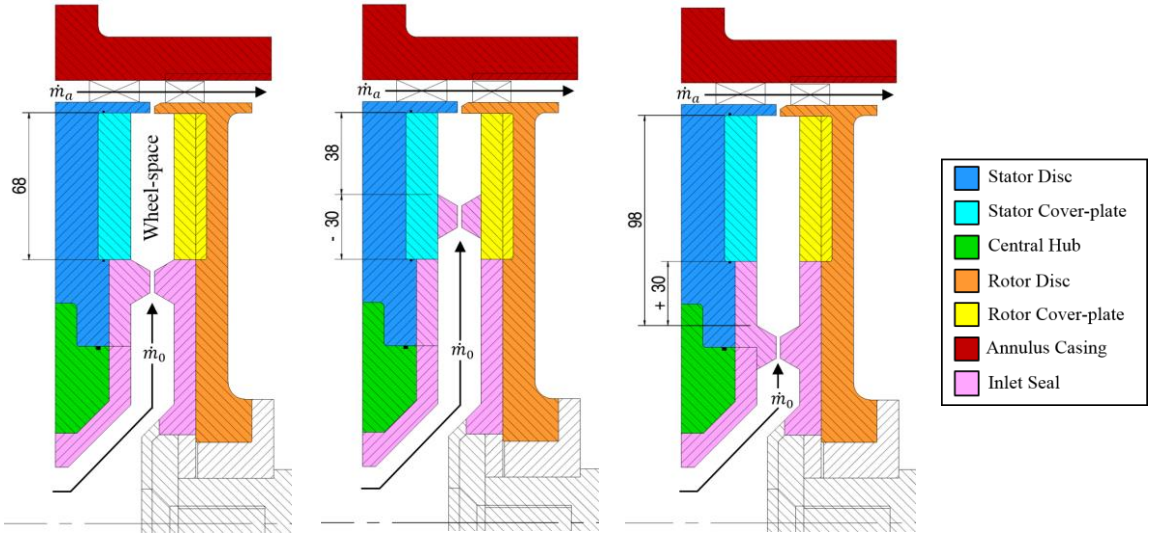

(a) (b) (c)

Geometric properties for wheel-space	Width (S) (mm)	Height (H) (mm)	Inlet seal radius (mm)	CP width (mm)	Gap ratio (S/b)	Aspect ratio (S/H)
(a)	20	68	122	15	0.105	0.294
(b)	20	38	152	15	0.105	0.526
(c)	20	98	92	15	0.105	0.204

(CP: cover-plate; b: outer radius of the wheel-space)

Figure 3.21 Variation of wheel-space height

The variation of the wheel-space geometries was aimed to validate a hypothesis: for a certain rim-seal configuration, the variation of ingress with sealing flow rate was expected to be unaffected by the change in wheel-space geometries. According to the orifice model developed at Bath (Owen (2011)), which provided an excellent prediction for the experimental data as shown earlier in Chapter 2, ingress is driven by the local pressure difference across the rim seal. With a certain mass flow rate for the sealant, the pressure in the wheel-space is unchanged by the dimension adjustments to satisfy

the conservation of mass. The external pressure is identical for every wheel-space scenario, thus leading to a fixed radial pressure difference across the seal for a given angular location. Therefore, theoretically the ingress with any given sealant mass flow rate would not be influenced by the wheel-space geometries. This hypothesis could be validated experimentally using the test rig.

3.3.5 Variation of gas path blading

The stator and rotor assemblies were designed with the capability to vary gas path blading in the mainstream annulus. The modular turbine discs are interchangeable with a different set of counterparts, which features a different vane-blade configuration, resulting in the variation of aerodynamics in the mainstream. The same cover-plates and rim-seal attachments could be applied to the new discs to form a consistent wheel-space configuration. This enables the impacts on ingress from gas-path aerodynamics to be explored.

For the design programme documented in this thesis, a second modular stator was designed with vane positions different from those shown in Figure 3.13 (Figure 3.13 shows the baseline configuration). The vanes were located further downstream by 40% of the baseline distance from the trailing edge to the rim-seal clearance. This is demonstrated in Figure 3.22.

A different external pressure variation for the wheel-space is expected to be generated due to the change in the vane-blade spacing. For experiments with the new spacing, the mainstream flow rate could be set the same as that for the baseline configuration; but the pressure asymmetries at the rim-seal clearance may be different between the two scenarios.

The EI ingress could be determined experimentally with the new configuration and compared with the baseline results. This comparison could be used to reinforce the aforementioned theoretical model, which regards the external pressure asymmetries as the driving potential for externally-induced ingress into the wheel-space.

In addition, the rotor assembly also consists of modular components, enabling the change of the rotor disc with different blading features. Although the symmetric blade profile is already shown in this chapter, it is highly convenient to switch to another rotor with a different blade profile, such as a turned blade with 3D aerodynamics features. Therefore the vane-blade interaction can be studied extensively with unsteady pressure measurements in the mainstream annulus.

It is also possible to have no blade incorporated, by employing a bladeless rotor which is interchangeable with the baseline counterpart. This allows the pressure field of vanes to be isolated from that of rotating blades. Experimental measurements could be conducted to determine the specific effect of rotor blades on EI ingress through the rim seal.

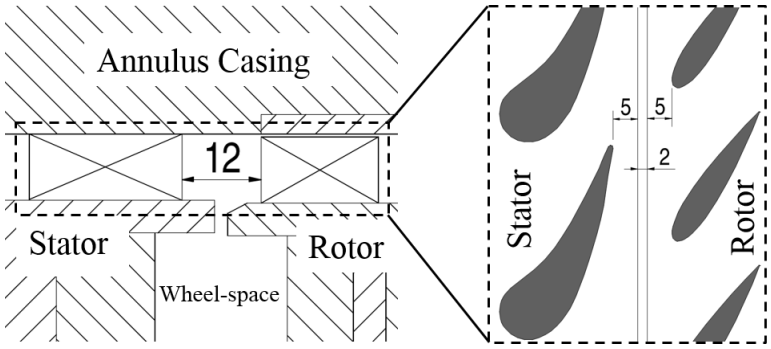

(a) Baseline vane-blade spacing (dimensions in mm)

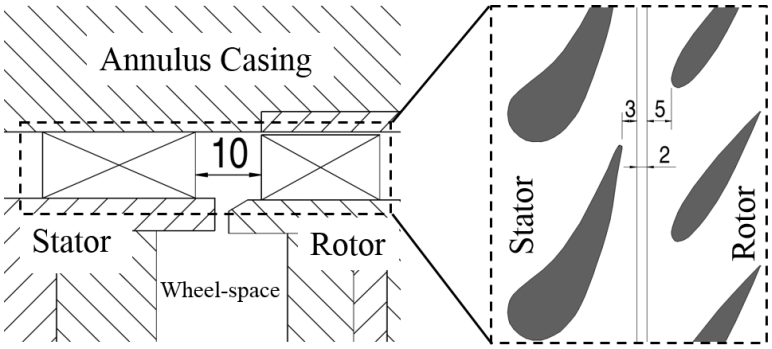

(b) Decreased vane-blade spacing (dimensions in mm)

Figure 3.22 Variation of gas path blading

3.4 Instrumentation

The cross-section of the turbine stage with instrumentation capability is shown in Figure 3.23. The radial and axial positions for various measurements are labelled with colour-coded symbols. It should be noted that not all instrumentation shown in the figure was employed altogether and used simultaneously. When fluid dynamics of ingress is to be studied, measurements of gas concentration and pressure usually take place, without the temperature in the wheel-space being taken. If thermal effects of ingress become the research aim, some of the instrumentation for pressure and gas concentration may not be required. When certain instrumentation is unused or detached for a specific test, any hollow space will be filled or covered to avoid any leakage flow.

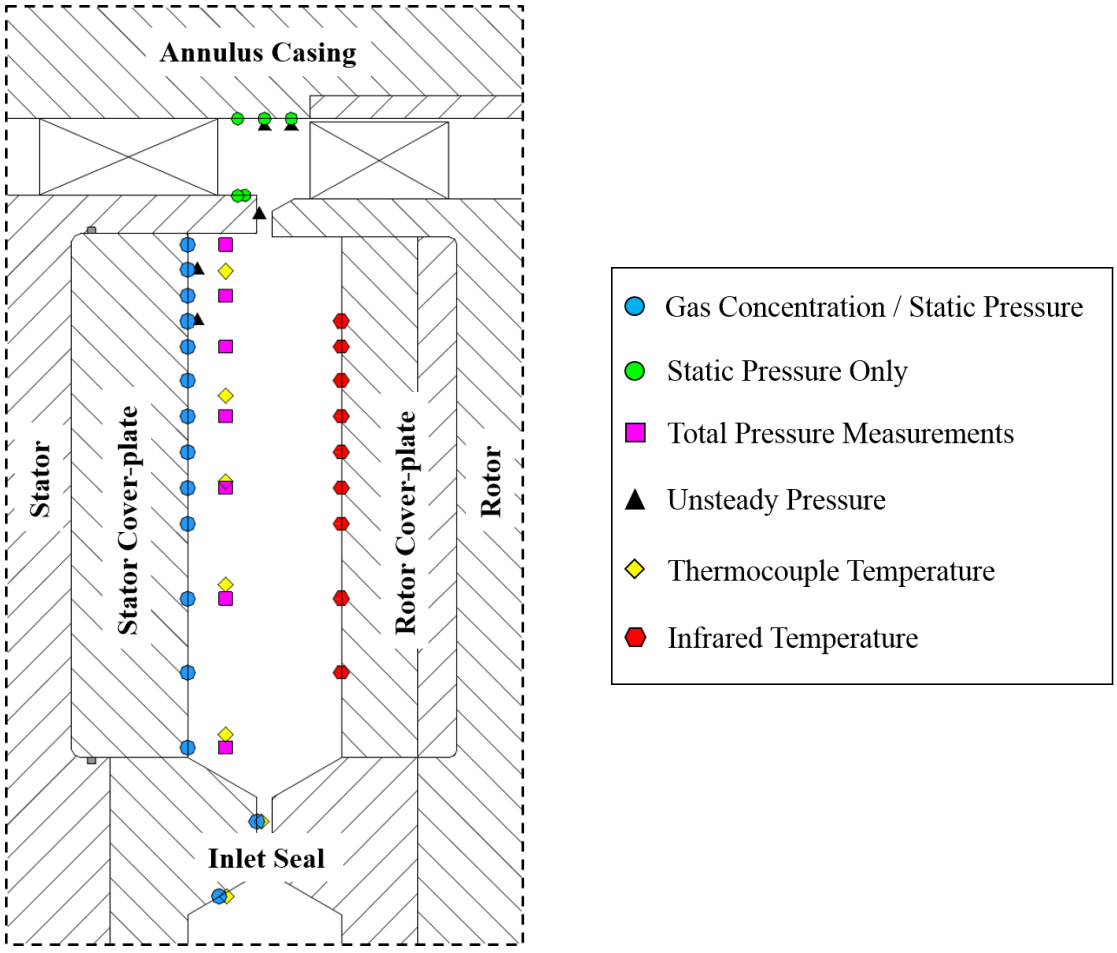

Figure 3.23 Overview of instrumentation for the turbine stage

In addition to those for experimental measurements as shown in Figure 3.23, instrumentation for tuning the turbine rig was employed, with respect to rotor disc speeds and flow rates. An optical laser probe was mounted to the bearing unit for the measurement of disc speeds. The laser beam from the

probe is focused on a tooth-wheel fitted on the shaft, which features 41 evenly distributed slots corresponding to the same number of rotor blades. Reflective tape is used for each slot, and a voltage signal is recorded for each reflection. The laser measurement provides rotational speeds with an uncertainty of $\pm$ 0.1%, as well as the blade-passing indications based on the variation of signals.

Orifice plates manufactured in compliance with ISO standards are used to measure mainstream and sealing mass flow rates. One of the orifice plate was fitted to the mainstream flow pipe with a 4-inch diameter, and another was fitted to the 2-inch sealant line. A coaxial pipe was formed by these two lines joining together to supply air flow for the facility, which can be seen from the general assembly shown in section 3.1. Pneumatically controlled actuator valves were employed to regulate the flows.

A Micro-Epsilon® laser proximity sensor was employed to measure the rotor shroud deformation under rotating conditions. The laser beam projected from the sensor was focused on a target spot in close proximity to the shroud edge. The reflection from the surface was imaged by a receiver onto a position-sensitive element inside the sensor. Any change in the target position was evaluated by the sensor, which has a stated uncertainty of 0.6 μm.

A control program built with LabVIEW coding was applied, in conjunction with a multi-channel control tower, to tune the rig and perform data acquisition. The program consists of several modules listed as follows:

Module I: it is for the control of rotational speed and mass flow rates, together with the measurements of pressure and temperature in both flow lines for fluid property calculations. Once the tuning is finished and the rig operates with a steady state, the objective of the first module is accomplished.

Module II: it is for the monitoring and recording of CO_2 gas concentration measured inside and outside the wheel-space, for the flow conditions already set in Module I. The sampling rate and duration can be set with appropriate values during the initialisation of the program.

Module III: it is for the monitoring and recording of pressure measured in the turbine stage. Two sub-modules were included. One is for time-averaged pressure, taken at multiple locations with a low sampling rate; the other is for time-dependent pressure, measured with fast-response transducers at several points for unsteadiness associated with the rotating blades.

For heat transfer experiments, an additional module was developed and could be used in conjunction with this main program. All experimental data can be recorded and output to individual files for further analysis, according to specific research objectives.

3.4.1 Instrumentation for the wheel-space

Figure 3.24 shows the arrangements of instrumentation on the stator disc and cover-plate. The instrumentation was employed for the measurements of pressure, gas concentration and temperature from the stationary side of the system. Table 3.2 details the radial positions of instrumentation in the wheel-space. The pressure and concentration taps are more closely spaced near the rim-seal region, to promote the resolution of measurements where external fluid is ingested into the wheel-space.

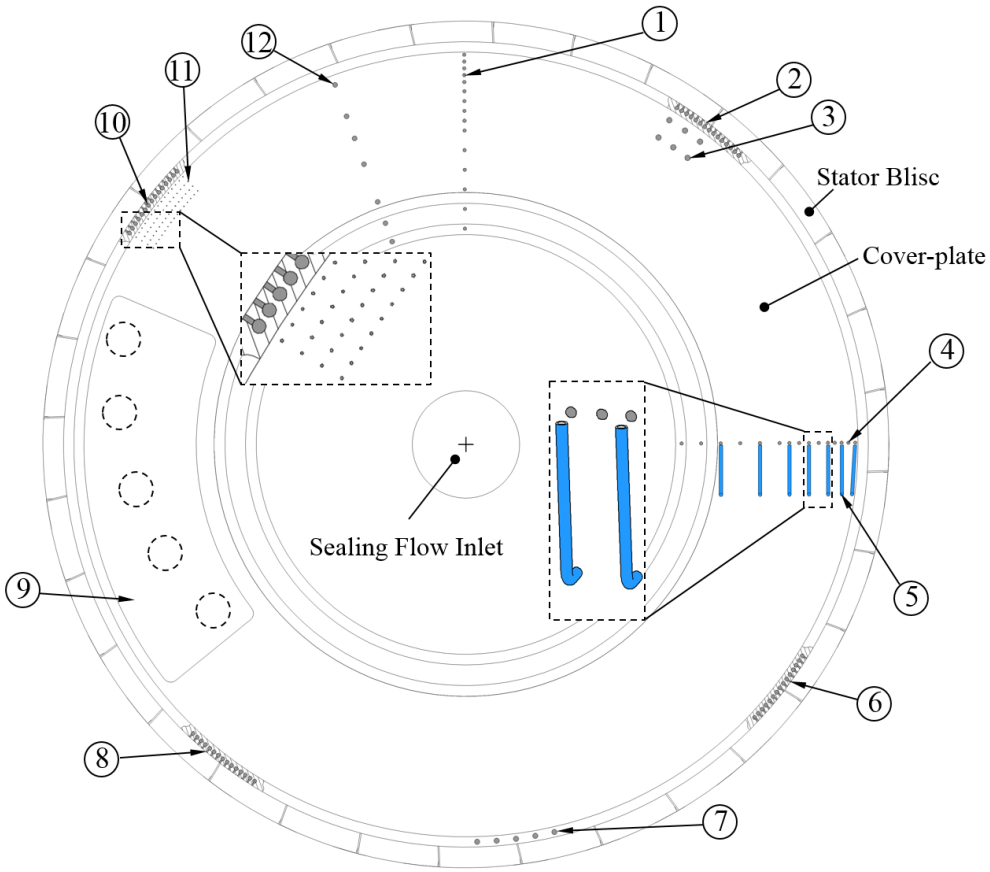

No.	Description
1	Gas concentration taps
2	First set of pressure taps on the vane platform
3	Unsteady pressure probes in the wheel-space
4	Radial pressure taps in the wheel-space
5	Pitot tubes in the wheel-space
6	Second set of pressure taps on the vane platform
7	Unsteady pressure probes at the rim-seal
8	Third set of pressure taps on the vane platform
9	Area for mounting infrared probes
10	Fourth set of pressure taps on the vane platform
11	Circumferential pressure taps in the wheel-space
12	Thermocouples in the wheel-space

Figure 3.24 Instrumentation arrangements for the stator disc and cover-plate

Table 3.2 Radial positions of instrumentation in the wheel-space

Non-dimensional radius (*r/b*)	**Aims of instrumentation**			
	Concentration/ Static pressure	Total pressure with pitot tubes	Temperature with thermocouples	Temperature with infrared probes
0.55	√	—	√	—
0.6	√	—	√	—
0.65	√	√	√	—
0.7	√	—	—	√
0.75	√	√	—	√
0.76	—	—	√	—
0.8	√	—	—	√
0.825	√	√	√	√
0.85	√	—	—	√
0.875	√	√	—	√
0.89	—	—	√	—
0.9	√	—	—	√
0.923	√	√	—	√
0.941	√	—	—	√
0.958	√	√	—	—
0.975	√	—	√	—
0.993	√	√	—	—

Static pressure taps were positioned on the stator wall at multiple radii to assess the radial distribution of time-averaged pressure. For those locations from r/b = 0.941 to 0.993, circumferentially distributed pressure taps were positioned on the cover-plate over a 11.25° scalloped sector (one vane pitch), as displayed in Figure 3.24. Thus effects of circumferential pressure asymmetries found in the mainstream annulus are monitored in the wheel-space. The pressure taps are 1.65 mm stainless steel hypodermic tubes installed in clearance holes drilled in the cover-plate. With one end of the tubing flush with the stator surface in the wheel-space, the other end passed through slot sections of the stator disc, to be connected to a Druck® pressure transducer via a Scanivalve® device, an automated multi-channel pressure scanner. This arrangement enables multiple pressure measurements in each testing set with consistent instrumentation. The Druck transducers used in the experiments has an uncertainty of $\pm$ 0.06% across a 70 mbar range.

Total pressure in the core region of fluid was measured using pitot tubes in the wheel-space. These tubes were mounted on the cover-plate, and also connected to the aforementioned Scanivalve® system. They are aligned to the tangential direction to face the swirl velocity component. The axial distance from the pitot tubes to the stator surface was set as approximately 25% of the wheel-space gap. Radial positions were set to every second radial location of static pressure, as illustrated graphically in Figure 3.24. In conjunction with the static pressure, the total pressure measurements were used to determine swirl velocities in the wheel-space.

CO_2 gas concentration taps were positioned on the stator wall at multiple radial locations that matched the static pressure; circumferentially the two sets of taps were 90° apart. The stainless steel tubing employed is exactly the same as that for pressure taps. They are connected to a Signal® 9000 MGA dual-channel infrared gas analyser through a multiplexor, a device that could switch between multiple channels, each connected to a concentration tap. When a channel is selected for measurement, the sampled mixture of air and CO_2 in that channel is pumped to the gas analyser for assessment. The analyser offers an overall uncertainty of 0.015% of its ranges.

Time-dependent pressure was measured at several points for unsteadiness associated with rotating blades. Measurement points are on the stator surface in the wheel-space and on the stator disc shroud towards the rim-seal clearance. XT and XCQ series of Kulite® fast-response pressure probes were employed, with diameters of 2.8 mm and 1.7 mm respectively. The mounting holes were dimensioned according to the geometries of these probes. The unsteady transducers have an uncertainty of $\pm$ 0.1% across a 70 mbar range.

Thermocouples were used for temperature measurements in the core region of fluid. Each thermocouple was made using ultra-thin wire beads fitted into a ceramic sleeve with an outer diameter of 2.4 mm. After careful calibrations of the thermocouples, temperatures can be measured in the rig with an accuracy of 0.5 K.

Infrared probes were used to measure the rotor surface temperature with these probes being flush mounted on the stator side. Each probe features a diameter of 17 mm, including a sleeve for controlling its own temperature to reduce inaccuracy. The temperature within a spot size area of 6 mm in diameter could be acquired at a distance of 20 mm, the gap between the stator and rotor surfaces.

Each probe occupies a 25% of the radial height for the wheel-space. To acquire a detailed radial distribution of temperature for the rotor surface, these probes must be staggered and spread circumferentially on the stator side. Multiple probes at different radii could be positioned in a specific area on the cover-plate; a corresponding window section was designed on the stator disc to accommodate the instrumentation, visible in Figure 3.13.

Every infrared temperature probe can be directly mounted within the cover-plate, with the front face flush with the stator wall. Protruding from the back of the cover-plate, the body of each probe along with the wirings, passes through the stator disc through the window section. In order to prevent leakage incurred by the window and slot sections, a sealing arrangement with O-ring cord was applied at the circumferential surfaces in contact between the stator disc and cover-plate.

3.4.2 Instrumentation for the mainstream annulus

Pressure taps on the stator vane platform are indicated in Figure 3.24. These taps were manufactured in the stator shroud and were employed as an important part of instrumentation in the annulus. Figure 3.25, 3.26 and 3.27 detail the instrumentation arrangements in the annulus flow path, for pressure measurements at various positions. The locations are labelled by an 'A' series on the vane platform, and by a 'B' series on the outer casing as illustrated in Figure 3.25.

For each location, a set of 15 taps was placed evenly across a single vane pitch of 11.25°, to determine the circumferential pressure variation downstream of the stator vanes. For measurements at A1 and A2, two sets of taps were designed for each location, distributed every 180° for averaging. These measurements provide the driving potential for EI ingress into the wheel-space. On the outer casing, seven locations were designed for mounting unsteady pressure probes across a vane pitch to assess unsteadiness associated with the rotating blades.

The pressure taps positioned in the annulus were also connected to the aforementioned Scanivalve® system, with the same transducer used for the wheel-space. This arrangement enables a complete evaluation of internal and external pressure distributions within each testing set using consistent instrumentation.

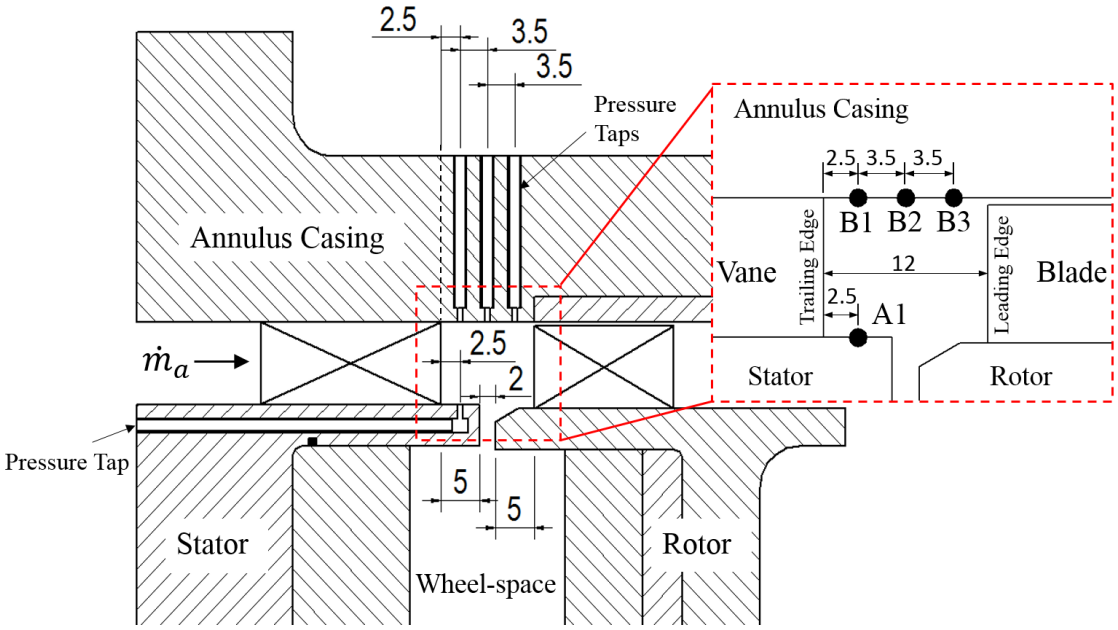

Figure 3.25 Pressure taps on the vane platform and annulus casing (dimensions in mm)

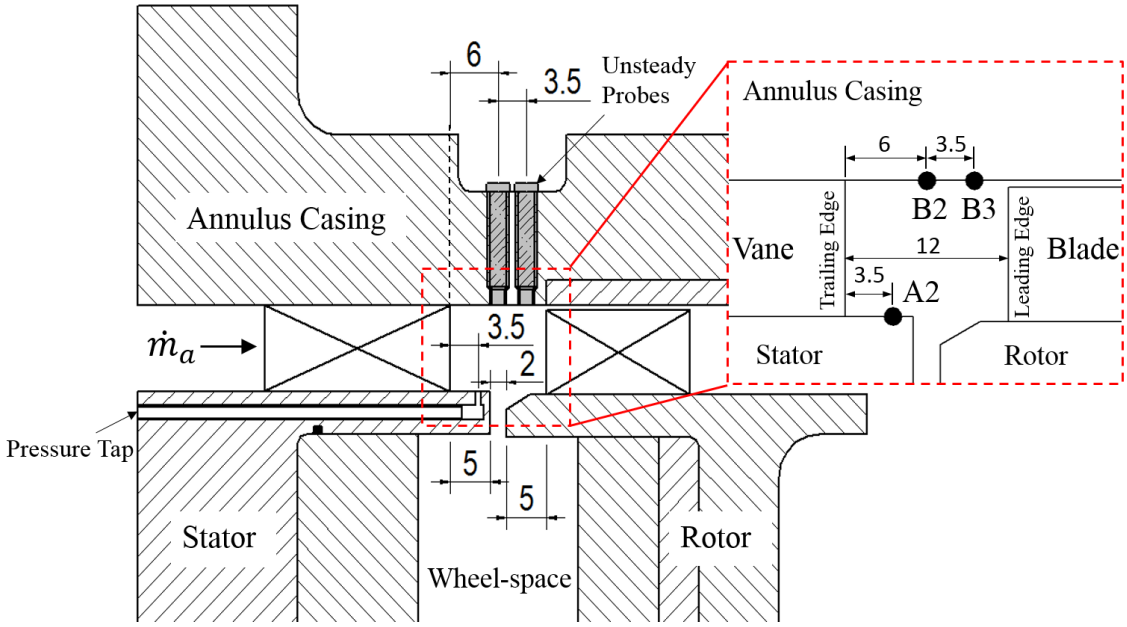

Figure 3.26 Additional pressure taps and unsteady pressure probes in the annulus (dimensions in mm)

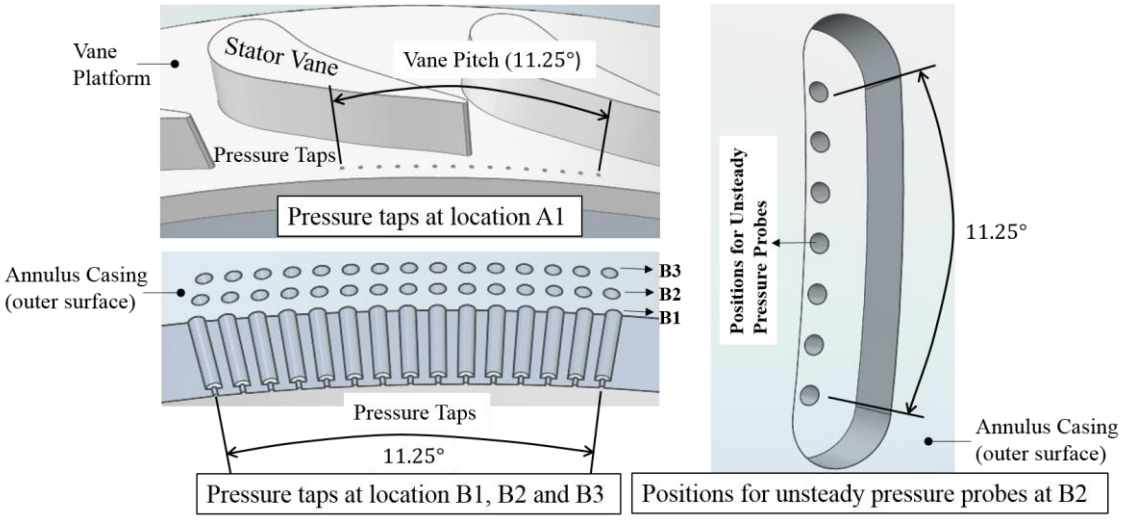

Figure 3.27 CAD images of instrumentation in the annulus

3.5 Design for the modelling of leakage flow paths

The modelling of leakage flow paths in actual gas turbines was incorporated in the design to explore novel techniques that could exploit leakage flow to reduce hot gas ingress. The leakage flow modelled in the rig can be found in the first stationary vane stage of the high pressure turbine in several Siemens engines. The flow, referred to as the chordal-hinge leakage flow, leaves the vane row to enter the rim-seal region in the turbine wheel-space; there are multiple flow paths distributed circumferentially with each one corresponding to a vane segment. This leakage flow could be utilised potentially to reduce ingress, which would considerably benefit the secondary air system and decrease the sealant demand. With this unique feature, the facility will offer capability in new areas of ingress research and help provide valuable insights for engine designers.

3.5.1 Chordal-hinge leakage flow in gas turbine engines

In a gas turbine, the first-stage stationary nozzles are constituted by nozzle segments, each including one or more nozzle guide vanes. Outer and inner bands are formed when the nozzle segments are assembled. The nozzle assembly is supported by the outer shroud and the inner support ring, through the outer and inner band respectively. Inner chordal-hinge seals are employed to seal between the inner band and the support ring. These seals are of necessity due to a temperature difference between the compressor discharge air and the hot gas in the mainstream. In addition, movements of the first-stage nozzles are allowed by these seals when the inner support ring encounters thermal expansions.

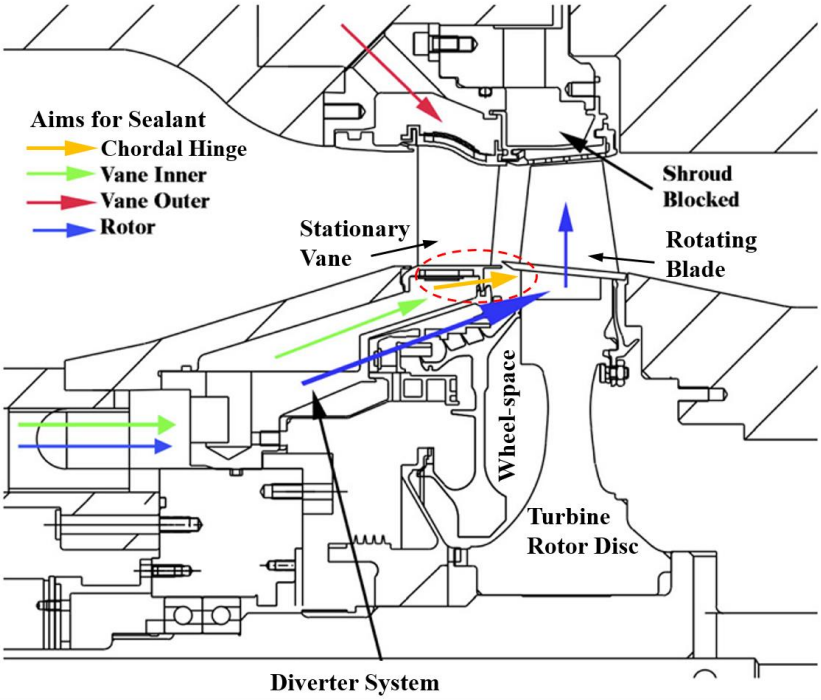

Figure 3.28 Chordal hinge leakage flow in a typical high-pressure turbine stage – adapted from Dunn and Mathison (2014)

During turbine operations, however, the chordal hinge seals prove insufficient to completely prevent leakage, due to the warpage resulting from non-uniform temperature distributions. The chordal-hinge leakage flow in a typical high-pressure turbine stage is shown diagrammatically in Figure 3.28. Not shown in this cross-sectional view, there are multiple flow paths distributed circumferentially on the stator side, with each one corresponding to a vane segment. Supplemental seals can be employed to reduce the leakage flow, but with increased complexity and cost. However, this flow could be potentially exploited for reducing hot gas ingress, due to its close proximity to the rim-seal arrangement.

3.5.2 Modelling of chordal hinge leakage flow

In order to model the chordal-hinge leakage flow that escapes from underneath the nozzle vanes to the rim-seal region, a modular stator disc was designed featuring open slot sections in the shroud. A total of 32 slots were evenly distributed, each corresponding to one of the stator vanes. Inserts with holes could be fitted in these slots to introduce air flows to the rim-seal region in the wheel-space, as illustrated in Figure 3.29. This air can be bled from the sealant line and directed into a manifold, where the flow is evenly distributed and supplied to every insert fitted inside the stator shroud.

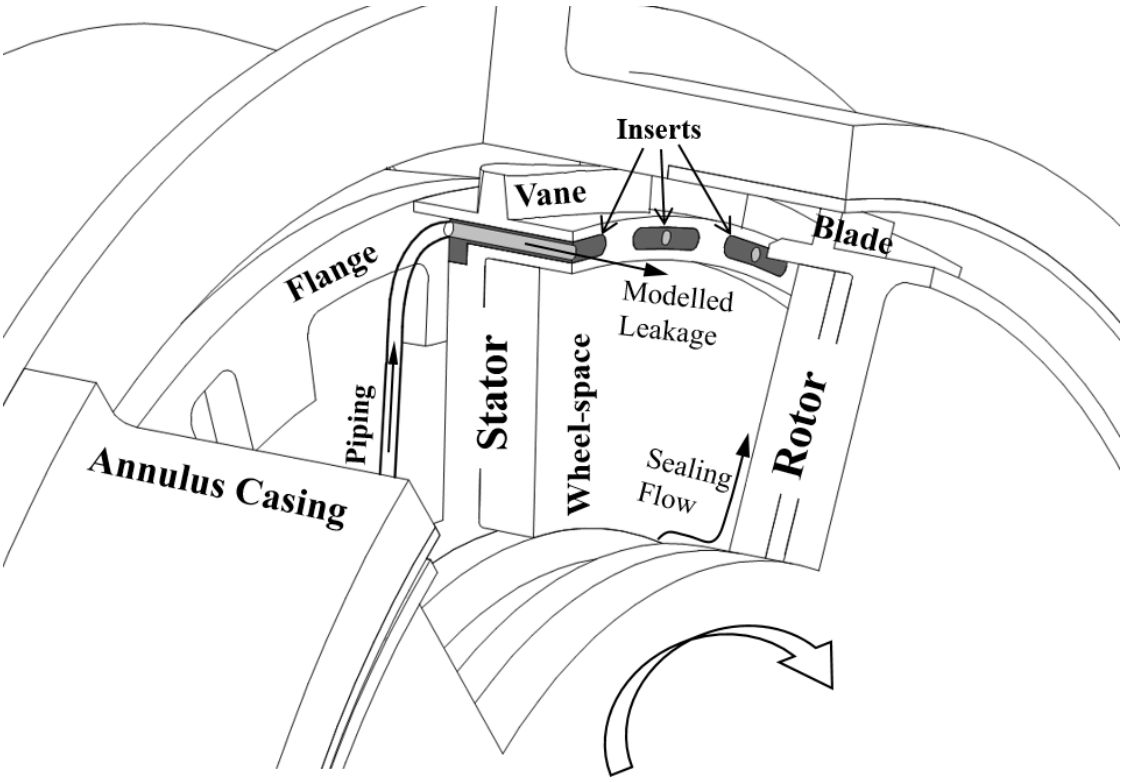

Figure 3.29 Turbine stage configuration for the modelling of leakage flow paths

The aim for the experimental modelling is to explore how this leakage flow could reduce ingress. Therefore the conditions of the flow would be controlled in respect of the flow angle and mass flow rate in order to perform a parametric study. The modelled leakage flow can be injected with a range of angles relative to the axial direction, through specifically designed pre-swirl holes fabricated in the inserts. The case of zero injection angle (straight hole) is displayed in Figure 3.29; however, a range of $\pm$ 60° can be achieved for the permissible spacing in the shroud. A maximum mass flow rate of 0.037 kg/s can be achieved for all the 32 leakage paths combined. This is the same magnitude as the sealing flow rate required to seal the wheel-space (no ingress) with an single-clearance rim seal. Therefore the design enables a substantial amount of leakage flow to be injected into the wheel-space for the impacts on ingress to be studied.

Like the sealing flow, the leakage flow can be seeded with CO_2 tracer gas and treated as a secondary sealing flow to the wheel-space. Concentration measurements conducted in the wheel-space is expected to determine the combined effects of both the sealing flow introduced from the low radius and the leakage flow injected at the high radius. Alternatively, a second type of tracer gas, such as N_2O, can be used for the leakage flow. Dual gas concentration measurements will enable the study for the respective effects of the sealing and leakage flows on hot gas ingress. It is envisaged that this experimental modelling shall help engine designers transform the chordal-hinge leakage flow to a practical advantage for the design of secondary air systems.

3.6 Summary

This chapter describes the design of a single stage gas turbine research facility. The turbine stage consists of a rotor-stator disc system with an annulus casing to form the mainstream flow path. The stator and rotor assemblies are highly versatile, enabling the study of engine-representative rim seals Research into new area of ingestion problem is made possible, including the utilisation of leakage flows found in engines for reducing ingress into the wheel-space. The entire design and all the drawings shown in this chapter were completely accomplished by the author of this thesis.

The feed system for the turbine stage is shown, including the sealant line and the annulus flow pipes. The circumferential pressure distribution upstream of the stator vanes are shown to be axis-symmetric in line with the design aim. The flow passes the vanes and blades to create the pressure asymmetries in the annulus driving the EI ingress. The sealing flow is introduced into the system from the stator centre. For concentration measurements used to determine the sealing effectiveness of the wheel-space, the sealing flow is seeded with CO_2 tracer gas upstream of the inlet to the disc system.

The turbine rotor is driven by a powertrain including an electric motor connected to a belt transmission. The complete powertrain is mounted onto a carriage system that can slide on linear guide rails. The carriage system is specifically designed to achieve high-precision alignment between the turbine discs, which is essential for testing engine-representative rim seals. The end-stop sub-system ensures the repeatability in alignment after the rotor-stator system is re-assembled.

The on-design operating points are determined based on the velocity triangle corresponding to the vane-blade configuration. The stator and rotor discs were designed to be bladed discs (bliscs) and the blading profiles were shaped by high-precision CNC machining. The material for the stator and rotor discs is selected to be aerospace-grade aluminium alloy.

The components for stator and rotor assemblies are detailed in this chapter. Cover-plates, attached to the turbine discs, are designed for several aims. For the stator, cover-plates allow the adaptability and enhance the capability of instrumentation. For the rotor, cover-plates made of low-density material can reduce the torque requirement and mechanical stress level. The modular cover-plates are interchangeable, thus allowing the wheel-space geometry to be varied. For the heat transfer measurements using hot sealing flow, a complete insulation in the wheel-space is made possible by the cover-plates, in order to reduce unwanted heat loss to the metal surfaces.

The stator and rotor discs are also interchangeable. Modular turbine discs with different gas path blading can be installed in the rig, to investigate the annulus aerodynamics associated with various blading configurations. A stator was designed to model the leakage flow paths near the rim seal found in gas turbine engines. The design enables a fundamental study on the complex flow interactions among the ingress, sealing flow and the leakage flow close to the rim-seal clearance. The study is aimed to explore a novel way of exploiting the leakage flow to reduce ingress into the wheel-space, which is a new area of research into hot gas ingestion.

Instrumentation arrangement incorporated in the turbine stage is illustrated. Locations for the instrumentation applied in the wheel-space and the mainstream annulus are described in detail. Extensive measurements of pressure, swirl velocity, gas concentration and temperature can be made to improve the understanding of fluid dynamics, as well as the thermal effects of ingestion.

The capability and versatility of the rig is fully demonstrated in this chapter. Experimental research conducted with this facility will be described in the following chapters. However, it is envisaged that the research work enabled by the design of this facility will far exceed the experimental measurements documented in this thesis.

Chapter 4 Baseline testing of the rig and measurements for a datum single-clearance seal

This chapter describes the baseline testing of the facility and experimental measurements for a generic single-clearance rim seal. The baseline testing was aimed to study the rotor dynamics of the turbine disc and to investigate the driving potential for the EI ingress. The radial deformation of the rotor was measured to assess the variations in the blade-tip and rim-seal clearances under rotating conditions. A structural FEA was performed providing predictions that agreed well with the measurement. Time-averaged measurements of static pressure were taken in the annulus between the vane and blade row to assess the external pressure asymmetries. Unsteady pressure measurements were also conducted to evaluate the unsteadiness associated with the passing of blades.

The experimental measurements for a generic single-clearance rim seal were aimed to establish the datum for a further study of engine-representative double-clearance seal configurations. Measurements of CO_2 gas concentration, pressure and swirl velocities were conducted for the single-clearance radial seal SR. The seal performance was assessed based on the concentration measurements and the fluid dynamics in the wheel-space was studied with the pressure and swirl velocities determined experimentally.

4.1 Radial deformation of the rotor

The radial deformation of the rotating turbine disc, including the radial growth, must be evaluated due to the following reasons: firstly, the deformation reduces the blade tip clearance between the blades and the outer casing, and this may cause abrasions between the rotating and stationary components leading to mechanical failures; and secondly, when a radial-clearance rim seal is in place, the shroud deformation leads to a difference between the rotating and static seal configurations, the latter featuring designed geometries.

The radial deformation was evaluated on the rotor shroud with a structural FEA, reported in Chapter 3 for the calculations of stresses in the rotor disc. Figure 4.1 shows the variation of radial deformation δ at 3000 rpm rotor speed, plotted versus the axial distance on the blade platform. A broadly uniform distribution is shown, with an average value of approximately 23 μm. There is a slight increase in δ towards the frontal edge, which is on the rim-seal side, and the maximum deformation is shown to be 27 μm on the edge. This axial variation of δ is probably due to the configuration of the shrouded disc, and the effect of the blades, which are not shown in the figure. There may be a blade-induced bending moment exerted on the rotor, in addition to the growth of the disc.

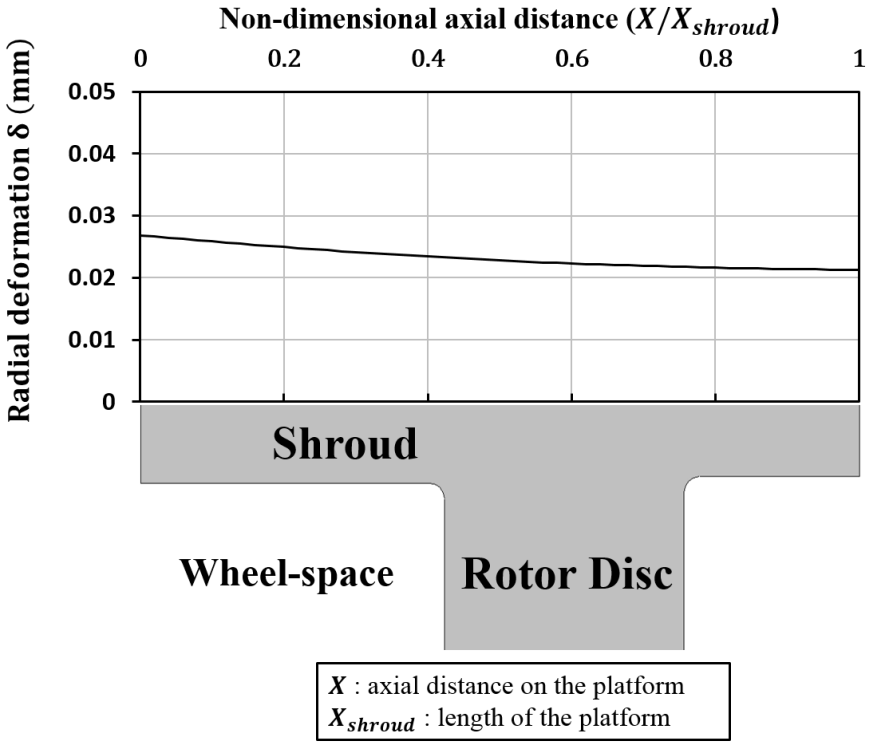

Figure 4.1 Radial deformation of the rotor shroud at 3000 rpm from FEA

The radial deformation was also assessed experimentally. A Micro-Epsilon® laser proximity sensor was employed to measure the shroud deformation on the frontal edge, in order to acquire δ_{max}, the maximum value of δ. The laser beam projected from the sensor was focused on a target spot in close proximity to the shroud edge. The reflection from the surface was imaged by a receiver onto a position-sensitive element inside the sensor. Any change in the target position was evaluated by the sensor, which has a stated uncertainty of 0.6 μm.

Figure 4.2 shows the variation of δ_{max} with rotational velocity (Ωb) over a range of operating points. The δ_{max} is shown to be broadly proportional to $(\Omega b)^2$. At the design rotor speed 3000 rpm ($(\Omega b)^2 \approx 3560\ m^2/s^2$), δ_{max} was determined from the laser measurement, with a value of 29 μm. There is a good agreement between the FEA and measurements over the complete range of speeds.

The maximum radial deformation could be used to represent the maximum change in the radial-seal clearance and the blade tip clearance. The percent variations of the these clearances are tabulated in Table 4.1. The variation in the seal clearance, 2.3%, is smaller than the alignment tolerance 5%; and the decrease in the blade tip clearance accounts for just 6% of the static value, leaving sufficient margin for the safe operation of the rig.

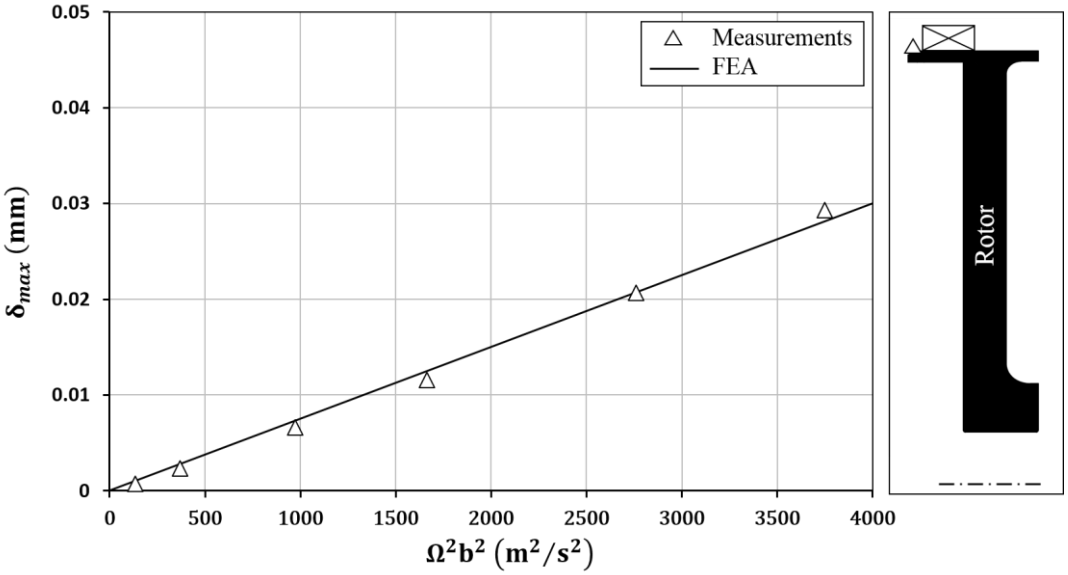

Figure 4.2 Variation of the radial deformation with rotational velocity

Table 4.1 Percent variations of clearances in the turbine stage

Geometric property	**Value**
Static radial-seal clearance $s_{c,rad}$ (mm)	1.28
Static rotor blade tip clearance t_c (mm)	0.5
Static wheel-space outer radius b (mm)	190
Maximum radial deformation δ_{max} (mm)	0.029
$\delta_{max}/s_{c,rad}$	2.3 %
δ_{max}/t_c	6 %
δ_{max}/b	0.015%

4.2 Variation of pressure in the mainstream annulus

Between the stator vanes and the rotor blades, variation of pressure was evaluated on the vane platform and the annulus casing. The aim was to determine the driving potential for the externally-induced ingress, which was experienced by the turbine wheel-space investigated in this thesis. This is supported by the pressure and swirl measurements shown later, which leads to ${\Gamma_{\Delta p}}^{1/2} = 4.9$ indicating the EI dominated ingress regime (Owen (2011b)). Time-averaged pressure measurements were made at five different positions which were introduced in Chapter 3. The relation between flow coefficient and the peak-to-trough pressure difference in the annulus was determined experimentally; and the spoiling effect of egress which interacted with the mainstream flow was also investigated. Moreover, unsteady pressure measurements were made in the annulus to assess the unsteadiness resulting from the vane-blade interactions.

A pressure coefficient C_p is employed to determine the pressure variation in the annulus, which is defined as follows:

$$C_p = \frac{(p - \bar{p})}{(1/2)\,\rho\Omega^2 b^2} \tag{4.1}$$

where p is the time-averaged static pressure measured in the annulus; $\bar{p}$ is the mean static pressure over one vane pitch.

The peak-to-trough pressure difference is evaluated with ΔC_p, equivalent to the maximum difference of C_p in a vane pitch. The definition of ΔC_p is shown as follows:

$$\Delta C_p = \frac{(p_{max} - p_{min})}{(1/2)\,\rho\Omega^2 b^2} \tag{4.2}$$

where p_{max} and p_{min} denotes the maximum and minimum pressure respectively in the vane pitch.

Figure 4.3 shows the circumferential variations of C_p in one vane pitch, evaluated with time-averaged pressure measurements conducted on the vane platform (location A1 and A2). Measurements were conducted at $Re_\phi = 7.9 \times 10^5$ and with the on-design flow condition ($C_F = 0.38$), as no sealing flow was supplied to the system ($\Phi_0 = 0$). An axial decay of ΔC_p can be seen along the platform, and a similar trend was shown by Gentilhomme *et al*. (2003). The value of ΔC_p, the driving potential for the EI ingress, depends on the location of measurements in the annulus.

Figure 4.4 shows the circumferential variations of C_p in one vane pitch, evaluated with time-averaged pressure measurements conducted on the annulus casing (location B1, B2 and B3). The discussion for the vane platform also applies to these positions on the outer casing. The axial decay of ΔC_p indicates that the driving potential for ingress is dominated by the pressure field of the vanes.

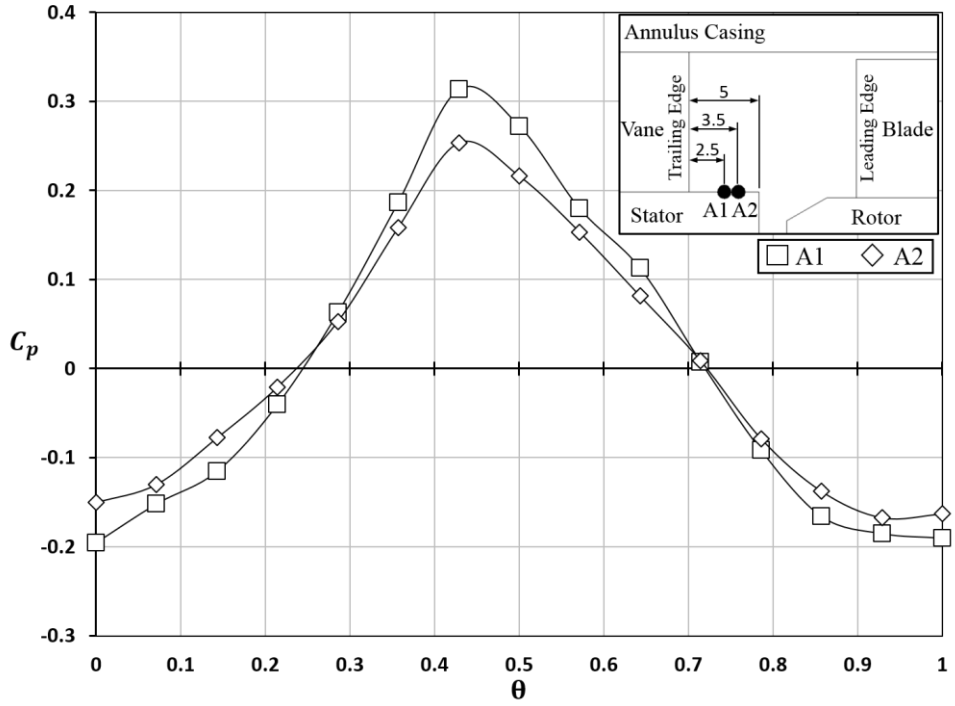

Figure 4.3 Circumferential variation of C_p on the vane platform (dimensions in mm)

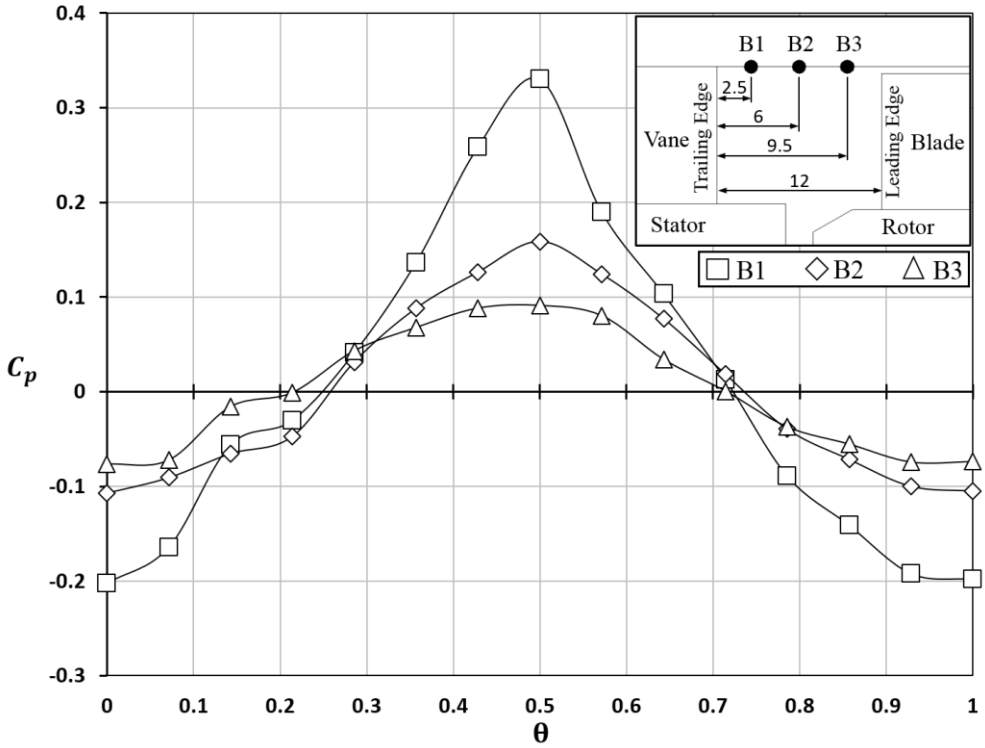

Figure 4.4 Circumferential variation of C_p on the annulus casing (dimensions in mm)

For the EI ingress, the relation between the minimum sealing flow rate, $\Phi_{min,EI}$, and the annulus pressure difference ΔC_p, was described by Owen (2011b). It was suggested by the authors that a physical consistency could be achieved, by using the same relative locations for determining ΔC_p, in extrapolating data from a rig to an engine for similar rim-seal configurations.

Figure 4.5 demonstrates the effect of flow coefficient C_F on the circumferential variation of C_p at position A1 (shown in Figure 4.3) on the vane platform. The experimental data included in the figure is for the measurements conducted at $Re_\phi = 7.9 \times 10^5$ and with no sealing flow ($\Phi_0 = 0$). Re_w was varied through the change of mainstream mass flow rate, thus resulting in the variation of flow coefficient ($C_F = Re_w/Re_\phi$). The ΔC_p is shown to increase with C_F, because a higher mainstream flow rate leads to a greater circumferential pressure variation resulting from the vane pressure field.

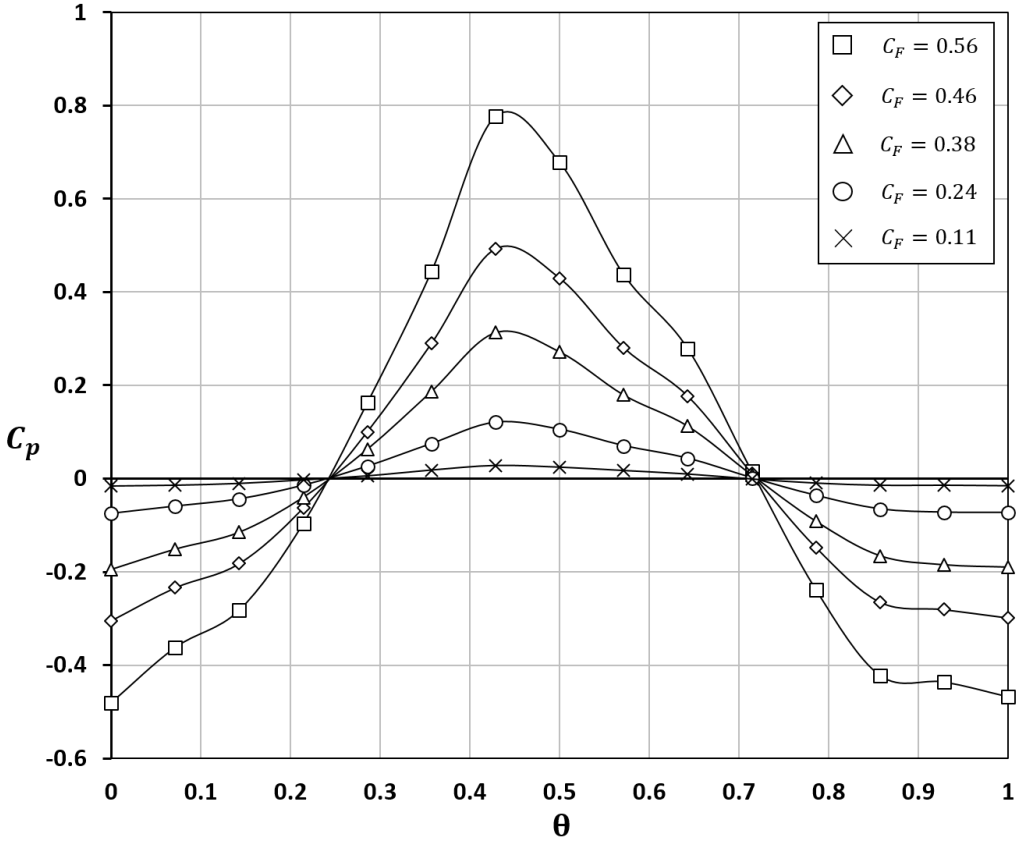

Figure 4.5 Effect of flow coefficient C_F on the circumferential variation of C_p

Figure 4.6 shows the variations of ${\Delta C_p}^{1/2}$ with C_F, evaluated on the vane platform for both axial locations (A1 and A2, as shown in Figure 5.3). Measurements were made at $Re_\phi = 7.9 \times 10^5$ and $Re_\phi = 5.3 \times 10^5$ to assess the effect of rotational speed. The ${\Delta C_p}^{1/2}$ is shown to increase linearly with C_F, irrespective of Re_ϕ. It is encouraging to see that the pressure asymmetries were not affected

by the rotational Reynolds number; this indicates an engine-representative annulus flow field can be achieved in the rig despite the values of Re_ϕ are lower than those for engines.

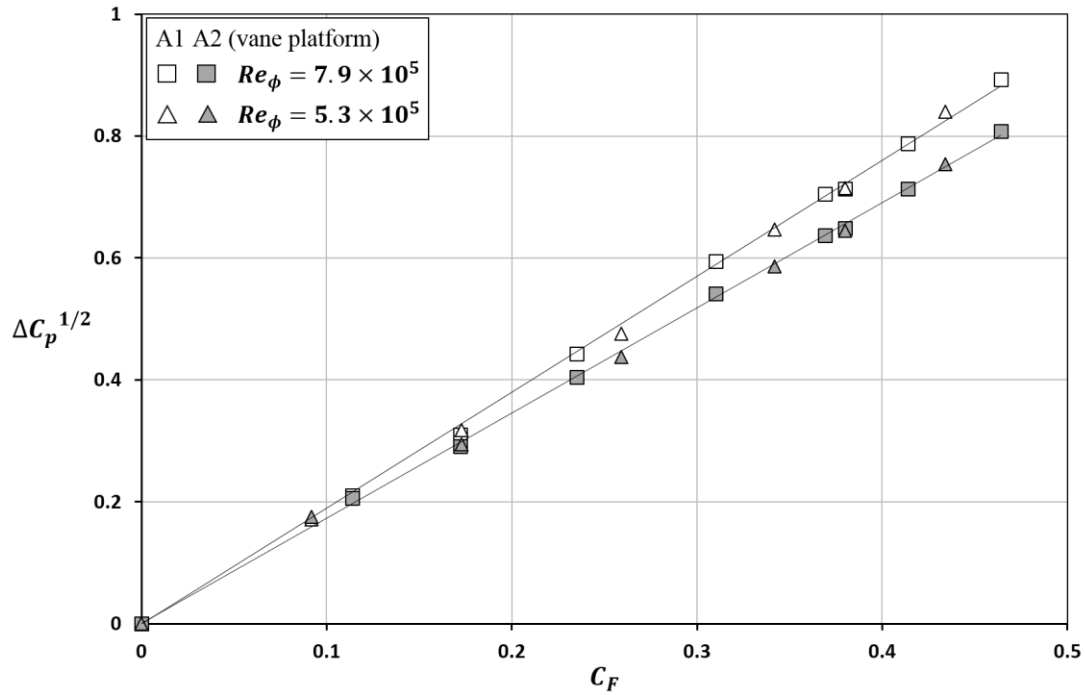

Figure 4.6 Variation of $\Delta C_p^{1/2}$ with C_F on the vane plarform

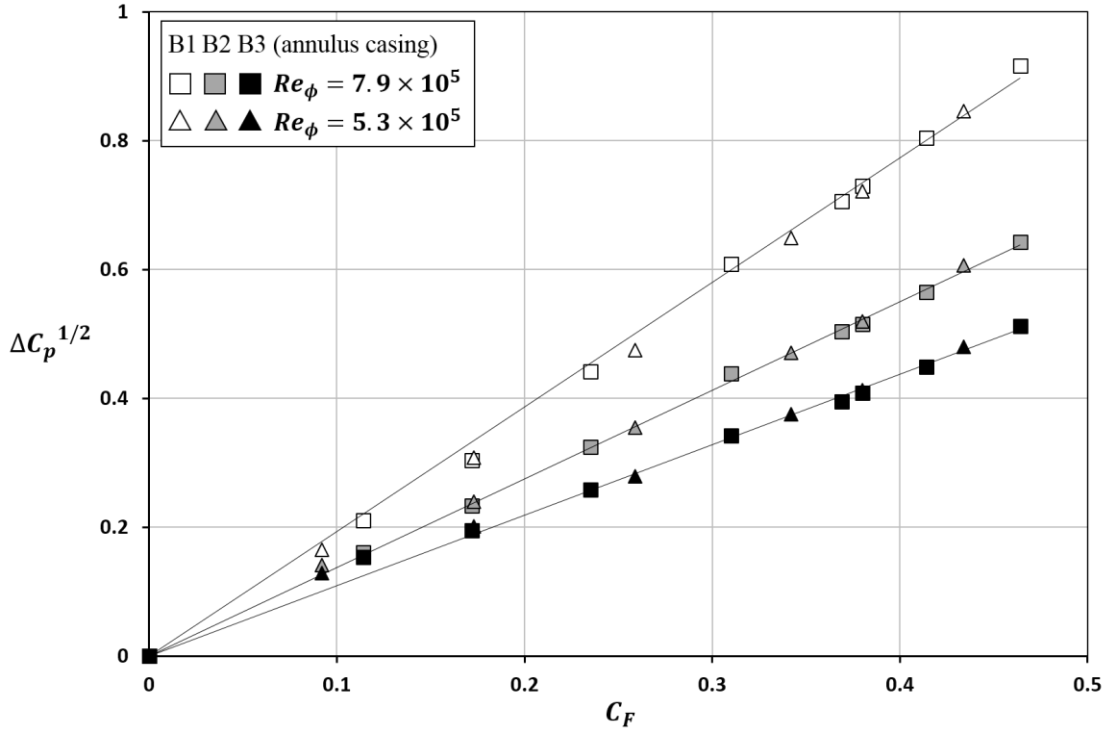

Figure 4.7 Variation of $\Delta C_p^{1/2}$ with C_F on the annulus casing

The variations of $\Delta C_p{}^{1/2}$ with C_F were also evaluated on the annulus casing as shown in Figure 4.7 for three positions. The same discussion for the vane platform also applies to these positions on the annulus casing. Larger differences are shown among the gradients for the linear relations between $\Delta C_p{}^{1/2}$ and C_F, compared with the measurements on the platform. At the same C_F, there is a greater decay of $\Delta C_p{}^{1/2}$ along the axial direction corresponding to the wider spacing among the three positions on the casing; a consistency of the axial decay can be seen between Figure 4.7 and 4.4.

The magnitude of ΔC_p is also affected by the sealing flow from the wheel-space through the rim-seal clearance. This so-called spoiling effect was shown by Bohn *et al*. (2006), with pressure measurements made on the vane platform of the turbine rig used by the authors. In the study documented in this chapter, the spoiling effect was also evaluated for different levels of sealing flow rates.

The variation of ΔC_p with sealing flow rate was measured on the vane platform; the values for both locations were shown respectively in (a) and (b) of Figure 4.8. A single-clearance rim seal was employed and the measurements were made at $Re_\phi = 7.9 \times 10^5$ with the on-design flow condition ($C_F = 0.38$). For each one of positions, the magnitude of ΔC_p is shown to decrease with increasing sealing flow rate, and this behaviour is in line with that described by Bohn *et al*. (2006).

Compared with measurements made at the upstream location (A1), those conducted further downstream (A2) showed a slightly larger decrease in ΔC_p; this indicates a stronger spoiling effect closer to the rim-seal clearance through which the sealing flow left the wheel-space.

The spoiling effect, resulting from the interaction between the sealing flow and the mainstream, decreases the driving potential for the EI ingress. The sealing flow is shown to reduce ingress through decreasing the pressure asymmetries, together with increasing the pressure in the wheel-space.

Unsteady pressure measurements were conducted in the annulus to assess the unsteady effect from the rotating blades. Using fast-response transducers, static pressure was measured with a sampling rate of 20 KHz, which was above 15 times the blade passing frequency (1.03KHz), thus allowing a sufficient data resolution for analysis. Two operating points with $Re_\phi = 4 \times 10^5$ were set for the measurements: the on-design condition ($C_F = 0.38$) and an off-design condition ($C_F = 0.8$) with a higher annulus flow rate. No sealing flow was supplied during the test ($\Phi_0 = 0$). The time-dependent pressure data was processed with a fast Fourier transform (FFT) to acquire a frequency spectrum.

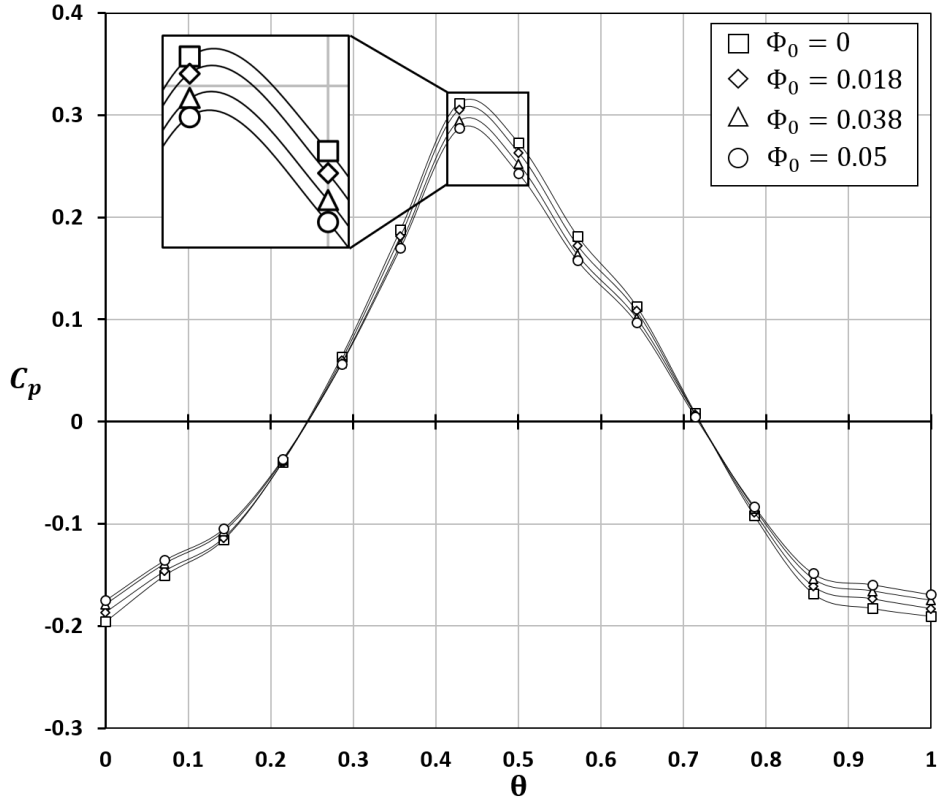

(a) For location A1 on the vane platform

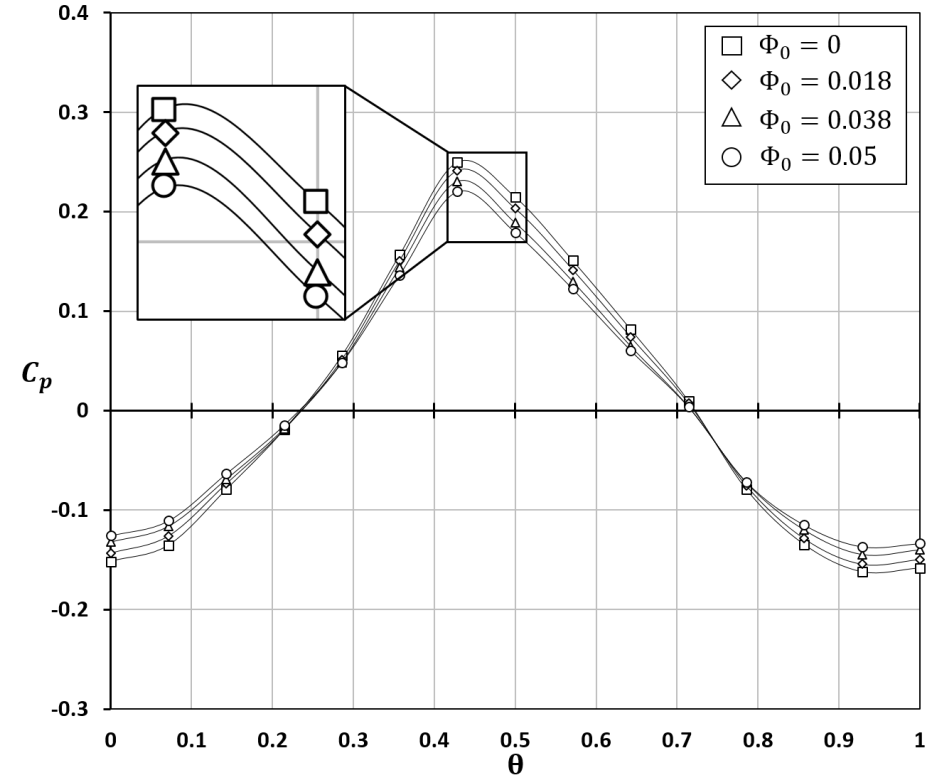

(b) For location A2 on the vane platform

Figure 4.8 Spoiling effect of the sealing flow on ΔC_p in the annulus

Figure 4.9 shows the frequency spectrums of the unsteady pressure taken on the annulus casing and on the edge of seal clearance. A frequency spike is seen at 41 times the rotational frequency corresponding to the blade count per revolution, and the blade passing frequency is thus identified. Between (a) and (b), the blade unsteadiness is greater for the off-design condition, due to the higher mass flow rate passing through the blade row. Between (b) and (c), the unsteadiness evaluated on the casing is shown to be greater, and that at the seal clearance significantly weaker, because of a decreasing unsteady effect with increasing distance upstream of the blades.

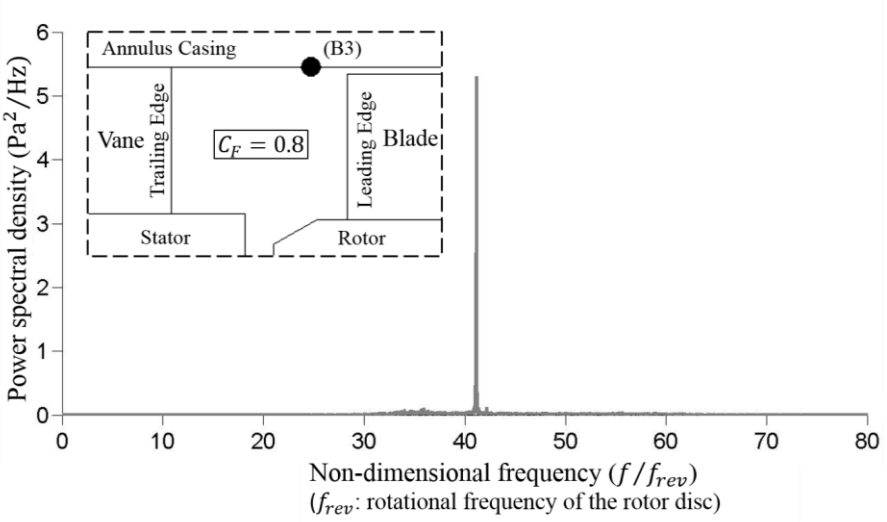

(a) On the annulus casing for $C_F = 0.8$

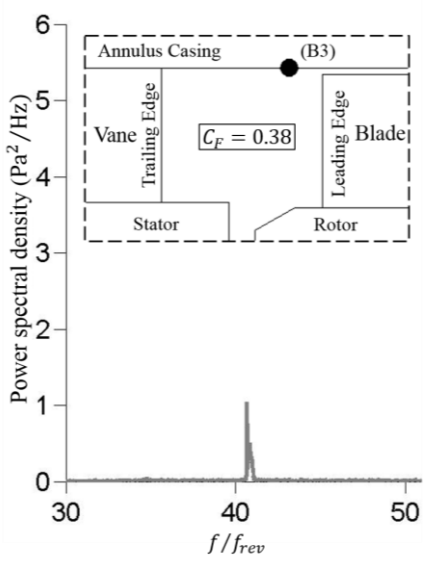

(b) On the annulus casing for $C_F = 0.38$

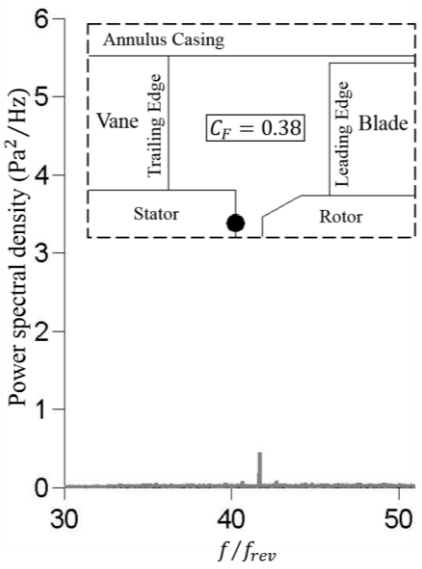

(c) At the seal clearance for $C_F = 0.38$

Figure 4.9 Frequency spectrum of unsteady pressure in the annulus flow

The time-dependent pressure variation is shown in Figure 4.10, for the three measurements respectively specified in Figure 4.9. The non-dimensional pressure variation is plotted versus the angle of rotation. In the range between 0° and 90°, $10\frac{1}{4}$ cycles of variation are identified which correspond to 10.25 blade count in a quarter of revolution. Compared with the magnitude of ΔC_p from time-averaged measurements, the unsteady variation is relatively too insignificant. Therefore the pressure asymmetries, as the driving potential for the EI ingress, are dominated by the vanes in the annulus. This limited unsteadiness resulting from the rotor blades is probably attributed to the symmetric aerofoil; a cambered blade profile would probably lead to a greater unsteady effect on the pressure variation. However, the mainstream flow field produced with the current blading configuration is sufficiently satisfactory for the research into hot gas ingress, supported by previous Siemens computations.

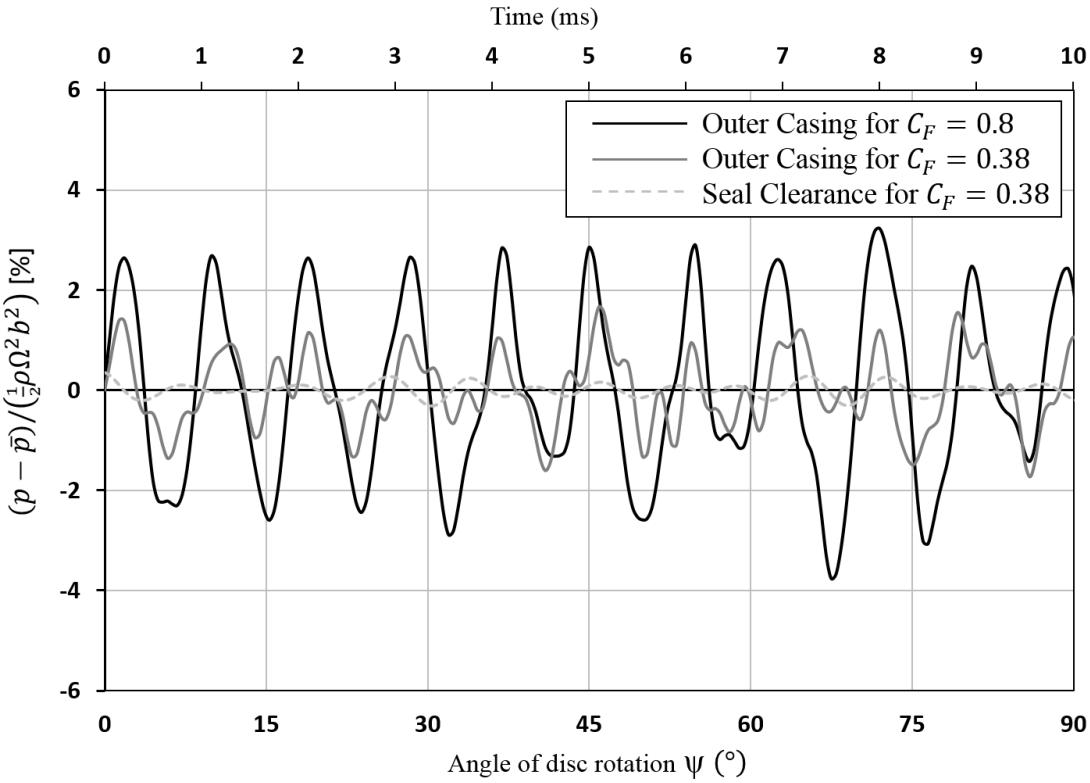

Figure 4.10 Time-dependent variation of unsteady pressure in the annulus flow

4.3 Experimental measurements with a baseline single-clearance rim-seal configuration

This section describes an experimental study of a baseline single-clearance radial seal configuration, referred to as the SR. Measurements of CO_2 gas concentration, pressure and swirl velocities were conducted to investigate the seal performance and fluid dynamics in the wheel-space. It was determined from pressure and swirl measurements (to be shown later) that $\Gamma_{\Delta p}{}^{1/2} = 4.9$, indicating the seal operates under EI dominated ingress regime (Owen (2011b)). This study provides a baseline for further research on engine-representative double-clearance rim seals, which is documented in the following chapters.

4.3.1 Parameters employed in the study

Parameters for flows and sealing effectiveness are used in the study to help interpret the experimental data and evaluate the seal performance. These parameters are summarised as follows. Measurement uncertainties are analysed and summarised in Appendix I.

A sealing flow parameter, Φ_0, is used to denote the non-dimensional sealing mass flow rate. This parameter combines the flow rate parameter $C_{w,o}$, seal clearance ratio G_c and rotational Reynolds number Re_ϕ; it was previously used by Owen (2011a) with a definition as follows:

$$\Phi_0 = \frac{C_{w,o}}{2\pi G_c Re_\phi} \tag{4.3}$$

It is an inviscid parameter due to the cancellation of viscous terms. The minimum value of Φ_0 required to completely prevent ingress is denoted by Φ_{min}.

The definition of turbulent flow parameter λ_T is as follows:

$$\lambda_T = C_{w,o} Re_\phi{}^{-0.8} \tag{4.4}$$

The free-disc entrainment rate is characterised by $\lambda_{T,fd} = 0.22$ (Owen and Rogers (1989)). The core rotation in the wheel-space is expected to be completely suppressed when $\lambda_T \geq \lambda_{T,fd}$ for the superposed flow. For all the seal flow conditions documented in this thesis, $\lambda_T < \lambda_{T,fd}$.

In the wheel-space, the tangential flow velocity component relative to the rotor velocity is characterised by a swirl ratio β, which is defined as follows:

$$\beta = \frac{V_\phi}{\Omega r} \tag{4.5}$$

where V_ϕ is the tangential flow velocity component, determined using:

$$V_\phi = \sqrt{2\,(p^* - p)/\rho} \tag{4.6}$$

where p^* and p are the total and static pressure respectively at the same radius. As described in Chapter 3, measurements of p^* were made with pitot tubes set at approximately 25% of the wheel-space width from the stator. The swirl ratio is thus assessed outside the boundary layers.

The CO_2 gas concentration effectiveness ε_c was determined experimentally to represent the sealing effectiveness ε for a specific rim-seal configuration. The injection of CO_2 tracer gas into the sealant line was introduced in Chapter 3. The following definition of ε_c demonstrates how the effectiveness is determined with concentration measurements:

$$\varepsilon_c = \frac{c_s - c_a}{c_o - c_a} \tag{4.7}$$

where c_s, c_a and c_o denote respectively the CO_2 concentration taken on the stator surface in the wheel-space, in the annulus and in the sealant line upstream of the wheel-space inlet. The ε_c equals unity when $c_s = c_o$, indicating no ingress has occurred and the sealing flow has not been diluted; ε_c equals zero when $c_s = c_a$, a condition when sealing flow is not supplied and there is a consistent level of CO_2 concentration between the wheel-space and the (ambient) annulus flow.

4.3.2 Geometry of the baseline single-clearance seal

Figure 4.11 shows the geometry of the baseline single seal configuration SR. The detailed dimensions are listed in Table 4.2. A rim-seal attachment was bolted under the rotor platform, and a single-clearance radial seal was formed between the rotor and its adjacent stator shroud. The wheel-space was formed between the stator and rotor radially inboard of the rim seal.

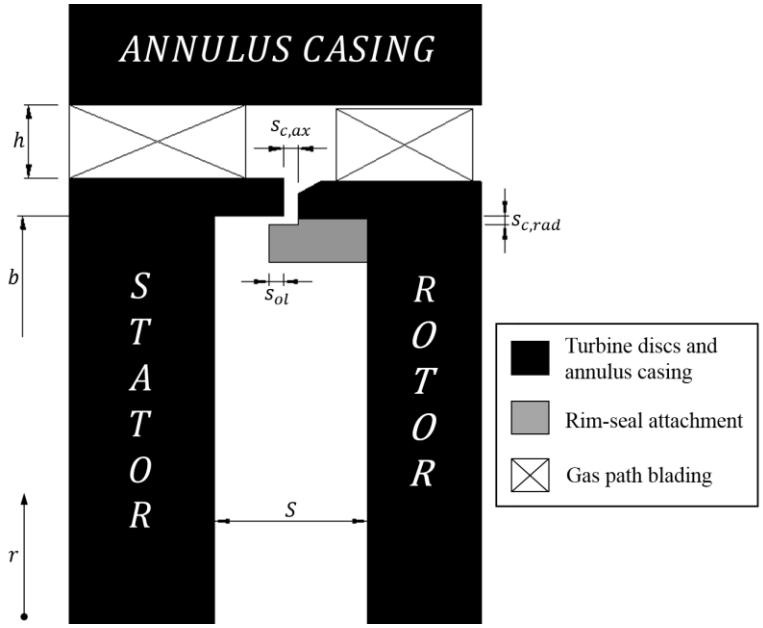

Figure 4.11 Geometry of the rim-seal configuration SR

Table 4.2 Geometric properties for seal configuration SR

(Dimensions in mm under static condition)

Geometric symbol	**Seal configuration SR**
	Value
h	10.0
b	190
S	20.0
$s_{c,ax}$	2.00
$s_{c,rad}$	1.28
s_{ol}	1.86

The rotor experiences a radial deformation under rotation, thus leading to a variation in the radial clearance of the seal, $s_{c,rad}$. A percent variation of 2.3% was determined from displacement measurements and a FEA analysis described in section 4.1. These assessments show the variation due to rotation is smaller than the alignment tolerance, 5%.

4.3.3 Variation of sealing effectiveness in the wheel-space

Figure 4.12 shows the radial variation of sealing effectiveness ε_c for configuration SR, determined with CO_2 concentration measurements on the stator surface. The ε_c is plotted versus non-dimensional radius (r/b) in the range between 0.55 and 0.993. Gas concentration measurements were made at $Re_\phi = 7.9 \times 10^5$ and the on-design condition ($C_F = 0.38$), for three different levels of sealing flow rate denoted by Φ_0/Φ_{min} (Φ_{min} was determined from the measurements shown in Figure 4.13). The corresponding values of the turbulent flow parameter λ_T for the sealing flow are also labelled.

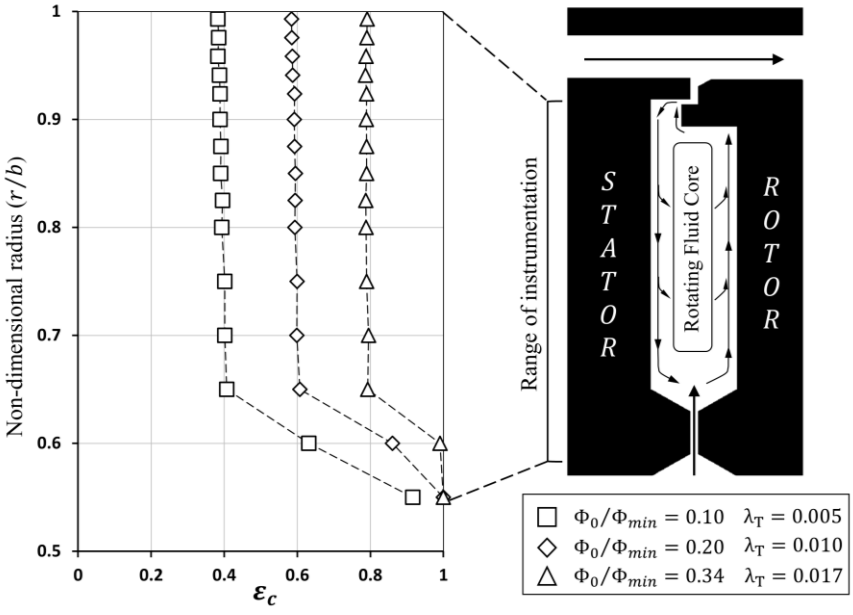

Figure 4.12 Radial variation of ε_c for the baseline single-clearance seal

The ε_c is shown to increase with sealing flow rate at all radial locations. For each flow condition, ε_c is shown to be almost invariant with radius in the wheel-space; a significant increase in ε_c is seen radially inboard, where the sealing flow entered through the inlet seal arrangement. The uniform distribution of CO_2 concentration along the stator surface indicates a complete mixing of the ingested fluid with the sealing air, which occurs in the outer region close to the seal clearance. The fully mixed fluid enters the stator boundary layer and moves radially inward, leading to an uniform distribution of concentration effectiveness.

Figure 4.13 shows the variation of ε_c with non-dimensional sealing flow parameter Φ_0. The measurement of CO_2 concentration was made at a radial location of $r/b = 0.958$, the outermost one that was radially inboard of the rotor-side seal component. This sampling location is representative of the wheel-space, due to the uniform radial distribution of ε_c shown in Figure 4.12. The experiments were conducted for the on-design condition at $Re_\phi = 5.3 \times 10^5$ and $Re_\phi = 7.9 \times 10^5$, and over an extensive range of sealing flow rate from $\Phi_0 = 0$, when no sealing flow was supplied, to the level of Φ_0 when the wheel-space was completely sealed (no ingress occurred).

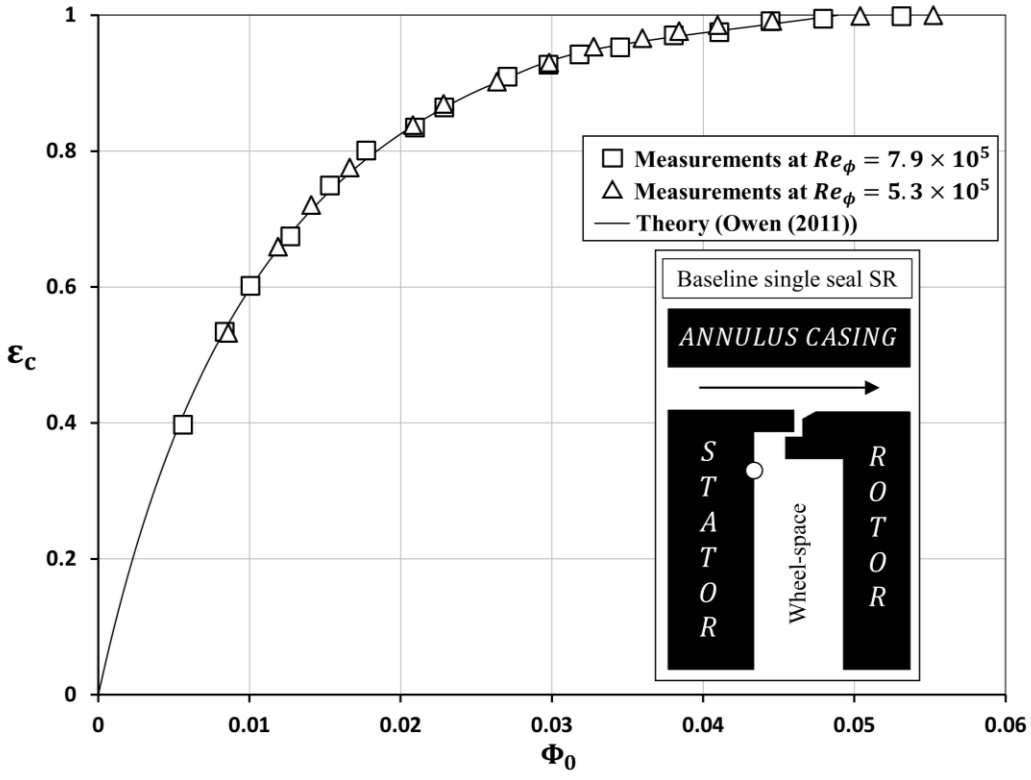

Figure 4.13 Variation of ε_c with Φ_0 for the baseline single-clearance seal

The ε_c is shown to increase with Φ_0, and the variation of ε_c with Φ_0 is independent of Re_ϕ. The experimental data was compared with the theoretical model for EI ingress described by Owen (2011) in conjunction with a statistical fitting method described by Zhou *et al*. (2013). An utility code was

used to generate the theoretical curve, with the experimental data shown in Figure 4.13 as input parameters. There is a very good agreement between the experimental data and the theoretical curve shown in the figure. The theoretical curve provides the minimum sealing flow rate to prevent ingress, $\Phi_{\min} \approx 0.049$, for the configuration SR with EI ingress.

4.3.4 Variation of pressure and swirl ratio in the wheel-space

Figure 4.14 shows the radial variation of the swirl ratio β and the radial variation of a pressure coefficient $C_{p,w}$ for the wheel-space, with the definition of $C_{p,w}$ as follows:

$$C_{p,w} = \frac{p - p_{ref}}{(1/2)\rho\Omega^2 b^2} \tag{4.8}$$

where p is the static pressure measured on the stator surface; p_{ref} is the static pressure taken at a referential radius x_{ref} ($x = r/b$). For this measurement, the reference pressure was taken at $x_{ref} = 0.6$, at the inlet of the wheel-space.

Measurements of static pressure and swirl velocities were performed at $Re_\phi = 7.9 \times 10^5$ for the on-design condition, with three different levels of sealing flow rate denoted by Φ_0/Φ_{min}. The corresponding values of the turbulent flow parameter λ_T are also labelled in the figure.

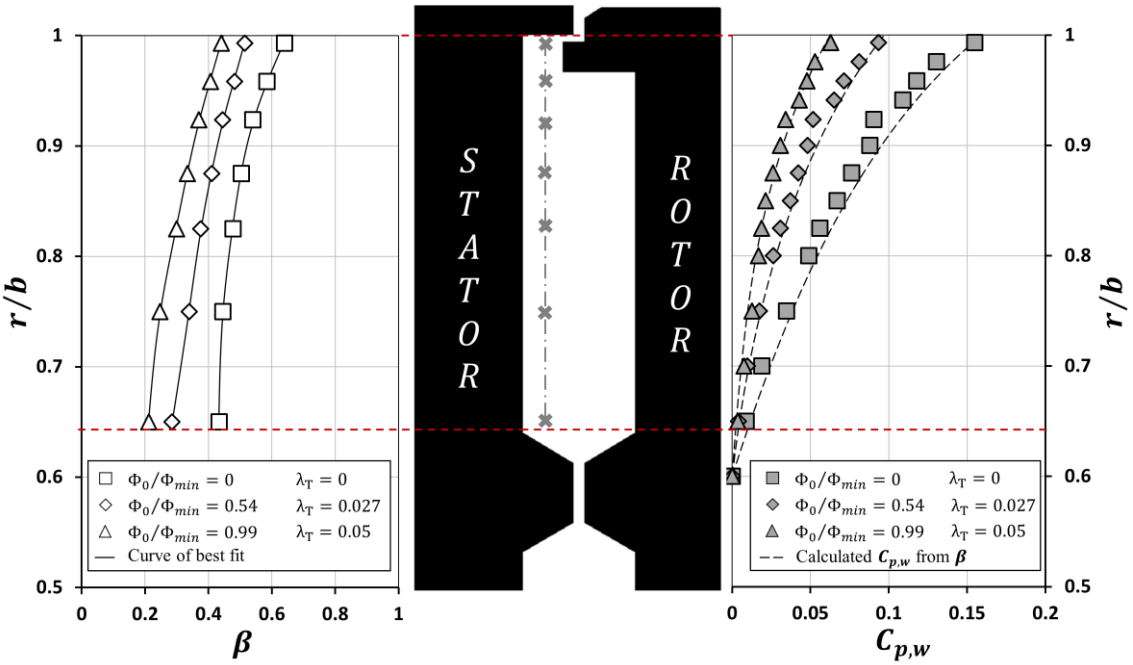

Figure 4.14 Radial variations of swirl ratio and pressure coefficient in the wheel-space for the baseline single-clearance seal

The swirl β is shown to increase with radius, and decrease with increasing sealing flow rate for all radii. As the swirl velocities are taken in the rotating core of fluid in the wheel-space, the reduction in β indicates a suppression to the fluid core when the sealing flow rate is raised. In this inviscid core, there is a balance between the pressure gradient and the centrifugal acceleration so that

$$\frac{1}{\rho}\frac{dp}{dr} = \frac{{V_\phi}^2}{r} \tag{4.9}$$

It follows that

$$C_{p,w} = 2\int_{x_{ref}}^{x} x\beta^2 dx \tag{4.10}$$

where $x_{ref} = 0.6$. The calculation of $C_{p,w}$ was conducted through a numerical integration using the Simpson's rule, with the radial variation of β obtained from a least-squares cubic spline fitted to the experimental data. The calculated distribution of $C_{p,w}$ is shown to agree well with the measurements as shown in Figure 4.14. Therefore the radial distribution of $C_{p,w}$ in the wheel-space is determined by the variation of β in the rotating core of fluid.

4.4 Summary

This chapter reports the baseline testing of the rig, followed by the experiment measurements for a baseline single-clearance rim-seal configuration. The deformation of the rotating disc is assessed experimentally. The measurement of rotor shroud displacement was made over a range of disc speed. The displacement was also acquired from a structural FEA analysis, which was previously shown in Chapter 3 for the prediction of rotor stresses. There is a good agreement between the FEA result and the measurement. It is shown that the rotor deformation due to rotation is too insignificant relative to the rim-seal clearances and the blade tip clearance.

Pressure measurements were conducted in the annulus to evaluate the mainstream flow condition. The circumferential variation of pressure coefficient, C_p, was determined downstream of the stator vane. The pressure asymmetry ΔC_p, which is the peak-to-trough difference of C_p in a vane pitch, is evaluated at different positions in the annulus for different rotational Reynolds number and for different flow coefficient. The effect of interaction between sealing flow and the mainstream on ΔC_p is also investigated.

A generic single-clearance rim seal is introduced as a baseline configuration. The sealing effectiveness for this seal was determined with gas concentration measurements. The radial variation of effectiveness is shown for different levels of sealing flow rate. The variation of sealing

effectiveness over the complete range of non-dimensional sealing flow rate is shown. The data can be well predicted by the theoretical orifice model in conjunction with a statistical fitting method.

The radial variation of pressure in the wheel-space was evaluated. Swirl velocities were measured in the rotating core of the wheel-space flow. The radial variation of pressure was calculated from the swirl ratios using a simplified radial moment equation. The calculation is in good agreement with the measurements, indicating the pressure variation determined by the swirl velocities.

The measurements for the baseline single-clearance seal form the basis for the study of more engine-representative double-clearance seals to be described in the following chapters. The same operating conditions shown in this chapter will continue to be applied in the following studies. The methods for evaluating the sealing effectiveness and analysing the flow physics shall be used again to investigate the relative performance of different rim-seal configurations.

Chapter 5 Study of double-clearance rim seals with different stator-side features

This chapter describes a parametric study on generic, but engine-representative double-clearance rim seals with different stator-side features. This study investigates sealing effectiveness and fluid dynamics of ingress associated with these rim-seal features, in comparison with a datum double-clearance seal. Experimental measurements of gas concentration, pressure and swirl velocities were conducted to assess the relative performance of each double-clearance rim seal. The ranking of sealing effectiveness is shown. This study is aimed to achieve an improved understanding of how double-clearance rim seals with various stator-side features operate, and provide insights into the fluid dynamics of ingestion.

Section 5.1 introduces the geometries of double-clearance rim-seal configurations with different stator-side features. Section 5.2 describes a comparison in seal performance and fluid dynamics between the baseline single-clearance and double-clearance seals. Section 5.3 reports the experimental measurements of sealing effectiveness for rim seals characterised by different stationary features. Section 5.4 describes the evaluation of fluid dynamics in the wheel-space by measurements of pressure and swirl velocities in the wheel-space. Section 5.5 concludes the chapter with a ranking of seal performance.

5.1 Rim-seal configurations

Figure 5.1 shows the baseline double-clearance rim-seal configuration, referred to as the DS-0. It is a generic, but engine-representative rim seal, consisting of an outer seal positioned at the periphery of turbine discs and an inner seal located radially inboard. An annular rotor-stator cavity, referred to as the outer wheel-space in this chapter, is created between the outer and inner seal; an inner wheel-space is formed radially inward of the inner seal arrangement as illustrated in the figure.

Schematic representation of the flow paths for the system is also shown in Figure 5.1. The sealing flow enters the system through an inlet clearance, and interacts with the flow in the inner wheel-space. The sealing flow is then entrained into the boundary layer on the rotor surface, and moves radially outwards. On the stator surface, fluid ingested into the inner wheel-space enters the stator-side boundary layer and moves radially inwards. Under the flow conditions when ingress is not completely prevented, the Batchelor flow model (introduced in Chapter 2) applies to the inner wheel-space (Poncet *et al*. (2005)). There is a rotating core of fluid between the two separate boundary layers; the fluid in the stator boundary layer is entrained to the rotor surface through the core.

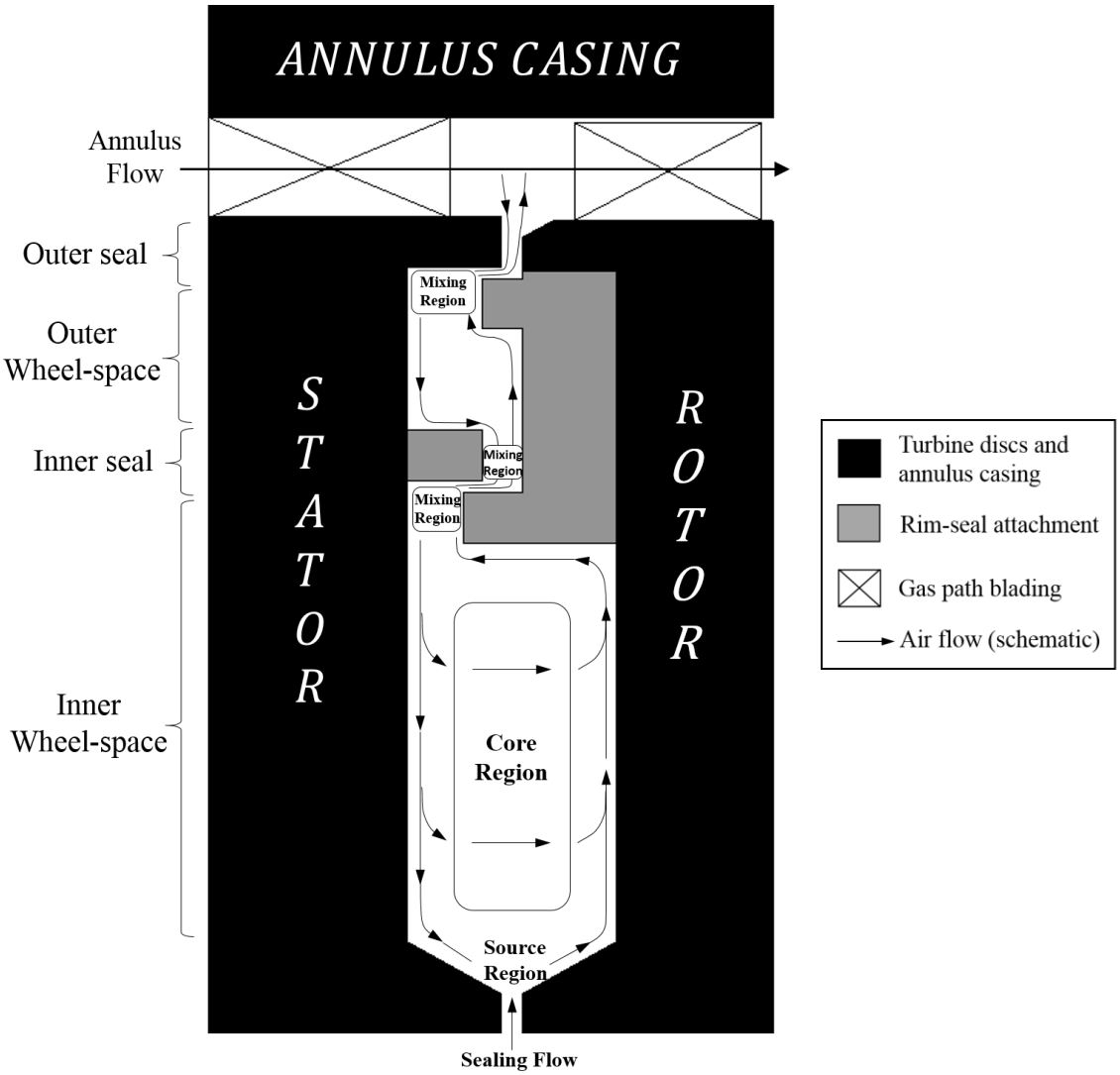

Figure 5.1 Configuration of the baseline double-clearance seal with schematic diagram of flows

Through the inner-seal clearance, the sealing flow enters the outer wheel-space, where the ingested fluid from the mainstream is confined. The outer wheel-space, acting as a buffer volume, reduces the ingress into the inner wheel-space. This discussion is supported by experimental measurements with this baseline double-clearance seal compared with those for a single-clearance seal, which will be shown in section 5.2. For an industrial gas turbine engine equipped with a double-clearance rim seal, the outer wheel-space protected by heat-resistant alloys may be predominantly exposed to hot gas ingestion, while the turbine discs can operate at a moderate temperature radially inboard of the inner seal.

Figure 5.2 shows the geometries of four double seal configurations with different stator-side seal features, including the datum seal. Geometric properties under static condition are stated in Table 5.1.

Compared with the datum configuration DS-0 shown in (a), configuration DS-1 features a reduced height for the outer wheel-space, as illustrated in (b). The study of DS-1 was aimed to investigate the effect of the buffer volume height on ingestion into both the outer and inner wheel-spaces. For configuration DS-2 shown in (c), the inner-seal overlap was increased by approximately 100% relative to the datum configuration. For configuration DS-3 shown in (d), a radial protrusion was added to the stationary component of DS-2, to constitute an arrangement referred to as the 'angel-wing' seal, representative of those often applied in engines. Among the four seal configurations, the rotor-side seal feature was kept consistent, thus allowing the specific effects of stator-side seal features to be investigated.

These different seal configurations were created by applying modular attachments to the turbine discs, as illustrated in Figure 5.2. The stator-side inner seal component was attached directly onto the stator surface; and the rotor-side counterpart was bolted under the rotor platform. For geometric features shared by these seals, such as the outer-seal axial clearance $s_{c,ax}$, the repeatability and consistency were successfully maintained among different configurations due to the high-precision alignment system.

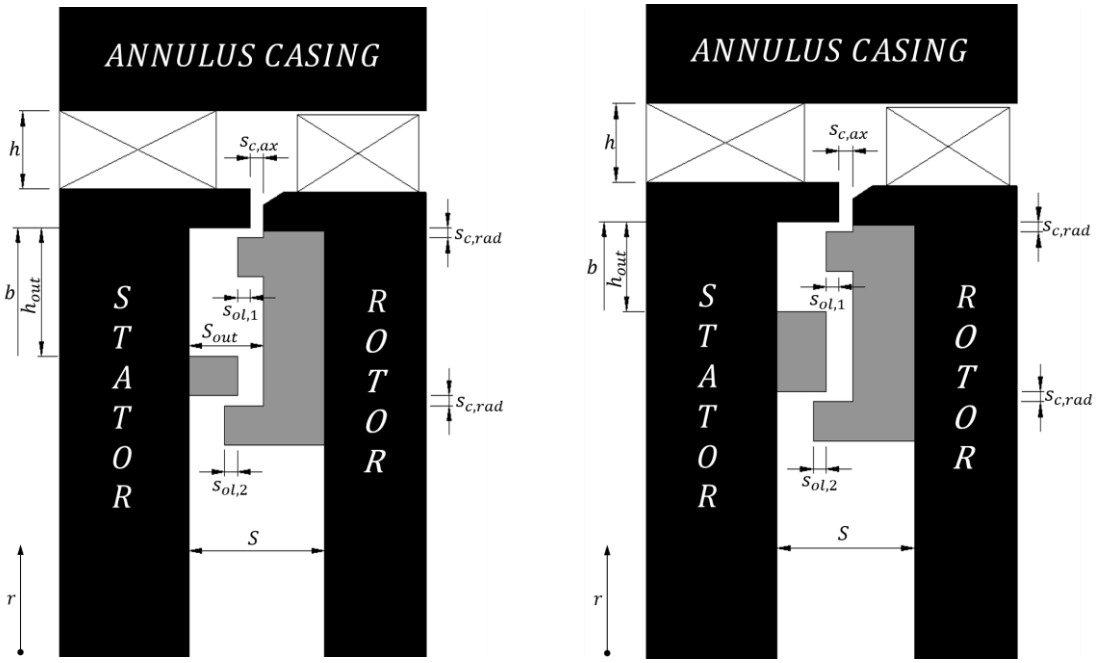

(a) DS-0 (b) DS-1

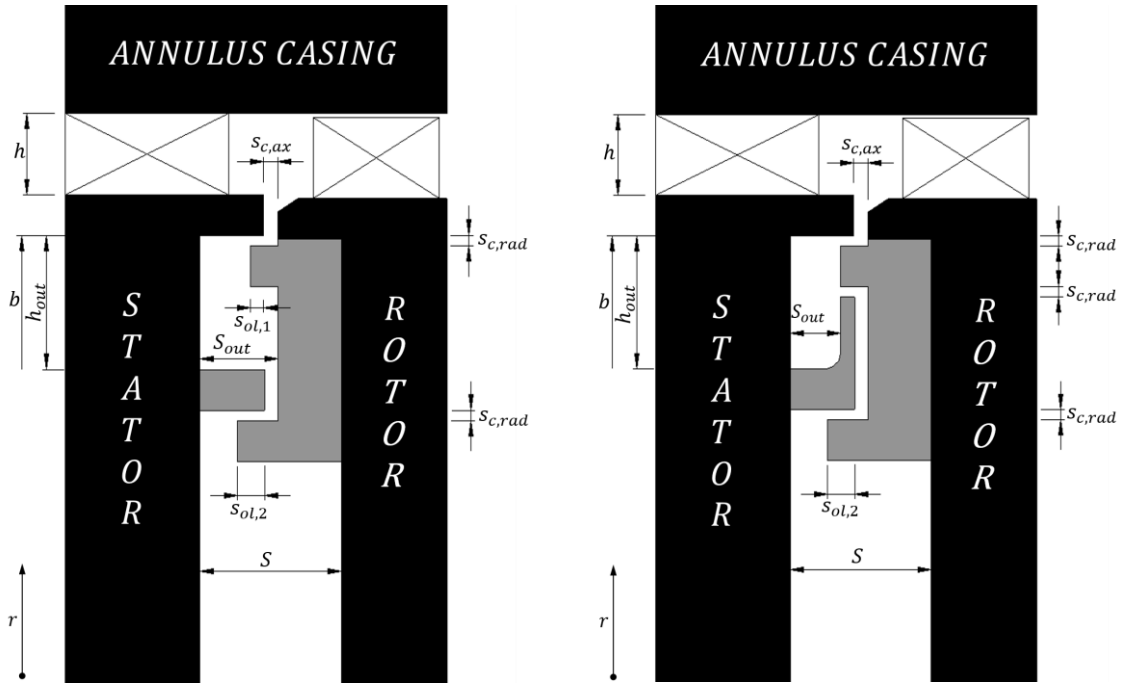

(c) DS-2 (d) DS-3

Figure 5.2 Double-clearance seal configurations with different stator-side features

Table 5.1 Geometric properties for double-clearance seals with different stator-side features (Dimensions in mm under static condition)

Geometric symbol	**Seal configuration**			
	DS-0	**DS-1**	**DS-2**	**DS-3**
h	10.0			
b	190			
S	20.0			
$s_{c,ax}$	2.00			
$s_{c,rad}$	1.28			
$s_{ol,1}$	1.86			
$s_{ol,2}$	1.86	1.86	3.86	3.86
h_{out}	16.5	11.5	16.5	16.5
S_{out}	11.0	11.0	11.0	7.14

5.2 Comparison between the baseline single-clearance and double-clearance seals

This section presents experimental measurements for the baseline double-clearance seal configuration DS-0, in comparison with the baseline single-clearance seal SR, which have been described in Chapter 4. The differences in sealing effectiveness and fluid dynamics are highlighted, to demonstrate the general behaviour and advantage of double-clearance rim seals.

5.2.1 Variation of sealing effectiveness in the wheel-space

Figure 5.3 shows the radial variation of sealing effectiveness ε_c for seal configuration DS-0, determined with CO_2 concentration measurements on the stator surface. The results were compared with those for the single-clearance seal SR documented in Chapter 4. The ε_c is plotted versus non-dimensional radius (r/b) in the range between 0.55 and 0.993. Gas concentration measurements were made at $Re_\phi = 7.9 \times 10^5$ and the on-design condition ($C_F = 0.38$), for three different levels of sealing flow rate (Φ_0).

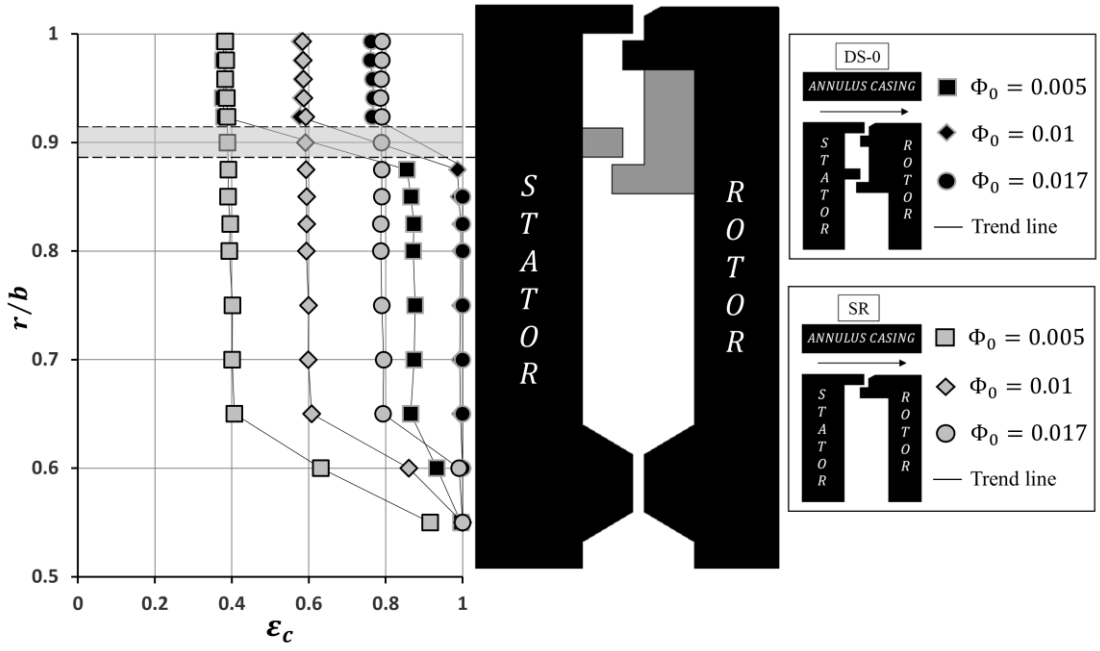

Figure 5.3 Radial variation of ε_c for seal configuration DS-0 and SR

For both seals, ε_c is shown to increase with Φ_0, as the ingress is reduced with increasing sealing flow. In the outer wheel-space of DS-0, ε_c is seen to be almost invariant with radius, indicating a complete mixing of ingress and sealant in the outer region close to the seal clearance. The same discussion

also applies to the inner wheel-space. For DS-0, there is an obvious increase in ε_c across the inner seal; the ε_c inboard of the inner seal is significantly higher compared with SR. Radially outboard of the inner seal, there is a good agreement in ε_c between the two configurations. The measurements show the ingress is predominantly confined in the outer wheel-space; the addition of the inner seal enables the turbine discs to operate at more benign conditions radially inboard.

Figure 5.4 shows the variation of ε_c with non-dimensional sealing flow parameter Φ_0 for DS-0, in comparison with single-clearance seal SR. The measurements of CO_2 concentration were made at the radial location of $r/b = 0.958$ for the outer wheel-space (consistent with measurement for the single-clearance seal), and also at the radial location of $r/b = 0.85$ for the inner wheel-space, radially inboard of the inner seal arrangement. The concentration sampled at these locations is representative for each wheel-space, due to the uniform radial distributions of ε_c shown in Figure 5.3. The experiment was conducted for the on-design condition at $Re_\phi = 5.3 \times 10^5$ and $Re_\phi = 7.9 \times 10^5$, and over an extensive range of sealing flow rate.

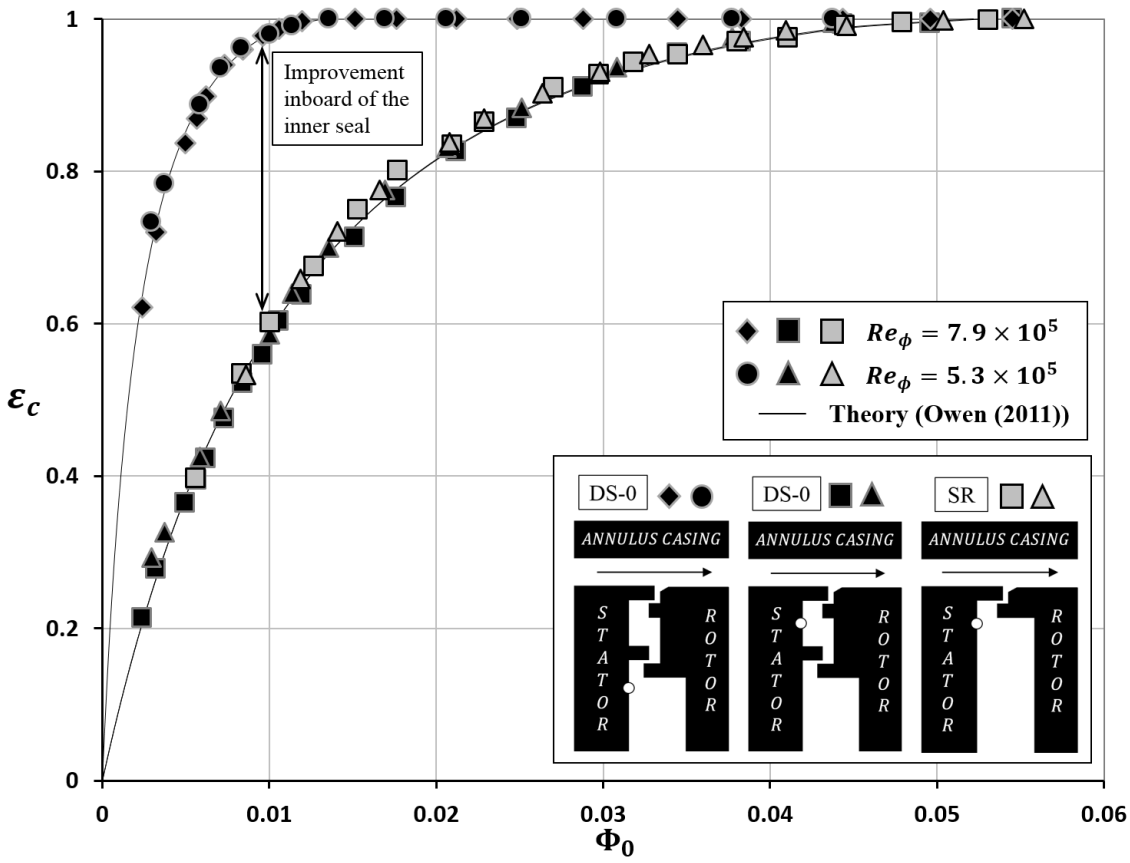

Figure 5.4 Variation of ε_c with Φ_0 for seal configuration DS-0 and SR

The ε_c is shown to increase with Φ_0, in line with Figure 5.3. The variation of ε_c with Φ_0 is independent of Re_ϕ, and the seal performance is characterised by Φ_{min}. The experimental data was compared with the theoretical model for EI ingress described by Owen (2011) in conjunction with a statistical fitting method described by Zhou *et al*. (2013). The utility code mentioned in the previous chapter, is used once again for the double-clearance seals to generate the theoretical curves. There is a very good agreement between the experimental data and the theoretical curves for DS-0. The minimum sealing flow rate Φ_{min} and the ratio of discharge coefficients Γ_c ($\Gamma_c = C_{d,i}/C_{d,e}$) were optimised by the fitting, and the respective values for each seal configuration are summarised in section 5.5. The ε_c for the outer wheel-space of DS-0 is shown to agree well with that for SR over the complete range of Φ_0. For the inner wheel-space of DS-0, the improvement in ε_c resulting from the double-clearance seal is illustrated in the figure.

5.2.2 Variation of pressure and swirl ratio in the wheel-space

Measurements of static pressure and swirl velocities in the wheel-space were performed at $Re_\phi = 7.9 \times 10^5$ for the on-design condition, with different levels of sealing flow rate. Figure 5.5 shows the radial variation of swirl ratio β for DS-0, in comparison with that for SR. The sealing flow rate is denoted by Φ_0/Φ_{min} (here Φ_{min} denotes the minimum level of Φ_0 to seal the outer wheel-space); the corresponding values of the turbulent flow parameter λ_T are also labelled in the figure. The swirl β is shown to decrease with increasing sealing flow rate for all radii, in line with that suggested by Childs (2011).

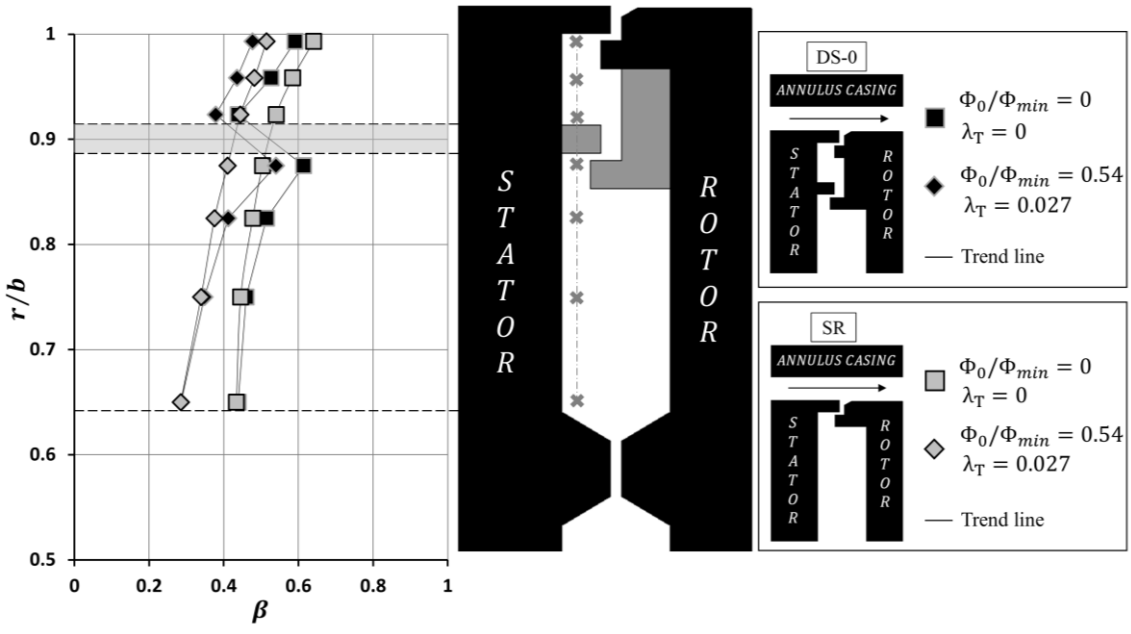

Figure 5.5 Radial variation of swirl ratio for seal configuration DS-0 and SR

For the inner wheel-space, β for the two seal configurations agree for each λ_T, except for the location close to the rotating seal lip that enhances the swirl velocity. β is shown to be predominantly governed by λ_T, despite the significant difference in ε_c between DS-0 and SR. This suggests a flow structure featuring a rotating core between separate turbulent boundary layers on the disc surfaces; and these boundary layers are principally governed by λ_T (Owen and Rogers (1989)). In the outer wheel-space, β for the double-clearance seal is shown to be lower relative to the single-clearance seal, especially in the region close to the stationary inner-seal component. The fluid outboard of the inner seal is probably decelerated by friction near the stator-side component.

Figure 5.6 shows the radial variation of the pressure gradient: (a) for the inner wheel-space, $C_{p,in}$ and (b) for the outer wheel-space, $C_{p,out}$. The definitions of $C_{p,in}$ and $C_{p,out}$ are given as follows:

$$C_{p,in} = \frac{p - p_{r,in}}{(1/2)\rho\Omega^2 b^2} \tag{5.1}$$

and

$$C_{p,out} = \frac{p - p_{r,out}}{(1/2)\rho\Omega^2 b^2} \tag{5.2}$$

where p is the static pressure measured on the stator surface; $p_{r,in}$ and $p_{r,out}$ are reference pressures in the inner and outer wheel-spaces respectively.

The $p_{r,in}$ was taken at $x_{ref} = 0.6$ ($x = r/b$), the innermost location for the inner wheel-space; the $p_{r,out}$ was taken at $x_{ref} = 0.923$, the innermost location for the outer wheel-space.

The $C_{p,in}$ for DS-0 agrees reasonably well with that for SR at each sealing flow rate. In connection with the swirl ratio for DS-0 shown in Figure 5.6, the radial variation of $C_{p,in}$ was calculated using Eq. (4.10) introduced in the previous chapter. There is a good agreement between the measurements and the calculated $C_{p,in}$, indicating the pressure distribution is determined by the swirl ratio in the inner wheel-space.

The $C_{p,out}$ for DS-0 is shown to be lower relative to SR at each sealing flow rate. In connection with the swirl ratio shown in Figure 5.5, the decrease in pressure gradient corresponds to the decrease in swirl ratio from SR to DS-0 in the outer wheel-space. This correlation of $C_{p,out}$ and β can probably be attributed to the equilibrium between the radial pressure gradient and the centrifugal force resulting from the swirling motion.

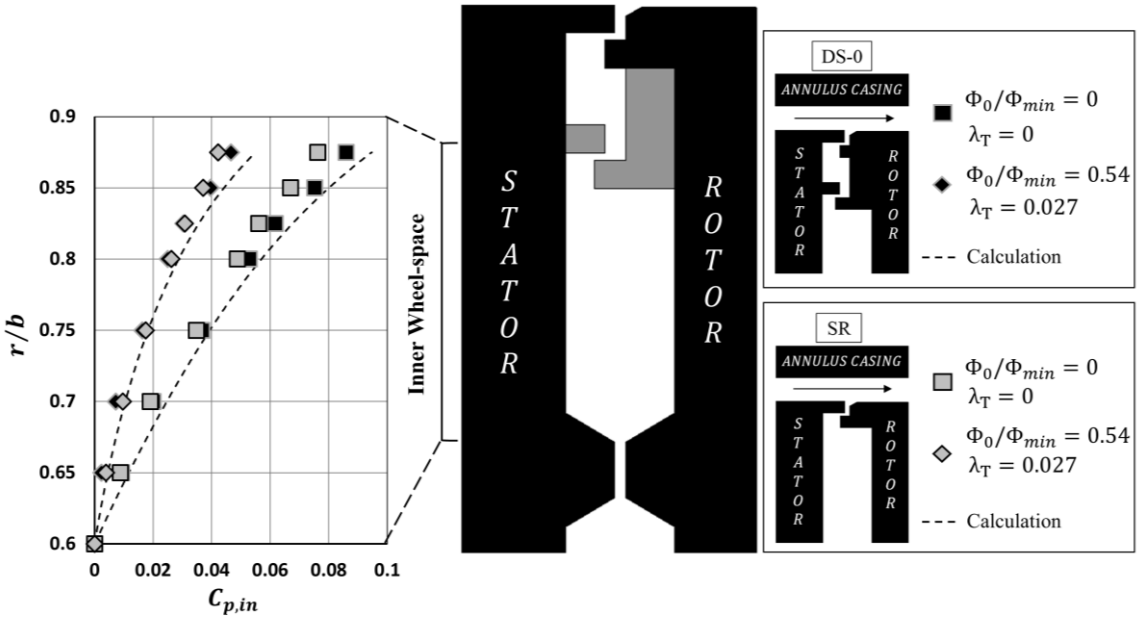

(a) For the inner wheel-space

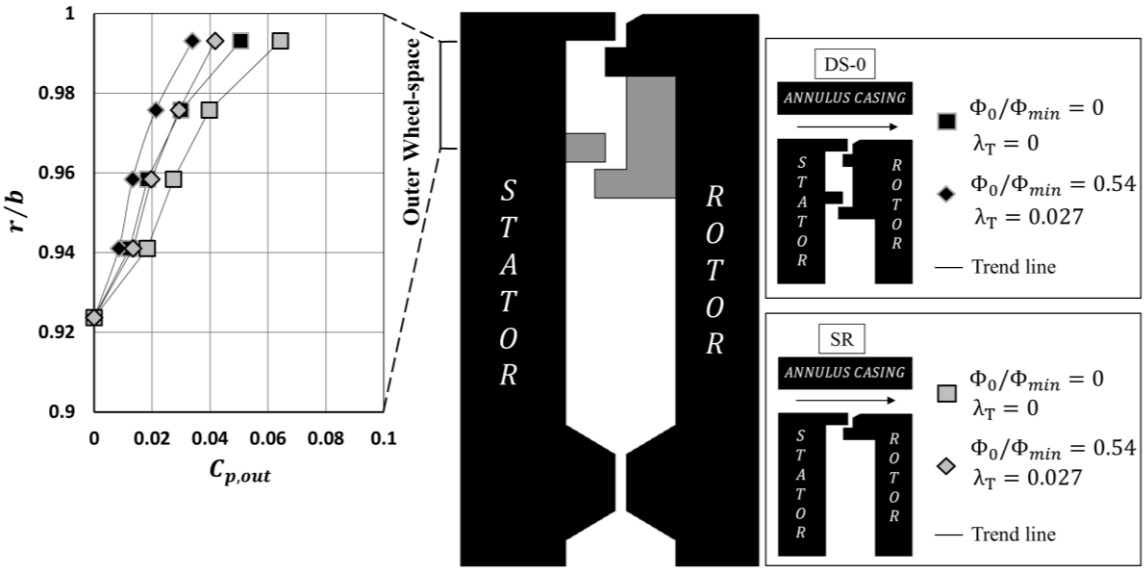

(b) For the outer wheel-space

Figure 5.6 Radial variations of pressure coefficients for seal configuration DS-0 and SR

5.3 Sealing effectiveness for double-clearance rim seals with different stator-side features

This section presents the sealing effectiveness for double-clearance rim seals with different stator-side features, including seal configuration DS-0 (baseline), DS-1, DS-2 and DS-3. Geometries of these seals have been given in section 5.1. CO_2 gas concentration measurements were conducted to determine the sealing effectiveness, and the relative performance of each seal is shown.

5.3.1 Seal configuration DS-1 relative to DS-0: effect of the outer wheel-space height

This section describes the sealing effectiveness for seal configuration DS-1 in comparison with the baseline seal DS-0. The inner seal of DS-1 features a different stator-side component relative to DS-0, which reduces the height of outer wheel-space by 30%. Axial overlaps and radial clearances remain consistent between the two seal configurations.

Figure 5.7 shows the radial variation of sealing effectiveness ε_c for DS-0 and DS-1, determined with CO_2 concentration measurements on the stator surface. The ε_c is plotted versus the non-dimensional radius (r/b) between 0.55 and 0.993. Gas concentration measurements were made at $Re_\phi = 7.9 \times 10^5$ and at the on-design condition ($C_F = 0.38$), for three different levels of sealing flow rate (Φ_0).

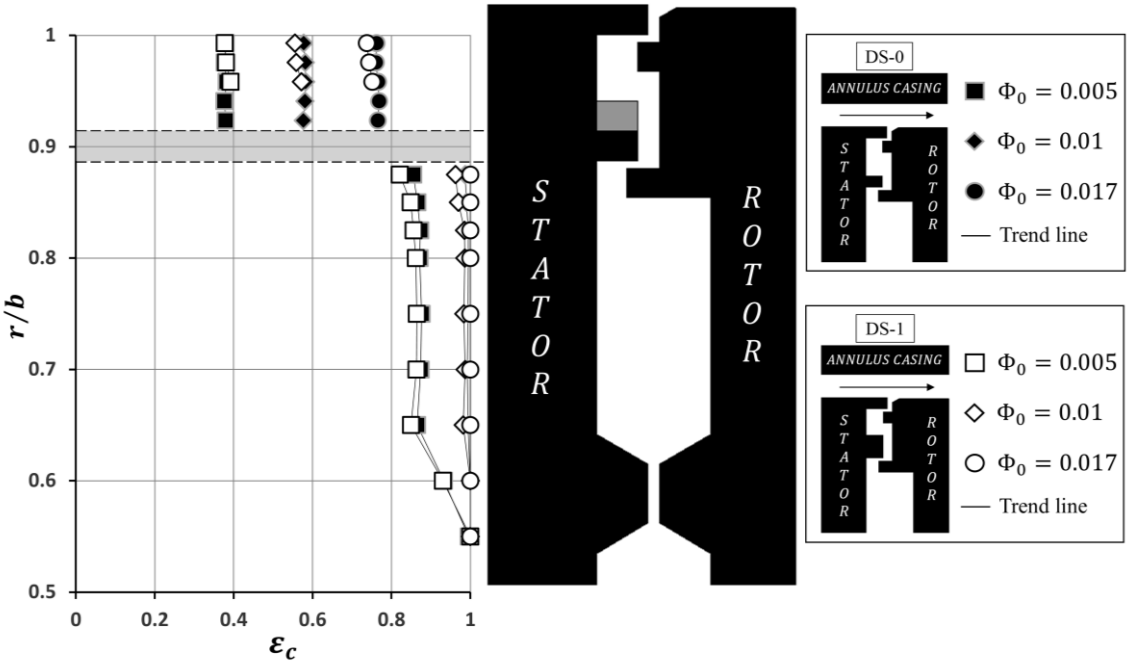

Figure 5.7 Radial variation of ε_c for seal configuration DS-0 and DS-1

The ε_c is shown to increase with Φ_0 in both wheel-spaces. For each level of sealing flow rate, there is a good agreement in effectiveness between the two configurations over the complete range of radius. The variation of ε_c is shown to be insensitive to the height of outer wheel-space h_{out}, within the scope of this study. For this comparison, h_{out} was reduced by 30% without causing a change in ε_c; however, a further reduction in h_{out} may gradually weaken the functioning of the outer wheel-space in containing ingress, and could lead to a decrease in ε_c for the inner wheel-space.

Figure 5.8 shows the variation of ε_c with Φ_0 for DS-0 and DS-1. CO_2 gas concentration measurements were made at $r/b = 0.958$ for the outer wheel-space and $r/b = 0.85$ for the inner wheel-space. The experiment was conducted for the on-design condition at $Re_\phi = 5.3 \times 10^5$ and $Re_\phi = 7.9 \times 10^5$, and over an extensive range of sealing flow rate.

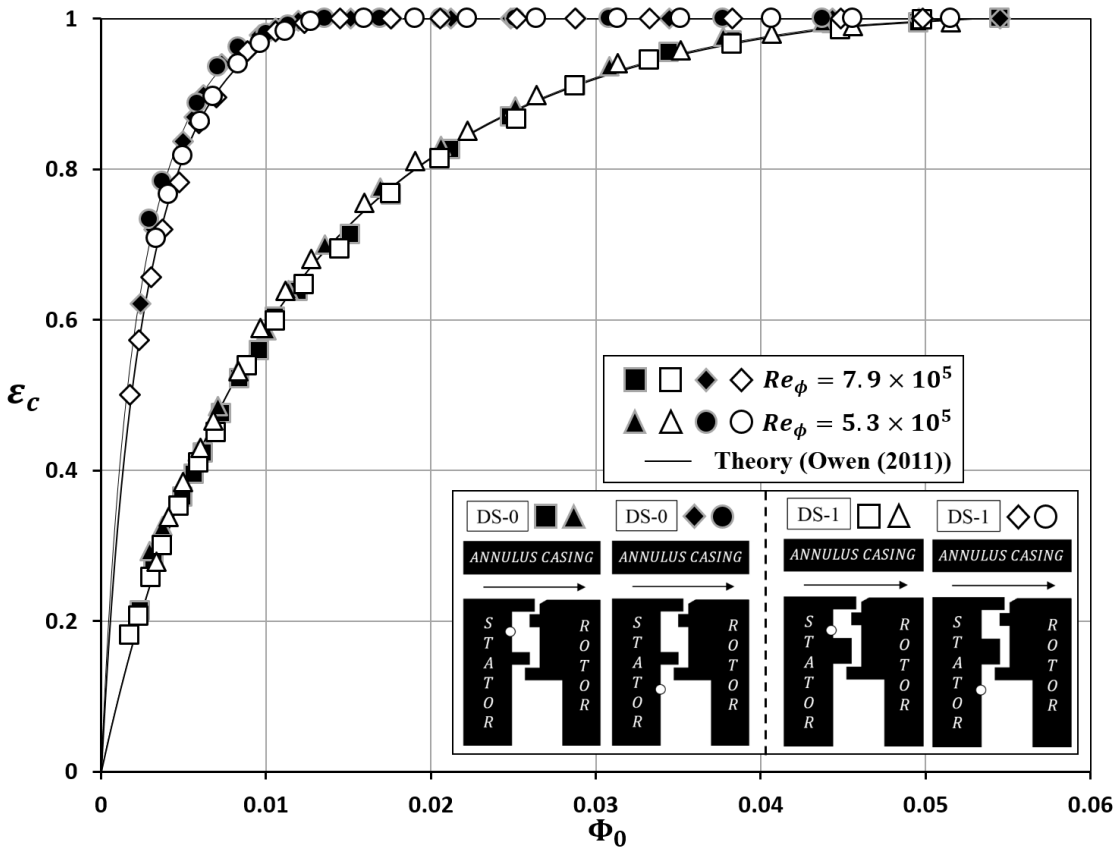

Figure 5.8 Variation of ε_c with Φ_0 for seal configuration DS-0 and DS-1

For DS-1, ε_c is shown to increase with Φ_0, and the variation of ε_c with Φ_0 is independent of Re_ϕ. The experimental data was compared with a theoretical model in conjunction with a statistical fitting technique, same as that previously described for DS-0 in section 5.2. There is a very good agreement

between the experimental data and the theoretical curves for both seals. The Φ_{min} and Γ_c ($\Gamma_c = C_{d,i}/C_{d,e}$) for DS-1 optimised by the fitting are summarised in section 5.5. The variation of ε_c for DS-1 is shown to match the datum seal in both wheel-spaces over the complete range of Φ_0, in support of that shown in Figure 5.7.

5.3.2 Seal configuration DS-2 relative to DS-0: effect of the inner-seal overlap

This section describes the sealing effectiveness for seal configuration DS-2 in comparison with the baseline seal DS-0. The inner seal of DS-2 features a different stator-side component relative to DS-0, which increases the overlap of inner seal by approximately 100%. Radial clearances remain consistent between the two seal configurations.

Figure 5.9 shows the radial variation of sealing effectiveness ε_c for DS-2, in comparison with the datum double-clearance seal DS-0. The ε_c was plotted versus the non-dimensional radius (r/b) between 0.55 and 0.993. Gas concentration measurements were made at $Re_\phi = 7.9 \times 10^5$ and the on-design condition for three different levels of sealing flow rate (Φ_0).

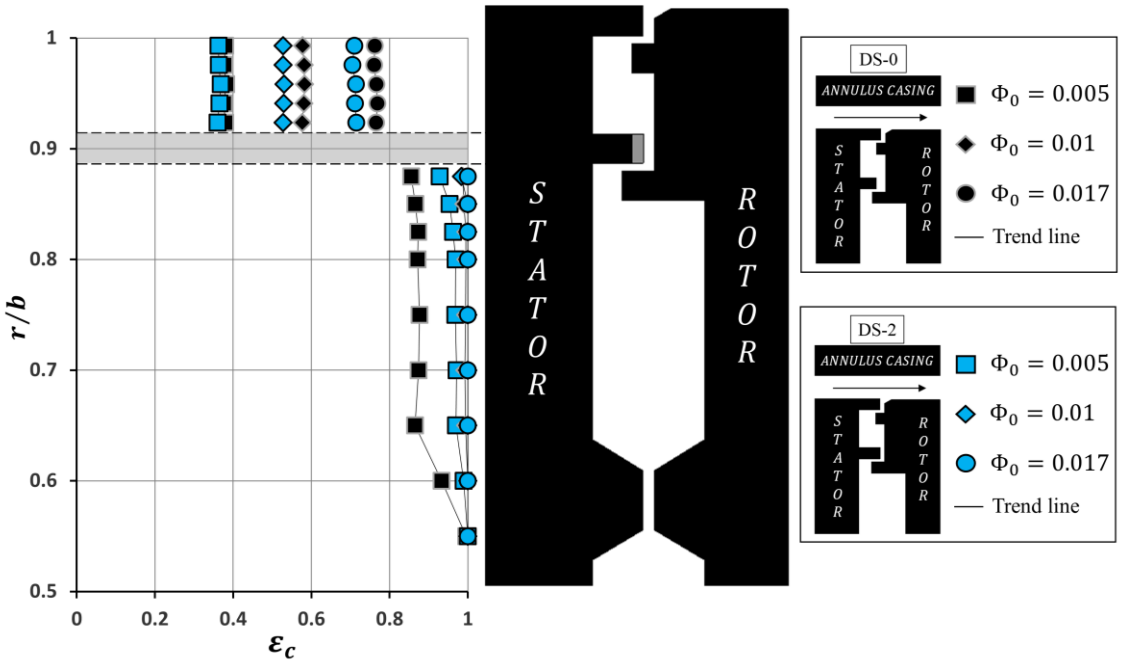

Figure 5.9 Radial variation of ε_c for DS-0 and DS-2

At the same Φ_0, the ε_c for the inner wheel-space of DS-2 is shown to be higher relative to the baseline, but the ε_c for the outer wheel-space is lower than the datum. The increase in the inner-seal overlap of DS-2 enhances the performance of that seal; ingress is more effectively contained in the outer wheel-space causing the decrease in ε_c within that wheel-space.

Figure 5.10 shows the variation of ε_c with Φ_0 for DS-0 and DS-2. Gas concentration measurements were made at $r/b = 0.958$ for the outer wheel-space and $r/b = 0.85$ for the inner wheel-space. The experiment was conducted for the on-design condition at $Re_\phi = 5.3 \times 10^5$ and $Re_\phi = 7.9 \times 10^5$.

The ε_c in the inner wheel-space of DS-2 is shown to be improved compared with the baseline seal DS-0. However, ε_c for the outer wheel-space of DS-2 is decreased relative to DS-0. The trend in the variation of ε_c shown in Figure 5.9 is valid over the complete range of Φ_0.

The experimental data was compared with a theoretical model in conjunction with a statistical fitting technique, same as that previously described for DS-0 in section 5.2. There is a good agreement between the experimental data and the theoretical curves for DS-2. The Φ_{min} and Γ_c ($\Gamma_c = C_{d,i}/C_{d,e}$) for DS-2 optimised by the fitting are summarised in section 5.5.

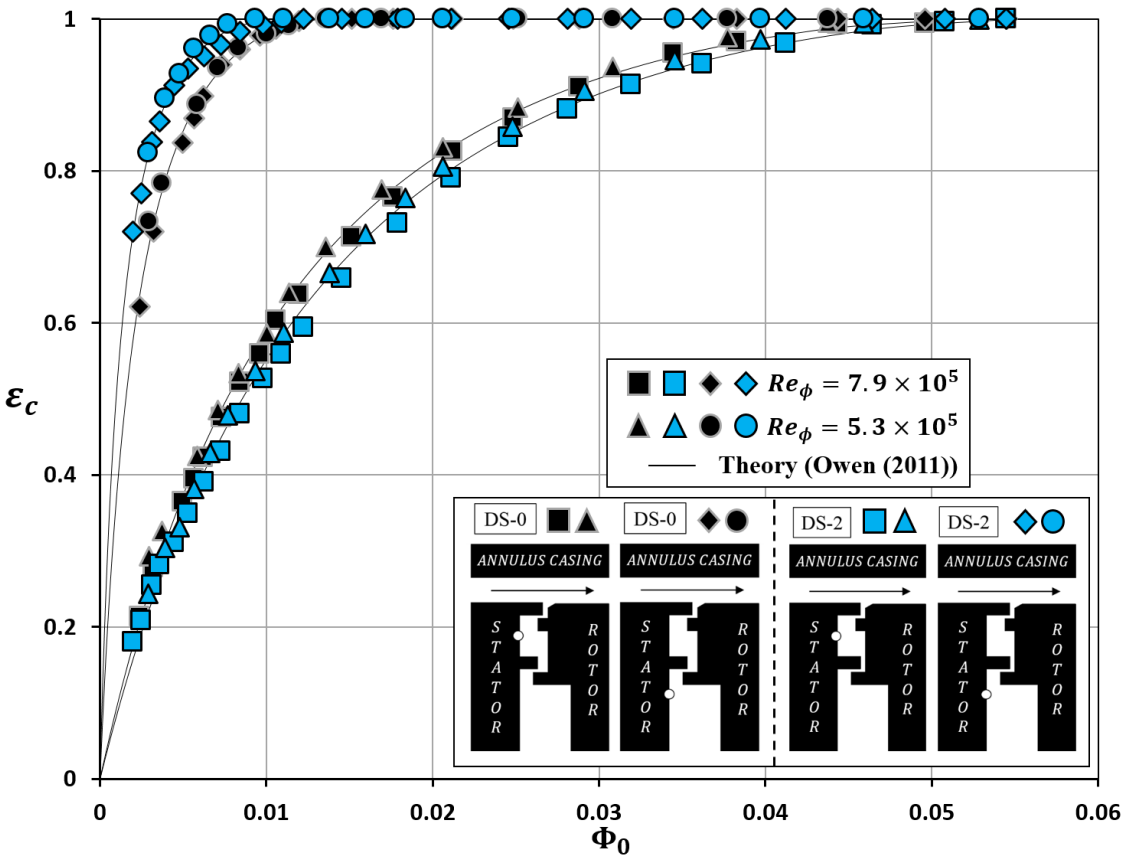

Figure 5.10 Variation of ε_c with Φ_0 for seal configuration DS-0 and DS-2

5.3.3 Seal configuration DS-3 relative to DS-0: effect of the angel-wing feature

This section describes the sealing effectiveness for seal configuration DS-3 in comparison with the baseline seal DS-0. The inner seal of DS-3 features an angel-wing configuration, which is shown diagrammatically in section 5.1. This generic seal configuration is also representative of those often applied in engines.

Figure 5.11 shows the radial variation of sealing effectiveness ε_c for DS-3, in comparison with the baseline seal configuration DS-0. The ε_c was plotted versus the non-dimensional radius (r/b) between 0.55 and 0.993. Gas concentration measurements were made at $Re_\phi = 7.9 \times 10^5$ and for three different levels of sealing flow rate (Φ_0).

At the same Φ_0, the ε_c for the inner wheel-space of DS-3 is shown to be higher relative to the baseline, but the ε_c for the outer wheel-space is lower than the datum. The addition of the angel-wing significantly improves the inner-seal performance; ingress is predominantly contained in the outer wheel-space causing the decrease in ε_c within that wheel-space. The sealing effectiveness of DS-3 is probably associated with the fluid dynamics in the wheel-space, supported by measurements of pressure and swirl velocities which shall be reported in the following sections.

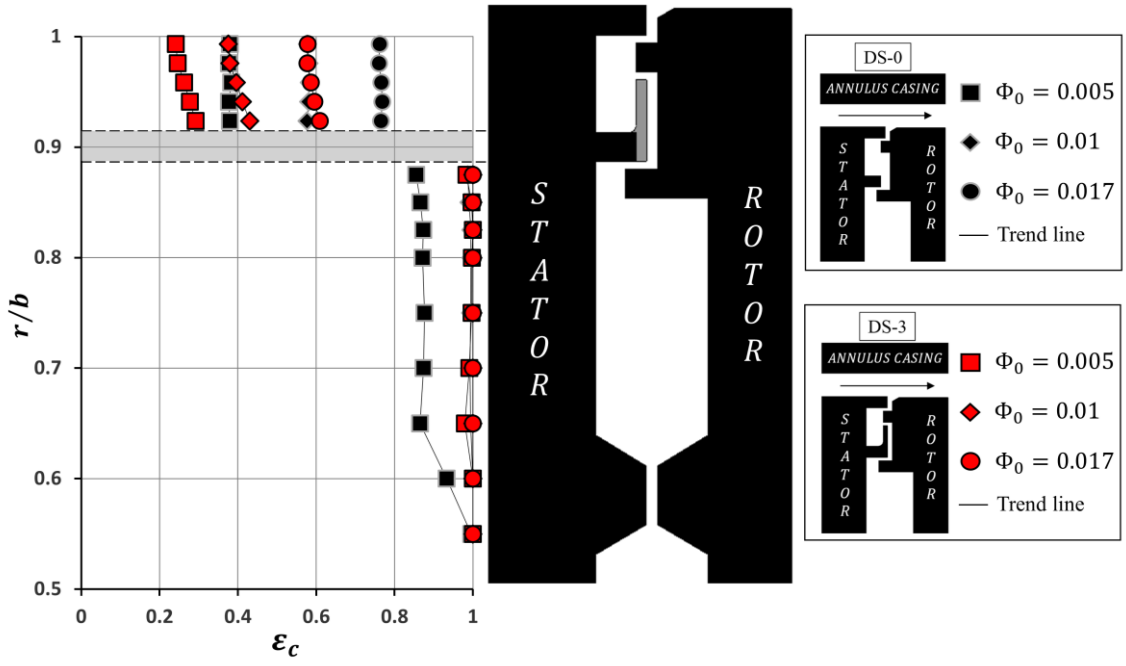

Figure 5.11 Radial variation of ε_c for DS-0 and DS-3

Figure 5.12 shows the variation of ε_c with Φ_0 for DS-0 and DS-3. Gas concentration measurements were made at $r/b = 0.958$ for the outer wheel-space and $r/b = 0.85$ for the inner wheel-space. The

experiment was conducted for the on-design condition at $Re_\phi = 5.3 \times 10^5$ and $Re_\phi = 7.9 \times 10^5$. It is shown that the trend in the variation of ε_c shown in Figure 5.11 is valid over the complete range of Φ_0. Relative to the baseline seal, the ε_c in the inner wheel-space of DS-3 is shown to be significantly improved, but ε_c for the outer wheel-space is decreased. The experimental data was compared with a theoretical model in conjunction with a statistical fitting technique, same as that previously described for DS-0 in section 5.2. Again there is a good agreement between the experimental data and the theoretical curves for DS-3. The Φ_{min} and Γ_c ($\Gamma_c = C_{d,i}/C_{d,e}$) for DS-3 optimised by the fitting are summarised in section 5.5.

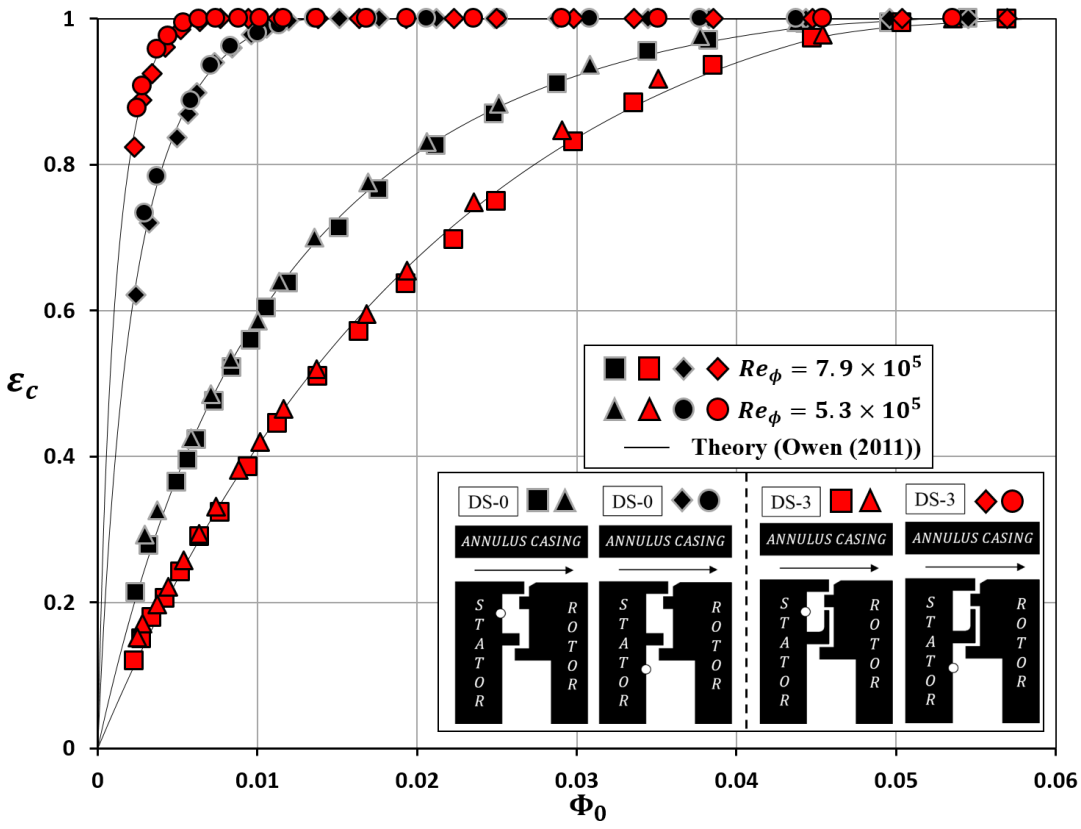

Figure 5.12 Variation of ε_c with Φ_0 for seal configuration DS-0 and DS-3

Figure 5.13 shows the variation of ε_c with Φ_0 for DS-3, evaluated at different positions including those on the angel-wing seal component. It is shown that the level of sealing effectiveness measured on the angel-wing is lower than that for the inner wheel-space, but higher relative to the outer wheel-space. An intermediate region is formed between the inner and outer wheel-spaces, and a tortuous path is created for the ingress flow and the sealing flow to reach the inner wheel-space and outer wheel-space respectively.

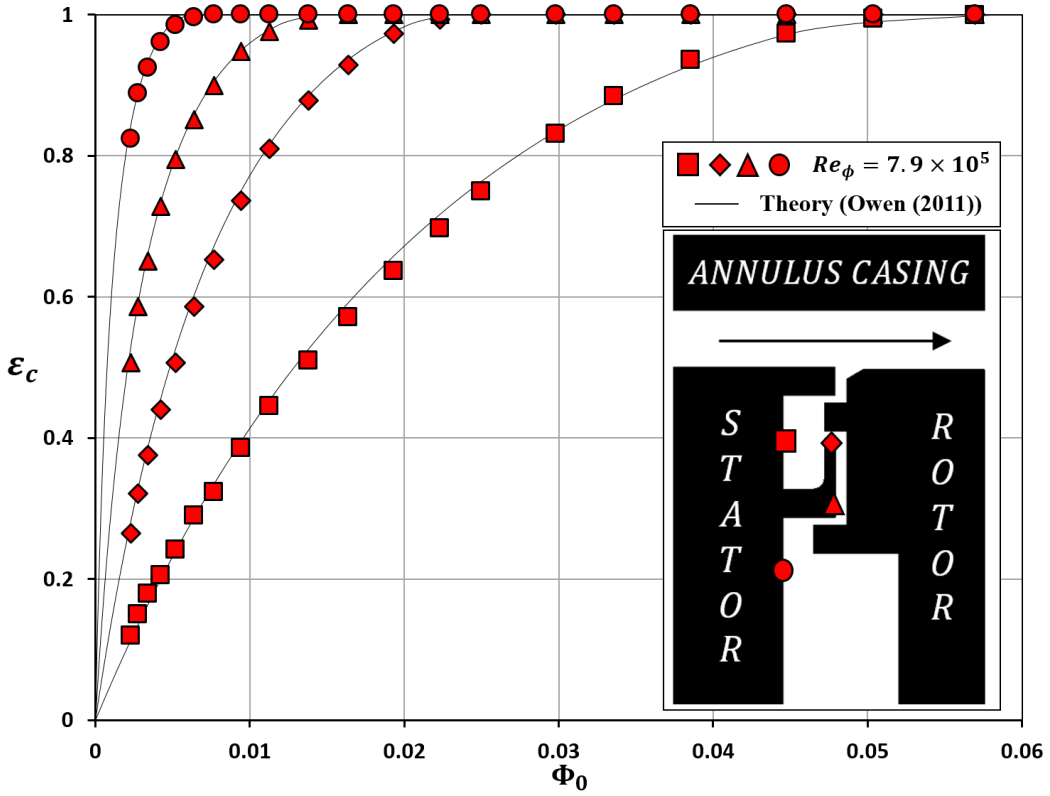

Figure 5.13 Variation of ε_c with Φ_0 for seal configuration DS-3 assessed at different positions

5.4 Fluid dynamics for double-clearance rim seals with different stator-side features

This section describes experimental measurements of pressure and swirl ratio for double-clearance rim seals with different stator-side features, including seal configuration DS-0 (baseline), DS-1, DS-2 and DS-3. Experiments were conducted at $Re_\phi = 7.9 \times 10^5$ for the on-design condition and with different levels of sealing flow rate.

5.4.1 Variation of swirl ratio in the wheel-space

Figure 5.14 shows the radial variation of the swirl ratio β for DS-0 and DS-1, with three different levels of sealing flow rate denoted by Φ_0/Φ_{min}; the corresponding values of the turbulent flow parameter λ_T are also labelled in the figure. The swirl β is shown to decrease with increasing sealing flow rate for all radii. There is an excellent agreement in β between DS-0 and DS-1 for both wheel-spaces, indicating similar fluid dynamics for the two seal configurations. The swirl velocity is also shown to be insensitive to the outer wheel-space height.

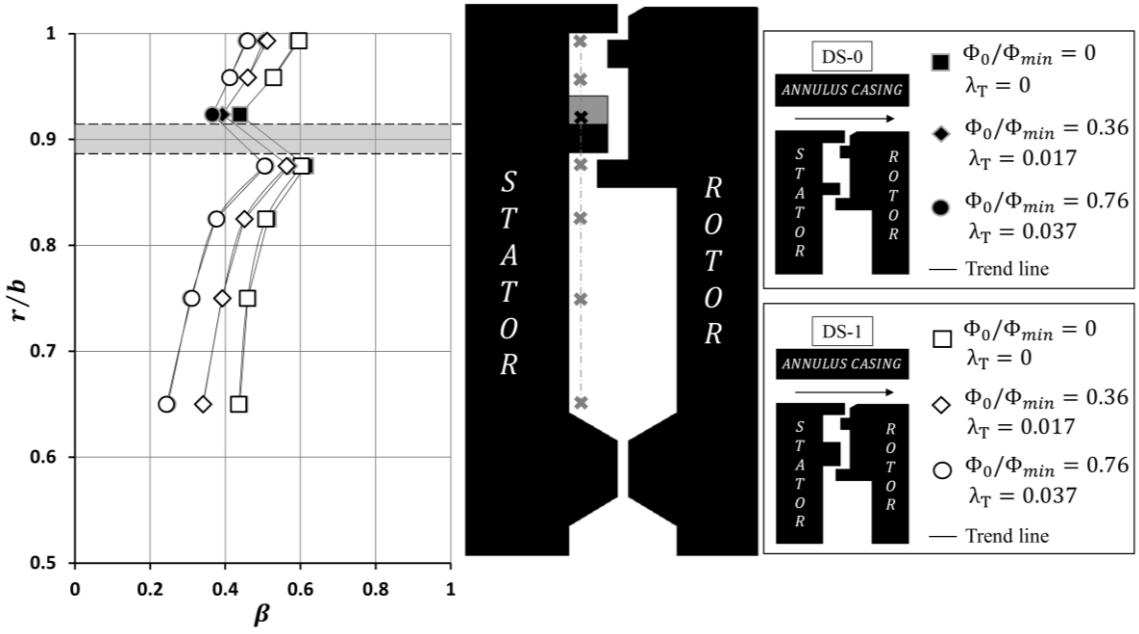

Figure 5.14 Radial variation of swirl ratio for seal configuration DS-0 and DS-1

Figure 5.15 (a) shows the radial variation of the swirl ratio β for DS-0, DS-2 and DS-3, with two different levels of sealing flow rate denoted by Φ_0/Φ_{min}; the corresponding values of the turbulent flow parameter λ_T are also labelled in the figure. For the inner wheel-space, β for the three seals agree well for each λ_T. The swirl ratio is shown to be predominantly governed by λ_T, despite the

difference in ε_c. This suggests a flow structure featuring a rotating core between boundary layers on the stator and rotor surfaces, as previously discussed in section 5.2. The increase in Φ_0 results in a reduction in β, indicating the rotating core of fluid being suppressed gradually.

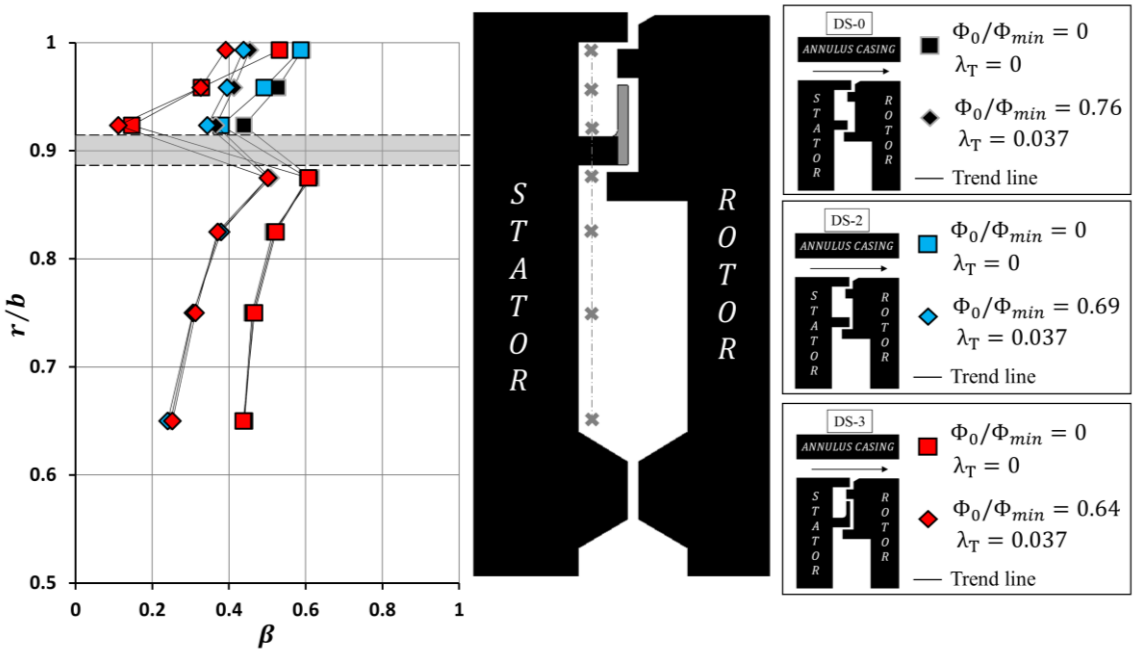

(a) Radial variation of swirl ratio for seal configuration DS-0, DS-2 and DS-3

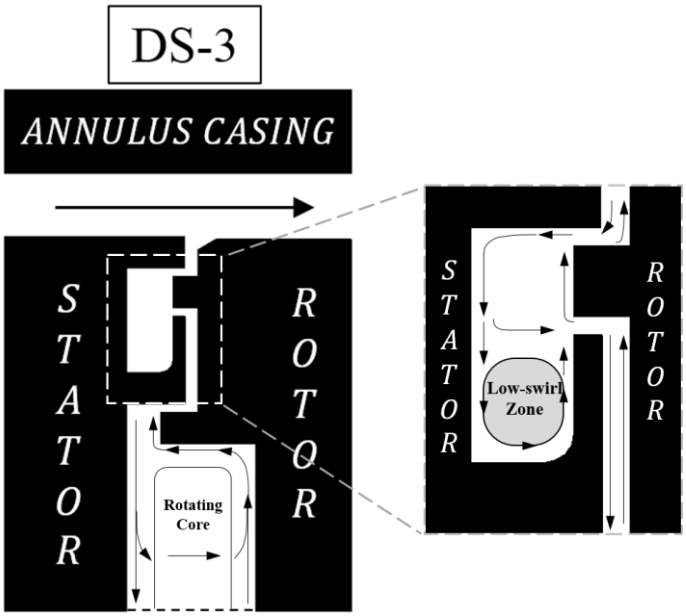

(b) Schematic diagram of the flow in the outer wheel-space of DS-3

Figure 5.15 Radial variations of swirl ratio for seal configuration DS-0, DS-2 and DS-3

In the outer wheel-space, β for DS-2 is shown to be slightly lower relative to the baseline, especially in the region close to the stationary inner-seal component. The β for DS-3 is shown to be

significantly lower relative to the datum configuration in the space between the stator surface and the angel-wing feature; within this region β is shown to be almost independent of λ_T. It is anticipated that there is a limited interaction between the sealing flow and the low-swirl fluid within the region. Figure 5.15 (b) illustrates a simplified flow pattern in the outer wheel-space of DS-3, conjectured based on the experimental measurements.

5.4.2 Variation of pressure in the wheel-space

Figure 5.16 shows the radial variation of the pressure coefficient in the inner wheel-space, $C_{p,in}$, for DS-0, DS-2 and DS-3. The definition of $C_{p,in}$ has been given in section 5.2; this parameter indicates the radial pressure gradient in the inner wheel-space. Static pressure measurements were made on the stator surface, with three different levels of sealing flow rate denoted by Φ_0/Φ_{min}; the corresponding values of the turbulent flow parameter λ_T are also labelled in the figure.

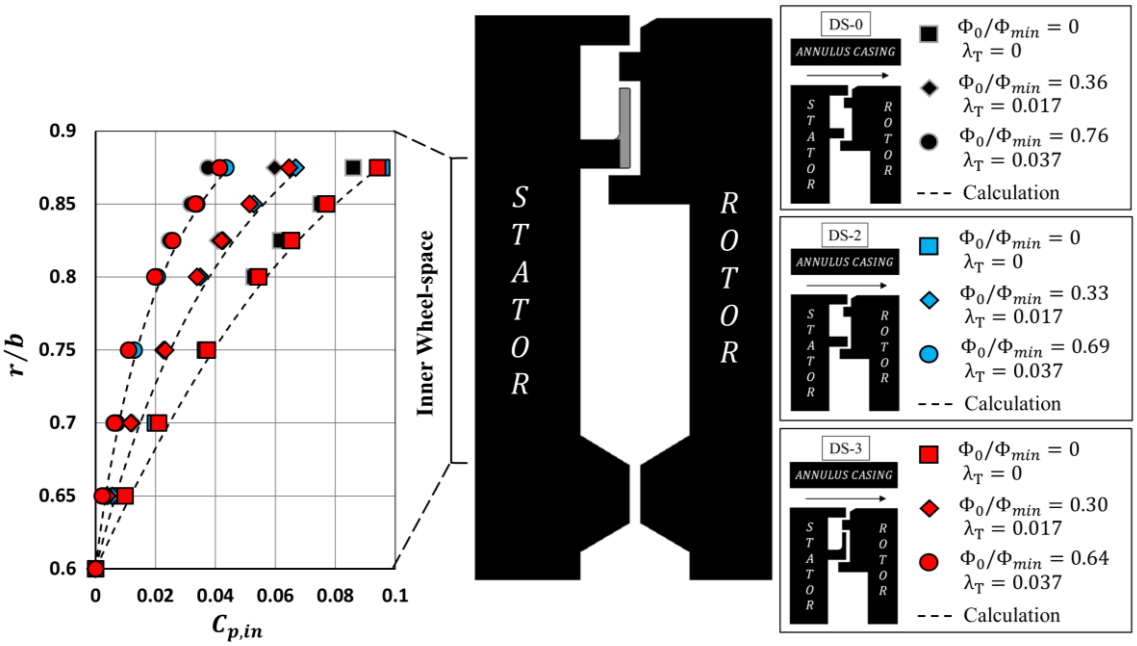

Figure 5.16 Variation of pressure for the inner wheel-space of DS-0, DS-2 and DS-3

The $C_{p,in}$ for DS-2 and DS-3 both agree with that for the datum configuration DS-0. In connection with the measurements of swirl ratio, the radial variation of $C_{p,in}$ was calculated using Eq. (4.10) introduced in the previous chapter. For each seal, there is a good agreement between the measurements and the calculated $C_{p,in}$; the pressure gradient is shown to be determined by the swirl ratio in the inner wheel-space, which is governed by λ_T.

Figure 5.17 shows the radial variation of the pressure coefficient in the outer wheel-space, $C_{p,out}$, for DS-2 and DS-3 in comparison with DS-0. The definition of $C_{p,out}$ has been given in section 5.2; this parameter indicates the radial pressure gradient in the outer wheel-space. Static pressure measurements were made on the stator surface for two different levels of sealing flow rate shown in (a) and (b) respectively.

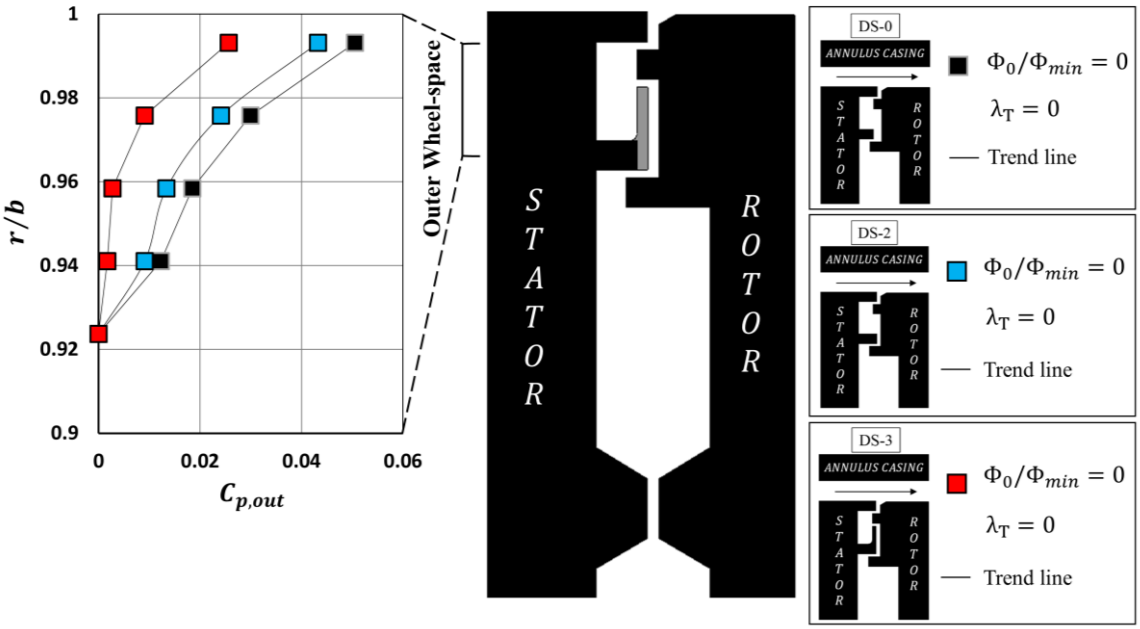

(a) For $\lambda_T = 0$

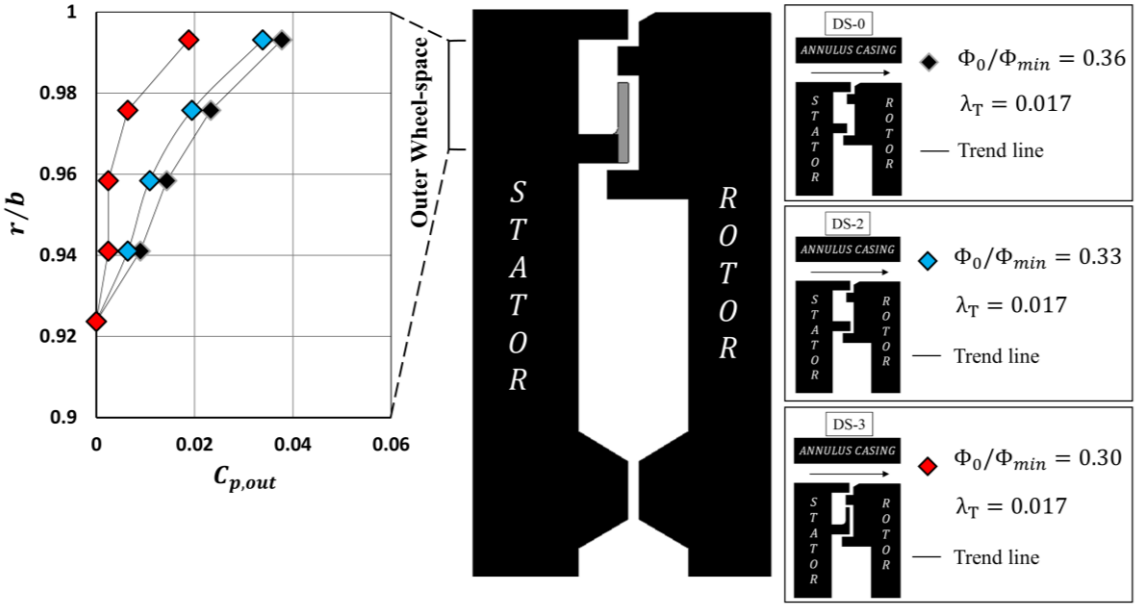

(b) For $\lambda_T = 0.017$

Figure 5.17 Variation of pressure for the outer wheel-space of DS-0, DS-2 and DS-3

For each sealing flow rate, $C_{p,out}$ for DS-2 is shown to be slightly lower relative to the baseline; the $C_{p,out}$ for DS-3 is seen to be significantly lower relative to DS-0 and DS-2. In connection with the swirl ratio shown in Figure 5.15, the ranking of pressure gradient corresponds to the ranking of swirl ratio in the outer wheel-space among these seal configurations.

Relative to the datum, the variation of stationary seal components creates different swirl distributions, which may result in an unique pressure distribution (gradient) for a specific seal such as DS-3. A higher level of β corresponds to a higher level of $C_{p,out}$; this may be attributed to the radial equilibrium between the centrifugal force of the swirling fluid and the radial pressure gradient in the outer wheel-space.

5.5 Summary

This chapter describes a parametric study on generic, but engine-representative double-clearance rim seals with different stator-side features. This study investigates sealing effectiveness and fluid dynamics of ingress associated with these rim-seal features, in comparison with a datum double-clearance seal. Experimental measurements of gas concentration, pressure and swirl velocities were conducted to assess the relative performance of each double-clearance rim seal.

A comparison in seal performance and fluid dynamics is shown between the baseline single-clearance seal and the datum double-clearance seal. The latter significantly improves the effectiveness inboard of the inner seal by confining ingress outboard, in line with expectation. The swirl and pressure inboard of the inner seal is governed by the turbulent flow parameter, consistent with the single-clearance seal.

Experimental measurements for different stationary seal features are shown relative to the baseline configuration. The sealing effectiveness and swirl ratio for both the inner and outer wheel-spaces are insensitive to the height of outer wheel-space within the scope of this study. The 'angel-wing' seal is shown to significantly reduce ingress into the inner wheel-space, but decrease the effectiveness in the outer wheel-space. A decrease in swirl is also seen resulting from the angel-wing arrangement.

Figure 5.18 demonstrates the ranking of ε_c in both wheel-spaces for all double-clearance seal configurations studied in this chapter. The ε_c is evaluated at $\Phi_0 = 0.008$, corresponding to a sealing effectiveness of $\varepsilon_c = 0.95$ for the inner wheel-space of DS-0. The relative performance of each seal configuration, discussed in previous sections of this chapter, is summarised in the figure.

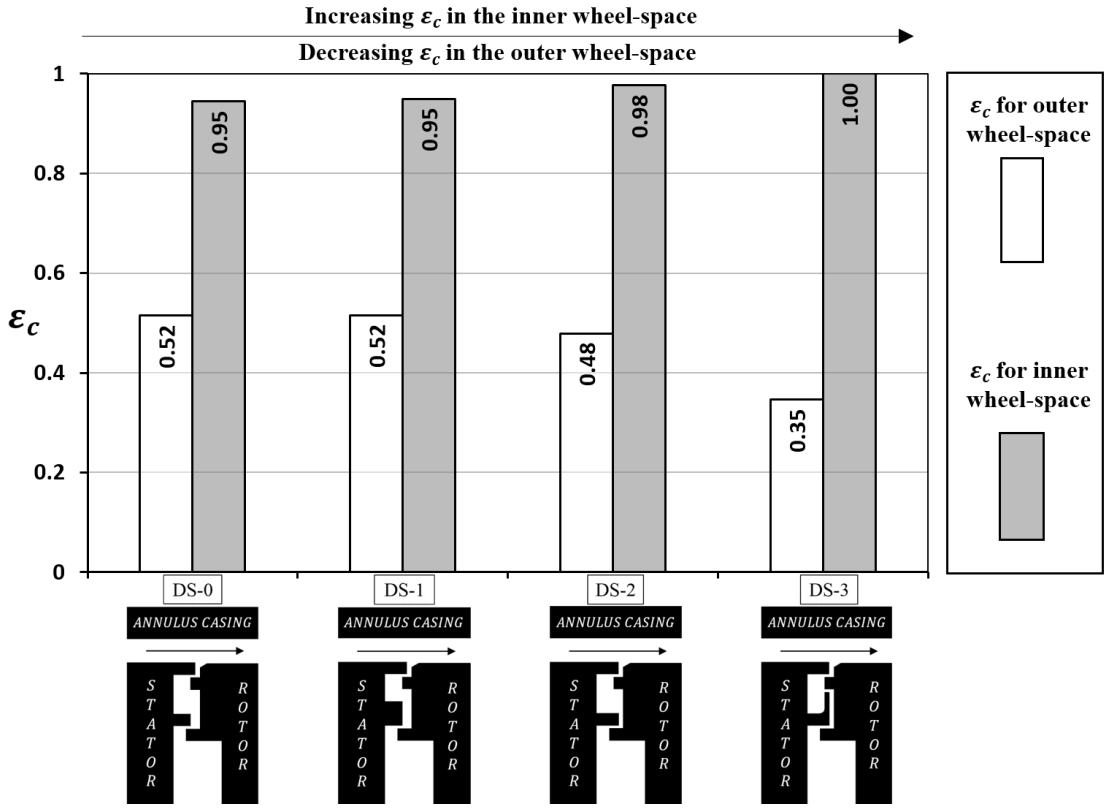

Figure 5.18 Ranking of sealing effectiveness for double-clearance seals with different stator-side features at $\Phi_0 = 0.008$

The parameter for the minimum seal flow Φ_{min} and ratio of discharge coefficients Γ_c are evaluated by a statistical fitting (Zhou *et al*. (2013)) of the theoretical model (Owen (2011)) to the measurements. The excellent agreement between the model and measurements for each rim-seal configuration is shown in previous sections of this chapter. The Φ_{min} and Γ_c for all the seal configurations are tabulated in Table 5.2, which can be exploited to support the design methodology of Siemens gas turbines.

Table 5.2 Φ_{min} and Γ_c for all rim-seal configurations studied in this chapter

Seal configuration		$\boldsymbol{\Phi_{min}}$	$\boldsymbol{\Gamma_c}$ $(C_{d,i}/C_{d,e})$
SR		0.0489	0.379
DS-0	**Inner** wheel-space	0.0132	0.240
	Outer wheel-space	0.0522	0.349
DS-1	**Inner** wheel-space	0.0142	0.280
	Outer wheel-space	0.0529	0.340
DS-2	**Inner** wheel-space	0.0103	0.170
	Outer wheel-space	0.0553	0.387
DS-3	**Inner** wheel-space	0.00602	0.267
	Outer wheel-space	0.0587	1.06

The Γ_c is an empirical parameter that accounts for viscous losses in the theoretical orifice model. The value of Γ_c for each seal, determined from the model fitted to the measurements, could be used to indicate the performance of that seal. For different seal configurations with similar values of Φ_{min}, a relatively lower value of Γ_c often corresponds to a higher sealing effectiveness at a given Φ_0.

For the inner wheel-space, β is shown to be predominantly governed by λ_T, irrespective of different levels of ε_c for different seal configurations. This suggests a flow structure featuring separate boundary layers on the stator and rotor surfaces, which are governed by λ_T; a rotating core of fluid exists between the boundary layers in line with the Batchelor flow mode. The pressure distribution is shown to be determined by the swirl ratio and also dominated by λ_T.

For the outer wheel-space, the variation of stator-side seal features creates different swirl distributions, which may result in an unique pressure distribution (gradient) for a specific seal such as DS-3. A higher level of swirl corresponds to a higher level of pressure gradient; this may be attributed to the radial equilibrium between the centrifugal force of the swirling fluid and the radial pressure gradient in the outer wheel-space.

The sealing effectiveness and fluid dynamics for all the tested double-clearance seals are correlated qualitatively, which will be described in Chapter 7.

Chapter 6 Study of double-clearance rim seals with different rotor-side features

This chapter describes a parametric study on generic, but engine-representative double-clearance rim seals with different rotor-side features. This study investigates sealing effectiveness and fluid dynamics of ingress associated with these rotor-side features, in comparison with a datum double-clearance seal. Experimental measurements of gas concentration, pressure and swirl velocities were conducted to assess the relative performance of each double-clearance rim seal. The ranking of sealing effectiveness is shown. This study is aimed to achieve an improved understanding of how double-clearance rim seals with various rotor-side features operate, and provide insights into the fluid dynamics of ingestion.

Section 6.1 introduces the geometries of double-clearance rim-seal configurations with different rotor-side features. Section 6.2 reports the experimental measurements of sealing effectiveness for each rim-seal configuration in comparison with the datum seal. Section 6.3 describes the evaluation of fluid dynamics in the wheel-space by measurements of pressure and swirl velocities in the wheel-space. Section 6.4 concludes this chapter with a ranking of seal performance.

6.1 Rim-seal configurations

The datum double-clearance seal configuration DS-0 has been described explicitly in section 5.1. The comparison in sealing effectiveness and fluid dynamics, between a baseline single-clearance seal SR and the configuration DS-0, has been reported in section 5.2.

Figure 6.1 shows three double-clearance seal configurations, all of which are equipped with radial-fin features on the rotor side, as illustrated in (a). Geometric properties under static condition are stated in Table 6.1. The radial fins are evenly distributed circumferentially on the rotor surface, dividing the rotor-side space into multiple smaller pockets outboard of the inner seal. Different numbers of radial fins were included: seal configuration FS-19, FS-37 and FS-73 are characterised by 19, 37 and 73 rotor-side fins respectively. There is a consistency of stator-side components between the datum seal DS-0 and these finned seals.

The different seal configurations were created by applying modular attachments to the turbine rotor, as illustrated in Figure 6.1. The stationary inner-seal component was attached directly onto the stator surface; and the rotor-side component with the radial fins incorporated was bolted under the rotor platform. For geometric features shared by these seals, such as the outer-seal axial clearance $s_{c,ax}$,

the repeatability and consistency were successfully maintained among different configurations due to the high-precision alignment system.

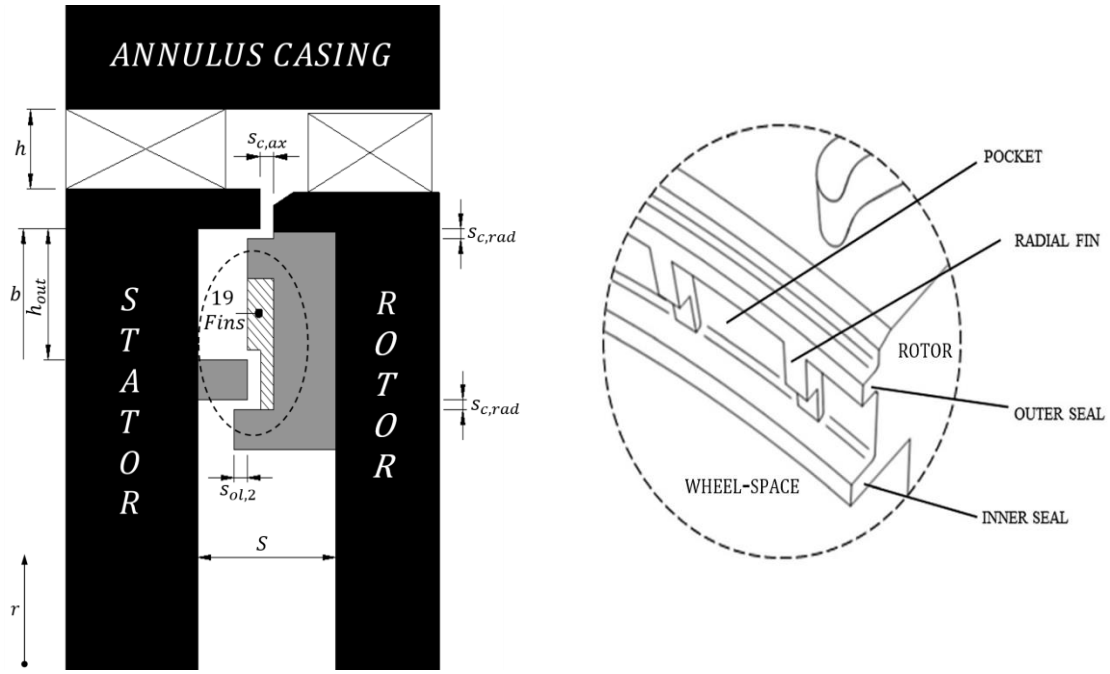

(a) FS-19

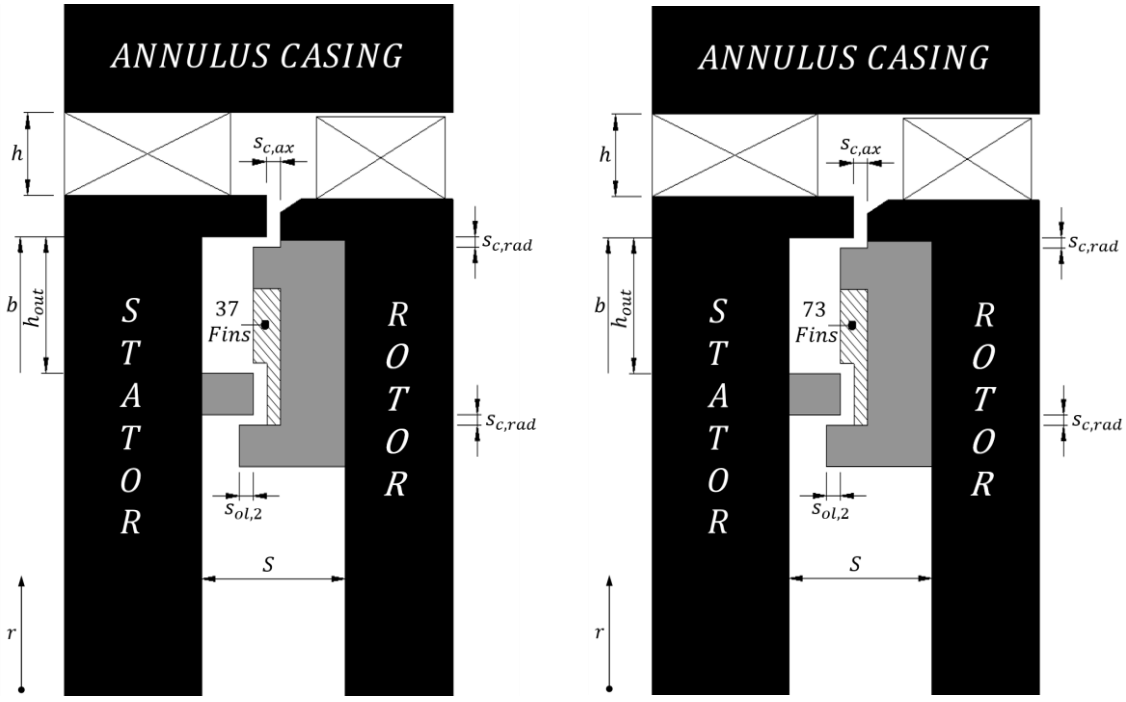

(b) FS-37 (c) FS-73

Figure 6.1 Double-clearance seal configurations with different rotor-side features

Table 6.1 Geometric properties for double-clearance seals with different rotor-side features (Dimensions in mm under static condition)

Geometric symbol	Seal configuration			
	DS-0	**FS-19**	**FS-37**	**FS-73**
h	10.0			
b	190			
S	20.0			
$s_{c,ax}$	2.00			
$s_{c,rad}$	1.28			
$s_{ol,1}$	1.86			
$s_{ol,2}$	1.86			
h_{out}	16.5			
No. of fins	—	19	37	73

6.2 Sealing effectiveness for double-clearance seals with different rotor-side features

This section presents the sealing effectiveness for double-clearance rim seals with different rotor-side features, including seal configuration DS-0 (baseline), FS-19, FS-37 and FS-73. Geometries of these seals have been given in section 6.1. CO_2 gas concentration measurement was conducted to determine the sealing effectiveness, and the relative performance of each seal is shown.

6.2.1 Seal configuration FS-73 relative to DS-0: effect of the rotor-side radial fins

This section describes the sealing effectiveness for seal configuration FS-73 in comparison with the baseline seal DS-0. The rotor-side component of FS-73 features 73 radial fins, while no such fins were included for the datum seal. Axial overlaps and radial clearances remain consistent between the two seal configurations.

Figure 6.2 shows the radial variation of sealing effectiveness ε_c for DS-0 and FS-73, determined with CO_2 concentration measurements on the stator surface. The ε_c is plotted versus the non-dimensional radius (r/b) between 0.55 and 0.993. Gas concentration measurements were made at $Re_\phi = 7.9 \times 10^5$ and at the on-design condition ($C_F = 0.38$), for three different levels of sealing flow rate (Φ_0). At the same level of Φ_0, the ε_c for the outer wheel-space of FS-73 is shown to be significantly higher relative to the baseline; there is little difference for the inner wheel-space. The addition of the fins enhances the outer-seal effectiveness.

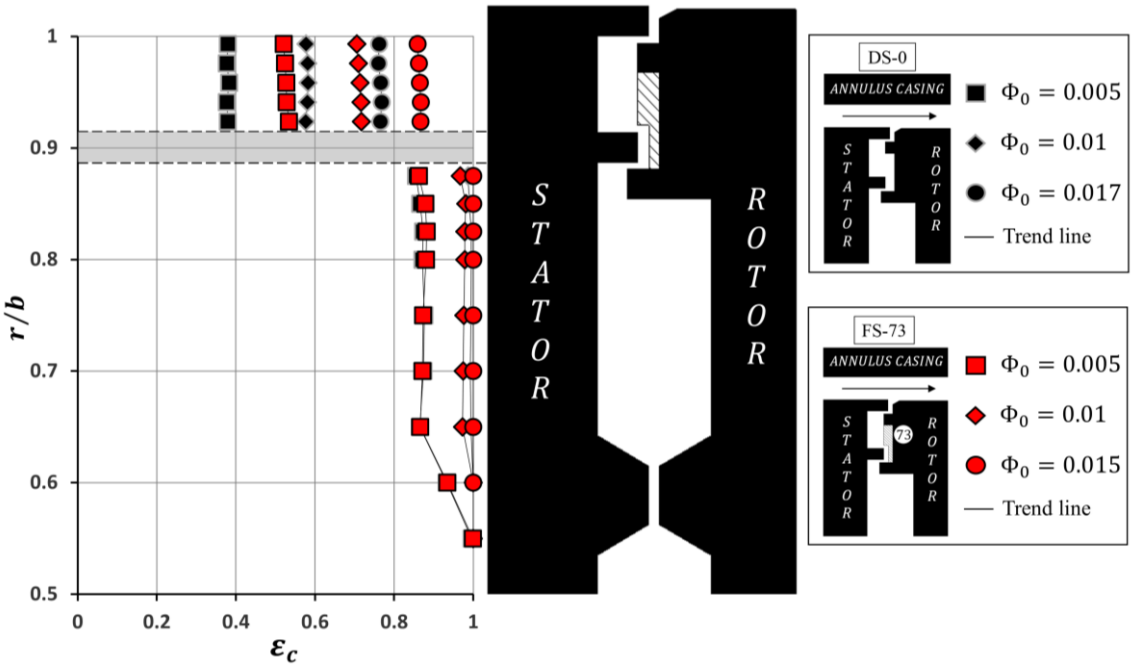

Figure 6.2 Radial variation of ε_c for seal configuration DS-0 and FS-73

Figure 6.3 shows the above trend for FS-73 is valid over the complete range of Φ_0. The concentration measurements were made at $r/b = 0.958$ for the outer wheel-space and $r/b = 0.85$ for the inner wheel-space. The experiment was conducted for the on-design condition at $Re_\phi = 5.3 \times 10^5$ and $Re_\phi = 7.9 \times 10^5$. The variation of ε_c with Φ_0 is shown to be independent of Re_ϕ.

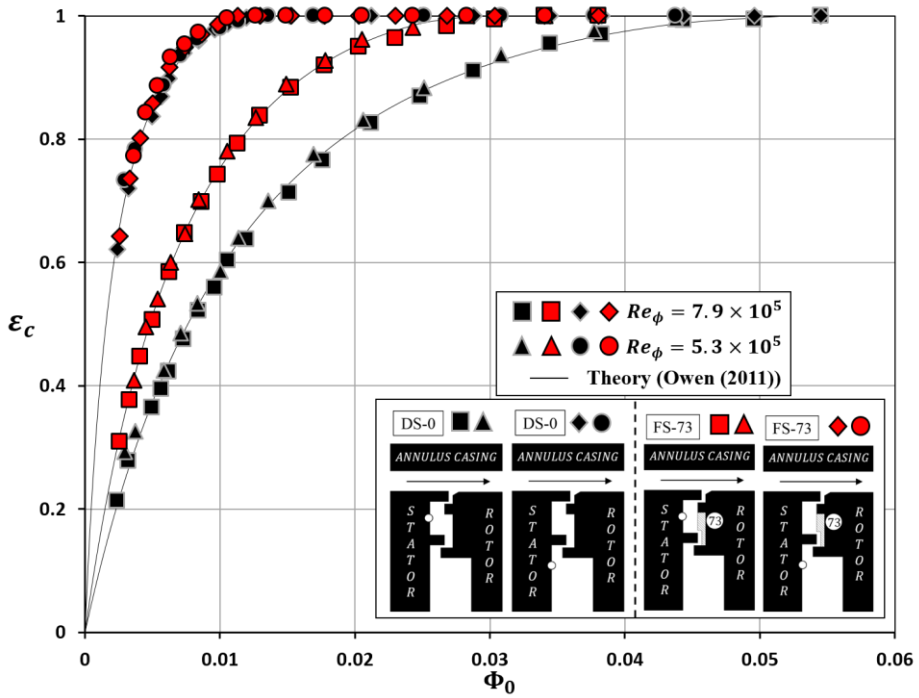

Figure 6.3 Variation of ε_c with Φ_0 for seal configuration DS-0 and FS-73

Over the complete range of Φ_0, ε_c is seen to be significantly higher in the outer wheel-space of FS-73 compared with DS-0. The experimental data was compared with the theoretical model described by Owen (2011) in conjunction with a statistical fitting method described by Zhou *et al*. (2013). There is a very good agreement between the experimental data and the theoretical curves for FS-73. The minimum sealing flow rate Φ_{min} and the ratio of discharge coefficients Γ_c ($\Gamma_c = C_{d,i}/C_{d,e}$) for FS-73 were optimised by the fitting, and the values are summarised in section 6.4.

The increase in ε_c for the outer wheel-space of FS-73 may be associated with the fluid dynamics resulting from the rotating fin features. More discussion will be made in section 6.3, supported by the measurements of pressure and swirl velocities.

6.2.2 Seal configuration FS-19, FS-37 and FS-73: effect of the number of rotor-side fins

This section describes the sealing effectiveness for seal configuration FS-19, FS-37 and FS-73. The study was aimed to reveal the effect of the number of rotor-side fins in the outer wheel-space. Axial overlaps and radial clearances remain consistent between these seal configurations. Figure 6.4 shows the radial variation of sealing effectiveness ε_c for the three finned seal configurations. The ε_c was plotted versus the non-dimensional radius (r/b) between 0.55 and 0.993. Gas concentration measurements were made at $Re_\phi = 7.9 \times 10^5$ and at the on-design condition ($C_F = 0.38$), for two different levels of Φ_0. For each Φ_0, ε_c in the outer wheel-space is shown to increase with increasing number of rotor-side fins. For the inner wheel-space, the ε_c for FS-37 and FS-73 virtually agree; the ε_c for FS-19 is relatively lower.

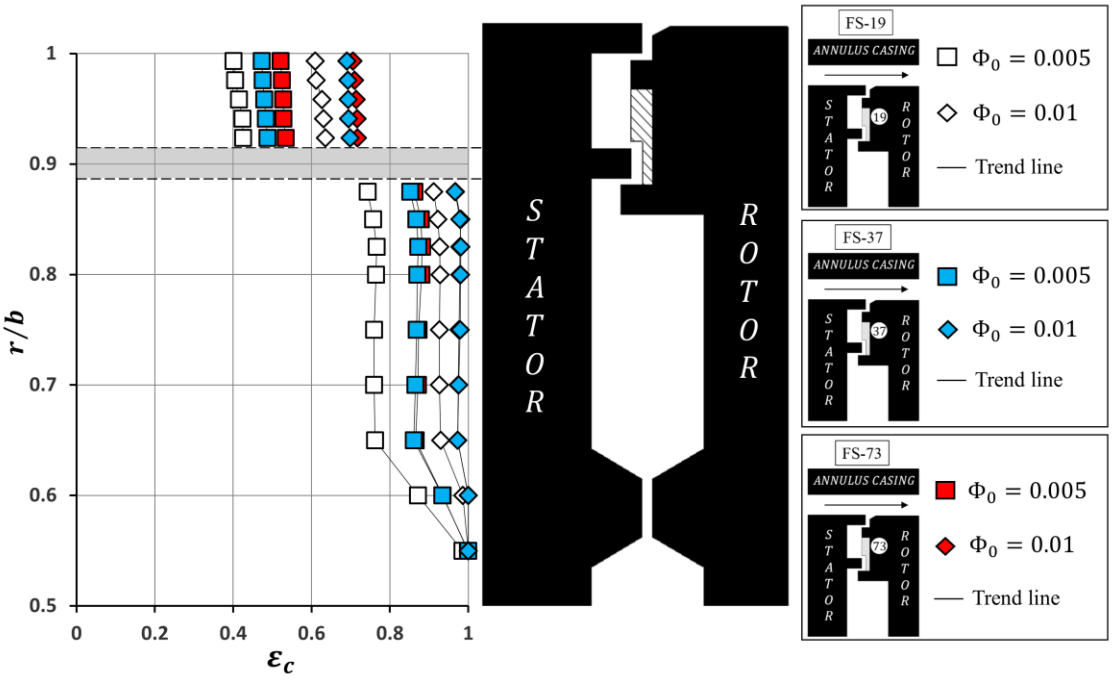

Figure 6.4 Radial variation of ε_c for FS-19, FS-37 and FS-73

Figure 6.5 shows the variation of ε_c with Φ_0 in the outer wheel-space for FS-19, FS-37 and FS-73 in comparison with the baseline seal DS-0. Gas concentration measurement was made at $r/b = 0.958$ for the outer wheel-space, for the on-design condition at $Re_\phi = 5.3 \times 10^5$ and $Re_\phi = 7.9 \times 10^5$. Figure 6.6 shows the variation of ε_c with Φ_0 in the inner wheel-space for these four seal configurations. Gas concentration measurement was made at $r/b = 0.85$ for the inner wheel-space.

The variation of ε_c with Φ_0 is independent of Re_ϕ. It is shown once again that there is a good agreement between the experimental data and the theoretical curves for both wheel-spaces. The Φ_{min} and Γ_c for FS-37 and FS-19 were optimised by the fitting, and the values are summarised in section 6.4.

For the outer wheel-space, all the finned seals feature higher values of ε_c relative to the datum seal and ε_c increases with increasing number of rotor-side fins, over the complete range of Φ_0. For the inner wheel-space, ε_c for FS-37 and FS-73 broadly agree with DS-0; however, ε_c for FS-19 is shown to be lower relative to DS-0 and the other two finned seals. A possible explanation for the behaviour of FS-19 shall be discussed based on pressure measurements in section 6.3.

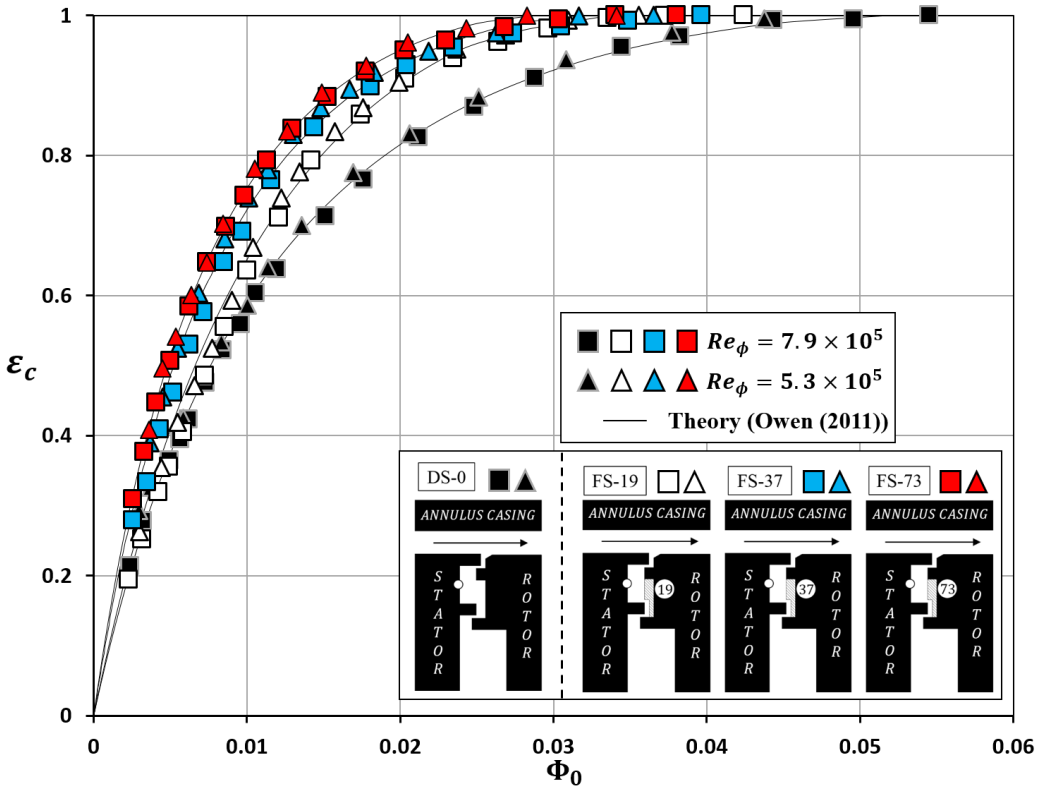

Figure 6.5 Variation of ε_c with Φ_0 for the outer wheel-space of finned seals

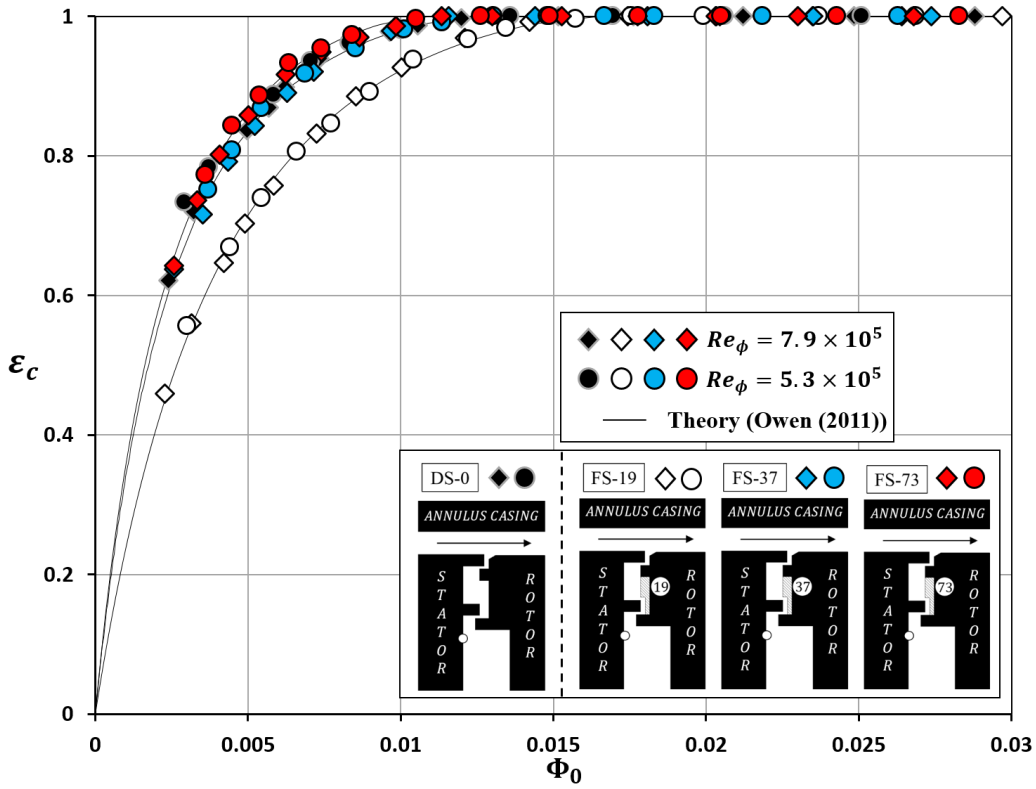

Figure 6.6 Variation of ε_c with Φ_0 for the inner wheel-space of finned seals

6.3 Fluid dynamics for double-clearance rim seals with different rotor-side features

This section describes experimental measurements of pressure and swirl ratio for double-clearance rim seals with different rotor-side features, including seal configuration DS-0 (baseline), FS-19, FS-37 and FS-73. Experiments were conducted at $Re_\phi = 7.9 \times 10^5$ for the on-design condition and with different levels of sealing flow rate.

6.3.1 Variation of swirl ratio in the wheel-space

Figure 6.7 shows the radial variation of the swirl ratio β for DS-0 and FS-73, with three levels of sealing flow rate denoted by Φ_0/Φ_{min}; the corresponding values of the turbulent flow parameter λ_T are also labelled in the figure. In the outer wheel-space, β for FS-73 is shown to be significantly higher than the datum seal. The addition of radial fins enhances the swirl velocity significantly, and probably results in a solid-body rotation of fluid in the outer wheel-space (variation of β insensitive to λ_T). The increase in sealing effectiveness for FS-73, as shown in Figure 6.2, could be attributed to the enhanced swirling motion, which improves the circumferential mixing and decreases the driving potential for EI ingress in the rim-seal region. Although the rotating fins enhance the disc

pumping of fluid and increase the RI ingress, the improved mixing significantly reduces the EI ingress; the net results are shown to be the increase in sealing effectiveness because the seal operates in an EI dominated ingress regime (shown in Chapter 4). For the inner wheel-space, β is shown to be predominantly governed by λ_T. Figure 6.8 shows the radial variation of β for the three finned-seal configurations, with two levels of sealing flow rate, denoted by Φ_0/Φ_{min} and λ_T. The swirl in the outer wheel-space is shown to increase with a greater number of radial fins on the rotor side.

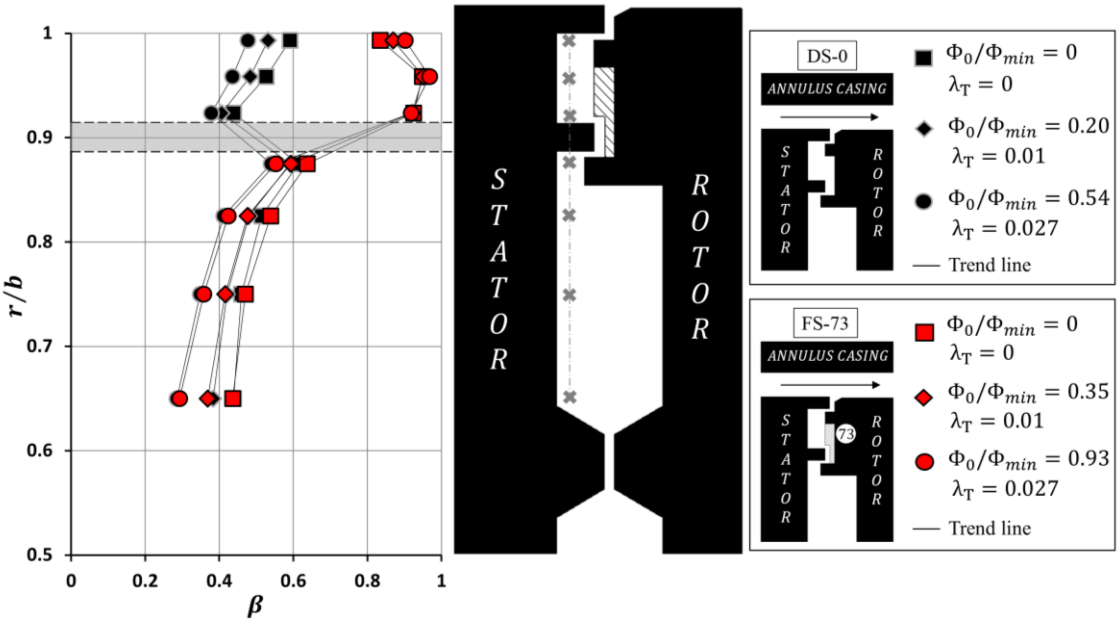

Figure 6.7 Radial variation of swirl ratio for seal configuration DS-0 and FS-73

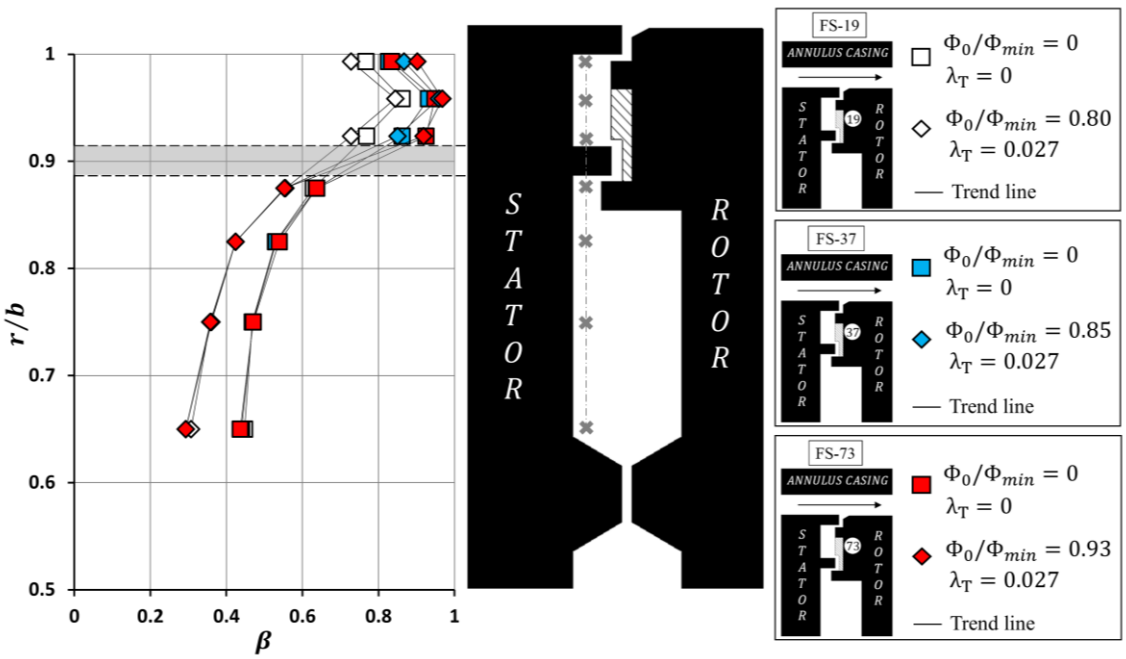

Figure 6.8 Radial variation of swirl ratio for seal configuration FS-19, FS-37 and FS-73

6.3.2 Variation of pressure in the wheel-space

Figure 6.9 shows the radial variation of the pressure coefficient in the inner wheel-space, $C_{p,in}$, for DS-0 and FS-73. The definition of $C_{p,in}$ has been given in section 5.2; this parameter indicates the radial pressure gradient in the inner wheel-space. Static pressure measurements were made on the stator surface, with two levels of sealing flow rate denoted by $\Phi_0/\Phi_{\min}$; the corresponding values of the turbulent flow parameter λ_T are also labelled in the figure.

The $C_{p,in}$ for FS-73 and DS-0 agrees with each λ_T. In connection with the swirl ratio, the radial variation of $C_{p,in}$ was calculated using Eq. (4.10). For each seal, there is a good agreement between the measurements and the calculated $C_{p,in}$; the pressure gradient is determined by the swirl ratio in the inner wheel-space, which is governed by λ_T.

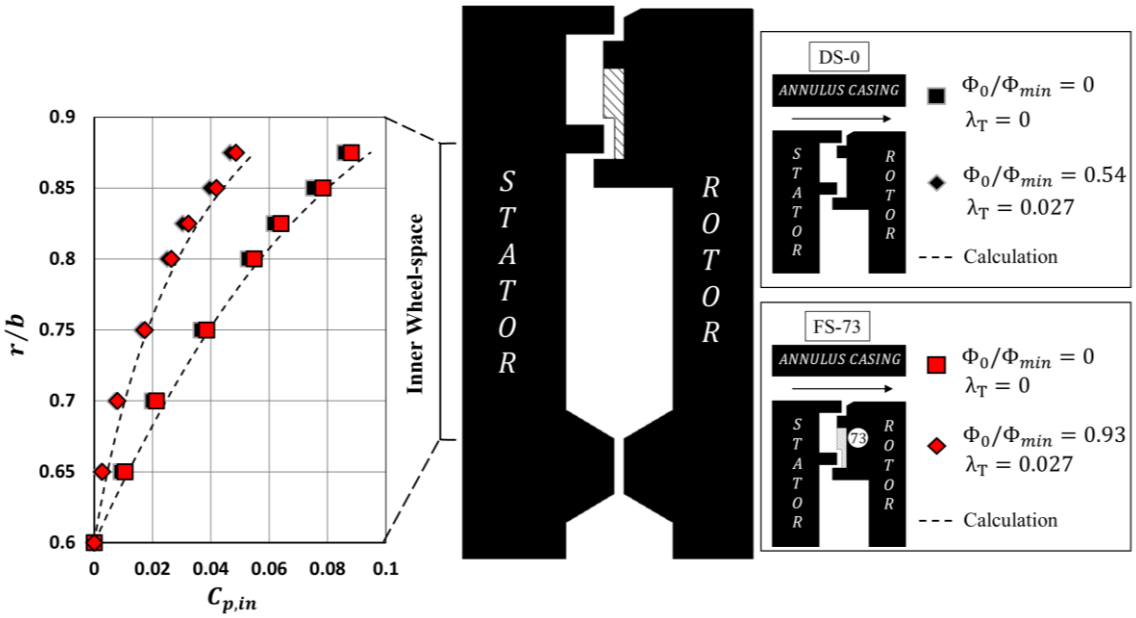

Figure 6.9 Variation of pressure for the inner wheel-space of DS-0 and FS-73

Figure 6.10 shows the radial variation of the pressure coefficient in the outer wheel-space, $C_{p,out}$, for FS-73 and DS-0. The definition of $C_{p,out}$ has been given in section 5.2; this parameter indicates the radial pressure gradient in the outer wheel-space. Figure 6.11 shows the $C_{p,out}$ for all three finned-seal configurations.

For each sealing flow rate, $C_{p,out}$ for FS-73 is shown to be significantly higher relative to the baseline. Among the finned seals, $C_{p,out}$ is seen to be higher for a greater number of fins. In connection with the swirl ratio shown in Figure 6.8, the ranking of pressure gradient corresponds to the ranking of swirl ratio in the outer wheel-space. Relative to the datum seal, the addition of the rotor-side fins

promotes the swirl velocity, which probably leads to an increase in the pressure gradient in the outer wheel-space to satisfy the radial equilibrium of forces.

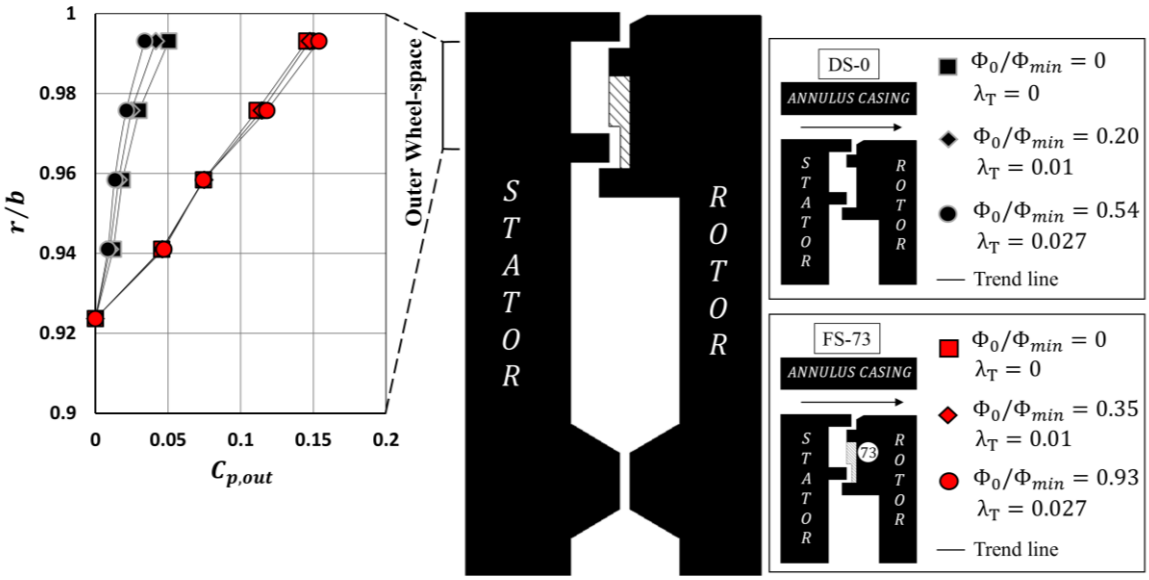

Figure 6.10 Variation of pressure for the outer wheel-space of DS-0 and FS-73

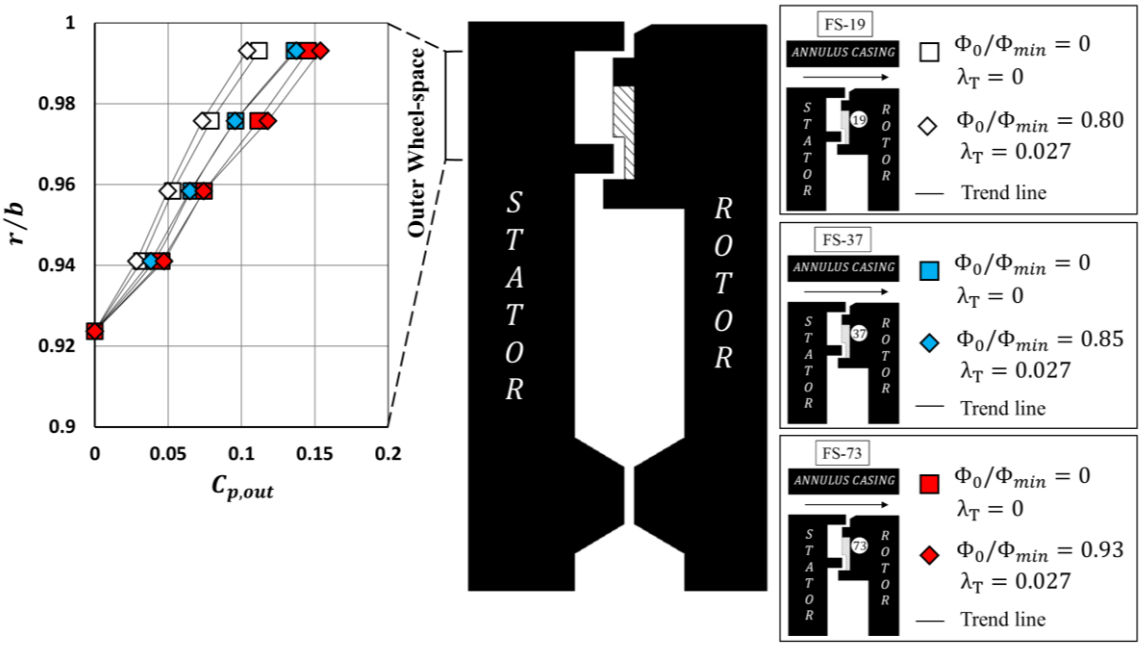

Figure 6.11 Variation of pressure for the outer wheel-space of the finned-seal configurations

6.3.3 An analysis of FS-19 based on the measurements of unsteady pressure

For the inner wheel-space, it has been shown in section 6.2 that the ε_c for FS-19 is lower relative to DS-0 and the other two finned seals, while ε_c for FS-37 and FS-73 broadly agree with DS-0. The uniqueness of FS-19 may be associated with the flow dynamics near the inner-seal, supported by unsteady pressure measurements documented in this section.

In addition to the evaluation of time-averaged pressure, measurements of unsteady pressure were also conducted in the outer wheel-space, to investigate the effect of rotating blades and radial fins on sealing effectiveness. A Kulite® XT fast-response pressure probe was employed to assess the time-dependent pressure variation on the stator surface at a radius of $r/b = 0.973$. The unsteady pressure measurements were made at $Re_\phi = 5.3 \times 10^5$ with $\lambda_T = 0.01$.

The target frequencies, including the blade-passing frequency and the fin-passing frequency for the finned seals, are listed in Table 6.2. The effective range of frequency response and the sampling rate used for the measurements are also shown. It should be noted that the sampling was set as 20 kHz, ensuring an appropriate resolution for the pressure data in every cycle of variation.

Table 6.2 Frequencies for unsteady pressure measurements in the outer wheel-space

Frequency	**Seal configuration**			
	DS-0	**FS-19**	**FS-37**	**FS-73**
Disc rotation (Hz)	33.3			
Blade-passing (Hz)	1366.7			
Fin-passing (Hz)	—	633.3	1233.3	2433.3
Range of frequency response for the transducer (kHz)	$0 - 175$			
Sampling rate (kHz)	20			

Figure 6.12 shows the frequency spectrum of unsteady pressure taken in the outer wheel-space of (a) FS-19, (b) FS-37 and (c) DS-0. For each seal configuration, there is no corresponding spike for the blade-passing frequency expected at 41 times the rotational frequency. For seal configuration FS-19, a frequency spike is seen at 19 times the rotational frequency, corresponding to the fin-passing frequency. Different from FS-19, the measurement for FS-37 does not show the fin-passing frequency (a similar result was acquired for FS-73 and thus not included in the figure).

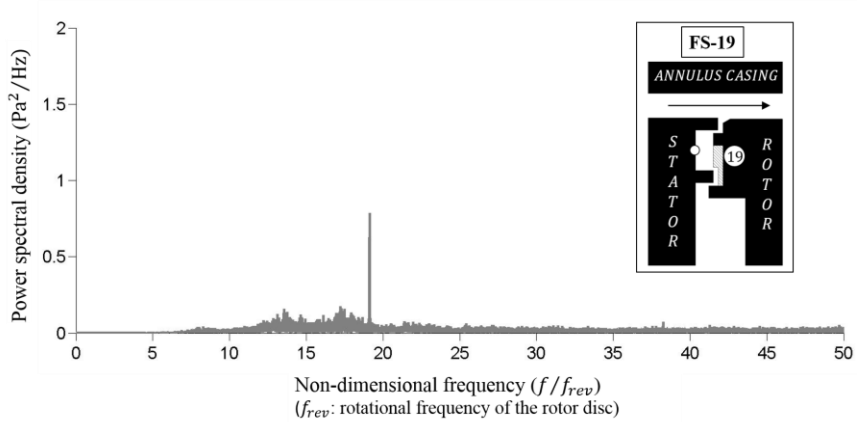

(a) Frequency spectrum for FS-19

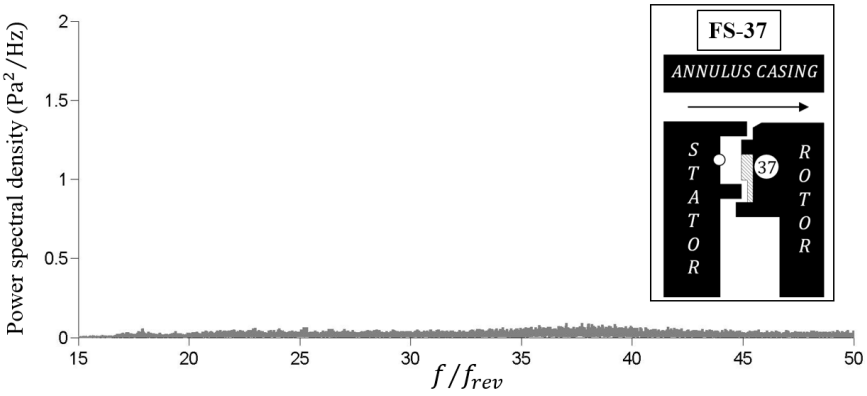

(b) Frequency spectrum for FS-37

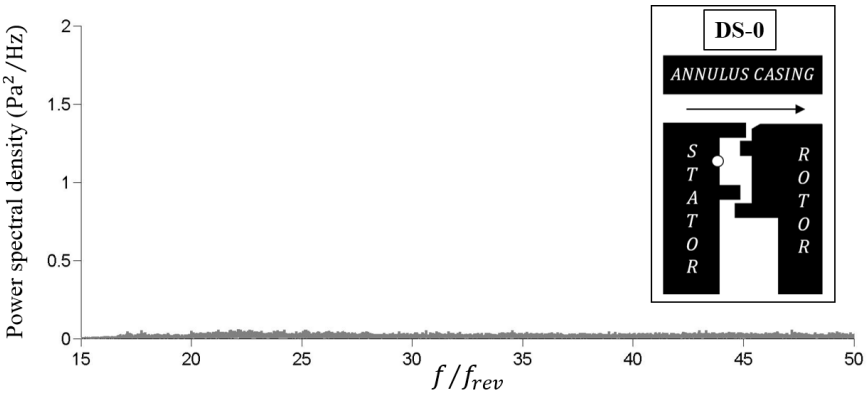

(c) Frequency spectrum for DS-0

Figure 6.12 Frequency spectrum of unsteady pressure measured in the outer wheel-space of FS-19, FS-37 and DS-0

The time-dependent variation of pressure is shown in Figure 6.13 for the three seals respectively. The percent variation in pressure is plotted versus the angle of rotation. In the range between 0° and 90°, $4\frac{3}{4}$ cycles of variation are identified for FS-19, which corresponds to 4.75 fins passing by the pressure probe in a quarter of revolution. For the other seals, no cyclic variation is seen and the

pressure in the outer wheel-space is shown to be virtually invariant with time. The non-axisymmetric unsteady pressure variation in the outer wheel-space, though not significant in amplitude, may increase the amount of ingress through the inner seal of FS-19.

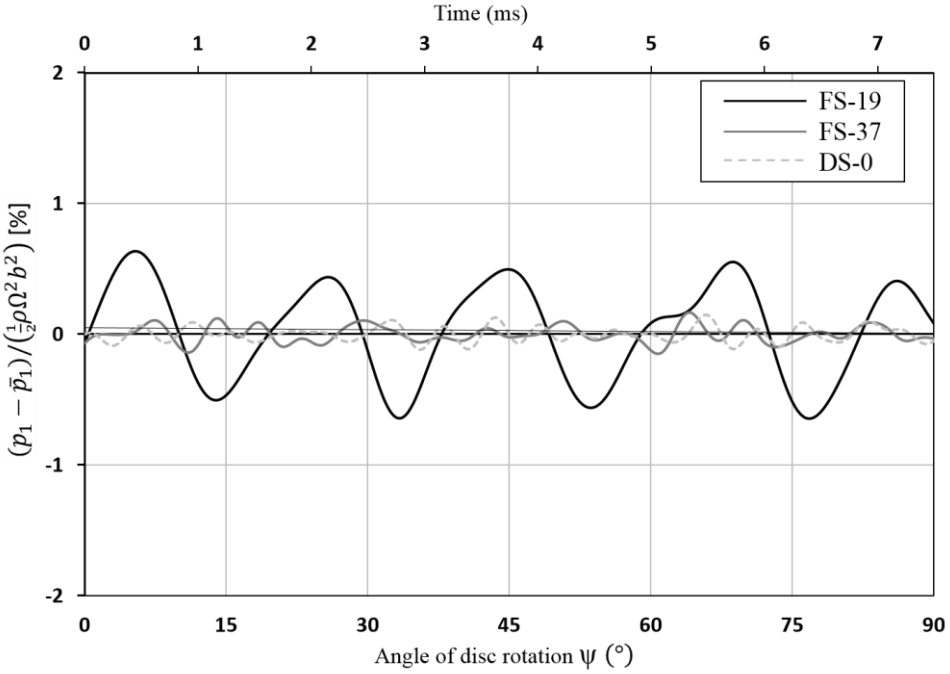

Figure 6.13 Time-dependent variation of unsteady pressure in the outer wheel-space

6.4 Summary

This chapter describes a parametric study on generic, but engine-representative double-clearance rim seals with different rotor-side features. This study investigates sealing effectiveness and fluid dynamics of ingress associated with these rim-seal features, in comparison with a datum double-clearance seal. Experimental measurements of gas concentration, pressure and swirl velocities were conducted to assess the relative performance of each double-clearance rim seal. The three double-clearance seals investigated in the study feature different numbers of rotor-side radial fins. The sealing effectiveness and swirl velocity in the outer wheel-space of each finned seal are significantly increased relative to the baseline seal; this increase is enhanced with a greater number of fins incorporated on the rotor side.

Figure 6.14 demonstrates the ranking of ε_c in both wheel-spaces for all double-clearance seal configurations studied in this chapter. The ε_c is evaluated at $\Phi_0 = 0.008$, corresponding to a sealing effectiveness of $\varepsilon_c = 0.95$ for the inner wheel-space of DS-0. The relative performance of each seal configuration, discussed in previous sections of this chapter, is summarised in the figure.

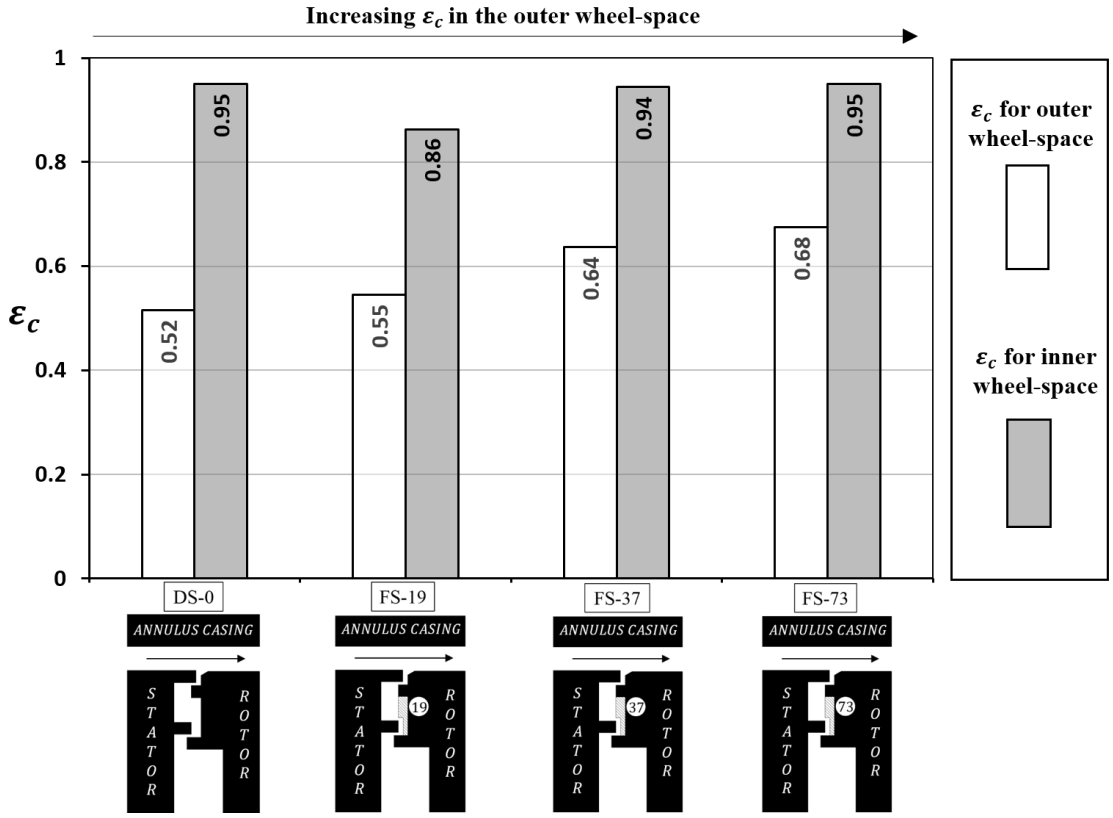

Figure 6.14 Ranking of sealing effectiveness for double-clearance seals with different rotor-side features at $\Phi_0 = 0.008$

The parameter for the minimum seal flow Φ_{min} and the ratio of discharge coefficients Γ_c are evaluated by a statistical fitting (Zhou *et al*. (2013)) of the theoretical model (Owen (2011)) to the measurements. The excellent agreement between the model and measurements for each rim-seal configuration is shown in previous sections of this chapter. The Φ_{min} and Γ_c for all the seal configurations are tabulated in Table 6.3, which can be exploited to support the design methodology of Siemens gas turbines.

Table 6.3 Φ_{min} and Γ_c for double-clearance rim-seal configurations studied in this chapter

Seal configuration		$\boldsymbol{\Phi_{min}}$	$\boldsymbol{\Gamma_c}$ $(C_{d,i}/C_{d,e})$
DS-0	**Inner** wheel-space	0.0132	0.240
	Outer wheel-space	0.0522	0.349
FS-19	**Inner** wheel-space	0.0166	0.416
	Outer wheel-space	0.0338	1.05
FS-37	**Inner** wheel-space	0.0127	0.310
	Outer wheel-space	0.0318	0.528
FS-73	**Inner** wheel-space	0.0110	0.354
	Outer wheel-space	0.0288	0.444

For the inner wheel-space, β is shown to be predominantly governed by λ_T, irrespective of different levels of ε_c for different seal configurations. This suggests a flow structure featuring separate boundary layers on the stator and rotor surfaces, which are governed by λ_T; a rotating core of fluid exists between the boundary layers in line with the Batchelor flow mode. The pressure distribution is shown to be determined by the swirl ratio and also dominated by λ_T.

For the outer wheel-space, the addition of the radial fins significantly enhances the swirl velocity. An increased level of swirl also corresponds to a higher level of pressure gradient; this may be attributed to the radial equilibrium between the centrifugal force of the swirling fluid and the radial pressure gradient in the outer wheel-space. The sealing effectiveness and fluid dynamics for all the tested double-clearance seals are correlated qualitatively, which will be described in Chapter 7.

It is worth mentioning that the utilisation of the rotor-side fins increases the windage losses and the extraction of otherwise useful turbine work. However, it was determined by engine designers that those effects could be overcome, due to the fact that the decrease in the sealing air demand for the finned seals could result in a net benefit for the overall engine efficiency.

Chapter 7 A further understanding of double-clearance rim seals

This chapter presents the correlation of sealing effectiveness and fluid dynamics for the double-clearance rim-seal configurations studied in Chapter 5 and 6. This study is aimed to provide an improved understanding of how these generic, but engine-representative seals operate in reducing hot gas ingress. The analysis reported in this chapter can support engine designers for the design and optimisation of rim seals employed in the secondary air system.

7.1 Comparison in sealing effectiveness and swirl ratio

Figure 7.1 shows the radial variation of ε_c and β at $Re_\phi = 7.9 \times 10^5$ with the same λ_T, for double-clearance seals with different stator-side features as described in Chapter 5. The ε_c and β are plotted over the complete range of radius in both wheel-spaces. For the outer wheel-space, the reduction in β is associated with the decrease in ε_c, as shown by DS-2 and DS-3 in comparison with DS-0. In contrast, β for the inner wheel-space is governed by λ_T irrespective of ε_c.

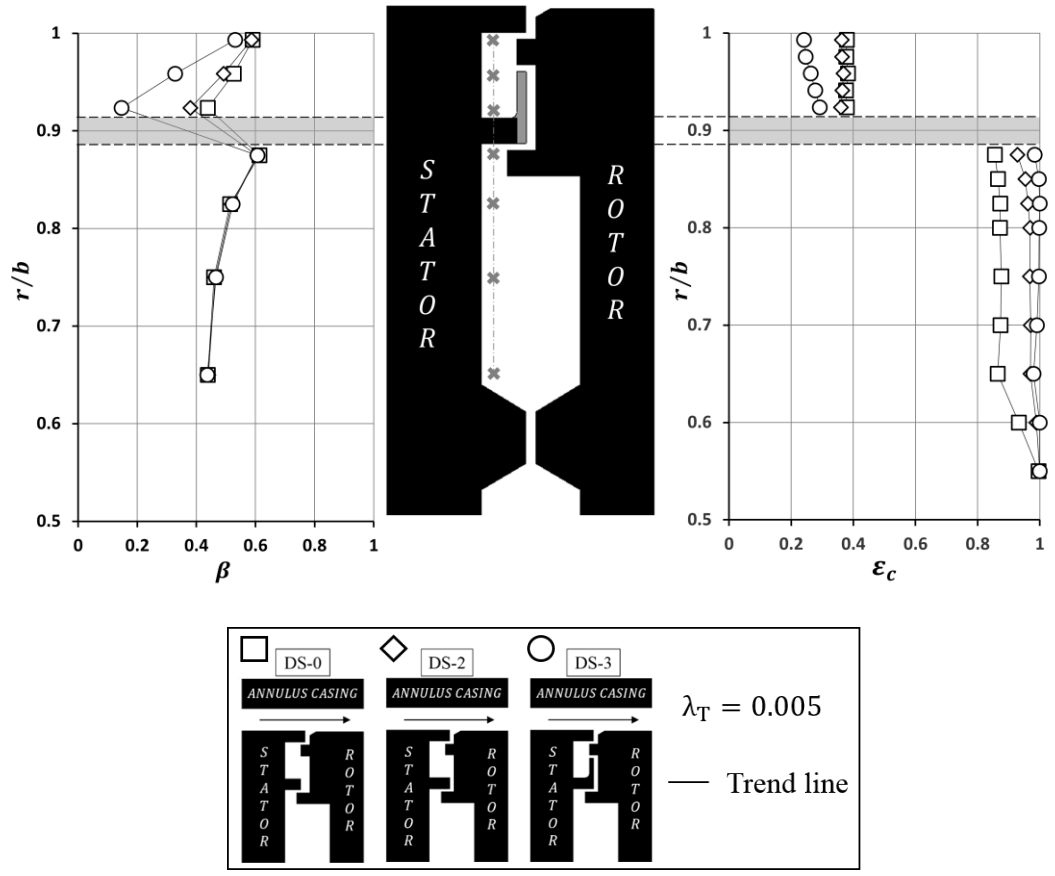

Figure 7.1 Radial variation of sealing effectiveness and swirl ratio for DS-0, DS-2 and DS-3

Figure 7.2 shows the radial variation of ε_c and β at $Re_\phi = 7.9 \times 10^5$ with the same λ_T, for double-clearance seals with different rotor-side features as described in Chapter 6. The ε_c and β are plotted over the complete range of radius in both wheel-spaces. For the outer wheel-space, a higher level of ε_c is shown to always correspond to a greater magnitude of β, which is promoted by the rotating fins, featured by FS-19, FS-37 and FS-73. The ε_c and β in the outer wheel-space also increase with increasing number of fins incorporated on the rotor side. It is shown once again that β for the inner wheel-space is governed by λ_T irrespective of ε_c.

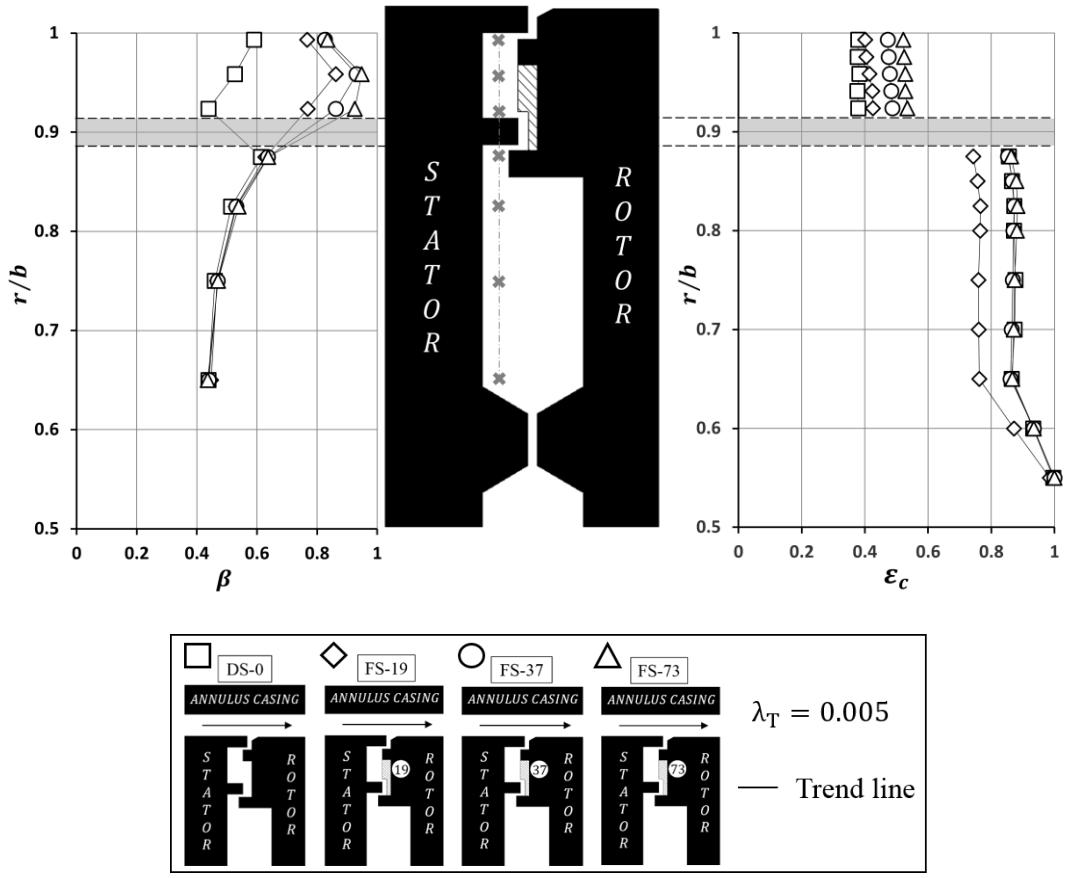

Figure 7.2 Radial variation of sealing effectiveness and swirl ratio for DS-0, FS-19, FS-37 and FS-73

7.2 Correlation of sealing effectiveness with swirl and pressure for double-clearance seals

Figure 7.3 shows the correlation of ε_c with $\bar{\beta}$ and $\hat{C}_{p.out}$ for the outer wheel-space, where $\bar{\beta}$ denotes the averaged swirl ratio determined using

$$\bar{\beta} = \frac{\sum_{k=1}^{n} \beta_k}{n} \tag{7.1}$$

where β_k is the swirl ratio measured at each location; n is the total number of measurement locations.

and $\hat{C}_{p.out}$ denotes the $C_{p,out}$ evaluated at the outermost position ($r/b = 0.993$) in the outer wheel-space. This parameter shows the pressure gradient over the complete range of radius in that wheel-space.

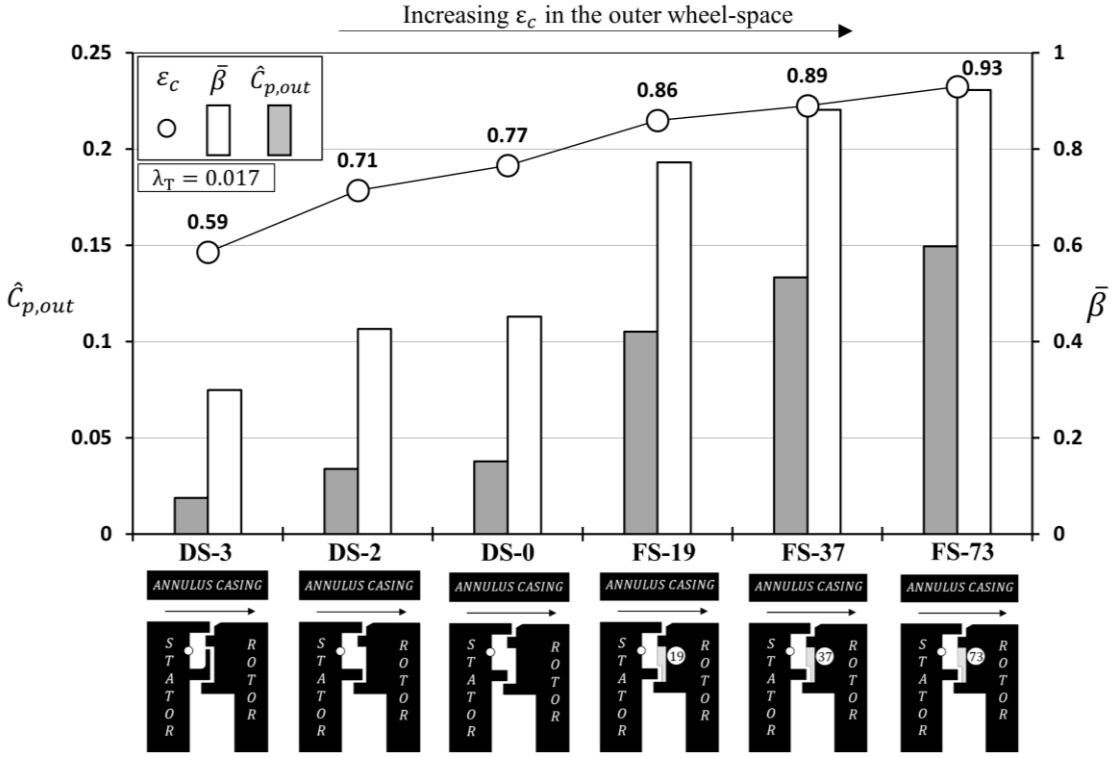

Figure 7.3 Correlation of sealing effectiveness with swirl and pressure for the outer wheel-space

The ε_c in the outer wheel-space for $\lambda_T = 0.017$ is shown for each double-clearance rim seal; the ranking of sealing effectiveness with this value of λ_T is representative of the trend over the complete range of sealing flow rate. The correlation shows that an increased magnitude of swirl results in a higher sealing effectiveness in the outer wheel-space, and the swirl predominately governs the pressure gradient. This trend is seen for all seal configurations with various stator-side and rotor-side features. The enhanced swirling motion of the fluid may have improved the circumferential mixing and attenuated the pressure asymmetries driving EI ingress into the outer wheel-space.

Figure 7.4 shows the correlation of ε_c with $\bar{\beta}$ and $\hat{C}_{p.in}$ for the inner wheel-space, where $\hat{C}_{p.in}$ denotes the $C_{p,in}$ evaluated at the position immediately inboard of the inner seal ($r/b = 0.875$). The $\hat{C}_{p.in}$ shows the pressure gradient over the complete range of radius in that wheel-space. It is seen the

swirl ratio and pressure gradient in the inner wheel-space depend only on λ_T, despite the significant difference in ε_c among all the seal configurations. This suggests a flow structure featuring separate boundary layers on the stator and rotor surfaces, which are governed by λ_T (Owen and Rogers (1989)); a rotating core of fluid exists between the boundary layers in line with the Batchelor flow mode introduced in Chapter 2.

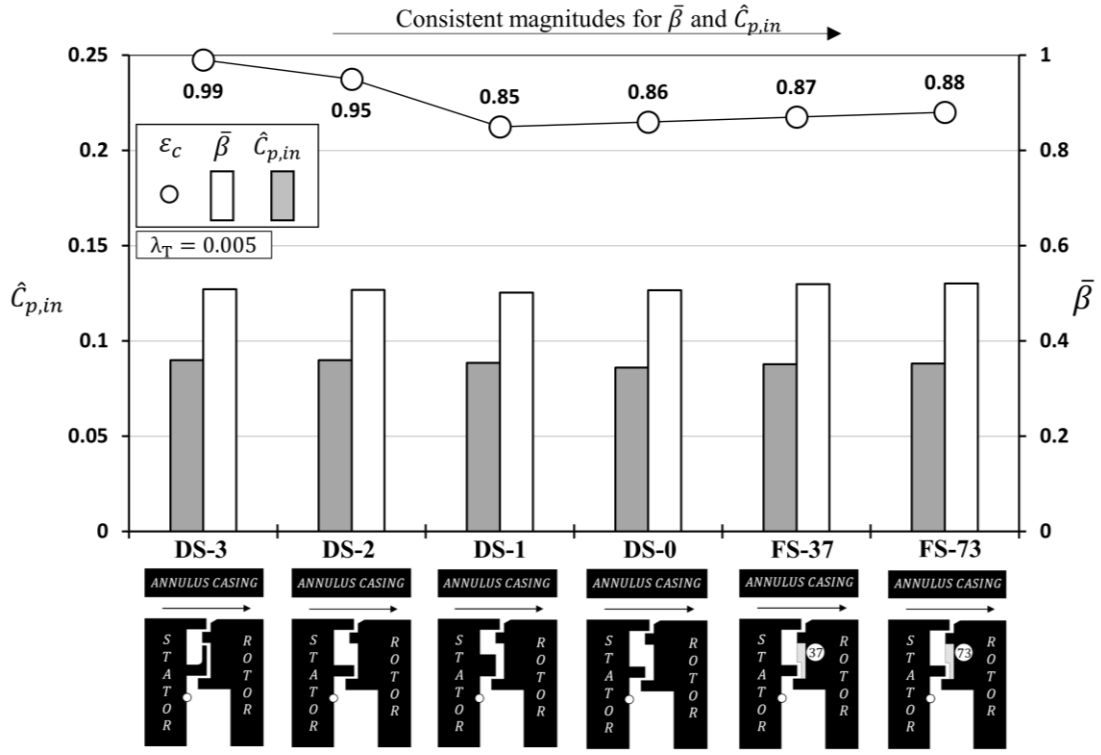

Figure 7.4 Correlation of sealing effectiveness with swirl and pressure for the inner wheel-space

Based on the ranking of sealing effectiveness, DS-3 has the best relative inner-seal performance; FS-73 features the most effective outer seal within the scope of this study. The rotating fins enhance the disc pumping of fluid, while significantly attenuating the pressure asymmetries close to the seal; the net results are the increase in sealing effectiveness for an EI dominated ingress regime. The utilisation of the rotor-side fins also increases the windage losses and the extraction of otherwise useful turbine work. However, these effects could be outweighed by the decrease in the sealing air demand resulting in a net benefit for the overall engine efficiency.

It is envisaged that an optimised double-clearance seal could possibly be configured through the combination of the characteristics of DS-3 and FS-73. Modification may be required to ensure the compatibility of the angel-wing and radial-fin features. Nevertheless, this study provides insights into how generic, but engine-representative double-clearance seals operate and how these seals could be optimised by engine designers.

7.3 Additional analysis for the inner wheel-space

The EI ingress is mostly concerned by engine designers, and it has been experienced by the single-clearance seal and the outer wheel-space of double-clearance seals studied in this thesis. However, as the outer wheel-space can attenuate the external pressure asymmetries, the RI ingress may occur to the inner wheel-space of double-clearance seals. Pressure asymmetries were assessed in the outer wheel-space of DS-0 and compared with the external pressure variation as shown in Figure 7.5.

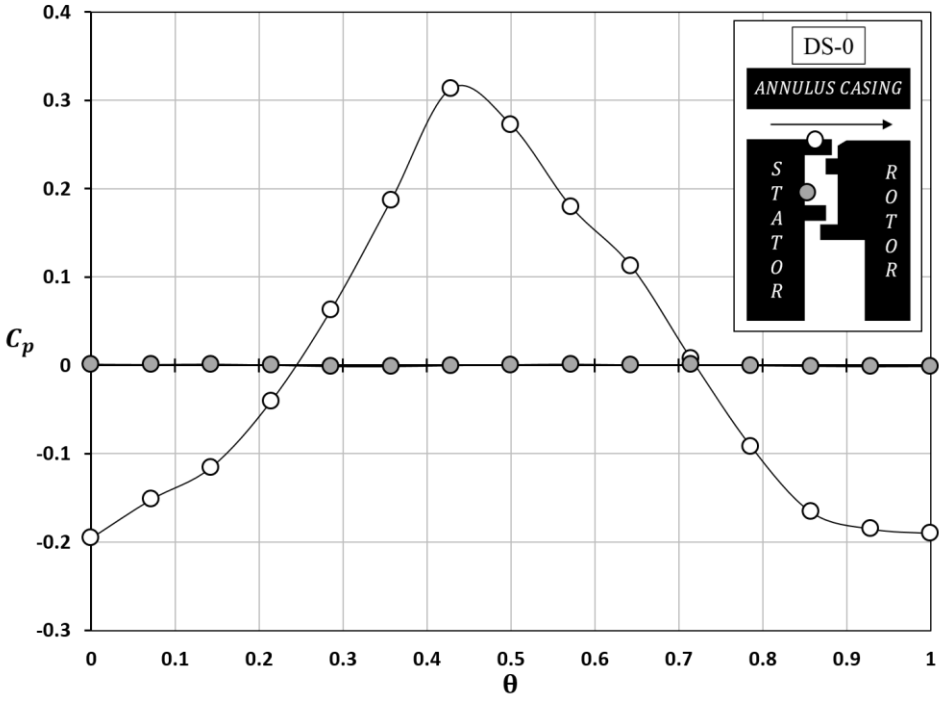

Figure 7.5 Circumferential variation of C_p on the vane platform and in the outer wheel-space

Pressure measurements were made on the stator surface in the outer wheel-space, at a radius of $r/b = 0.941$ close to the inner-seal arrangement. A circumferential distribution of pressure was acquired over the range of a vane pitch, and compared with the external pressure variation (assessed at location A1) previously shown in Chapter 3. It is seen that the pressure is virtually invariant circumferentially. Therefore the pressure asymmetries from the mainstream have been damped out almost completely; the inner wheel-space experiences the RI dominated ingress.

The research work documented in this section is aimed to correlate the sealing effectiveness determined with gas concentration measurements, and the pressure drop across the inner seal, which governs the RI ingress. The inner wheel-space is treated as a stand-alone rotor-stator system. The flow in the outer wheel-space is regarded as the 'external flow'. Different from previous discussions,

the inner-seal performance is evaluated from a new perspective, with new parameters defined with regard to the inner wheel-space.

The concentration sealing effectiveness for the inner wheel-space, $\varepsilon_{c,in}$ is defined as follows,

$$\varepsilon_{c,in} = \left(\frac{c_s - c_a}{c_o - c_a}\right)_{in} \tag{7.2}$$

where $c_{a,in}$ is the CO_2 gas concentration in the outer wheel-space, also the 'external flow' for the inner wheel-space. It is assumed that $c_{a,in} = c_{s,out}$, where the latter denotes the gas concentration taken at the radial position immediately above the inner seal. Subscripts *in* and *out* are employed to indicate the inner wheel-space and outer wheel-space respectively.

The sealing flow parameter for the inner wheel-space, $\Phi_{0,in}$, is defined as follows,

$$\Phi_{0,in} = \left(\frac{U}{\Omega b}\right)_{in} \tag{7.3}$$

where U_{in} is the bulk mean velocity of sealing flow through the inner-seal clearance, so that

$$U_{in} = \frac{\dot{m}_o}{2\pi\rho b_{in} s_{c,in}} \tag{7.4}$$

where b_{in} is the radius of the inner-seal, and $s_{c,in}$ is the inner-seal clearance.

The experimental measurements for DS-0 reported in Chapter 5 are used again for the above parameters, and the variation of $\varepsilon_{c,in}$ with $\Phi_{0,in}$ for the inner wheel-space is shown in Figure 7.6. The experimental data was compared with the theoretical model for RI ingress described by Owen (2011a) in conjunction with a statistical fitting method described by Zhou *et al*. (2013). The theoretical curve is shown to be in good agreement with the measurements, and the inner wheel-space is shown to be completely sealed when $\Phi_{min,in} \approx 0.03$.

According to the theoretical orifice model for RI ingress (Owen (2011a)), if the external swirl velocity can be neglected, there would be no RI ingress when the pressure drop ($\Delta p_{in} = p_{out} - p_{in}$) across the inner seal equals zero. With positive external swirl velocities, the RI ingress decreases compared with that for the no-swirling condition; a positive Δp_{in} is therefore anticipated when the inner wheel-space is completely sealed.

For each double-clearance seal configuration studied, including the baseline DS-0, the magnitude of swirl velocity is above zero in the outer wheel-space. Figure 7.7 shows the variation of normalised pressure drop across the inner seal with $\Phi_{0,in}$ for the baseline double-clearance seal DS-0. It is shown that when the inner wheel-space was fully sealed ($\varepsilon_{c,in} = 1$), the pressure drop $\Delta p_{in} > 0$, in line with the theoretical model. If $\Delta p_{in} = 0$ is used as a criterion to determine the minimum sealing flow rate

required to prevent the RI ingress, a conservative prediction can be obtained to ensure the wheel-space is fully sealed ($\varepsilon_{c,in} = 1$).

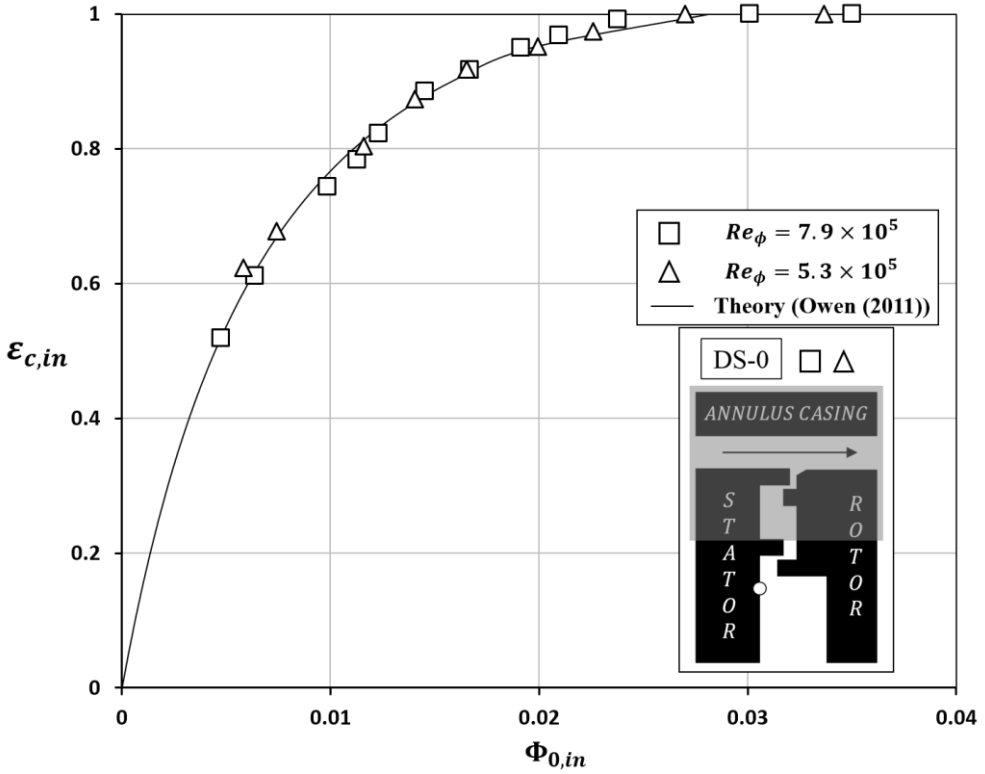

Figure 7.6 Variation of $\varepsilon_{c,in}$ with $\Phi_{0,in}$ for DS-0

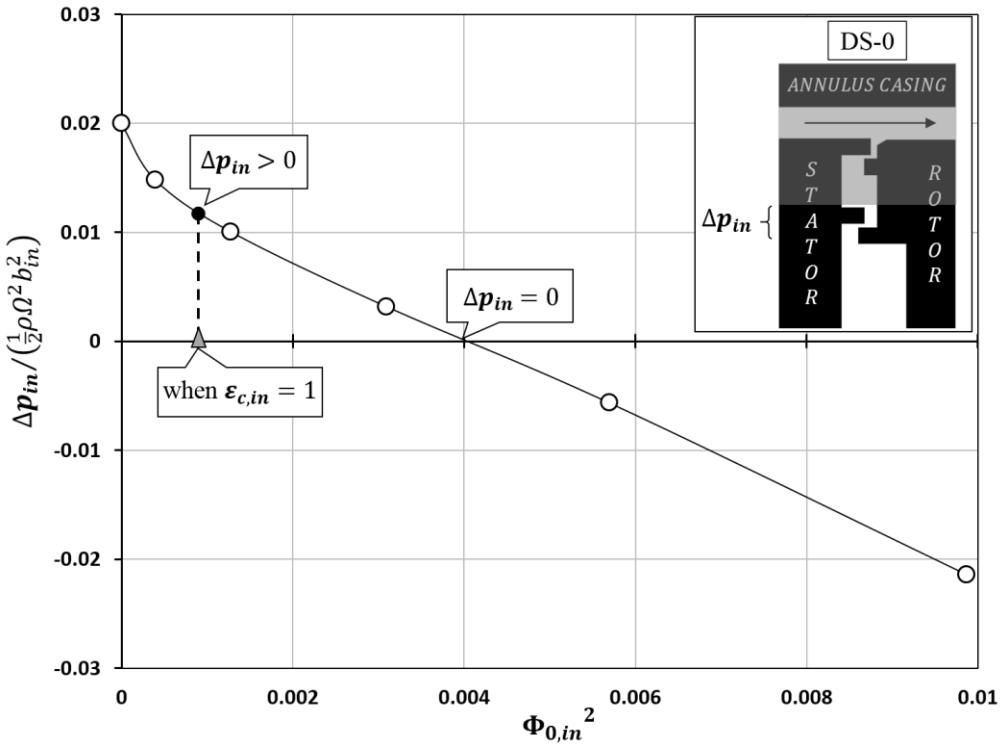

Figure 7.7 Variation of pressure drop across the inner seal with $\Phi_{0,in}$ for DS-0

7.4 Summary

This chapter describes a comprehensive analysis for double-clearance rim seals investigated in Chapter 5 and 6. A comparison in sealing effectiveness and swirl ratio is reported based on the measurements documented in these chapters. For the outer wheel-space, the reduction in β is associated with the decrease in ε_c, as shown by DS-2 and DS-3 in comparison with DS-0. For the finned-seal configurations, a higher level of ε_c corresponds to a greater magnitude of β promoted by the rotating fins. The ε_c and β in the outer wheel-space also increase with increasing number of fins incorporated on the rotor side. It is shown that β for the inner wheel-space is governed by λ_T irrespective of ε_c.

Qualitative correlation of sealing effectiveness with pressure gradient and swirl ratio was performed for all the double-clearance seal configurations. General trends for sealing effectiveness in conjunction with flow dynamics found in both wheel-spaces are shown. The enhanced swirling motion of the fluid in the outer wheel-space probably improves the circumferential mixing and attenuates the external pressure asymmetries driving ingress through the seal clearance. The inner wheel-space features a flow structure dominated by separate boundary layers on the stator and rotor surfaces, which are governed by λ_T; a rotating core of fluid exists between the boundary layers in line with the Batchelor flow mode introduced in Chapter 2.

Additional discussion is reported on the behaviour of the inner-seal. Pressure measurements show the inner wheel-space of DS-0 experiences the RI ingress, governed by the pressure drop across the inner seal Δp_{in}. If the criterion $\Delta p_{in} = 0$ is used to determine the minimum sealing flow rate required to prevent the RI ingress, a conservative prediction can be obtained to ensure the inner wheel-space is fully sealed. An explanation is given in conjunction with the theoretical model (Owen (2011a)).

This chapter is aimed to provide an improved understanding of how generic, but double-clearance rim seals operate and insights into the fluid dynamics of ingestion. Analysis based on the experimental measurements is reported to support the design and optimisation of rim-seal configurations utilised in the secondary air system of gas turbine engines.

Chapter 8 Conclusions

8.1 Design of the experimental facility

The design of a single stage gas turbine research facility is described. The turbine stage consists of a rotor-stator disc system with an annulus casing to form the mainstream flow path. The stator and rotor assemblies are highly versatile, enabling the study of engine-representative rim seals. Research into a new area of ingestion problem is made possible, including the utilisation of leakage flows for reducing hot gas ingress into the wheel-space.

The feed system for the turbine stage is shown, including the sealant line and the annulus flow pipes. The circumferential pressure distribution upstream of the stator vanes is shown to be axis-symmetric in line with the design aim. The flow passes the vanes and blades to create the pressure asymmetries in the annulus driving the EI ingress. The sealing flow is introduced into the system from the stator centre. For concentration measurements to determine the sealing effectiveness of the wheel-space, the sealing flow can be seeded with CO_2 tracer gas upstream of the inlet to the disc system.

The turbine rotor is driven by a powertrain including an electric motor connected to a belt transmission. The complete powertrain was mounted onto a carriage system that can slide on linear guide rails. The carriage system was specifically designed to achieve high-precision alignment between the turbine discs, which is essential for testing engine-representative rim seals. The end-stop sub-system ensures the repeatability in alignment after the rotor-stator system is re-assembled.

The on-design operating points were determined based on the velocity triangle corresponding to the vane-blade configuration. The stator and rotor discs were designed to be bladed discs (bliscs) and the blading profiles were shaped by high-precision CNC machining. The material for the stator and rotor discs was selected to be aerospace-grade aluminium alloy.

The components for stator and rotor assemblies are detailed. Cover-plates, attached to the turbine discs, were designed for several purposes. For the stator, cover-plates enhance the adaptability and capability of instrumentation. For the rotor, cover-plates made of low-density materials can reduce the stress level and torque requirement. The modular cover-plates are interchangeable, thus allowing the wheel-space geometries to be varied. For the heat transfer measurements using heated sealing flow, a complete insulation of the wheel-space is made possible by specifically designed cover-plates, in order to reduce unwanted heat losses to the metal surfaces.

The stator and rotor discs are also interchangeable. Modular turbine discs with different gas path blading can be installed in the rig, enabling the study of aerodynamics associated with various blading

configurations and the effect on ingress. A stator was designed to model the leakage flow paths close to the rim seal found in gas turbine engines. The design enables a fundamental study on the complex flow interactions among the ingress, sealing flow and the leakage flow in the wheel-space. This research possibility is aimed to explore a novel way of exploiting leakage flows for reducing ingress into the wheel-space.

Instrumentation arrangements incorporated in the turbine stage are demonstrated in detail. Locations for the instrumentation applied in the wheel-space and the mainstream annulus are described. Extensive measurements of pressure, swirl velocity, gas concentration and temperature can be made to improve the understanding of fluid dynamics, as well as the thermal effects of ingestion.

The entire design and all the relevant drawings were completely accomplished by the author of this thesis. It is envisaged that the research work enabled by the design of this facility will far exceed the experimental measurements documented in this thesis.

8.2 Baseline testing and measurements for a baseline single-clearance seal

The baseline testing of the rig is reported, followed by the experiment measurements for a baseline single-clearance rim seal. The deformation of the rotating disc was assessed experimentally for a range of rotor speed. The displacement was also acquired from a structural FEA analysis. There is a good agreement between the FEA results and the measurements. It is shown the rotor deformation due to rotation is too insignificant relative to the rim-seal clearances and the blade tip clearance.

Pressure measurements were conducted in the annulus to evaluate the mainstream flow condition. The circumferential variation of pressure coefficient, C_p, was determined downstream of the stator vanes. The pressure asymmetry ΔC_p, which is the peak-to-trough difference of C_p in a vane pitch, is evaluated at different positions in the annulus for different rotational Reynolds number and for different flow coefficient. The effect of interaction between sealing flow and the mainstream on ΔC_p was also investigated.

A generic single-clearance rim seal was introduced as a baseline configuration. The sealing effectiveness for this seal was determined with gas concentration measurements. The radial variation of effectiveness is shown for different levels of sealing flow rate. The variation of sealing effectiveness over the complete range of sealing flow parameter is shown. The data can be well predicted by the theoretical orifice model in conjunction with a statistical fitting method.

The radial variation of pressure in the wheel-space was evaluated. Swirl velocities were measured in the rotating core of the wheel-space flow. The radial variation of pressure was calculated from the

swirl ratios using a simplified radial moment equation. The calculation is in good agreement with the measurements, indicating the pressure variation is predominantly determined by the swirl velocities.

The measurements for the baseline single-clearance seal form the basis for the study of engine-representative double-clearance seals. The same operating conditions for the single-clearance seal will continue to be applied for the double-clearance seals. The methods for evaluating the sealing effectiveness and analysing the flow physics shall also be used again to investigate the relative performance of different double-clearance seal configurations.

8.3 Parametric studies of double-clearance rim-seal configurations

Parametric studies on generic, but engine-representative double-clearance rim seals are documented. Experimental measurements of gas concentration, pressure and swirl velocities were conducted to assess the relative performance of each double-clearance rim seal. The effectiveness and fluid dynamics of each seal are compared with a baseline double-clearance seal configuration.

A comparison in seal performance and fluid dynamics is shown between the baseline single-clearance and double-clearance seals. The double-clearance seal significantly improves the effectiveness inboard of the inner seal, in line with expectation. The swirl and pressure inboard of the inner seal is governed by the turbulent flow parameter, consistent with the single-clearance seal.

Experimental measurements for different stator-side seal features are shown relative to the baseline configuration. The ‘angel-wing’ seal is shown to significantly improve the inner wheel-space, but decrease the effectiveness in the outer wheel-space. A decrease in swirl is also seen resulting from the angel-wing feature.

Measurements for different rotor-side seal features are shown relative to the baseline configuration. The fins added to the rotor disc are shown to enhance the swirl ratio significantly. The sealing effectiveness for the finned seals in the outer wheel-space is significantly increased compared with the baseline seal. The greatest increase in swirl and effectiveness is seen for the configuration with the most fins on the rotor side.

Qualitative correlations of sealing effectiveness with pressure gradients and swirl ratios were performed for all the configurations included in the study. General trends for sealing effectiveness in connection with flow dynamics in the wheel-space are shown. Additional discussion is made on the performance of the inner-seal, in conjunction with the theoretical orifice model for RI ingress. The study is aimed to achieve an improved understanding of how double-clearance rim seals operate, thus providing insights into the fluid dynamics of ingestion.

8.4 Future work

The design of the gas turbine research facility has enabled many possibilities of future research, thanks to its versatility and adaptability. For instance, the effect of wheel-space geometries on ingestion can be experimentally determined, and the results could be compared with theoretical predictions and CFD results. The conclusion from this study is expected to deepen the understanding of fluid dynamics found in secondary air systems, providing valuable support for engine designers.

Moreover, the effect of gas path blading can be investigated, for an extensive range of vane-blade configurations enabled by the interchangeability of turbine discs. The turned rotor blades are expected to create a complex unsteady pressure variation in engines. Under certain flow conditions, this unsteady pressure variation may be significant in amplitude and must be considered for the driving potential of EI ingestion, in addition to the circumferential variation resulting from the stator vanes. The effect of different blade profiles can be conveniently tested in the rig, by employing interchangeable rotors. A comparative study is also possible between a bladed rotor and a bladeless rotor, to identify the effect of a specific blade configuration. It is envisaged that the gas path flow physics representative of different engines can be created, significantly enhancing the research impact on the gas turbine industry.

Nevertheless, the modelling of leakage flow in the rig can expand on the research into ingestion, by exploring effective ways of using the leakage flow to decrease ingress. Measurements of sealing effectiveness and fluid dynamics could potentially determine the most appropriate range of angle and mass flow rate for the leakage flow to improve the sealing effectiveness of the wheel-space. Different tracer gases can be used for the sealing and leakage flows supplied to the turbine stage. Gas concentration measurements are expected to reveal the complex mixing and interaction of flows found in the wheel-space.

Extensive heat transfer measurements can be conducted using the facility with a heated sealing flow to study the thermal effects of ingress on both the stator and rotor components. This is also of direct relevance to designers as the cooling effect of the sealing air could determine the temperatures at which turbine rotors operate and the level of thermal stresses.

3D time-dependent CFD and further theoretical modelling work can be conducted in future, in conjunction with the experimental research discussed above. It is hoped that the future research enabled by this facility shall contribute to the development of modern-day gas turbine technologies, and advancement in the applications of flow dynamics to turbomachinery in general.

Reference

Abe, T., Kikuchi, J. and Takeuchi, H., 1979. "An Investigation of Turbine Disk Cooling (Experimental Investigation and Observation for Hot Gas Flow into a Wheel Space)". CIMAG – 13th International Congress on Combustion Engines.

ASME, 2007. "The World's First Industrial Gas Turbine Set at Neuchatel (1939)". ASME International Historic Mechanical Engineering Landmark, H135.

Batchelor, G. K., 1951. "Note on the Class of Solutions of the Navier-Stokes Equations Representing Steady Rotationally Symmetric Flow". *Quarterly Journal of Applied Mathematics,* 4 (1), pp. 29-41.

Bayley, F. J. and Owen, J. M., 1970. "The Fluid Dynamics of a Shrouded Disk System with a Radial Outflow of Coolant". ASME *J. Eng. Power,* 92 (3), pp. 335-341.

Bohn, D. E., Johann, E. and Kruger, U., 1995. "Experimental and Numerical Investigations of Aerodynamic Aspects of Hot Gas Ingestion in Rotor-Stator Systems with Superimposed Cooling Mass Flow". ASME Paper 95-GT-143.

Bohn, D. E., Rudzinski, B., Surken, N. and Gartner, W., 1999. "Influence of Rim Seal Geometry on Hot Gas Ingestion into the Upstream Cavity of an Axial Turbine Stage". ASME Paper 99-GT-248.

Bohn, D. E. and Wolff, M., 2003. "Improved Formulation to Determine Minimum Sealing Flow – Cw,min – for Different Sealing Configurations". ASME Paper GT2003-38465.

Bohn, D. E., Decker, A., Hongwei, M. and Wolff., 2003. "Influence of Sealing Air Mass Flow on the Velocity Distribution in and inside the Rim Seal of the Upstream Cavity of a 1.5-Stage Turbine". ASME Paper GT2003-38459.

Bohn, D. E., Decker, A., Ohlendorf, N. and Jakoby, R., 2006. "Influence of an Axial and Radial Rim Seal Geometry on Hot Gas Ingestion into the Upstream Cavity of a 1.5-Stage Turbine". ASME Paper GT2006-90453.

Balasubramanian, J., Junnarkar, N., Zhou, D. W., Roy, R. P., Kim, Y. W. and Moon, H. K., 2011. "Experiments on Aft-Disk Cavity Ingestion in a Model 1.5-Stage Axial-Flow Turbine". ASME Paper GT2011-45895.

Balasubramanian, J., Pathak, P. S., Thiagarajan, J. K., Singh, P., Roy, R. P. and Mirzamoghadam, A. V., 2015. "Experimental Study of Ingestion in the Rotor–Stator Disk Cavity of a Subscale Axial Turbine Stage". ASME *J. Turbomach.*, 137(9), p.091010.

Barringer, M., Coward, A., Clark, K., Thole, K. A., Schmitz, J., Wagner, J., Alvin, M. A., Burke, P. and Dennis, R., 2014. "Development of a Steady Aero Thermal Research Turbine (START) for Studying Secondary Flow Leakages and Airfoil Heat Transfer". ASME Paper GT2014-25570.

Chew, J. W., 1991. "A Theoretical Study of Ingress for Shrouded Rotating Disk Systems with Radial Outflow". ASME *J. Turbomach.*, 113(1), pp. 91-97.

Chew, J. W., Dadkhah, S. and Turner, A. B., 1992. "Rim Sealing of Rotor–Stator Wheelspaces in the Absence of External Flow". ASME *J. Turbomach.*, 114(2), pp. 433-438.

Chew, J. W., Green, T. and Turner, A. B., 1994. "Rim Sealing of Rotor-Stator Wheelspaces in the Presence of External Flow". ASME Paper 94-GT-126.

Cao, C., Chew, J. W., Millington, P. R. and Hogg, S. I., 2004. "Interaction of Rim Seal and Annulus Flows in an Axial Flow Turbine". *J. Eng. Gas Turbines Power*, 126(4), pp. 786-793.

Childs, P. R. N., 2011. *Rotating Flow*. Oxford: Butterworth-Heinemann.

Daily, J. W. and Nece, R. E., 1960. "Chamber Dimension Effects on Induced Flow and Frictional Resistance of Enclosed Rotating Disks". *Journal of Basic Engineering*, 82(1), pp. 217-232.

Dadkhah, S., Turner, A. B. and Chew, J. W., 1992. "Performance of Radial Clearance Rim Seals in Upstream and Downstream Rotor–Stator Wheelspaces". ASME *J. Turbomach.*, 114(2), pp. 439-445.

Daniels, W. A., Johnson, B. V., Graber, D. J. and Martin, R. J., 1992. "Rim Seal Experiments and Analysis for Turbine Applications". ASME *J. Turbomach.*, 114(2), pp. 426-432.

Diakunchak, I., Kiesow, H. J. and McQuiggan, G., 2008. "The History of the Siemens Gas Turbine". ASME Paper GT2008-50507.

Eastwood, D., Core, D. D., Long, C. A., Atkins N. R., Childs, P. R. N., Scanlon, T. J. and Guijarro-Valencia, A., 2012. "Experimental Investigation of Turbine Stator Well Rim Seal, Re-Ingestion and Interstage Seal Flows Using Gas Concentration Techniques and Displacement Measurements". ASME *J. Turbomach.*, 134, pp. 082501.

Graber, D. J., Daniels, W. A. and Johnson, B. V., 1987. "Disc Pumping Test, Final Report". *Air Force Wright Aeronautical Laboratories*, Report No. AFWAL-TR-87-2050.

Green, T. and Turner, A. B., 1994. "Ingestion into the Upstream Wheelspace of an Axial Turbine Stage". ASME *J. Turbomach.*, 116(2), pp. 327-332.

Gallier, K. D., Lawless, P. B. and Fleeter, S., 2000. "Investigation of Seal Purge Flow Effects on the Hub Flow Field in a Turbine Stage using Particle Image Velocimetry". AIAA Paper AIAA-2000-3370.

Gentilhomme, O., Hills, N. J., Turner, A. B. and Chew, J. W., 2003. "Measurement and Analysis of Ingestion through a Turbine Rim Seal". ASME *J. Turbomach.*, 125(3), pp. 505-512.

Hamabe, K. and Ishida, K., 1991. "A Simplified Model for Estimating Ingress of Gas Turbine Rotor-Stator Systems". Yokohama International Gas Turbine Congress.

Hamabe, K. and Ishida, K., 1992. "Rim Seal Experiments and Analysis of a Rotor-Stator System with Nonaxisymmetric Main Flow". ASME Paper 92-GT-160.

Hills, N. J., Chew, J. W. and Turner, A. B., 2002. "Computational and Mathematical Modeling of Turbine Rim Seal Ingestion". ASME *J. Turbomach.*, 124(2), pp. 306-315.

Hunt, R. J., 2011. "The History of the Industrial Gas Turbine: Part 1 – The First Fifty Years 1940 – 1990". IDGTE Paper 582.

Johnson, B. V., Jakoby, R., Bohn, D. E. and Cunat, D., 2006. "A Method for Estimating the Influence of Time-Dependent Vane and Blade Pressure Fields on Turbine Rim Seal Ingestion". ASME Paper GT2006-90853.

Johnson, B. V., Wang, C. Z. and Roy, R. P., 2008. "A Rim Seal Orifice Model with Two Cd's and Effects of Swirl in Seals". ASME Paper GT2008-50650.

Mellor, G. L., Chapple P. J. and Stokes V. K., 1968. "On the Flow between a Rotating and a Stationary Disc". *Journal of Fluid Mechanics*, pp. 95-122.

Morley, A., 1944. *Strength of Materials*. Longmans Green.

Owen, J. M. and Rogers, R. H., 1989. *Flow and Heat Transfer in Rotating-Disc Systems, Volume 1: Rotor-Stator Systems*. Taunton: Research Studies Press Ltd.

Owen, J. M., 2011a. "Prediction of Ingestion through Turbine Rim Seals—Part I: Rotationally Induced Ingress". ASME *J. Turbomach.*, 133(3), p.031005.

Owen, J. M., 2011b. "Prediction of Ingestion through Turbine Rim Seals—Part II: Externally Induced Ingress". ASME *J. Turbomach.*, 133(3), p.031006.

Owen, J. M., Zhou, K., Pountney, O. J., Wilson, M., and Lock, G. D., 2012. " Prediction of Ingress through Turbine Rim Seals—Part I: Externally-Induced Ingress". ASME *J. Turbomach.*, 134, p.031012.

Owen, J. M., Wu, K., Scobie, J. A., Sangan, C. M., Cho, G. H. and Lock, G. D., 2015. "Use of Pressure Measurements to Determine Effectiveness of Turbine Rim Seals". *J. Eng. Gas Turbines Power*, 137(3), p. 032510.

Peterson, R., 1974. *Stress Concentration Factors*. London: Wiley-Interscience.

Picha, K. G. and Eckert E.R.G., 1958. "Study of the Air Flow between Coaxial Discs Rotating with Arbitrary Velocities in an Open or Closed Space". *Proceedings of the 3rd U.S. National Congress of Applied Mechanics*, pp. 791-798.

Phadke, U. P. and Owen, J. M., 1983. "An Investigation of Ingress for an "Air-Cooled" Shrouded Rotating Disk System with Radial-Clearance Seals". ASME *J. Eng. Power*, 105(1), pp. 178-183.

Phadke, U. P. and Owen, J. M., 1988a. "Aerodynamic Aspects of the Sealing of Gas-Turbine Rotor-Stator Systems. Part 1: The Behaviour of Simple Shrouded Rotating Disk Systems in a Quiescent Environment". *International Journal of Heat and Fluid Flow*, 9(2), pp. 98-105.

Phadke, U. P. and Owen, J. M., 1988b. "Aerodynamic Aspects of the Sealing of Gas-Turbine Rotor-Stator Systems. Part 2: The Performance of Seals in a Quasiaxisymmetric External Flow". *International Journal of Heat and Fluid Flow*, 9(2), pp. 106-112.

Phadke, U. P. and Owen, J. M., 1988c. "Aerodynamic Aspects of the Sealing of Gas-Turbine Rotor-Stator Systems. Part 3: The Effect of Nonaxisymmetric External Flow on Seal Performance". *International Journal of Heat and Fluid Flow*, 9(2), pp. 113-117.

Poncet, S., Chauve, M-P. and Schiestel. R., 2005. "Batchelor versus Stewartson Flow Structures in a Rotor-Stator Cavity with Throughflow". *Physics of Fluids*, 17 (7).

Palafox, P., Ding, Z., Bailey, J., Vanduser, T., Kirtley, K., Moore, K. and Chupp, R., 2013. "A New 1.5 Stage Turbine Wheelspace Hot Gas Ingestion Rig (HGIR) – Part I: Experimental Test Vehicle, Measurement Capability and Baseline Results". ASME Paper GT2013-96020.

Rolls-Royce, 1996. *The Jet Engine*, 5th ed. Derby: Rolls-Royce plc.

Roy, R. P., Feng, J., Narzary, D. and Paolillo, R. E., 2005. "Experiment on Gas Ingestion through Axial-Flow Turbine Rim Seals". *J. Eng. Gas Turbines Power*, 127(3), pp. 573-582.

Roy, R. P., Zhou, D. W., Ganesan, S., Wang, C. Z., Paolillo, R. E. and Johnson, B, V., 2007. "The Flow Field and Main Gas Ingestion in a Rotor-Stator Cavity". ASME Paper GT2007-27671.

Stewartson, K., 1953. "On the Flow between Two Rotating Coaxial Discs". *Proceedings of the Cambridge Philosophical Society*, 49(1), pp. 333-341.

Schmitz, J. T., 2010. "Experimental Measurements in a Highly Loaded Low Pressure Turbine Stage". PhD thesis, University of Notre Dame, Indiana.

Sangan, C. M., Pountney, O. J., Zhou, K., Wilson, M., Owen, J. M. and Lock, G. D., 2013a. "Experimental Measurements of Ingestion through Turbine Rim Seals—Part 1: Externally-Induced Ingress". ASME *J. Turbomach.*, 135(2), p.021012.

Sangan, C. M., Pountney, O. J., Zhou, K., Wilson, M., Owen, J. M. and Lock, G. D., 2013b. "Experimental Measurements of Ingestion through Turbine Rim Seals—Part 2: Rotationally-Induced Ingress". ASME *J. Turbomach.*, 135(2), p.021013.

Scobie, J. A., Sangan, C. M., Owen, J. M., Wilson, M. and Lock, G. D., 2014. "Experimental Measurements of Hot Gas Ingestion through Turbine Rim Seals at Off-Design Conditions. *Proceedings of the Institution of Mechanical Engineers, Part A: Journal of Power and Energy*, 228(5), pp. 491-507.

Wang, C. Z., Mathiyalagan, S. P., Johnson, B. V., Glahn, J. A. and Cloud, D. F., 2013. "Rim Seal Ingestion in a Turbine Stage from 360-Degree Time-Dependent Numerical Simulations". ASME *J. Turbomach.*, 136(3), p.031007.

Zhou, D. W., Roy, R. P., Wang, C. Z. and Glahn, J. A., 2011. "Main Gas Ingestion in a Turbine Stage for Three Rim Cavity Configurations". ASME *J. Turbomach.*, 133(3), p. 031023.

Zhou, K., Wood, S. N. and Owen, J. M., 2013. "Statistical and Theoretical Models of Ingestion through Turbine Rim Seals". ASME *J. Turbomach.*, 135(2), p.021014.

Appendix I: Uncertainty analysis for important parameters used in the experimental studies

1. Sealing effectiveness ε_c

The sealing effectiveness ε_c was determined with gas concentration measurements. CO_2 gas concentration was taken in the wheel-space (c_s), in the sealant line (c_o) and in the annulus (c_a). The definition of the sealing effectiveness (ε_c denoted here for simplicity as ε) can be expressed as follows:

$$\varepsilon = \frac{c_s - c_a}{c_o - c_a} \tag{A1}$$

Let U_ε, U_s, U_o and U_a be uncertainties in ε, c_s, c_o and c_a respectively, so that

$$\varepsilon \pm U_\varepsilon = \frac{c_s \pm U_s - (c_a \pm U_a)}{c_o \pm U_o - (c_a \pm U_a)} = \varepsilon \frac{[1 + (\pm U_s \pm U_a)/(c_s - c_a)]}{[1 + (\pm U_o \pm U_a)/(c_o - c_a)]} \tag{A2}$$

If $(\pm U_o \pm U_a)/(c_o - c_a) \ll 1$, then it follows that

$$\varepsilon \pm |U_\varepsilon| \leq \varepsilon \left(1 + \frac{|U_s| + |U_a|}{c_s - c_a} + \frac{|U_o| + |U_a|}{c_o - c_a}\right) \tag{A3}$$

Hence,

$$\frac{|U_\varepsilon|}{\varepsilon} \leq \left(\frac{|U_s| + |U_a|}{c_s - c_a} + \frac{|U_o| + |U_a|}{c_o - c_a}\right) \tag{A4}$$

For the concentration measurements, $U_s = U_o = U_a = \delta$, (δ is the uncertainty in CO_2 concentration measured using the gas analyser), so that

$$\frac{|U_\varepsilon|}{\varepsilon} \leq 2\delta \frac{1 + \varepsilon^{-1}}{c_o - c_a} \tag{A5}$$

or

$$|U_\varepsilon| \leq 2\delta \frac{1 + \varepsilon}{c_o - c_a} \tag{A6}$$

The average standard deviation, σ, in the range of $0 < \varepsilon < 1$ can be calculated by

$$\sigma = \frac{2\delta}{c_o - c_a}\sqrt{\int_0^1 (1+\varepsilon)^2 d\varepsilon} = 3.06\frac{\delta}{c_o - c_a} \tag{A7}$$

The CO_2 gas analyser used in the experiments has an overall uncertainty of 1.5% of each of its range. For the concentration measurements, the 1% range was used. The nominal value of c_o was set close to the 1% concentration; the value of c_a was close to zero, equivalent to the CO_2 concentration in the ambient air. Hence $\delta/(c_o - c_a) \approx 0.015$, and it follows that $\sigma \approx 0.046$.

2. Non-dimensional sealing flow parameter Φ_0

The definition for Φ_0 can be expressed as follows:

$$\Phi_0 = \frac{C_{w,o}}{2\pi G_c Re_\phi} = \frac{\dot{m}}{2\pi G_c \rho \Omega b^3} \tag{A8}$$

where the air density ρ was determined using the ideal gas law, based on the reference pressure (p_{ref}) and temperature (T_{ref}) measured in the wheel-space, so that

$$\Phi_0 = \frac{C_{w,o}}{2\pi G_c Re_\phi} = \frac{\dot{m} R T_{ref}}{2\pi s_c p_{ref} \Omega b^2} \tag{A9}$$

Based on the Taylor Series Method, the uncertainty in Φ_0 is given by

$$\begin{aligned}\frac{U_{\Phi_0}{}^2}{\Phi_0{}^2} = &\left[UMF_{\dot{m}}\left(\frac{U_{\dot{m}}}{\dot{m}}\right)\right]^2 + \left[UMF_{T_{ref}}\left(\frac{U_{T_{ref}}}{T_{ref}}\right)\right]^2 + \left[UMF_{s_c}\left(\frac{U_{s_c}}{s_c}\right)\right]^2 \\ &+ \left[UMF_{p_{ref}}\left(\frac{U_{p_{ref}}}{p_{ref}}\right)\right]^2 + \left[UMF_{\Omega}\left(\frac{U_{\Omega}}{\Omega}\right)\right]^2 + \left[UMF_{b}\left(\frac{U_{b}}{b}\right)\right]^2\end{aligned} \tag{A10}$$

where UMF denotes the uncertainty magnification factor. For each one of variables (x_i) in the definition of parameter y, it follows that $UMF_{x_i} = (x_i/y)\cdot(\delta y/\delta x_i)$.

The values of the UMF for each variable are tabulated in Table A1.

Table A1 *UMF* Values for Φ_0

Variable	Value of *UMF*
$\dot{m}$	1
T_{ref}	1
s_c	-1

p_{ref}	-1
Ω	-1
b	-2

The measurement uncertainties and nominal values for the variables are stated in Table A2. Over the range of experimental conditions, the uncertainty for Φ_0 was assessed using Eq. (A3): $U_{\Phi_0}/\Phi_0 <$ 3.5%.

Table A2 Measurement uncertainties and nominal values for the variables of parameter Φ_0

Variable	Measurement uncertainty	Nominal value
$\dot{m}$	0.00015 kg/s	Variable
T_{ref}	0.5 K	288 K
s_c	0.05 mm	2 mm
p_{ref}	8 Pa	1000 Pa (gauge)
Ω	1 rpm	3000 rpm
b	0.1 mm	190 mm

3. Non-dimensional peak-to-trough pressure difference ΔC_p in a vane pitch for $C_F = 0.38$

The definition for ΔC_p can be expressed as follows:

$$\Delta C_p = \frac{(p_{2,max} - p_{2,min})}{(1/2)\,\rho\Omega^2 b^2} = \frac{(p_{2,max} - p_{2,min})RT_{ref}}{(1/2)\,p_{ref}\Omega^2 b^2} \tag{A11}$$

where ρ was determined using the ideal gas law, as discussed previously for the parameter Φ_0. $p_{2,max}$ and $p_{2,min}$ are the maximum and minimum static pressure over a vane pitch in the annulus.

The uncertainty in ΔC_p is given by

$$\begin{aligned}\frac{{U_{\Delta C_p}}^2}{{\Delta C_p}^2} = &\left[UMF_{p_{2,max}}\left(\frac{U_{p_{2,max}}}{p_{2,max}}\right)\right]^2 + \left[UMF_{p_{2,min}}\left(\frac{U_{p_{2,min}}}{p_{2,min}}\right)\right]^2 \\ &+ \left[UMF_{T_{ref}}\left(\frac{U_{T_{ref}}}{T_{ref}}\right)\right]^2 + \left[UMF_{p_{ref}}\left(\frac{U_{p_{ref}}}{p_{ref}}\right)\right]^2 \\ &+ \left[UMF_{\Omega}\left(\frac{U_{\Omega}}{\Omega}\right)\right]^2 + \left[UMF_{b}\left(\frac{U_{b}}{b}\right)\right]^2\end{aligned} \tag{A12}$$

The values and expressions of the UMF for each variable are tabulated in Table A3.

Table A3 *UMF* for ΔC_p

Variable	Value of *UMF*
$p_{2,max}$	$\frac{p_{2,max}}{p_{2,max} - p_{2,min}}$
$p_{2,min}$	$\frac{-p_{2,min}}{p_{2,max} - p_{2,min}}$
T_{ref}	1
p_{ref}	-1
Ω	-2
b	-2

The measurement uncertainties and nominal values for the variables are stated in Table A4. Over the range of experimental conditions, the uncertainty for ΔC_p is assessed using Eq. (A7): $U_{\Delta C_p}/\Delta C_p \approx$ 1.2%.

Table A4 Measurement uncertainties and nominal values for the variables of parameter ΔC_p

Variable	Measurement uncertainty	Nominal value
$p_{2,max}$	8 Pa	1500 Pa (gauge)
$p_{2,min}$	8 Pa	450 Pa (gauge)
T_{ref}	0.5 K	288 K
p_{ref}	8 Pa	1500 Pa (gauge)
Ω	1 rpm	3000 rpm
b	0.1 mm	190 mm

4. Swirl ratio β

The definition for β can be expressed as follows:

$$\beta = \frac{V_\phi}{\Omega r} = \frac{\left(\frac{(p_T - p)RT_{ref}}{(1/2)\,p_{ref}}\right)^{1/2}}{\Omega r} \tag{A13}$$

where p_T and p are the local total and static pressure respectively at a radial location r in the wheel-space.

The uncertainty in β is given by

$$\frac{U_\beta{}^2}{\beta^2} = \left[UMF_{p_T}\left(\frac{U_{p_T}}{p_T}\right)\right]^2 + \left[UMF_p\left(\frac{U_p}{p}\right)\right]^2 + \left[UMF_{T_{ref}}\left(\frac{U_{T_{ref}}}{T_{ref}}\right)\right]^2 + \left[UMF_{p_{ref}}\left(\frac{U_{p_{ref}}}{p_{ref}}\right)\right]^2 + \left[UMF_\Omega\left(\frac{U_\Omega}{\Omega}\right)\right]^2 + \left[UMF_r\left(\frac{U_r}{r}\right)\right]^2 \quad \text{(A14)}$$

The values and expressions of the UMF for each variable are tabulated in Table A5.

Table A5 *UMF* for β

Variable	Value of *UMF*
p_T	$\frac{p_T}{2(p_T - p)}$
p	$\frac{-p}{2(p_T - p)}$
T_{ref}	$\frac{1}{2}$
p_{ref}	$-\frac{1}{2}$
Ω	-1
r	-1

The measurement uncertainties and nominal values for the variables are stated in Table A6. Over the range of experimental conditions, the uncertainty for β was assessed using Eq. (A9): $U_\beta/\beta < 1.7\%$.

Table A6 Measurement uncertainties and nominal values for the variables of parameter β

Variable	Measurement uncertainty	Nominal value
p_T	8 Pa	Variable
p	8 Pa	1000 Pa (gauge)
T_{ref}	0.5 K	288 K
p_{ref}	8 Pa	1000 Pa (gauge)
Ω	1 rpm	3000 rpm
r	0.1 mm	182 mm

Appendix II: Important equations for the Bath orifice model

The theoretical orifice model developed at University of Bath (Owen (2011a,b)) is based on an imaginary 'orifice ring' for a simple axial-clearance rim seal. The ingress and egress were assumed to cross the ring through flow areas, δA_i and δA_e respectively. The sum of these two areas was equal to the area of the seal clearance, A_c. While location 1 and 2 denoted the wheel-space and the annulus respectively, ingress flowed from the annulus where static pressure was p_2 to the wheel-space where the pressure was p_1. Conversely, egress started in the wheel-space and emerged in the annulus. The model used variations of Bernoulli's equation, including the swirl terms, to correlate the sealing flow rate and the pressure difference across the rim seal.

The fluid is assumed to be inviscid inside the separate stream tubes for ingress and egress, where there is continuity of mass and energy. Across the orifice ring, however, there is a discontinuity in the pressure. Conservation of angular momentum is satisfied which is equivalent to that rV_ϕ remains constant. In addition, $(r_2 - r_1)/r_1 \ll 1$ and ${V_{r,1}}^2 \ll {V_{r,2}}^2$ for egress flow and vice versa for ingress flow. Due to the inviscid assumption, discharge coefficients: $C_{d,i}$ for ingress flow and $C_{d,e}$ for egress flow are therefore used to account for viscous losses.

Although compressible flow occurs in the annulus for a turbine, Owen (2011a) suggested that incompressible orifice equations are acceptably accurate for the theoretical model. For incompressible flow, the Bernoulli's equation applies to the flow through the stream tubes, hence

$$p_1 + \frac{1}{2}\rho {U_1}^2 = p_2 + \frac{1}{2}\rho {U_2}^2 \tag{A15}$$

For egress, it is assumed that ${V_{z,1}}^2, {V_{r,1}}^2 \ll {V_{\phi,1}}^2$, $r_1 V_{\phi,1} = r_2 V_{\phi,2}$, and ${U_2}^2 \approx {V_{\phi,2}}^2 + {V_{r,2}}^2$, so that

$$V_{r,e} = \left\{ 2\frac{p_1 - p_2}{\rho} + {V_{\phi,1}}^2 \left[1 - \left(\frac{r_1}{r_2} \right)^2 \right] \right\}^{1/2} \tag{A16}$$

where $V_{r,e}$ is used in place of $V_{r,2}$ for egress.

For ingress, the equivalent equation is

$$V_{r,i} = \left\{ 2\frac{p_2 - p_1}{\rho} - {V_{\phi,2}}^2 \left[\left(\frac{r_2}{r_1} \right)^2 - 1 \right] \right\}^{1/2} \tag{A17}$$

where $V_{r,i}$ is used in place of $V_{r,1}$ for ingress.

The swirl ratio β used in this model is defined as

$$\beta = \frac{V_\phi}{\Omega b} \tag{A18}$$

Therefore Eq.(3.2) and Eq.(3.3) can be written as

$$\frac{V_{r,e}}{\Omega b} = \left\{ \frac{p_1 - p_2}{(1/2)\,\rho\Omega^2 b^2} + {\beta_1}^2 \left[1 - \left(\frac{r_1}{r_2} \right)^2 \right] \right\}^{1/2} \tag{A19}$$

And

$$\frac{V_{r,i}}{\Omega b} = \left\{ \frac{p_2 - p_1}{(1/2)\,\rho\Omega^2 b^2} - {\beta_2}^2 \left[\left(\frac{r_2}{r_1} \right)^2 - 1 \right] \right\}^{1/2} \tag{A20}$$

The above two equations are valid both RI and EI ingress. At this point, discharge coefficients are introduced to the equations.

$$\frac{V_{r,e}}{\Omega b} = C_{d,e} \sqrt{C_{\beta_1} - C_p} \tag{A21}$$

when $C_p \geq C_{\beta_2}$. And

$$\frac{V_{r,i}}{\Omega b} = C_{d,i} \sqrt{C_p - C_{\beta_2}} \tag{A22}$$

when $C_{\beta_1} \geq C_p$. where

$$C_p = \frac{p_2 - p_1}{(1/2)\rho\Omega^2 b^2} \tag{A23}$$

$$C_{\beta_1} = {\beta_1}^2 \left(1 - \frac{{r_1}^2}{{r_2}^2} \right) \tag{A24}$$

$$C_{\beta_2} = {\beta_2}^2 \left(\frac{{r_2}^2}{{r_1}^2} - 1 \right) \tag{A25}$$

The mass flow rate of ingress ($\dot{m}_i$) and egress ($\dot{m}_e$) could be calculated by integrating the velocity components across the seal as follows:

$$\dot{m}_e = \rho \int_{A_e} V_{r,e}\, dA_e \tag{A26}$$

And

$$\dot{m}_i = \rho \int_{A_i} V_{r,i}\, dA_i \tag{A27}$$

The superposed mass flow rate $\dot{m}_0$ was given by

$$\dot{m}_0 = \dot{m}_e - \dot{m}_i \tag{A28}$$

The sealing effectiveness is defined as

$$\varepsilon = 1 - \frac{\dot{m}_i}{\dot{m}_e} = 1 - \frac{C_{w,i}}{C_{w,e}} = \frac{C_{w,o}}{C_{w,e}} \tag{A29}$$

where $C_w = \dot{m}/\mu b$. The effectiveness $\varepsilon = 0$ when no sealing flow is superposed, and $\varepsilon = 1$ when there is no ingress into the system.

Relevant non-dimensional parameters are defined for further analysis. The non-dimensional sealing flow parameter, Φ_0, was defined to combine the effects of $C_{w,o}, G_c$ and Re_ϕ as follows:

$$\Phi_0 = \frac{C_{w,o}}{2\pi G_c Re_\phi} \tag{A30}$$

where G_c is the seal clearance ratio, $G_c = s_c/b$. This parameter is an inviscid parameter due to the cancellation of viscous terms included in both $C_{w,o}$ and Re_ϕ. An alternative definition may be more appropriate:

$$\Phi_0 = \frac{U}{\Omega b} \tag{A31}$$

where U denotes the bulk mean radial velocity of sealing flow through the rim-seal clearance. Φ_{min} is the minimum value of Φ_0 required to seal the wheel-space completely, so that

$$\Phi_{min} = \frac{U_{min}}{\Omega b} = \frac{C_{w,min}}{2\pi G_c Re_\phi} \tag{A32}$$

Eq.(3.15) can be written as

$$\varepsilon = 1 - \frac{\dot{m}_i}{\dot{m}_e} = 1 - \frac{\Phi_i}{\Phi_e} = \frac{\Phi_0}{\Phi_e} \tag{A33}$$

where Φ_i and Φ_e are the flow parameters for ingress and egress respectively.

The general solution for RI incompressible orifice equation is given by

$$\Phi_{min,RI} = C_{d,e} {C_{\beta_1}}^{1/2} \left(1 - \Gamma_\beta\right)^{1/2} \tag{A34}$$

where $\Gamma_\beta = C_{\beta_2}/C_{\beta_1} \approx (\beta_2/\beta_1)^2$

and

$$\frac{\Phi_{e,RI}}{\Phi_{min,RI}} = \frac{1 - \Gamma_p}{\Gamma_T} \tag{A35}$$

$$\frac{\Phi_{i,RI}}{\Phi_{min,RI}} = \frac{{\Gamma_c}^2 \left(\Gamma_p - \Gamma_\beta\right)}{\Gamma_T} \tag{A36}$$

And

$$\frac{\Phi_o}{\Phi_{min,RI}} = \frac{\Phi_{e,RI} - \Phi_{i,RI}}{\Phi_{min,RI}} = \frac{1 - \Gamma_p - {\Gamma_c}^2 \left(\Gamma_p - \Gamma_\beta\right)}{\Gamma_T} \tag{A37}$$

where $\Gamma_c = C_{d,i}/C_{d,e}$, $\Gamma_p = C_p/C_{\beta_1}$ and $\Gamma_T = \left(1 - \Gamma_\beta\right)^{1/2} \left[\left(1 - \Gamma_p\right)^{1/2} + \Gamma_c \left(\Gamma_p - \Gamma_\beta\right)^{1/2}\right]$.

It follows that the sealing effectiveness is given by

$$\varepsilon = 1 - \frac{\Phi_i}{\Phi_e} = \frac{1 + \Gamma_c{}^2\Gamma_\beta - \Gamma_p\left(1 + \Gamma_c{}^2\right)}{1 - \Gamma_p} \tag{A38}$$

A simplified RI case is discussed when the external swirl is negligible ($\Gamma_\beta = 0$). Therefore Eq.(A29), Eq.(A32) and Eq.(A33) can be simplified to

$$\Phi_{min,RI} = C_{d,e}{C_{\beta_1}}^{1/2} \tag{A39}$$

$$\frac{\Phi_o}{\Phi_{min,RI}} = \frac{1 - \Gamma_p\left(1 + \Gamma_c{}^2\right)}{\Gamma_T} \tag{A40}$$

and

$$\varepsilon = \frac{1 - \Gamma_p\left(1 + \Gamma_c{}^2\right)}{1 - \Gamma_p} \tag{A41}$$

This can be expressed as

$$\Gamma_p = \frac{1 - \varepsilon}{1 - \varepsilon + \Gamma_c{}^2} \tag{A42}$$

It follows that

$$\frac{\Phi_0}{\Phi_{min,RI}} = \frac{\varepsilon}{[1 + (1 - \varepsilon)^{1/2}]\left[1 + \Gamma_c{}^{-2}(1 - \varepsilon)\right]^{1/2}} \tag{A43}$$

when $\Phi_0 \ll \Phi_{min,RI}$; $\varepsilon = 1$ when $\Phi_0 > \Phi_{min,RI}$. Eq. (A38) was referred to as the RI effectiveness equation by Sangan *et al*. (2013b).

Owen (2011b) detailed the solving of orifice equations analytically for EI ingress. Only the principle solutions are described in this section.

With a 'saw-tooth' model used to approximate the circumferential pressure distribution in the annulus. the orifice equations were solved analytically, so that

$$\Phi_{min,EI} = \frac{2}{3}C_{d,e}{\Delta C_p}^{1/2} \tag{A44}$$

where ΔC_p is the non-dimensional pressure distribution driving the EI ingress, which is defined as

$$\Delta C_p = \frac{\Delta p}{(1/2)\rho\Omega^2 b^2} \tag{A45}$$

where Δp is the peak-to-trough pressure difference in a vane pitch.

A normalised pressure parameter, g, is introduced to account for the pressure difference between the annulus and the wheel-space, so that

$$g = \frac{p_1 - p_{2,min}}{\Delta p} \tag{A46}$$

The solution for EI ingress can be expressed in terms of g:

$$\frac{\Phi_0}{\Phi_{min,EI}} = g^{3/2} - \Gamma_c(1-g)^{3/2} \tag{A47}$$

and

$$\varepsilon = 1 - \Gamma_c\left(\frac{1-g}{g}\right)^{3/2} \tag{A48}$$

It follows that

$$\frac{\Phi_0}{\Phi_{min,EI}} = \frac{\varepsilon}{\left[1 + \Gamma_c{}^{-2/3}(1-\varepsilon)^{2/3}\right]^{3/2}} \tag{A49}$$

when $\Phi_0 \ll \Phi_{min,EI}$; $\varepsilon = 1$ when $\Phi_0 > \Phi_{min,EI}$. The above equation was referred to as the EI effectiveness equation by Sangan *et al*. (2013a). The orifice model for EI ingress uncoupled ingress from its driving potential, ΔC_p, as the variation of ε with Φ_0 only depends on $\Phi_{min,EI}$ and Γ_c. However, care must be taken in selecting the position in the annulus where ΔC_p is evaluated, when experimentally determined $\Phi_{min,EI}$ is extrapolated to engine conditions.

Appendix III: Calibrations of instrumentation

Calibrations were individually conducted for instrumentation employed to measure pressure, rotor speed and displacement. Druck® transducers were used for time-averaged pressure measurements. Kulte® fast-response pressure probes were used for unsteady pressure measurements. A Compact® laser optical speed sensor was used to measure the rotational speed. Sensonics® eddy current proximity probes were used to monitor the rotor displacement during operation of the rig.

Table A7 details the operating features for all instrumentation, evaluated by calibrations conducted during the commissioning of the facility. The acquired calibration functions were applied in the LabVIEW code used to control the rig and record measurements. Therefore the voltage outputs from the transducers were transformed to meaningful physical properties that can be displayed and monitored constantly during experiments. No interference was found when all transducers were in concurrent uses.

Table A7 Operating features of the calibrated instrumentation

Transducer	**Calibration function**	**x**	**y**	$\mathbf{R^2}$	**Standard deviation**		
					σ_{slope}	$\sigma_{intercept}$	σ_y
Druck® #1	$y = 0.14 * x + 0.0048$	Gauge pressure (mbar)	Voltage (volt)	1	5.7×10^{-5}	1.8×10^{-3}	3.4×10^{-3}
Druck® #2	$y = 0.14 * x - 0.023$	Gauge pressure (mbar)	Voltage (volt)	1	2.0×10^{-4}	7.6×10^{-3}	1.5×10^{-2}
Kulite® XCQ-062	$y = 0.060 * x + 0.18$	Gauge pressure (mbar)	Voltage (volt)	1	2.6×10^{-5}	1.1×10^{-3}	2.2×10^{-3}
Kulite® XT-140	$y = 0.056 * x - 0.015$	Gauge pressure (mbar)	Voltage (volt)	1	8.8×10^{-5}	3.6×10^{-3}	7.4×10^{-3}
Compact®	$y = 0.0015 * x + 0.041$	Rotor speed (rpm)	Voltage (volt)	1	2.1×10^{-5}	4.1×10^{-2}	4.4×10^{-2}
Sensonics® #1	$y = -9.7 * x + 9.9$	Displacement (mm)	Voltage (volt)	1	2.5×10^{-2}	2.4×10^{-2}	3.8×10^{-2}
Sensonics® #2	$y = -9.7 * x + 9.9$	Displacement (mm)	Voltage (volt)	1	1.2×10^{-1}	1.3×10^{-1}	2.1×10^{-1}